NASA CONTRACTOR REPORT

NASA CR-134883

NASA CR-134883

PREDICTION OF EXTERNALLY BLOWN FLAP NOISE AND TURBOMACHINERY STRUT NOISE

By Martin R. Fink

Prepared by

UNITED TECHNOLOGIES RESEARCH CENTER

East Hartford, Conn. 06108

for Lewis Research Center

OCT 1975
RECEIVED
NASA STI FACILITY
INPUT BRANCH

NATIONAL AERONAUTICS AND SPACE ADMINISTRATION, WASHINGTON, D.C. AUGUST 1975

Page intentionally left blank

CONTENTS

CONTENTS (Cont'd)

PREDICTION OF EXTERNALLY BLOWN FLAP NOISE
AND TURBOMACHINERY STRUT NOISE

By Martin R. Fink

United Technologies Research Center

SUMMARY

Methods were developed for predicting externally blown flap (EBF) noise and turbomachinery strut noise. The method for under-the-wing EBF includes separately calculated contributions from (1) lift dipoles perpendicular to each wing and flap segment and caused by large-scale vortex structure of the exhaust jet, (2) trailing edge noise from exhaust jet turbulence convected past the last trailing edge, (3) direct and reflected quadrupole jet noise from the initial undistorted portion of the exhaust jet, and (4) direct and reflected quadrupole jet noise from the deflected distorted portion of the exhaust jet. Resulting predictions of amplitudes and spectra were in good agreement with data from small-scale models over the available range of exhaust velocity, flap deflection, exhaust nozzle position relative to the wing, and ratio of exhaust nozzle diameter to wing chord. Measured changes of directivity shape with exhaust velocity and of spectrum shape with flap deflection were predicted to be caused by deflected-jet quadrupole noise.

Noise from upper-surface-blowing EBF was calculated as the sum of (1) lift dipoles perpendicular to each flap segment, (2) trailing edge noise, (3) quadrupole jet noise from the portion of the exhaust jet downstream of the wing trailing edge, (4) quadrupole noise from a deflected distorted jet if a canted nozzle was used, and (5) measured deflector noise if a jet deflector plate was used. Because upper-surface-blowing flaps are deflected away from the exhaust jet rather than into the jet, calculated lift dipole noise is decreased rather than increased by flap deflection. Resulting calculated directivities are relatively omnidirectional rather than being dominated by a dipole lobe perpendicular to the deflected flaps. Predicted amplitudes and spectra are in good agreement with data for small-scale models having circular or D-nozzle exhaust jets with deflectors. Slot nozzle configurations with 5:1 aspect ratio were louder, and those with 10:1 aspect ratio were quieter, than was calculated for area-equivalent circular nozzles.

A semi-empirical method for predicting dipole noise radiation from a strut with incident turbulence was in good agreement with data. It predicted a more rapid high-frequency spectrum decay than that given by other analyses. Tests of numerous leading and trailing-edge modifications intended to reduce noise from struts and splitters with incident turbulence showed that most were ineffective. However, up to 7dB noise reduction over a limited

frequency range was achieved by replacing the forward 9% chord with perforated plate backed by a bulk acoustic absorber.

Radial turbulence in a turbofan exit duct was found to have an amplitude of about five percent that corresponded to mean velocity defects in the rotor viscous wake. Duct turbulence was not isotropic, and radial turbulence spectra had more high-frequency content than would be predicted from the measured radial integral scale lengths. Use of these spectra and a dipole noise radiation equation from NASA SP-346 gave general prediction of measured aft-radiated sound power caused by a splitter ring in a full-scale fan exit duct. The semi-empirical method developed herein greatly underestimated this noise.

SYMBOLS

Values of dimensional quantities are given in both SI and U.S. Customary Units.

a speed of sound, m/sec (ft/sec)

A_j nozzle exit area, m^2 (ft^2)

b strut span, m (ft)

c airfoil chord, m (ft)

C_L lift coefficient, $F/(1/2 \rho U^2 bc)$

D nozzle exit diameter, m (ft)

E spectral density of turbulence intensity, m^2/sec (ft^2/sec)

f frequency, Hz

F lift force, n (lb)

h height from vortex trajectory to scrubbed surface, m (ft)

H height of USB nozzle lower lip above wing trailing edge, m (ft)

I acoustic intensity, w/m^2 (w/ft^2)

K nondimensional empirical constant for scrubbing noise

ℓ	turbulence integral scale length, m (ft)
$\mathcal{L}$	ratio of unsteady lift coefficient to quasi-steady lift coefficient
M	Mach number, U/a
p	acoustic pressure, n/m^2 (lb/ft^2)
r	far-field radius, m (ft)
St	Strouhal number, fD/U
T	static temperature, $^\circ C$ ($^\circ F$)
U	flow velocity, m/sec (ft/sec)
$\overline{v^2}$	mean square turbulence upwash velocity, m^2/sec^2 (ft^2/sec^2)
W	acoustic power, w
X	streamwise distance from nozzle exit plane to trailing edge, m (ft)
α	impingement angle of nozzle exit flow relative to last flap segment, deg
β	ratio of turbulence integral scale length to half-chord, $2\ell/c$
θ	measurement direction angle in plane containing nozzle centerline, deg
ρ	density, kg/m^3 ($lb\ sec^2/ft^4$)
σ_0	angular reduced frequency, $\omega c/2U$
ω	angular frequency, $2\pi f$

Subscripts

a	ambient
c	convective
i	impingement
ISA	International Standard Atmosphere
J	jet

n	segment number for wing and flap panels
N	nozzle exhaust
ref	reference value
T	trailing edge
∞	ambient atmospheric condition

INTRODUCTION

Noise generated by solid bodies in the presence of engine airflow determines the inherent minimum noise of installed aircraft engines. For example, acoustically treated splitters within the engine inlet and exhaust ducts can attenuate turbomachinery noise but produce noise at their outer edges. Internal struts, necessary for structural support of the engine and splitters, are likely to be immersed in high-velocity turbulent engine airflows. Externally blown flaps utilize engine exit airflow to generate wing supercirculation lift force at low flight speeds while impinging the high turbulence levels of a jet mixing region onto the wing surface. In all these cases, a solid surface of finite extent is scrubbed by airflow containing velocity and pressure fluctuations generated upstream, within the boundary layer and within the near wake. The same relatively small number of basic aeroacoustic mechanisms should be present for all of these examples; the magnitude of noise generated by each mechanism should be predictable if the airstream mean velocity, rms turbulence intensity, integral scale lengths, and turbulence spectrum shape are known.

The first portion of this investigation had examined the processes by which noise is generated by an airfoil in a turbulent airstream, turbulence convected past a trailing edge, and an exhaust jet passing near an airfoil. Results of those experimental studies of simplified configurations, and comparisons with theories, were reported in references 1 through 3. An additional type of noise, quadrupole noise generated by an exhaust jet impinging against and deflected by a large solid surface, was also found to be important. A next step in this investigation would be to determine whether a combination of recommended analyses for these noise mechanisms would be a useful noise prediction design tool. These predictions could be tested by comparing with available far-field data for practical strut, splitter plate, and externally blown flap (EBF) installations. Small-scale EBF data are available for a much larger range of geometric parameters than those from relatively large or full-scale models. Therefore, the EBF prediction method was evaluated by comparisons with data for small-scale configurations selected and tested at NASA Lewis Research Center.

EXTERNALLY BLOWN FLAP NOISE PREDICTION METHOD

Basic Concepts

Noise radiation from externally blown flap configurations is assumed to be the sum of noise radiation generated by each of three aeroacoustic mechanisms. Typical directivity patterns and relative amplitudes are sketched in figure 1 for each noise mechanism as it occurs for under-the-wing (UTW) and upper-surface-blowing (USB) configurations. Additional processes such as refraction are neglected. Scrubbing noise, sketched in the upper part of this figure, is defined as an acoustically compact lift dipole noise oriented perpendicular to each chordwise segment of the wing. Such noise has also been called fluctuating-lift noise and inflow noise. As shown experimentally in references 1 and 3, large-scale vortex instabilities of the exhaust jet were found to generate local fluctuations of airfoil loading. These fluctuations were coherent along the width of the region scrubbed by the exhaust jet. They moved downstream along the surface at the eddy convection velocity of about 80 percent of local maximum velocity. Local pressure fluctuations induced by this process resemble those caused by discrete vortices convected past an isolated airfoil. Amplitudes of these pressure fluctuations are small compared with pressure fluctuations generated by the shear-layer mixing process and impressed onto the scrubbed surface. Thus the regions having strongest surface pressure fluctuations generally do not have strongest local dipole source strength. This result that local dipole source strength is not necessarily proportional to local surface pressure fluctuation has been found in other studies (e.g., reference 4) of noise generation processes investigated by cross-correlation techniques.

As sketched in the upper part of this figure, far-field scrubbing noise from the undeflected portion of a wing and from each separately deflected vane and flap was represented by a separate dipole. Because a UTW flap (upper left sketch) is deflected into the jet exhaust and therefore closer to the vortices at the outer edge of the jet, the dipole associated with the aft flap segment is relatively strong. In contrast, an USB flap (upper right sketch) is deflected away from the jet exhaust. Its strongest dipole tends to be that from the undeflected part of the wing.

Trailing edge noise, sketched in the second row from the top, has a directivity pattern that is strongest directly upstream from the deflected trailing edge. Other properties of trailing edge noise are discussed in references 1 and 2. Noise generated at intermediate trailing edges such as that of the undeflected forward part of the wing are assumed to be canceled by leading edge noise from the immediately adjacent vane or flap. Thus the calculation method developed here does not predict more trailing edge noise for multiple slotted flaps than for single slotted or unslotted flaps. Note that the directivity pattern of trailing edge noise tends to fill the gap in the upper forward quadrant between lobes of scrubbing noise.

Quadrupole noise, sketched in the third row, is represented as a sum of two components for both UTW and USB installations. One component is the jet mixing noise from undistorted, undeflected parts of the exhaust jet. This noise can be calculated or measured as that for the isolated exhaust nozzle, plus 3 dB to account for reflection of noise by the wing surface. Such noise is radiated beneath an UTW and above an USB configuration. UTW installations also generate a quadrupole noise from the region where the jet is deflected by the flap. This type of noise was called impact noise in reference 5. For conventional UTW installations, this quadrupole noise generated by deflection of the jet is stronger than that from the undeflected jet. This noise is radiated both above and below a slotted flap. USB configurations generate downward-radiated quadrupole noise from the shear layer that forms beneath the deflected exhaust jet downstream of the trailing edge. Finally, as sketched in the lower right portion of the figure, the flow deflection device which produces attached flow of the USB exhaust jet to the deflected flap can produce noise. Flow deflectors can generate dipole noise, and canted nozzles (not sketched) can generate quadrupole impact noise. Such noise is generally shielded by the wing but is radiated above the wing and deflected flap.

The major new feature of this analysis is the attribution of scrubbing noise to formation of large-scale vortex instabilities in the exhaust jet. Instabilities of this type have been modeled analytically as random trains of ring vortices. Impingement of these vortices against a rigid surface has been shown to merge part of each ring into the surface boundary layer. The remainder of each ring is stretched as it is convected downstream near the edge of the attached jet. Discrete vortices convected along an airfoil are known to induce local loadings concentrated near the vortex. The loading strength is a function of vortex chordwise position and varies approximately inversely with distance between the vortex and surface at constant chord. Too small a spacing will cause viscous dissipation of the vortex, reducing the scrubbing noise. Amplitude of this noise is calculated by an empirical process. If the spectrum of vortex strength is that for jet turbulence and the lift force response is that for a discrete vortex in subsonic compressible flow, power spectral density of an acoustically compact source should vary as frequency squared at low reduced frequencies and frequency to the -7/3 power at high reduced frequencies. The resulting one-third-octave slopes of 9 dB/octave and -4 dB/octave for low and high reduced frequencies, dipole directivity, and dependence on local velocity to the sixth power are typical properties of observed scrubbing noise.

The concept of scrubbing noise as a lift dipole noise radiated on both sides of a wing and deflected flap, but generated by large-scale coherent vortices in the exhaust jet on one side of the wing and flap, is fundamental to the prediction method. This explanation was validated by tests described in reference 1 in which far-field spectra measured on both sides of a wing were compared. If this concept is correct, spectra measured on the side that is not scrubbed by the jet should be a sum of trailing-edge noise and lift-dipole scrubbing noise. Spectra measured at the same angle from the wing

chord plane, but on the side scrubbed by the exhaust jet, should be the sum of those two noise processes plus jet mixing noise radiated directly to the far field, and jet mixing noise reflected from the wing to the far field. To test this assumption, spectra measured at three angles from the exhaust nozzle in both the scrubbed and unscrubbed directions from an undeflected wing were compared in figure 34 of reference 1. Spectra for the isolated nozzle at the same direction angles and pressure ratios also were shown. Part of this figure for 250 m/sec exhaust velocity is reproduced as figure 2 herein. At directions 60° and 90° from upstream, spectra measured on the scrubbed side (dotted line) were closely predicted (circles) by taking the spectra for the nozzle alone (dash line), adding 3 dB for reflection of jet noise from the wing, and adding that sum to the spectrum measured on the unscrubbed side (solid line). At aft directions such as 120°, spectra measured on the unscrubbed side were found (not shown) to contain significant high-frequency jet mixing noise from the portion of the jet exhaust downstream of the wing trailing edge. Spectra measured on the scrubbed side were found to be better predicted by adding the spectra measured with the nozzle alone to that for the unscrubbed side, neglecting the reflected jet noise. Further comparisons of spectra measured on the unscrubbed side at different directions and exhaust velocities, described in reference 1, substantiated that those spectra were a sum of two simpler spectra. One of these components had maximum amplitude at a relatively low frequency, decayed rapidly in amplitude at higher frequencies, and had the velocity and direction-angle dependence of trailing-edge noise. The other component had a broader spectrum with less rapid decay. Its amplitude varied with velocity to the sixth power, and its directivity was that of a lift dipole. This latter noise component is what has been described herein as scrubbing noise.

The same type of spectrum comparisons should be valid for all other tests conducted with UTW or USB configurations having retracted flaps and small wing incidence relative to the nozzle exit direction. Data were presented in references 6 and 7 for small and large UTW models with retracted flaps. As shown in figure 6(c) of reference 6 and figure 9(b) of reference 7, measured OASPL directivity patterns were approximately identical at the same angles above and below the wing for all but the highest pressure ratios. That is, OASPL on the unscrubbed side was about equal to OASPL on the scrubbed side when jet mixing noise was small. This result could occur only if scrubbing noise is the same on both the scrubbed and unscrubbed sides. Far-field spectra were measured approximately normal to the wing (90° from the nozzle exhaust on the unscrubbed side and 80° from the nozzle exhaust on the scrubbed side) of the small model of reference 6. These spectra, and those at 90° from the nozzle alone, are compared in figure 3 for pressure ratios of 1.25 and 1.7. As with figure 2, a prediction of spectra in the scrubbed direction was obtained by adding 3 dB to spectra for the nozzle alone to include jet mixing noise reflected from the wing, and adding this to spectra measured on the unscrubbed side. The result (circle symbols) is in good agreement with spectra measured on the scrubbed side (dotted lines) except for frequencies above 10 kHz. This good agreement validates the assumption that the

sum of trailing edge noise and scrubbing noise is the same on both the scrubbed and unscrubbed sides of the wing. As had been shown in figure 8 of reference 8, measured OASPL directivity above and below this configuration at these two pressure ratios was closely predicted by a sum of trailing edge noise, scrubbing noise represented as a lift dipole normal to the wing, and direct plus reflected jet mixing noise. It should be noted that the scrubbing noise mechanism hypothesized by this author in reference 8 was disproved by tests reported in references 1 and 3, and is different from that described herein.

Deflected-Jet Quadrupole Noise

Overall Sound Pressure Levels

As a start toward predicting quadrupole noise of a deflected jet, the NASA data of reference 9 for a jet impinging on a large flat board were examined. Acoustic data for those tests had been measured at impingement angles α of 15°, 30°, 60°, and 90° from the nozzle inlet direction to the board. Measurements were taken in a plane containing the nozzle centerline and inclined at the azimuth angle φ relative to the plane of symmetry (the plane containing the nozzle centerline and perpendicular to the flat board). Most data were taken in the flyover azimuthal plane ($\varphi = 0°$). Microphones were located in a circle centered at the impingement point (where the extended nozzle centerline intersected the flat board). Position angle θ was measured from the nozzle inlet direction, positive away from the board. All tests at impingement angles other than 90° were conducted with the distance from the impingement point to the nozzle exit held constant at 7.05 nozzle diameters.

The data correlation developed in reference 9 utilized a spatial integration of measured sound pressure levels to obtain sound power level spectra and total sound power level. Sound power for the nozzle alone was subtracted from these quantities to obtain impingement-only spectra and power. Impingement-only total sound power was shown to correlate with impingement velocity (velocity measured at the location of the impingement point for the nozzle without the board) to the eighth power, diameter squared, and sine squared of the impingement angle. This type of correlation would have been useful if impingement-only sound power level could then be distributed with the proper directivity and spectrum shape. However, two major difficulties are encountered. Directivity and spectrum of sound pressure level will be shown to be significantly different at large and small direction angles from the deflected jet. Directivity also can be shown to depend on reflection of acoustic waves from the flat board, in addition to impingement which increases the total quadrupole acoustic power.

The effect of impingement angle on noise radiation pattern in the flyover plane was shown in figure 4 of reference 9 and is reproduced as figure 4 herein. All data were obtained at 286 m/sec nozzle exhaust velocity (256 m/sec impingement velocity). Overall sound pressure levels (OASPL) are plotted as functions of direction angle from upstream direction along the board, that is,

relative to 180° from the downstream deflected jet. The shape of OASPL directivity on the nozzle side of the board as measured for 15° and 30° impingement angle had a strong variation with direction angle and resembles that for the nozzle alone without a board. Maximum amplitude occurred at 20° to 30° from the downstream rotated direction and was about 10 dB higher than at the same angle from upstream. In contrast, acoustic radiation for 90° incidence was approximately omnidirectional on the nozzle side of the board. Directivity for 60° incidence was between those two, with a maximum at 20° from downstream but roughly constant amplitude in the forward quadrant.

Directivity measurements in the sideline azimuthal plane ($\phi = 90°$) were obtained only for 60° incidence and two velocities. These data and data taken in the flyover plane at the same incidence and velocities are shown in figure 5. OASPL was normalized with respect to impingement velocity by subtracting the quantity $10 \log_{10}(\rho_\infty^2 U_i^8/p_{ref}^2 a_\infty^4)$ from OASPL. This eighth-power normalization is only approximate; the actual velocity exponent should be somewhat larger than 8 for downstream angles and somewhat smaller for upstream angles by analogy with convection effects on noise of isolated subsonic jets (reference 10). Correlated directivities for these two velocities that differ by about 50 percent agree within 3 dB for each azimuth plane. It should be noted that the nozzle side of the board extends from 300° to 120° in the flyover plane and 270° to 90° in the sideline plane. Thus the difference between data for the two azimuthal angles, at direction angles near 100° and 280°, represents a difference between measurements in shielded or unshielded directions. The significant result is the 3 dB decrease from flyover to sideline, at constant velocity, for most downstream directions on the nozzle side of the board (θ from 20° to 80°). The microphone directions $\theta = 0°$ and 180° are identical for all azimuthal angles so curves drawn through the data for flyover sideline planes should coincide at those angles. Judged from differences between data for these planes at directions from 300° to 60°, reflection of jet noise occurs in the flyover plane for direction angles greater than 0 but less than $180°-\alpha$. Reflection apparently does not occur in the sideline plane.

Normalized Spectra

Directivity patterns measured in the flyover plane for small incidence angles resembled those for the isolated jet when plotted (figure 5) against direction angle relative to the board. Normalized spectra might then be expected to vary in the manner of those for an isolated jet at different directions in that rotated coordinate system. That is, peak frequency would be expected to decrease and spectrum shape should become more sharply peaked as the deflected jet's downstream direction is approached (reference 10). These changes would be largest within about 135° below the board (45° from downstream). One-third-octave spectra, normalized with respect to OASPL, are shown in figure 6 for the configurations and test conditions of figure 4 at angles nearly perpendicular to the board (70° to 80° and 110° to 120° below the board). At the first of these directions, just ahead of perpendicular to the

board, normalized spectra for 15°, 30°, and 60° incidence were in close
agreement (usually within 2 dB) with the normalized spectrum for the isolated
jet. The normalized spectrum for 90° incidence had a sharp peak at a frequency
less than that for the broad maximum measured with the other configurations.
This spectrum also differed from the others in rapidly approaching the large
decay rate of 5 dB per octave. At the highest frequencies, the other spectra
had just about reached the expected asymptotic decay rate of 4 dB per octave
for a direction normal to the jet. For full-scale nozzles an order of magni-
tude larger than these 5 cm (2 in.) diameters, the spectrum for 90° incidence
would have much smaller perceived noise level at constant OASPL.

Normalized spectra measured for 15° and 30° incidence at 110° to 120°
direction angles again were approximately identical to those for the isolated
jet. The normalized spectrum for 90° incidence again was sharply peaked and
decayed rapidly with increasing frequency. However, for this direction angle
the normalized spectrum for 60° incidence matched that for 90° incidence rather
than resembling the other three.

Normalized spectra are shown in figure 7 for these values of incidence and
shallow angles from the downstream direction (130° to 140° and 150° to 160°
below the board). At the first of these angle ranges (upper part of the fig-
ure), the peak frequency for the isolated jet's spectrum was decreased relative
to those for smaller direction angles from upstream. It was roughly equal to
that for the jet at 90° incidence. The spectrum shapes for these two cases
still differed, with that for the isolated jet being broader. Normalized
spectra for 15° and 30° deflection matched that for the isolated jet and the
mormalized spectrum for 60° matched that for 90° deflection. At the largest
angles (lower part of the figure) where OASPL was largest, the peak frequency
for the isolated jet's spectrum had decreased below that for 90° incidence.
The jet's spectrum shape at this angle was about as sharply peaked as that
for 90° incidence. Again, normalized spectra for 15° and 30° incidence
matched that for the isolated jet while the spectrum shape for 60° matched
that for 90° incidence. Sound power spectra for the isolated jet and the
smaller incidence angles was dominated by OASPL measured at these large
angles from the board upstream direction. Thus the impingement-only dimen-
sionless power spectral densities, shown in figure 23 of reference 9, had
similar shapes for all deflection angles but peaked at lower frequencies for
15° and 30° incidence than for 60° and 90° incidence. Use of a modified
Strouhal number in which diameter was divided by $\sin^2\alpha$ brought the dimension-
less power spectral densities (figure 23(b) of reference 9) for all four
incidence angles into general agreement. This empirical factor would correlate
the SPL spectra measured for all incidence angles at 150° to 160° direction
angles. However, the normalized spectra for different incidence at 130° to
140° directions differ not in peak frequency but in spectrum shape, and the
correction developed in reference 9 would be in the wrong direction for
smaller direction angles.

The measured directivities and spectra can be readily understood by recognizing that different flow phenomena occur at moderate (15° and 30°) and large (60° and 90°) deflection angles. For moderate angles, the noise is conventional jet exhaust noise rotated through the surface deflection angle, raised in amplitude by an amount that increases with deflection, and (for directions on the scrubbed side of the plate) further increased by reflection. Reflection from this large surface would be expected to double the acoustic intensity, causing a 3 dB increase of noise in the flyover plane. Then the increased amplitude caused by distortion of the deflected jet would be roughly 0.5 dB for 15° deflection and 3 dB for 30° deflection. These results are in general agreement with those obtained from the small model under-the-wing EBF data of reference 6 if it is assumed that noise measured in the direction 40° below the nozzle exhaust direction (15° below the last flap segment) at 10° to 20° flap deflection was dominated by jet exhaust noise. Measured OASPL's (figure 6(b) of reference 6) in this direction were 4 to 6 dB larger than those for the nozzle alone (figure 6(d) of reference 6) at pressure ratios that gave subsonic exhaust velocities. Thus the increased quadrupole noise for this EBF with 25° deflection was 1 to 3 dB plus the 3 dB increase caused by reflection from the flap surfaces.

For large deflection angles (60° and 90°), acoustic spectra generally were sharply peaked rather than gently rounded as with conventional jet noise. These peaks occurred as a one-third-octave sound pressure level more than 3 dB larger than those of the adjacent frequency bands. Narrowband measurements had established that these spectra generally were broadband rather than dominated by discrete tones. Because this change of spectrum shape occurred when the exhaust jet was greatly distorted, a possibility exists that acoustic feedback occurred between the inclined surface and the exhaust nozzle. An analytical and experimental study of the discrete-tone acoustic feedback process for deflected exhaust jets was described in reference 11. As with the theories for instability of the axisymmetric vortex mode for an isolated jet, feedback instability is predicted to occur for subsonic jets in air at exhaust Mach numbers greater than

$$M_{min} = \left[(4 + T_\infty/T_J)^{1/2} - (T_\infty/T_J)^{1/2}\right]/2 \qquad (1)$$

where T_∞ is the ambient temperature and T_J is the jet static temperature. This predicted minimum Mach number for vortex feedback instability is about 0.608 for an unheated jet. In tests described in reference 11, feedback was measured down to a Mach number of about 0.55 at 90° incidence. Measured peak frequencies of the feedback oscillation (figures 3 and 4 of reference 11) varied stepwise about a mean frequency as the ratio of impingement distance to nozzle diameter was varied from about 2 to 6 at constant nozzle velocity.

The resulting average Strouhal number for an unheated jet was found (figure 6 of reference 11) to decrease approximately linearly with increasing jet Mach number and could be approximated by

$$St = fD/U_N = 0.35 + 0.4\,(1 - M_J) \tag{2}$$

The range of incidence angle at which feedback occurred was found to increase with increasing ratio of jet temperature to ambient temperature, extending from $90°$ to $35°$ at 400 K temperature. As incidence was decreased, the blocking effect of the plate was reduced as was the amplitude of acoustic feedback. Feedback was not observed at impingment distances greater than about 6 diameters, and it was stated that feedback could occur only if a large stagnation region existed within the essentially inviscid jet core.

Most UTW externally blown flaps, and most of the configurations described in reference 9, had impingement distances of about 7 diameters. The resulting acoustic spectra for $60°$ and $90°$ incidence did not contain strong feedback tones but were clearly dominated (figures 6 and 7) by certain one-third-octave bands. These one-third-octave bands at which maximum sound power level occurred were predicted by equation (2) for the high subsonic Mach number (0.74 to 0.94 , velocities of 240 and 295 m/sec) test conditions of reference 9. They were overpredicted by about one third-octave band at lower exhaust Mach numbers. Sharply peaked spectra were measured at the lowest exhaust Mach number, 0.41 (velocity 138 m/sec), which is below the Mach number of 0.55 for which feedback tone instability was reported in reference 11 to disappear.

Comparisons With Slotted-Flap Spectra

Thus far, it has been implicitly assumed that quadrupole noise data for a jet deflected by a large board can be applied to prediction of quadrupole noise for under-the-wing externally blown flaps having slots and limited chordwise extent. The validity of this approach, and the need for including spectrum distortion caused by acoustic feedback at large deflection angles, was examined by comparing blown flap sound pressure spectra from reference 6 with deflected-jet data from reference 9. Both tests had been conducted at the same test stand with the same exhaust nozzle and microphone array. It was arbitrarily assumed that far-field spectra measured beneath the deflected flap, at the measurement direction closest to the flap, were dominated by quadrupole noise for a nozzle nominal pressure ratio of 1.7 (exhaust velocities near 285 m/sec, exhaust Mach numbers near 0.90). Exhaust velocities for this range of test configurations differed by a maximum of 4 m/sec; the resulting maximum adjustment of sound pressure levels for an eighth-power velocity dependence would be less than 0.5 dB and was not applied.

The spectrum measured 20° below the nozzle exhaust direction for the wing with retracted flap is compared in the upper part of figure 8 with the spectrum measured 20° from the isolated nozzle exhaust direction. These two spectra agree for frequencies up to 1000 Hz at which the wavelength was approximately equal to the airfoil chord. At larger frequencies the spectrum for the wing with retracted flap was about 3 dB larger (twice the acoustic energy) than that for the isolated nozzle. This result would be expected because the wing should have reflected sound at those smaller ratios of wavelength to chord. Overall sound pressure levels were dominated by the lower frequencies and was roughly the same for the two test points. However, if these small-model spectra were scaled to practical full-scale dimensions, perceived noise level would be dominated by the region where reflection was important and would be about 3 dB larger for the wing with retracted flap. Also shown is the spectrum measured 25° beneath the large flat board at 15° incidence to the nozzle centerline. This amount of jet deflection caused little increase of sound power but the board should have produced the effect of sound reflection over the entire frequency range. The high-frequency part of the spectrum beneath the wing with retracted flap would be overestimated about 2 dB by using this spectrum. Part of this difference is caused by the large shift of spectrum shape with direction angle at these angles close to the exhaust direction. The low-frequency part of the wing spectrum would be overpredicted 3 to 4 dB. Thus reflection must be included at frequencies that, when scaled, will have important contributions to perceived noise level. If applied arbitrarily at all frequencies, reflection would cause a 3 dB overestimate of OASPL.

The spectrum measured 40° below the nozzle exhaust direction for the wing model with takeoff (10°-20°) flap deflection is shown in the lower part of figure 8. Because the wing chord line was at 5° incidence relative to the nozzle, the aft flap panel was at 25° incidence relative to the nozzle. The measurement direction then was 15° below the chord line of that flap panel. Part of the exhaust jet passed through the flap slots, so the exhaust jet was turned through less than this panel's incidence. This blown flap noise spectrum is compared with spectra measured 10° and 30° beneath the large flat board at 30° incidence. The high-frequency part of the flap spectrum is underestimated by the board spectrum for 10° direction but is fairly well estimated by the spectrum for 30° direction. The general magnitude for 25° geometric incidence thus was correctly predicted with the flat board data for 30° incidence, but the spectrum shape measured at small angles from the flap did not exhibit the large variation with direction angle that occurred for the isolated jet and the flat board near the jet downstream direction.

The spectrum measured 80° below the nozzle exhaust direction for the wing model with approach (30°-60°) flap deflection is compared in figure 9 with spectra measured for two types of configurations. Spectra for the flat board at 60° incidence and direction angles 80° and 100° below the nozzle exit are shown in the upper part of the figure. They are more sharply peaked

than the spectrum for the wing with double slotted flap. That is, the spectrum distortion associated with acoustic feedback for the large board at 60° geometric incidence did not occur for the double slotted flap that had its aft segment at 65° geometric incidence. Spectra for directions 20° and 40° from the centerline of the undistorted jet, increased in amplitude by 8 and 10 dB, respectively, to yield the same OASPL are compared with the EBF spectrum in the lower part of figure 9. As with comparison for the small flap deflection, the spectrum measured at a shallow angle from the jet centerline underestimated the peak frequency and the high-frequency amplitudes. The spectrum measured 40° from the jet centerline closely predicted these important parts of the EBF spectrum. Of course, it underestimated the low-frequency amplitudes where reflection from the wing and flap would not be expected to occur.

Prediction Method

The preceding discussion has not specifically considered whether increased quadrupole jet noise depends on nozzle exit parameters or local properties of the jet exhaust at the impingement distance. Impingement-only total sound power level was shown in figure 10 of reference 9 to increase with nozzle exhaust velocity to an exponent greater than 8. Exhaust velocity was varied in those tests at only 60° and 90° incidence angles. To obtain better correlation, impingement distance was defined as the distance along the nozzle extended centerline from the nozzle exit plane to an intersection with the large board. Peak impingement velocity was defined as the maximum measured velocity in the exhaust of an undisturbed jet at the impingement distance. Impingement diameter was taken as the diameter of that portion of the measured velocity profile, at the impingement distance, where the velocity was 80 percent of the peak impingement velocity. The ratios of peak impingement velocity to exhaust velocity and impingement diameter to exhaust diameter are increased as exhaust velocity is increased at high subsonic speeds. Impingement diameter is a useful concept when comparing noise from single- and multiple-orifice deflected jets. However, the small variation of impingement diameter with exhaust Mach number for circular single jets has little effect on calculated noise. To simplify this prediction method, the dependence on impingement diameter has been neglected. When this was done, the added quadrupole noise was empirically found to vary as sine squared of the incidence angle.

Based upon the preceding discussion, the following semi-empirical method was developed for predicting jet mixing noise below a jet exhaust that is deflected by an under-the-wing externally blown flap.

1. Determine the radius, direction angle, and azimuth angle of the far field point in a coordinate system referenced to the deflected jet centerline. This line is the intersection of the aft flap segment's chord plane and a reference centerline plane containing the nozzle centerline. The angle

between the downstream deflected centerline and a line to the field point is the direction angle θ; the angle between the centerline plane and the plane defined by those two lines is the azimuth angle ϕ.

2. Determine the ratio of peak impingement velocity to nozzle exhaust velocity, U_i/U_N, for each U_N. For a conical nozzle, this ratio is given by equation (3) of reference 12.

$$U_i/U_N = \left\{ 1 + \left[0.14 \ (X/D) \ (1 + M_N)^{-1/2} \right]^4 \right\}^{-1/4} \tag{3}$$

3. Determine OASPL of an axisymmetric jet for the nozzle exhaust velocity V_N, direction angle θ, and ratio of far-field radius to nozzle diameter. Increase this OASPL by

$$\triangle OASPL = 10 \ \log \left[1 + 12 \ (U_i/U_N)^8 \ (1 + \cos^2 \phi) \sin^2 \alpha \right] \tag{4}$$

4. For direction angles θ greater than 40°, determine the normalized spectrum and distribute the calculated OASPL over this spectrum. For smaller direction angles, use the spectrum for 40° unless the flap is very long relative to nozzle diameter.

The resulting predicted effect of impingement angle on directivity is compared in figure 10 with the data of figure 4 for directions on the nozzle side of the board. Good agreement is obtained except for 60° impingement angle and shallow directions from the deflected jet.

Calculation of Externally Blown Flap Noise

Scrubbing Noise

In practical UTW installations, the major contributions to scrubbing noise come from deflected flap panels. Local flow velocities near these panels can be significantly less than the nozzle exit velocity. This calculation procedure uses the approach of reference 12 in which scrubbing noise was assumed to vary as the sixth power of a local impingement velocity U_i. The ratio of this velocity to the nozzle exit velocity was given by equations (3) and (4) of reference 12 for conical and coaxial nozzles, respectively. This ratio increases with increasing exhaust Mach number, causing the calculated noise of practical installations to vary with exhaust velocity raised to an exponent greater than 6. The velocity ratio decreases with increasing ratio

of impingement distance X to diameter. Impingement distance was defined in reference 12 as the distance measured along the nozzle centerline from the core exit plane to the point of intersection with the deflected flap. For USB configurations or UTW configurations at small deflections, this intersection does not occur. As sketched in figure 11(a), impingement distance therefore is defined here as the distance, measured parallel to the nozzle centerline, from the core exit plane to the trailing edge. The equation for impingement velocity of a conical nozzle was given as equation (3). Overall sound pressure level of scrubbing noise in the plane of symmetry is given by the empirical equation

$$OASPL_s = 10 \log \left(\rho U_i^3/a_{P_{ref}}\right)^2 (cD/r^2) (U_i/U_N)^2 \Sigma K_n \sin^2 \theta_n \qquad (5)$$

where scrubbing noise from the undeflected wing structure and from each flap panel is calculated separately. Each scrubbed surface is approximated by its chord line, and unslotted wings are approximated by three straight line segments.

For the assumed scrubbing noise process of discrete vortexes convected past a surface, the induced force fluctuations should vary inversely with height h from the vortex to the chord line. The geometric parameter K for a wing at constant distance from the vortex trajectory would then vary inversely with the height to chord ratio squared. The contribution of each scrubbed surface is then taken as proportional to the ratio of segment chord c_n to total airfoil chord c and inversely proportional to $(h/c)^2$. Vortex trajectory for small flap deflections was assumed, as sketched in figure 11(a), to follow a line parallel to the nozzle centerline and half a diameter below it. This behavior agrees with the exhaust deformation for shallow-angle oblique jets as described in reference 13. The empirical constant was taken as

$$K_n = 2 \times 10^{-7} (c_n/c) (h_n/c)^{-2} \qquad (6)$$

to match the data of reference 6 for scrubbing noise at zero flap deflection. Vortex height for a surface inclined to the nozzle centerline was taken as the root mean square height, as sketched in figure 11(a) and (b). For larger flap deflections or larger flap surfaces, vortex height of an UTW configuration was assumed never to become less than half a nozzle diameter (figure 11(b)). This minimum distance was picked to provide good agreement with the data of reference 6 for large flap deflections. Vortex trajectory of an USB configuration with attached jet flow, sketched in figure 11(c), was assumed to start at a height of one nozzle diameter and have a curvature half that of the deflected surface. This shape was arbitrarily chosen because noise radiation patterns

16

calculated for trajectories parallel to the nozzle centerline or parallel to the deflected surface bracketed the measured patterns.

It has been found that when the ratio of chord to diameter is sufficiently increased, either by increasing the flap chord or decreasing the nozzle diameter, measured scrubbing noise is decreased. The magnitude of this decrease is larger than would be predicted from the combined variations of trailing-edge velocity, chord, diameter, and vortex height. As one possible explanation, normalized vortex strength may be attenuated by viscous decay of the attached jet. Data for a limited range of geometry were matched by arbitrarily including within equation (5) a factor equal to the ratio of trailing-edge velocity to nozzle exhaust velocity squared. That is, calculated scrubbing noise is decreased when the flap trailing edge extends far downstream of the undistorted jet's potential core.

Vortex trajectory height of each flap segment as described above is a relatively arbitary dimension for both UTW and USB. Use of a minimum height of half a diameter for UTW is related to the assumptions of constant effective scrubbed span and isolated-jet axial decay of peak velocity. Improved analyses would include a better description of these aerodynamic inputs to the noise radiation process. Also, an improved analysis should give a less arbitrary dependence of each flap segment's noise radiation on local exhaust velocity and its spatial variation along the wing and flap.

Trailing Edge Noise

Because details of the jet exhaust turbulence at the flap trailing edge are not known, overall sound pressure level of trailing edge noise must be calculated using the form of an equation from reference 14 but with an empirical constant for absolute amplitude. Such an equation was given in reference 3 in terms of jet exhaust velocity. As with the empirical predicition method of reference 12, the equation should be rewritten in terms of impingement velocity. The empirical constant given in reference 3 had been arbitrarily decreased for calculations with retracted rather than deflected flaps. It would be convenient if the variation of calculated trailing edge noise with trailing edge position for under-the-wing externally blown flaps would also apply to trailing edge noise for CTOL over-the-wing engine installations with unattached jets. An empirical factor for predicting this effect of trailing edge position for such installations was given in equation (3) of reference 15 as $-10 \log[1+(H/D)^2]$ where H is the height of the nozzle lower lip above the trailing edge in the direction normal to the nozzle centerline. This correlation was based on data for a variation of height H at constant diameter and chord. Measured distributions of exhaust jet turbulence level vary with streamwise distance at constant height and are better correlated by the ratio of height to streamwise distance. The models of reference 15 had a streamwise distance of about 9.5 diameters, so the factor H/D would be replaced by $10H/X_T$. The resulting equation is

$$OASPL_T = 10 \log 10^{-5} (1 + 100 \, H^2/X_T^2)^{-1} (\rho^2 U_i^5/a P_{ref}^2) \, (D/r)^2 \cos^2 \phi \cos^2 (\theta_T/2) \qquad (7)$$

where the height H is taken equal to zero for OTW attached jets and UTW configurations with flaps deflected sufficiently to make H negative. As discussed later, USB directivity proved to be better predicted at small flap deflection angles if OASPL given by equation (7) was arbitrarily increased 3 dB.

Jet Mixing and Deflection Noise

Calculation of jet mixing noise for axisymmetric jets was based on the semi-empirical prediction method of reference 10. OASPL of subsonic jets and supersonic shock-free jets, measured in a direction perpendicular to the nozzle centerline, was given by equation (6) of reference 10 as

$$OASPL_{90} = 141 + 10 \log \left[M_j^{7.5} (1 + 0.010 M_j^{4.5})^{-1} \right] + 10 \log \left[(A_j/R^2)(\rho_a/\rho_{ISA})^2 (a_a/a_{ISA})^4 \right] +$$

$$10 \left[3 M_j^{3.5} (0.60 + M_j^{3.5})^{-1} - 1 \right] \log (\rho_j/\rho_a) \qquad (8)$$

where M_j is the ratio of jet velocity to ambient speed of sound. Directivity was calculated for other measurement direction angles (measured from the upstream centerline) by adding a convective factor

$$OASPL_j = OASPL_{90} - 30 \log \left[1 + M_c (1 + M_c^5)^{-1/5} \cos \theta \right] \qquad (9)$$

where the convective Mach number M_c was taken as $0.62 M_j$. This calculated directivity factor was shown in figure 4 of reference 10 to overestimate OASPL for angles greater than about 150° (directions within 30° of the exhaust centerline). The EBF noise calculations arbitrarily assumed that jet noise OASPL within this direction region was constant at the level calculated for 150° direction.

For UTW, jet noise of the isolated exhaust nozzle was calculated in the above manner using the nozzle exhaust velocity V_j as the jet velocity. The resulting directivity pattern was rotated through the deflection angle α of the last flap panel. Amplitude at all direction angles was increased for deflection and reflection using the empirical equation (4) developed to match quadrupole noise radiation from a jet impinging against an inclined large flat board. In calculating viscous decay of the exhaust jet, nozzle exhaust Mach number M_N was taken as the ratio of exhaust velocity to exhaust speed of sound. In contrast, jet Mach number M_j in equation (8) is referenced to ambient atmospheric speed of sound.

The above procedure allows calculation of jet mixing noise in the spatial hemisphere below the last flap panel of UTW installations. Experimentally, it is found (e.g., reference 6) that OASPL at small and moderate direction angles above the last flap panel are about as large as those at the same angle below the flap. The logic used in developing equation (4) had including the effect of sound reflection from the flap lower surface. However, data for direction angles above a highly deflected flap but below the horizon are best matched by assuming this noise to be roughly symmetrical about the flap. The additional quadrupole noise probably is generated in the thin shear layer which is formed above the deflected exhaust jet downstream of the trailing edge. This shear layer would be affected by the high turbulence levels generated by impingement of the jet against the deflected flap. Quadrupole noise from this upper shear layer was arbitrarily calculated as equal to that for a deflected jet whose impingement velocity was evaluated at the flap trailing edge. This noise was assumed to radiate both above and below the deflected jet. If two UTW configurations have the same deflection angle but different flap lengths, the one with the longer flap would be predicted to have less quadrupole noise above the flap. For slotted flaps, the quadrupole noise caused by jet deflection was assumed not to be reflected by the flaps but to radiate through the slots to the upper surface. Refraction of noise by the deflected exhaust jet, which could be affected by exhaust temperature, has been neglected. A detailed study of the spatial distribution of quadrupole noise sources near both UTW and USB configurations would be useful in distinguishing among the several assumed noise-generating locations. Cross-correlation of local flow-field fluctuating quantities and far-field acoustic pressures to establish source locations, combined with directional microphone measurements to determine the importance of refraction, would provide useful data.

For OTW installations, jet mixing noise was assumed to be generated by the free shear layer downstream of the flap trailing edge. Jet Mach number was determined from the impingement velocity calculated from equation (3) with downstream distance X taken as the trailing edge location. This smaller Mach number was then used in equations (8) and (9) for calculating OASPL jet noise directivity relative to the aft flap direction. Noise produced by nozzle deflectors, if used, seems to depend on the particular deflector configuration. As shown from sound power spectrum measurements such as were given in figures 9 and 10 of reference 16, deflectors can increase sound power by about 10 dB at high frequencies. Noise from the jet plus deflector in the presence of the unslotted wing and flaps, at a given direction angle more than 30° above the downstream direction, was assumed equal to that measured in the same direction with the jet plus deflector but without the wing. Jet plus deflector noise at angles above the deflected flap but less than 30° above the downstream direction were taken equal to that measured at 30° for the jet plus deflector. That is, noise radiated by the deflector in directions away from the wing was assumed to be unaltered by the wing. Noise radiated by the deflector toward the wing was assumed to be reflected at shallow angles to fill

the region above the flap. All of these USB jet plus deflector noise predictions are assumed to be independent of azimuth angle except insofar as a change of azimuth angle at constant direction angle may move the measurement field point above or below the wing. As with UTW configurations, noise above the wing and deflected flaps is of little importance in calculating effective perceived noise levels at ground certification points. It is of interest in validating the complete noise prediction method by demonstrating whether all available directivity data can be predicted.

Spectrum Calculations

Spectra for each noise process were calculated by use of empirical equations for normalized SPL spectral density (NSD). As in references 7 and 8, NSD is a pressure-squared density per unit Strouhal number, defined such that its integral over all Strouhal numbers has zero dB amplitude. It is related to one-third-octave SPL by

$$NSD = SPL_{1/3} - OASPL - 10 \log (0.232 \ fD/U_N) \tag{10}$$

An empirical equation for NSD of UTW models was given as equation (8) of reference 8 in terms of an arbitrary peak Strouhal number. This arbitrary constant had one value for configurations with retracted or takeoff flap deflection but a different value for approach flap deflection. Resulting spectra for approach flaps were predicted to have relatively more high-frequency and less low-frequency sound. The difference in spectrum shape can also be regarded as a result of relatively larger amounts of jet mixing noise, and relatively less trailing edge noise, in spectra dominated by scrubbing noise. Thus, NSD for scrubbing noise is assumed to be given by the empirical equation which matched the data for small flap deflections.

$$NSD_S = 10 \log 0.16 \ St^3 (St^{8/3} + 0.008)^{-2} \tag{11}$$

The resulting NSD varies inversely with Strouhal number St to the -7/3 power at large Strouhal numbers. The corresponding one-third-octave SPL decays 4 dB per octave.

An empirical equation for trailing edge noise spectra is

$$NSD_T = 10 \log (1/8) \ St^3 (St^{3/2} + 0.05)^{-4} \tag{12}$$

which varies inversely with Strouhal number cubed at large Strouhal numbers as is expected for trailing edge noise. The corresponding one-third-octave SPL decays 6 dB per octave. This equation was obtained as an arbitrary curve fit to OTW spectra for direction angles at which trailing edge noise should dominate other mechanisms. It gives maximum SPL at Strouhal numbers near 0.16 and omits the local peak SPL that is frequently measured at about half that Strouhal number. This use of one smooth curve to represent double-humped experimental spectra was regarded as acceptable because the omitted low-frequency portion of a full-scale spectrum would have little contribution to perceived noise level. This low-frequency peak might be caused by roll-up at the jet edges and would be expected to depend on configuration shape.

Jet mixing noise spectra are known to vary in shape as functions of direction angle and exhaust velocity. As shown in figure 5 of reference 10, the parameter which should coalesce these spectra by adjusting for effects of Mach number on convection was found to give agreement only for direction angles more than about 60° from downstream. An alternate approach would be to recognize that jet mixing noise will be important relative to other EBF noise processes only for large exhaust velocities and aft directions so that attention can be concentrated on measured spectra for one typical operating condition. Normalized one-third-octave spectra, $SPL_{1/3}-OASPL$, are plotted in figure 12 for the 5.2 cm diameter nozzle of reference 6 at nominal pressure ratios of 1.7 and 1.25 for direction angles 20° to 100° from the nozzle exhaust. Spectra for angles from 60° to 100° agree within about 2.5 dB at Strouhal numbers up to about 4. The spectra for smaller angles lie below those data for Strouhal numbers greater than about 1. Also shown is an empirical curve given by

$$SPL_{1/3} - OASPL = 10 \log 0.1 \, St^{4} \left(St^{17/12} + 0.11 \right)^{-4} \tag{13}$$

that falls very close to the 40° spectrum. This empirical curve was arbitrarily used for predicting EBF quadrupole jet mixing noise spectra for all direction angles. At direction angles for which the contribution of calculated jet mixing noise would have large effects on calculated EPNdB, this portion of the spectrum could be re-calculated for each direction angle and convective Mach number by the method of reference 10. Alternately, calculated or measured spectra of jet mixing noise and measured spectra of deflector noise could be supplied as input for each EBF spectrum calculation at each velocity and direction angle.

Summary of Calculation Method and Areas for Improvement

Calculation of OASPL directivity for EBF configurations at zero flight speed, using the above semi-empirical method, would use the following sequence of

21

steps. The calculations can be performed with a pocket-size scientific-function digital calculator or a conventional digital computer.

1. Determine the nozzle area-equivalent diameter, wing chord impingement distance, far-field radius, sideline azimuth angle, atmospheric density, and atmospheric speed of sound, and whether the configuration is UTW or USB.

2. Determine the deflection angle, chord length, trailing-edge distance from the nozzle exit plane, and vortex trajectory height (see figure 11) for each segment of the wing panel and flap assembly.

3. Choose the nozzle exhaust flow properties (velocity, density, and speed of sound). For coaxial nozzles or internal mixer nozzles, determine the effective exhaust velocity from equations (5) or (6), respectively, of reference 19.

4. Calculate the ratio of peak local velocity to nozzle exhaust velocity at the impingement point and at all segment trailing edges by use of equation (3) or use available data. For a mixer nozzle, use nozzle-alone velocity profiles.

5. For each segment of the wing and flap, calculate maximum scrubbing-noise mean square acoustic pressure by use of equations (6) and (5).

6. Calculate maximum trailing-edge-noise mean square acoustic pressure by use of equation (7) and the calculated velocity ratio at the last trailing edge. For UTW with a mixer nozzle or for USB, double this acoustic quantity.

7. For UTW, calculate OASPL of the isolated jet at 90° direction from equation (8). If a mixer nozzle is used, calculate this quantity from Appendix B of reference 10 or use data. Calculate the additional OASPL due to deflection by use of the impingement velocity ratio and the last flap segment deflection angle in equation (4). Calculate the quadrupole OASPL radiated by the downstream exhaust, at a direction 90° to that deflected exhaust, by use of the isolated-jet OASPL and the last flap segment trailing-edge velocity ratio and deflection angle in equation (4).

8. For USB, calculate OASPL of the isolated deflected jet downstream of the trailing edge, at 90° from that deflected jet, by use of equation (8) with the jet Mach number M_j multiplied by the last flap segment trailing-edge velocity ratio.

9. For a selected direction, or for each direction from 0° to 360° at a specified angular spacing, multiply the maximum scrubbing-noise mean square pressure for each segment (from step 5) by sine squared of the angle relative to that segment's chord line, and add these terms to obtain overall scrubbing noise.

10. For this direction, multiply the maximum trailing-edge-noise mean square pressure (from step 6) by cosine squared of half the angle from upstream of the last flap segment's trailing edge to obtain overall trailing edge noise.

11. For this direction, and UTW with slotted flaps, logarithmically add the three quadrupole OASPL's from step 7 plus the convective factor given by equation (9). The direction angle in this equation is taken relative to upstream of the deflected jet. At relative directions between 150° and 210° (within 30° of the deflected exhaust), set this convective factor equal to its value at 150°.

12. For this direction and USB, add the quadrupole noise convection factor given by equation (9) to the quadrupole noise calculated in step 8 using the procedure described for step 11. If this direction is in the upper hemisphere, add the measured noise from the isolated nozzle plus deflector. For a canted nozzle, add the quadrupole noise due to deflecting the exhaust jet through the cant angle as calculated from equation (4). For aft direction angles below that hemisphere but above the deflected flap, add the maximum OASPL produced by the isolated nozzle and deflector. For USB slot nozzles, see the discussion of figure 27 for arbitrary modifications that improved agreement with data.

13. For this direction, add the scrubbing noise from step 9, the trailing-edge noise from step 10, and the quadrupole and deflection noise from step 11 or 12 to obtain OASPL.

14. Select the next direction at this exhaust velocity and return to step 9. If exhaust velocity is changed, return to step 3.

To calculate the one-third-octave SPL spectrum for a previously calculated OASPL, input the three separate contributions to OASPL listed in step 13, plus a nozzle diameter and exhaust velocity.

15. Select a center frequency and calculate Strouhal number.

16. For UTW, calculate the contribution of scrubbing noise to that frequency band from equations (11) and (10), taking the overall scrubbing noise from step 9. For USB, use equation (12) rather than equation (11).

17. Calculate the contribution of trailing edge noise to that frequency band from equations (12) and (10), taking the overall trailing edge noise from step 10.

18. Calculate the contribution of quadrupole noise to that frequency band from equation (13), taking the overall quadrupole noise from step 11 for UTW or step 12 for USB.

19. Logarithmically add the three contributions to obtain one-third-octave SPL, and return to step 15.

Clearly, these procedures contain many crude approximations that could be improved with further effort. The exhaust jet is represented by a region having constant span, constant turbulence ratio, and a mean velocity that is constant at each axial station. Axial decay of the exhaust jet is calculated as that for an isolated jet (step 4). The aerodynamic description of the flow field should at least be modified to include effects of flap deflection on spanwise spreading of the exhaust. The empirical procedure for determining vortex trajectory height (step 2) and its effect on scrubbing noise source strength (step 5) should be placed on a more rational basis. Effects of the variation of exhaust flow properties along the flap length now are included in equation (5) in a highly arbitrary manner. If future UTW installations have increased ratios of deflected flap chord to nozzle diameter, these effects would become more important. Effects of USB slot nozzle shape on exhaust jet aerodynamic properties and noise radiation have been included only as arbitrary corrections for 5:1 and 10:1 aspect ratios. Flow-field data, and acoustic source-strength identification tests as could be obtained with directional microphones, are needed. Use of a different spectrum shape for UTW and USB scrubbing noise is a conceptual weak point of the USB analysis. Refraction of noise by the exhaust jet has been omitted completely, with a conservative constant intensity assumed for directions within 30° of the deflected jet exhaust. Finally, effects of flight speed on both turbulence intensity and ratio of local velocity to nozzle exhaust velocity, and their combined effects on source strength for each noise mechanism, have not been included. Tests are needed to establish these forward flight effects on local mean velocities and turbulence levels of the aerodynamic flow and on acoustic radiation from different EBF models dominated by different aeroacoustic mechanisms.

Alternate Prediction Methods

Alternate methods exist for predicting EBF noise. Some of these (references 17 and 18) utilize measured directivity and spectra for configurations resembling those of interest, tested at one exhaust velocity in the range of interest. These data are then scaled to other velocities by assuming that acoustic intensity varies with nozzle exhaust velocity to the sixth power at constant Strouhal number. Geometric scaling assumes dependence on exhaust area to the first power and far field distance to the inverse second power. The method of references 12 and 19 is somewhat more elaborate in that local flow velocity near a deflected UTW flap (denoted as impingement velocity) is recognized to vary more rapidly than nozzle exhaust velocity. As an empirical approximation for high subsonic exhaust velocities of practical interest, UTW acoustic intensity is assumed to vary with nozzle exhaust velocity to the 6.7

power. Intensity in the direction normal to the nozzle centerline in the fly-over plane was then determined as an empirical function of flap deflection angle. Directivity relative to intensity in that reference direction was also given by empirical curves for different flap angles, but this manner of pre-sentation made it easier to interpolate for other flap deflections. The directivity curve for a given flap deflection is scaled with velocity to the 6.7 power for UTW and the 6.0 power for USB. Thus the changes in directivity shape caused by locally dominant quadrupole noise would not be predicted. The need for separate prediction of quadrupole noise in subsequent analyses was noted in that study.

Spectra are calculated in these methods by use of one normalized spectrum for each configuration type, flap deflection, and sideline angle. For UTW the change in normalized spectrum shape with direction angle and pressure ratio was shown in reference 8 to be small, validating this approach. However, some USB configurations have large contributions from jet mixing noise at shallow angles from the deflected jet, changing the normalized spectrum shape at those directions and high pressure ratios. The method of reference 19, developed under the NASA Aircraft Noise Prediction Program (ANOPP), is the most recent and most elaborate of these simplified EBF noise prediction methods. Some comparisons between its results, those of the method developed herein, and NASA data are given in the next section of this report.

COMPARISON OF MEASURED AND PREDICTED EBF NOISE

The calculation method was applied to predicting OASPL directivity, and 1/3 octave spectra for measurement directions of practical interest, for a range of under-the-wing (UTW) and upper-surface-blowing (USB) configurations at zero flight speed. Sketches of these models are given in Table I along with an estimate of the quality of agreement between data and predictions. The UTW models were a double slotted flap at takeoff deflection ($10°$ vane and $20°$ aft flap) and approach deflection ($30°$ vane and $60°$ aft flap), a slotless wing that approximated the shape of the double-slotted flap at approach deflection, and the double slotted flap at approach deflection with a mixer nozzle, a range of single-nozzle positions, and a range of single-nozzle diameters. The USB models had closed slots, either $20°$ or $60°$ aft flap deflection, and either a circular nozzle with deflector, D nozzle with deflector, or canted 5:1 or 10:1 slot nozzles. Noise from a wing and double slotted flap mounted with the wing leading edge bisecting the nozzle exhaust plane was also examined. All of these configurations had been tested as small-scale models, usually with 32 cm (12.6 in.) retracted-flap wing chord and 5.08 cm (2.0 in.) nozzle diam-eter, at NASA Lewis Research Center. These configurations were designated by NASA Lewis Research Center for this comparison, and tabulated data were sup-plied by them.

25

Double Slotted Flaps

A comparison of calculated and measured noise radiation patterns for the UTW double slotted flap of reference 6 at 10° vane and 20° aft flap deflection is given in figure 13. Direction angles are plotted referenced to the nozzle inlet as is now standard, rather than the nozzle exhaust as in reference 6. The exit direction of the deflector flap is shown by an arrow. The breakdown of calculated OASPL into separate contributions from scrubbing noise (lift dipoles perpendicular to local chord lines), trailing edge noise, and quadrupole jet noise from the deflected jet is shown for the smaller of the two test pressure ratios. Also shown are OASPL directivity curves calculated from a method developed (reference 19) at NASA Lewis Research Center under the Aircraft Noise Prediction Program effort. Measured directivity is more closely predicted by the present method, which includes both dipole and quadrupole noise, than by the method of reference 19 which scaled the entire directivity pattern with exhaust velocity to the 6.7 power. The need for both dipole and quadrupole velocity scaling was noted in that reference. Spectra calculated for this configuration at measurement directions 120°, 100°, 80°, and 20° below the nozzle inlet direction are compared with data in figure 14. It should be noted that these are actual spectra and are not normalized with respect to OASPL. The calculation precedure begins with the model geometry, measurement distance, nozzle exhaust properties, and atmospheric temperature. Sound pressure level can then be calculated for any specified 1/3 octave band center frequency at any specified direction. The data have not been corrected for ground reflection. Such corrections would reduce but not eliminate the oscillations of measured spectrum shapes below 1 kHz center frequency. Because the resulting corrected spectra must still be smoothed arbitrarily, available tabulated corrections for ground reflection were not used. At center frequencies greater than 1.0 kHz, the correction to free-field data would cause about 1.0 dB reduction from the plotted values. Agreement is good except for the high pressure ratio at a shallow angle from the deflected jet (figure 14a) and both pressure ratios at low frequencies and small angles from the nozzle inlet direction (figure 14d). As noted in the discussion of deflected-jet noise spectra, low-frequency portions of UTW spectra are overpredicted because the wing does not reflect those frequencies.

OASPL data for this configuration at 30° vane and 60° flap deflection, and four subsonic pressure ratios, are compared with calculations in figure 15. For this large deflection angle, calculated quadrupole noise from the deflected jet is stronger than calculated maximum values of scrubbing noise at pressure ratios of 1.4 and 1.7. The constant directivity pattern of reference 19 gives a close match to the data for a pressure ratio of 1.25, which contained a prominent minimum at direction near the deflected jet. The present method predicts the measured change in shape of this directivity

pattern with increasing pressure ratio. Omission of this change would underestimate OASPL near 90° direction where distance to the ground is least. Both methods underestimate OASPL at the lowest pressure ratio where, judged from the directivity shape, the local velocity may have been higher than was specified.

Effects of systematic changes in nozzle position relative to the wing had been examined in tests reported in reference 6 for the 30° vane and 60° flap deflection at a pressure ratio of 1.7. Changes in sound radiation relative to that of the basic configuration are shown in figure 16. These measured effects of axial distance and wing height had been given in figure 20 of reference 6. Moving the nozzle exit plane from upstream to downstream of the wing leading edge was shown in figure 16(a) to cause about 2 dB measured and calculated increase of OASPL. This change was caused by decreased viscous decay of the exhaust jet along the distance occupied by the wing. Decreasing the height of the wing above the exhaust jet was shown in figure 16(b) to increase calculated noise about 5 dB above the wing and 2 dB beneath it. The calculated increase of scrubbing noise from the undeflected portion of the wing caused most of this increase. Measured OASPL above the wing agreed with this calculation, but OASPL below the deflected jet at directions 55° to 100° from the nozzle inlet was increased about 4 dB while calculations predicted little change at these directions. Measured spectrum shapes (not shown) were not significantly changed at these directions, so it is not likely that the additional noise was caused by acoustic feedback between the nozzle and wing. Because of the angular location of this increased noise, it is likely that jet mixing noise of the deflected jet was altered.

When azimuth angle is varied, scrubbing noise and trailing edge noise are calculated to decrease as cosine squared of the azimuth angle. Quadrupole noise of the deflected jet is calculated to decrease only a maximum of 3 dB because sound would be radiated laterally without reflection from the wing. As azimuth angle is increased from 0° to 90°, noise should decrease to a floor set by the quadrupole noise. Calculated and measured variations of the noise radiation pattern with azimuth angle are given in figure 17 for this double slotted flap at both flap deflections and 1.7 pressure ratio. For the smaller flap deflection, relative decreases caused by changing azimuth angle at constant angle from the nozzle exhaust direction were well predicted (6 dB decrease at 60° azimuth except near the exhaust jet) except for the largest azimuth angle. A noise floor seemed to occur in the upstream quadrants, with a local maximum upstream and slightly above the wing (330° from the nozzle inlet). For the larger flap deflection, a strong unpredicted minimum occurred near 90° from the nozzle inlet direction at 30° and 60° azimuth. At larger angles in the lower forward quadrant, measured noise levels increased and gave good agreement with predictions except for the apparent noise floor at 85° azimuth. Measured effects of azimuth angle at smaller exhaust velocities would have been useful in determining whether the local minimum and noise floor were set by quadrupole

or dipole noise. Fortunately, noise prediction at nonzero azimuth is important only for takeoff where flap deflection is small and agreement between calculations and data (figure 17a) was good.

Slotless Wing

The calculation method developed herein predicts the same scrubbing noise and trailing edge noise for slotless wings as for slotted wings having the same contour. Quadrupole noise from an exhaust jet deflected by a slotless wing was arbitrarily assumed to be shielded at direction angles above the deflected aft portion of the wing. The resulting noise radiation patterns calculated for the UTW 60° aft deflection slotless wing of reference 6 are compared in figure 16 with data for the two subsonic pressure ratios of 1.25 and 1.7. For the lower pressure ratio, the calculated directivity is in good agreement with data except for an underestimate at small angles above the highly deflected jet. Inclusion of quadrupole noise from the portion of the deflected distorted jet downstream of the trailing edge would improve agreement. In contrast, OASPL's measured at the larger pressure ratio generally were about 3 dB below the calculated levels for all measurement directions although the shape was properly predicted. Both scrubbing noise and deflected jet noise would have to be underestimated to produce this error.

A different analysis of the noise radiation pattern for this slotless wing had been developed in reference 5. Only two types of noise were considered: direct plus reflected quadrupole noise of a jet impacting against a solid surface as obtained from reference 9, and trailing edge noise. Trailing edge noise was calculated by a method shown in references 1 and 2 to overestimate such noise at moderate and high subsonic velocities. The noise radiation pattern calculated for a pressure ratio of 1.25 at directions below the wing and below the deflected jet was shown in figure 11 of reference 5 to give good agreement with data. As shown in figure 18 herein, quadrupole noise dominated the directivity in the lower aft quadrant. The level of trailing edge noise calculated in reference 5 for this exhaust velocity was about 5 dB above that shown in figure 18, giving qualitative agreement in the lower forward quadrant. It did not reproduce the local maximum noise at a direction normal to the deflected aft portion of the wing. That method overestimates measured noise by 5 to 8 dB in the upper forward quadrant, where trailing edge noise should be strongest. A comparison was not given in reference 5 with data for those directions, or for directions below the wing at the higher subsonic pressure ratio of 1.7. That method would overestimate the data below the wing by at least the 3 dB difference shown in figure 18 for the method given herein. It would be 9 to 10 dB above data for the upper forward quadrant, a region not considered in the comparisons given in reference 5.

Some understanding of the cause of this poor agreement for a high subsonic exhaust velocity can be obtained by examining the spectra for double slotted flaps and slotless wings. The measured and calculated 1/3 octave spectra for these two configurations at large deflection, at four directions beneath the deflected exhaust, are given in figure 19. For a pressure ratio of 1.25, measured spectra of both configurations were scattered about the calculated spectrum. For pressure ratios of 1.4 and 1.7, spectra of the double slotted flap were closely predicted at high frequencies but overestimated at low (less than 1250 Hz) frequencies. Spectra for the slotless wing at a pressure ratio of 1.7, and directions other than close to the deflected jet, were considerably below predictions at middle frequencies (1250 to 4000 Hz) where maximum 1/3 octave SPL's occurred. However, they were in good agreement with predictions at high frequencies (above 8000 Hz). It appears that the presence of a gently curved lower surface on the slotless wing caused a less abrupt deflection of the exhaust jet than that for impingement against a flat board (reference 9) or slotted wing. Additional quadrupole noise from the forward portion of the deflected jet, which generates low and mid-frequency noise, was reduced. Because the outer edge of the jet was probably displaced further below the deflected aft surface, scrubbing noise also was reduced. Turbulence level of the deflected jet also may have been decreased, causing noise in the upper forward quadrant to be less than that predicted for trailing edge noise.

Mixer Nozzle

Tests were reported in reference 20 for this double slotted flap UTW model and an 8 lobe mixer nozzle. The nozzle was simulated by an 8-lobe orifice plate. Measured peak velocity at the axial location of the impingement point was about 65% of the nozzle exit velocity. At 30° vane and 60° flap deflection, use of this nozzle was reported to cause about 6 dB less OASPL beneath the wing than that for an equal-area circular nozzle. Scrubbing noise and trailing edge noise of the wing and mixer nozzle were arbitrarily calculated as those for the wing and an equal-area circular nozzle. The wing trailing edge was assumed to be located 14.5 diameters downstream of the nozzle exit plane to match the jet axial velocity at the trailing edge. Resulting calculated levels were then arbitrarily increased 3 dB, as might be produced by higher turbulence levels in the mixing shear layer, to obtain improved agreement with data in the upper two quadrants. The sum of sound pressure levels calculated for these two noise mechanisms was at least 6 dB below OASPL measured below the wing.

The additional noise was calculated as noise from the mixer nozzle in the absence of the wing and noise from deflection of the decayed nozzle exhaust by the wing. Measured OASPL directivity of the mixer nozzle alone was increased 3 dB at angles from 0 to 180 deg below the nozzle inlet to account for reflection from the undeflected wing panel. Subsequent reflection and shielding by the deflected flaps was neglected. This noise was assumed to

be completely shielded in the two quadrants above the nozzle exhaust centerline. Deflected-jet quadrupole noise caused by impingement of the velocity-decayed jet against the deflected vane and flap was calculated in the usual manner. Unlike conventional exhaust nozzles for which noise from the deflected portion of the jet dominates that from the initial mixing region, this UTW configuration has about 2 dB more calculated noise from the undeflected part of the jet. Resulting calculated and measured noise radiation patterns at two pressure ratios are shown in figure 20. The two types of calculated quadrupole noise are not plotted separately but their calculated sum is denoted. Direct plus reflected mixing noise was calculated to be strongest 140° to 160° from the nozzle inlet direction, while calculated noise caused by deflecting the jet was strongest between 80° and 140° from that direction. The resulting calculated radiation patterns had relatively little variation with direction angle below the wing. They were in close agreement with data for the lower aft quadrant, but data for the lower forward quadrant were underestimated 2 to 3 dB. The shape of this discrepancy resembles a lobe of scrubbing noise oriented normal to the deflected vane. This added noise may have been caused by much higher local flow velocities near the vane than near the flap trailing edge.

Spectra measured with this mixer nozzle and wing at different flap deflections were compared in figure 9b of reference 20 for a pressure ratio of 1.74 and direction 80° from the nozzle inlet. At frequencies above roughly 5 kHz for this small model, spectra for the model with flaps retracted were only slightly below those for two different flap deflection angles. These levels were about 3 dB above those for the simulated mixer nozzle alone. Spectrum levels generally increased as flap deflection was increased at lower frequencies.

Measured and calculated spectra for the wing and mixer nozzle at 30° vane and 60° flap deflection, and measured spectra for the nozzle alone, are shown in figure 21 for the direction 80° from the nozzle inlet at pressure ratios of 1.23 and 1.74. Data for the wing and nozzle are shown as open symbols and data for the mixer nozzle alone as solid symbols. The spectrum of noise from the mixer nozzle alone at this direction was relatively flat at high frequencies. Spectrum shape at shallow angles to the exhaust jet, not shown, was relatively stronger at low frequencies and weaker at higher frequencies. The spectrum shape at a shallow angle was used for quadrupole noise of the deflected jet. Adding the two spectra for jet noise, adjusted for reflection, yielded the long-dash curves. Calculated scrubbing noise, shown by the short-dash curves, was stronger than the inferred jet noise at low frequencies. The sum of those calculated spectra, shown as solid curves, generally followed the trend of the data but underestimated the measured spectra at frequencies near 2.5 kHz while overestimating them above 10 kHz. The underestimate at frequencies 4 to 5 times the expected peak frequency of scrubbing noise may represent an additional scrubbing noise having a characteristic frequency associated with a mixer lobe dimension rather than the nozzle hydraulic diameter.

Effect of Diameter-to-Chord Ratio

One interesting test for UTW configurations had varied the nozzle exit diameter at constant wing geometry and constant 212 m/sec impingement velocity. Nozzle diameters were roughly 0.5, 0.8, and 1.5 times that for the tests described in reference 6. The wing was that of reference 6, with 30° vane and 60° flap deflection. These data had been given in figure XII-13 of reference 21 as the measured variation of OASPL with diameter at one measurement angle. Although a dependence on diameter squared would have been expected from geometric scaling of quadrupole noise, OASPL beneath the model was empirically found to vary with diameter to the first power. Calculated OASPL radiation patterns for the four configurations are compared with data in figure 22. Trends and levels were closely predicted except for directions above the wing at the larger diameters.

Measured and calculated variations of sound radiation with nozzle diameter are shown in figure 23 for directions 80° from the inlet (shown in reference 21) and 40° from the inlet. For both of these directions, trailing edge noise was calculated to have little contribution to OASPL and its calculated directivity is not shown. As diameter ratio was decreased, the increase of nozzle exhaust velocity needed to maintain constant impingement velocity caused an increase of calculated scrubbing noise from the forward wing panel. This increase approximately compensated for the decreased calculated scrubbing noise from the narrower scrubbed regions on the flap panels. Calculated scrubbing noise for the entire wing was therefore weakly dependent on nozzle diameter. In contrast, most of the calculated quadrupole noise was predicted to come from the deflected distorted portion of the jet where local velocity had been held constant, so this noise varied approximately with diameter squared. The sum of OASPL calculated for these two processes, and the measured OASPL, coincidentally varied approximately with diameter to the first power.

Calculated and measured variations of 1/3 octave spectra with nozzle diameter for these two measurement directions are given in figure 24. The measured small effect of nozzle diameter on spectrum levels at frequencies above 2000 Hz was predicted by the calculations. Agreement was good except for the largest nozzle at low frequencies where measured levels were considerable overestimated. It is likely that the small ratio of wing chord to nozzle size was not sufficient to deflect the jet through the physical turning angle. Quadrupole noise due to jet deflection probably was less than had been calculated.

Upper-Surface-Blowing Configurations

Noise Radiation Patterns

When noise radiation patterns were calculated for USB models with small flap deflection, it was found that data for the lower forward quadrant were

slightly underpredicted by the unmodified calculation method . Calculated trailing edge noise therefore was arbitrarily increased 3 dB above that for UTW configurations as might occur from increased turbulence levels produced by the nozzle deflector plate. A comparison of the resulting flyover noise radiation patterns calculated for an USB with 10° vane and 20° flap deflection, closed slots, and a circular nozzle, and measured with a circular nozzle and deflector (reference 23) and a D nozzle and deflector (reference 24), is given in figure 25(a) for pressure ratios of 1.25, 1.4 and 1.7. Calculated noise radiation patterns of trailing edge noise, scrubbing noise, and noise from the portion of the jet downstream of the flap trailing edge are shown for the lowest pressure ratio. Measured noise from the circular nozzle and deflector alone are shown for all pressure ratios at direction angles above the wing. There was essentially no difference between noise measured beneath the wing with the circular nozzle (open symbols) and D nozzle (solid symbols). Data for these directions were closely predicted for pressure ratios 1.7 and 1.4 and were underestimated about 2 dB for the lowest pressure ratio, 1.25. Both scrubbing noise and trailing edge noise were predicted to have important contributions to noise in the quadrants beneath the wing. Noise radiation patterns beneath the wing were slightly underestimated by the empirical NASA method of reference 19.

Above the wing, the D nozzle was about 5 dB noisier than the circular nozzle. Measured levels above the wing were generally predicted within 3 dB by the sum of OASPL measured with the circular nozzle and deflector alone and calculated for scrubbing and trailing edge noise. The cause of the measured increase of noise above the wing with the D nozzle rather than the circular nozzle is not known. As shown in figure 7 of reference 23, the two nozzles without deflectors produced about the same noise radiation patterns. Adding deflectors to these two nozzles caused about 10 dB increase of noise, but directivity and spectra were essentially the same for the two nozzle shapes.

Measured noise radiation patterns for these two nozzles at 63.5° azimuth angle, representing a high-noise position along the sideline after an aircraft has left the ground, are shown in figure 25 (b). At this angle, noise beneath the wing of the model with a circular nozzle and deflector had decreased only about half of the 7 dB increment expected from a cosine-squared variation with azimuth angle. The curves shown in figure 25 (b) were calculated by arbitrarily assuming that scrubbing noise and trailing edge noise varied only with cosine of this angle to the first power. Curves shown for directions above the wing are measured radiation patterns for the circular nozzle with its deflector but without the wing. The resulting predictions are in good agreement with data for the circular nozzle except for measurements angles somewhat larger than 120° from the nozzle inlet. Here, noise radiated from the flow deflector apparently ceased to be shielded by the wing and added to the measured far-field noise. Unlike the comparison shown in figure 25 (a) for zero azimuth angle, the D nozzle was about 2 dB noisier below the wing than the circular nozzle. It remained about 5 dB louder above the wing, as at zero azimuth.

Other USB nozzle shapes having about the same exit area and tested with the same wing model include slot nozzles canted 20° to the wing plane and having 5:1 and 10:1 ratios of width to height (references 24 and 16). The 10:1 slot nozzle was tested at two different wing chords (reference 24) to provide different ratios of wing upper-surface length to nozzle slot height. Noise radiation patterns measured in the flyover plane (zero azimuth angle) for these USB configurations, and those with the circular and D nozzle and deflector, are shown in figure 26 for two pressure ratios. Calculated directivity curves are shown for the circular nozzle and deflector (solid circle data symbols). The 5:1 slot nozzle would be expected to have a well attached exhaust jet on the wing upper surface. The wing surface boundary layer would be expected to cause greater viscous decay of mean velocity than that for the thicker deflected jet from a circular nozzle. Although the reduced velocity should cause less noise, USB noise with that nozzle was 2 to 3 dB louder than that with the circular nozzle. Above the wing, this canted nozzle without a deflector was about as loud as the circular nozzle with a deflector. At the highest exhaust velocity, measured directivity below the wing resembled what would be expected if jet noise of the entire isolated jet was rotated through the flap deflection angle and added to the calculated scrubbing and trailing-edge noise. To achieve this result, mean velocity of the exhaust jet at the wing flap trailing edge would have had to be about as large as the nozzle exit velocity.

Velocity distributions for a full-scale USB configuration tested with a circular nozzle and deflector and with a canted 4:1 slot nozzle were given in reference 25. At constant nozzle exhaust velocity, maximum local velocity at the trailing edge was shown in figure 19 of reference 25 to be larger for the slot nozzle than for the circular nozzle. With a short flap, maximum trailing edge velocity for the slot nozzle was greater than the nozzle exhaust velocity. For a ratio of flap length to nozzle size similar to that for the small-scale models, the difference in velocity decay between circular and slot nozzles would cause the slot nozzle to be about 2.6 dB noisier. This increment, which agrees with data for the small-scale model, was estimated by assuming that noise radiation was proportional to maximum trailing edge velocity raised to the sixth power.

The importance of quadrupole noise in USB noise prediction has been noted in reference 25 when comparing data from model and full-scale installations. Noise radiation patterns of the full-scale USB tested with both circular and slot nozzles differed in one important respect from those of the small-scale models. A strong lobe of jet mixing noise with its peak amplitude located about 30° below the deflected jet occurred at full scale but not at model scale. Noise radiation patterns measured with the full-scale models generally agreed in the lower forward quadrant with those scaled from small-model data. The additional quadrupole noise, which appeared in the full-scale spectra as a more gradual decay at Strouhal numbers larger than about 3, caused up to 5

dB more noise in the lower aft quadrant. It is not presently known whether this increased noise was caused by differences in test geometry, differences in test Reynolds number, or refraction and channeling of sound by the hot exhaust jet.

The 10:1 slot nozzle configuration was about 3 to 5 dB quieter than the circular nozzle configuration and about 3 dB quieter than the calculated directivity curves. As was noted in reference 16, this nozzle had a smaller exit area than did the other exhaust nozzles. If USB noise was scaled directly with nozzle exhaust area, these data should be increased 1.8 dB for comparison with the other data. The actual scaling law is uncertain because as discussed in reference 26 the edges of an USB slot nozzle exhaust jet tend to roll up as vortices rather than remaining attached to the deflected upper surface. Thus the flow produced by an USB slot nozzle may resemble that for an USB circular nozzle with the same exit area but would have a higher turbulence level and different turbulence scale length. Such behavior plus viscous decay of exhaust velocity near the wing surface would explain qualitatively the increased noise with the 5:1 slot nozzle and decreased noise with the 10:1 slot nozzle. Doubling the flap length for the 10:1 slot nozzle can be seen to have had little effect on noise radiation except for direction angles slightly below the deflected jet. The apparent lobe of jet mixing noise was approximately eliminated, as would be expected from increased viscous decay before the exhaust flow reached the trailing edge.

Noise radiation patterns for the USB model with a canted 5:1 slot nozzle were calculated by assuming that the trailing-edge velocity ratio was that measured with the 4:1 slot nozzle of reference 25. Noise radiated above the wing was taken as the sum of scrubbing noise, trailing edge noise, and noise of the exhaust jet deflected through the 20° nozzle cant angle. These calculated patterns are compared in the upper part of figure 27 with the data of reference 24 at three pressure ratios. Except for small lobes of jet mixing noise at angles within 40° from the deflected exhaust, this empirical modification to the calculation method gives good prediction of these data. Similarly, an arbitrary 3 dB decrease of scrubbing noise and trailing edge noise from that calculated for the circular nozzle, plus calculated noise from deflection of the canted exhaust by the wing upper surface, was assumed for the 10:1 slot nozzle. These calculated noise radiation patterns are shown in the lower part of figure 27 to give close agreement with the data of reference 24. Velocity measurements in the trailing-edge plane were not available for the 10:1 slot nozzle to justify the implicitly assumed velocity decay.

Measured noise radiation patterns in the flyover plane for the USB with 30° vane and 60° flap deflection, and circular nozzle with deflector (reference 27), are compared with calculations in figure 28. Noise beneath the wing is predicted to be dominated by scrubbing noise. Jet mixing noise from the portion of the exhaust jet downstream of the trailing edge was calculated to be

about 10 dB below the sum of scrubbing noise and trailing edge noise. Adding the measured noise of the circular jet with its deflector gave a good prediction of the noise radiation pattern above the wing. This good agreement between data and calculations had also occurred with this model at a smaller flap deflection (figure 25a). The NASA empirical prediction method of reference 19 also was in good agreement with these data. Good agreement would be expected because OASPL below the wing was calculated to be dominated by just one noise mechanism, scrubbing noise.

Measured noise radiation patterns for this larger flap deflection and the D nozzle and deflector are compared in figure 29 with those calculated for the circular nozzle and shown in figure 28. Unlike the close agreement for these two nozzles at the smaller flap deflection and the flyover plane (figure 25a), the D nozzle was about 5 dB louder at this larger deflection. The D nozzle at this flap deflection was about as loud as the 5:1 canted slot nozzle (reference 24), which had been the loudest nozzle at the smaller flap deflection (figure 26). No method is now available for predicting these measured effects of USB nozzle shape on noise radiation.

Acoustic Spectra

Calculated and measured spectra for the five nozzle shapes tested with the USB configuration at 10° vane and 20° flap deflection are compared in figure 30 for two directions at pressure ratios of 1.7 and 1.25. These measured spectra were not corrected for ground reflection. Because the microphones for the USB tests were mounted higher above the ground than for the UTW tests, spectrum waviness caused by ground reflection was considerably smaller. Free-field data would be about 0.7 dB below the plotted values at greater than 630 Hz center frequency. Spectra shown as solid lines were calculated for the circular exhaust nozzle with deflector (solid circle data symbols). At 80° from the nozzle inlet, measured spectra for all but the two 10:1 slot nozzles were closely predicted at a pressure ratio of 1.7 (figure 30(a)). Spectra for the circular and D nozzles with deflector were underestimated by about 3 dB at all frequencies at a pressure ratio of 1.25 (figure 30(b)). The 5:1 slot nozzle spectrum had a strong peak at 500 Hz which caused measured OASPL to exceed that for the circular and D nozzles. However, the high-frequency part of this spectrum was in good agreement with that calculated for the circular nozzle. It is not certain whether the low-frequency peak is a real phenomenon caused by trailing-edge noise generated by vortices at the edge of the exhaust jet or is an unusually strong ground reflection.

Spectra for the 10:1 slot nozzles were below those for the other nozzles. Arbitrarily decreasing the calculated curve 2 dB in amplitude and shifting it 2/3 octave lower in frequency produced the dash curve which is in good agreement with data for the shorter flap length (half-solid diamond data symbols). As noted in reference 16, scaling of frequency by assuming that the characteristic dimension is proportional to the square root of exit area should shift

this spectrum downward by another 1/3 octave for comparison at constant exit area. This scaling could also produce a 1.8 dB shift of amplitude. Thus the high-frequency parts of the spectra radiated with the 10:1 slot nozzle approximately match those for a 5:1 slot nozzle having the same exit area and same flap length, shifted one octave lower in frequency.

Measured and calculated spectra for the direction 120° from the nozzle inlet are shown in figures 30 (c) and (d). Jet mixing noise from the portion of the exhaust jet downstream of the trailing edge is calculated to dominate high-frequency noise for this direction at the higher pressure ratio. Thus the spectrum calculated for that case (figure 30 (c)) has a less rapid decay rate at high frequency than that calculated for a lower pressure ratio at the same direction (figure 30 (d)) or a direction further from the deflected exhaust at the same pressure ratio (figure 30 (a)). The NASA prediction method of reference 19, which uses one normalized spectrum shape for all pressure ratios, would not predict this less rapid decay rate and the resulting higher perceived noise level at full scale. At this higher pressure ratio, spectra measured with the circular nozzle were closely predicted. Those for the D nozzle were under-predicted at low and middle frequencies where jet noise would not be expected to dominate. Spectra for the 5:1 slot nozzle, and for the 10:1 slot nozzle without a long flap chord, had a smaller high-frequency decay rate than that for the circular and D nozzles. Such noise would correspond to jet mixing noise with a higher center frequency, as might be produced by rolled-up edges of the slot jet. This additional high-frequency noise would adversely affect perceived noise level of a full-scale EBF installation. The spectrum for the 10:1 slot nozzle and long flap had a more rapid high-frequency decay rate than the other spectra measured at this direction and pressure ratio. This decay rate approximately matches that for all of the configurations at directions further from the deflected exhaust (figures 30 (a) and (b)) and is approximately that which is expected for trailing edge noise. Spectra for this measurement direction and the smaller pressure ratio (figure 30 (d)) approximately match the calculated spectrum shape although amplitude was underestimated about 3 dB for the circular, D, and 5:1 nozzles.

One conceptual weakness of this analysis for USB configurations is that noise radiation patterns for trailing edge noise and scrubbing noise are calculated separately and then summed, but the same normalized spectrum shape is used for both mechanisms. That is, calculated scrubbing noise is assumed to have its own spectrum shape for UTW but to have the spectrum shape of trailing edge noise for USB. This was done as an empirical method for matching the measured shapes of OASPL noise radiation patterns and 1/3 octave spectra. The calculation method presented here is admittedly not logical unless the process of deflecting a USB exhaust jet against a wing upper surface is assumed to destroy spanwise coherence of large-scale vortex structure in the jet. Such a change would justify the difference in high-frequency decay rates assumed for UTW and USB scrubbing noise. Spectrum shapes measured directly above the UTW

wing of reference 1 tested with retracted flaps generally had the slower decay rate associated with UTW scrubbing noise, so impingement followed by expansion around the USB curved upper surface may have produced the change in spectrum shape.

Measured and calculated spectra for the USB model at 30° vane and 60° flap deflection with the circular nozzle and deflector are compared in figure 31. General levels and shapes are well predicted except for about 4 dB overestimate for high frequencies at the lowest of the three pressure ratios. Measured spectra had a double-humped shape at this flap deflection angle that was less apparent at the smaller deflection angle (figure 30). The local minimum occurred in the same range of frequencies for all pressure ratios, so it is not obvious whether this feature of the measured spectra is a ground-reflection effect. Spectra measured at this flap deflection with the D nozzle are compared in figure 32 with those calculated for the circular nozzle. The dip in measured spectra again occurred at the same frequencies independent of pressure ratio. The high-frequency parts of these spectra had the calculated decay rates but their amplitudes were about 4 dB higher than those with the circular nozzle. The cause of these differences in spectrum shape between the two nozzles tested at large flap deflection, or between either nozzle at large and small flap deflections, is not known.

Engine-in-Front-of-Wing Configuration

An alternate engine installation for externally blown flaps was examined in reference 28. The exhaust nozzle was placed in front of a wing with double slotted flaps. Both the wing upper and lower surfaces were scrubbed by the exhaust. The wing maximum thickness was about 60 percent of the nozzle exit diameter, so this installation provided a gross distortion of the exhaust flow. Such an installation would be expected to radiate noise having the properties of incidence fluctuation noise rather than scrubbing noise. Measured sound power spectra were compared in figure 8 of reference 28 with those for UTW and USB installations. High-frequency decay rate was much larger than was measured for those more conventional EBF installations, as would be expected for incidence fluctuation noise.

Analytical methods are not available for calculating the unsteady lift response to turbulence incident on an airfoil having double slotted flaps as a crude estimate, each of the three physical segments was assumed to respond like an isolated airfoil at the jet exhaust velocity. Each lift dipole was assumed to act normal to the local chord. A mean velocity equal to the exit velocity, turbulence rms intensity of 10 percent rather than the expected local maximum near 15 percent, and effective span equal to the nozzle diameter was assumed. Turbulence integral scale length was taken as one-fourth the

nozzle radius (half the width of the annulus between the nozzle centerbody and outer edge). Calculations were conducted using a method recommended in references 1 and 2. Because it was likely that immersing the model within the nozzle exhaust would cause increased viscous decay of the jet, neither deflected-jet quadrupole noise nor trailing edge noise was calculated.

Calculated OASPL directivity is compared in figure 33 with data from figures 5 and 6 of reference 28 for takeoff and approach flap deflections and 156 and 220 m/sec nozzle exit velocities. Two data symbols are shown corresponding to test configurations with the wing leading edge slightly inside the exit nozzle and one diameter downstream of the nozzle exit plane. There was essentially no difference between data for those two installations. Two calculated curves are shown for each flap deflection and velocity. The dash curves are the sum of calculated noise for the undeflected wing panel and both flap segments. They overestimate maximum measured OASPL and overestimate the rotation of noise directivity with increasing flap deflection. The solid curves are the sum of lift dipole noise calculated for the undeflected wing panel and just the forward flap segment. These calculations predict the measured trends and generally are within 2 dB of measured levels except for direction angles near forward and near the deflected jet.

As an alternate assumption that would yield roughly the same directivity, calculations were conducted for the lift response of a single large unslotted airfoil extending from the wing leading edge to the aft flap trailing edge. Use of the above assumptions for mean velocity, turbulence level, jet width, and turbulence scale length yielded levels of OASPL roughly 10 dB below data. This reduced level was caused by the acoustic noncompactness factor which produced considerable calculated decrease of power spectral density at frequencies where the measured spectra were strongest.

Calculated and measured 1/3 octave sound pressure levels are shown in figure 34 for both exhaust velocities and flap deflections. The measurement direction angles of 100° for takeoff deflection and 80° for approach deflection were those which would have caused maximum flyover OASPL. Data were taken from figures 7 and 8 of reference 28 and include measured spectra for the undeflected exhaust jet at the test exhaust velocities and directions. For each velocity, both combinations of flap deflection angle and measurement direction yielded approximately the same measured OASPL and spectrum. Measured spectra for the nozzle and wing were well above those for the isolated jet. The calculated spectra are for the undeflected wing panel and forward flap segment. As can be seen from figure 33, OASPL's of these calculated spectra underestimated those for the measured spectra by about 2 dB at takeoff flap deflection but were within 1 dB at approach. Calculated spectra were more sharply peaked than the data. Most of the discrepancies occurred at low frequencies where the data may have been increased by ground reflection. The absolute levels and rapid decay rates of measured spectra at

frequencies above 2500 Hz were closely predicted. Use of a larger assumed integral scale length would have increased the calculated response at low frequencies and reduced the frequency at which the abrupt decrease of sound pressure level occurred. It would have had relatively little effect on high-frequency sound pressure levels and overall sound pressure level. Thus the measured directivity and spectra of noise from an externally blown flap with a simulated engine in front of the wing were closely predicted by theory for noise radiation from an airfoil with incident turbulence if noise radiation from the last of the two flap segments is neglected.

STRUT AND SPLITTER PLATE NOISE

Analytical Methods

An approximate method had been developed in references 1 and 2 for predicting airfoil noise caused by incident turbulence. That method expressed the dipole sound spectrum as a product of the turbulence spectrum, the lift response spectrum developed by Filotas (reference 29), and an acoustic transfer function. This transfer function included a term developed by Hayden in reference 30 to represent qualitatively the effect of acoustic noncompactness. Filotas' solution for unsteady lift response uses two analytical equations, one for low and one for high reduced frequencies. The low-frequency solution was shown in reference 1 to give a good prediction of measured surface pressure spectra, while other analytical solutions overestimated those spectra at low reduced frequencies. Far-field one-third-octave sound pressure levels in the lateral plane of symmetry were given by

$$SPL_{1/3} = 10 \log\left(\overline{v^2}/U^2\right)(0.232\, \ell/c)\left(\pi\rho U^3 b\, \sin\theta/2\, a R p_{ref}\right)^2$$

$$+ 10 \log\left[1+(\pi f c/a)^2\right]^{-1}|\mathcal{L}|^2 + 30\log(fc/U) + 10\log(UE/\overline{v^2}\ell)$$

(14)

where ℓ is the turbulence transverse integral scale length. The transverse turbulence spectrum for isotropic turbulence was approximated by

$$UE/\overline{v^2}\ell = 4\left[1+(2\pi f\ell/U)^2\right]^{-1}$$

(15)

taken from Equations (1-95) of reference 31, and the magnitude of the lift response function squared in three-dimensional turbulence was obtained from the solution of Filotas (reference 29) as

$$|\mathcal{L}|^2 = \frac{\ln(1.2 + \pi^2 \beta^{-2})}{\ln 1.2 + 3\pi^2 \beta^{-2}} \qquad \sigma_0 \leq 1/\beta \qquad (16)$$

$$|\mathcal{L}|^2 = \frac{\ln(1.2 + \pi^2 \sigma_0^2)}{\ln 1.2 + 3\pi^2 \sigma_0^2} \qquad \sigma_0 \geq 1/\beta \qquad (17)$$

Reduced frequency σ_0 is defined by

$$\sigma_0 = \omega c/2U = \pi fc/U \qquad (18)$$

and β is the ratio of turbulence integral scale length to half-chord, $2\ell/c$. Nomenclature has been changed from that of reference 1 to match that of reference 32.

After that study had been conducted, the rigorous analysis given in Section 3.5.1 of reference 32 became available. An equation for spectral density of acoustic intensity was developed using different approximations for turbulence spectrum. For the plane of symmetry, this equation simplifies to

$$\overline{I_w} = \frac{3}{32} \, b\rho \, \overline{v^2} \left(\frac{c}{r}\right)^2 \left(\frac{U}{a}\right)^3 \frac{\sigma_0^2 \sin^2 \theta}{\beta\left(\beta^2 + \sigma_0^2\right)^{5/2}} \, |\mathcal{L}|^2 \qquad (19)$$

which yields one-third-octave SPL given by

$$SPL_{1/3} = 10 \log (3/32) \, (0.232/\pi) \left(\overline{v^2}/U\right)\left(\rho U^3/a \; p_{ref}\right)^2 (bc/r^2)$$
$$\sigma_0^3 \, \beta^{-1}\left(\beta^{-2} + \sigma_0^2\right)^{-5/2} |\mathcal{L}|^2 \sin^2 \theta \qquad (20)$$

The spectrum of acoustic intensity as obtained from equation (20) above, with Mugridge's approximate solution (reference 33) for the lift response function, was given between equations (3-81 and 3-82) of reference 32. A closed-form solution for mean acoustic intensity was given as equation (3-82) for this approximation to the lift response function.

These two solution methods give different functional dependence of calculated acoustic intensity on Strouhal number. As described in reference 30, it is convenient to regard the power spectral density of lift force as a product of an aerodynamic transfer function and a turbulence input spectrum.

Power spectral density of acoustic intensity then is the product of an acoustic transfer function and the lift force spectrum. Variations of these quantities with Strouhal number are sketched in figure 35 for the solution method recommended in reference 1 and given by equations (14) through (18). The product of acoustic transfer function and turbulence input spectrum varies as frequency squared at small Strouhal numbers and inversely with frequency squared at large Strouhal numbers. Aerodynamic transfer function given by equations (16) and (17) is independent of frequency at small Strouhal numbers. Thus the acoustic intensity calculated by this method varies as sketched in the lower right portion of figure 35, frequency squared and frequency to the inverse fourth power at small and large Strouhal numbers.

In contrast, the product of acoustic transfer function and turbulence input spectrum as given on page 216 of reference 32 and by equation (19) can be shown to vary as frequency to the fourth power at small Strouhal numbers and inversely with frequency at large Strouhal numbers. The aerodynamic transfer function of reference 33, used in reference 32, is independent of frequency at small Strouhal numbers and, like the Sears function squared, varies inversely with frequency at large Strouhal numbers. Acoustic intensity calculated from page 217 of reference 32 therefore varies with frequency to the fourth power and frequency to the inverse second power at small and large Strouhal numbers. Changing the aerodynamic transfer function to that of reference 29 would change the dependence to frequency to the inverse third power at large Strouhal numbers. Thus a difference exists between spectrum asymptotic slopes given by the two methods at both small and large Strouhal numbers. Use of the same unsteady-aerodynamics solution in both methods decreases but does not eliminate the difference at large Strouhal numbers.

Comparisons With Strut Noise Data

An experimental study of noise radiation from a strut in a turbulent exhaust jet, conducted by W. A. Olsen at NASA Lewis Research Center, was described on pages 218-219 of reference 32. The experimental configuration, sketched in figure 3-15 of reference 32 and reproduced as figure 35 (a) herein, has a 2.86 cm (1.125 in.) chord uncambered strut placed at zero incidence relative to the centerline of a 10 cm (4 in.) diameter nozzle. The strut leading edge was 4 nozzle diameters downstream of the nozzle exit and one radius away from the centerline. Thus the strut extended across a spatially nonuniform turbulent mixing region and, at its smallest distance from the centerline, was in the region of largest velocity fluctuation. Flow properties at the leading edge were described as a mean velocity 0.62 times the nozzle exhaust velocity, rms velocity fluctuation 13 percent of that mean velocity, and turbulence length scale 0.3 diameters. The airfoil chord was 9/32 diameter so the airfoil chord was approximately equal to the turbulence scale length. It was shown in figure 3-16 of reference 32 that if these local flow properties were assumed to act uniformly over the 1.73 diameter strut height, measured OASPL directivity in the far field 45 diameters from the airfoil was predicted at low velocities.

One-third-octave spectra measured in the far field at 90° direction and 4.56 m (15 ft) distance are shown in figures 36 (b) and (c) for the seven tested velocities. Data were corrected for background noise of the isolated jet, and only the measurements for the strut plus jet which exceeded background by at least 4 dB are presented. Spectra calculated for the specified flow conditions using the method recommended in references 1 and 2 and given by equations (14) through (17) are plotted as solid lines. These predict the general level of the data but are displaced toward smaller frequencies. Calculations were repeated assuming that the turbulence integral scale length was 0.15 diameter, half the assumed length stated on page 218 of reference 32. The resulting calculated spectra, shown as dash curves, generally are within ±2 dB of the data except for the lowest velocity and for the highest and lowest frequencies. At most velocities the high-frequency portion of measured spectra decayed more rapidly than was calculated.

Acoustic spectra also were calculated by the method of reference 32 which used the unsteady-aerodynamics solution of Mugridge (reference 33). These spectra are compared in figure 37 with the data previously shown in figure 36 (b). As in that figure, spectra calculated by the method of reference 1 for a turbulence scale length of 0.15 diameters are shown as dash lines. Spectra from the method of reference 31, shown as solid lines, were calculated for a turbulence scale length of 0.20 diameters to produce better agreement with data for low frequencies. These calculated spectra were in general agreement with data for frequencies up to 6300 Hz. However, their high-frequency decay rate was considerably less than that for the data.

As an attempt to provide closer agreement, the unsteady-aerodynamic solution of Filotas (reference 29) was used within the analysis developed in reference 32. This solution predicts less lift response at both small and large reduced frequencies than that of reference 33. Turbulence level for that calculation was arbitrarily assumed to be 50% higher than was used in the other two calculations so that OASPL would approximately match that for the method of reference 32. The resulting calculated spectra are shown in figure 37 as dot-dash lines. Their high-frequency decay rate is midway between those of the other two solutions. These calculated spectra are in better qualitative agreement with the data than those from the method of reference 31. However they undercut the data at moderate frequencies above the peak frequency and over-predict at high frequencies. Measured spectrum shapes at high frequencies, particularly those shown in figure 36 (c) for the higher velocities, are more closely predicted by the approximate method of reference 1 than by the presumably more rigorous method of reference 32 or a modification to that method.

Calculated and measured spectra for measurement directions 60° from upstream and 60° from downstream are shown in figure 38 for 57 and 114 m/sec velocities. The calculations used the method of reference 1 with a turbulence

integral length scale of 0.15 diameter, and these calculated curves are 20 log (sin 60°) or -1.25 dB from those given in figure 36. Although the same curve is predicted for equal direction angles measured from the upstream or downstream direction, measured spectrum shapes at the two directions were significantly different at high frequencies. Spectra measured in the upstream direction decayed more abruptly and then became parallel to the predicted curve at the highest frequencies. For the lower velocity shown, measured levels were underpredicted by about 4 dB above 6300 Hz frequency. Changing the direction angle from 60° to 90° (figure 36 (c)) shifted the start of abrupt decay towards higher frequencies. Also, directivity of the jet background noise caused such noise to be larger at high frequencies and downstream directions. Thus the portion of the airfoil signal that clearly exceeded background noise contained the rapid decay of spectrum amplitude but did not contain the change to a smaller decay at the highest measurement frequencies. As can be seen from figures 36 (b) and (c), increasing the velocity caused onset of rapid decay to begin at larger frequencies. Also, increasing the test velocity at the largest velocities caused an increase of high-frequency noise. Doubling the velocity as in figure 38 did not change the fact that spectra measured 60° from downstream, at frequencies above 4000 Hz, were about 6 dB larger than those measured 60° from upstream. It did change the general shape of the data so that the calculated curves were in best agreement with data for downstream directions at small velocities and upstream directions at large velocities. These changes might be caused by scattering of high-frequency sound by the jet mixing region, which contains stronger small turbulent eddies in the upstream direction, and by variations in the normalized turbulence properties with jet exhaust Mach number.

Strut Noise Reduction Tests

Apparatus and Procedure

Tests were conducted in the UTRC acoustic wind tunnel to determine whether strut noise caused by incident turbulence could be reduced by changes of strut edge properties or shape. This open-circuit wind tunnel, shown in figure 39 and described in reference 34, has an open test section located within an anechoic chamber. For these tests the open jet was 0.79 m (31 in.) high and 0.53 m (21 in.) wide. A circular jet collector approximately 1.1 m (42 in.) diameter, having a rounded lip lined with acoustic absorbing material, was located 3.6 m (142 in.) downstream of the nozzle inlet. Sideplates 1.5 m (60 in.) long, supported by brackets outside the airflow, constrained the forward portion of the open jet. The test airfoil was mounted between these sidewalls to assure that all of the airfoil noise was caused by the controlled turbulence test airflow. This open jet configuration, with a larger collector located further downstream of the nozzle exit, differs from that described in reference 34.

The tunnel inlet section has a contraction ratio of 16.5 and is equipped with screens and a honeycomb section to provide less than 0.2% turbulence level in the test section. For these tests, turbulence-generating grids were installed in the nozzle at a cross section area roughly twice the nozzle exit area. Two grids, denoted the large and medium grid, were used in these tests. Turbulence generated by these grids is documented in reference 1. Streamwise integral scale length was about 3.2 cm (1.27 in.) and transverse integral scale length was about 1.9 cm (0.75 in.) for both grids. Streamwise turbulence levels decayed slightly with increasing downstream distance and varied approximately with velocity to the -0.2 power. These levels, evaluated at midchord and midspan locations in the absence of the airfoil, were about 5.1% for the large grid and 3.4% for the medium grid at 80 m/sec (262 ft/sec) mean velocity.

The airfoil model was an instrumented flat plate which represents a hardwall splitter plate or engine duct strut. This model, shown in figure 40, had 46 cm (18 in.) chord and 53 cm (21 in.) span. It had constant 2.54 cm (1.0 in.) thickness except for the cylindrical leading edge and the aft 6.35 cm (2.5 in.) which had circular arc upper and lower surfaces and less than 0.05 cm (0.02 in.) trailing-edge thickness. Model thickness had been chosen to allow easy installation within the airfoil of conventional 0.635 cm ($\frac{1}{4}$ in.) diameter condenser microphones mounted on right-angle adaptors and preamplifiers. Microphones were flush mounted without protective grids on both the upper and lower surfaces at positions offset ±0.5 cm (0.2 in.) from midspan at three chordwise locations: 5 cm (2 in.), 23 cm (9 in.), and 41 cm (16 in.) downstream of the leading edge. This model had been used in tests described in references 1 and 2 to evaluate the validity of different analytical methods for calculating airfoil noise caused by incidence fluctuation.

Tests were conducted with the airfoil mounted at midheight in the test section at zero angle of attack. Test airspeeds were 31.5, 50, 80, 125, and 172 m/sec (102, 164, 262, 410 and 570 ft/sec) with both turbulence grids. Far-field measurements were obtained with conventional 0.635 cm ($\frac{1}{4}$ in.) diameter microphones placed on an arc of 2.14 cm (7 ft) radius centered at midchord. The microphones were located at 60, 90, and 120° angular positions relative to the flow direction. Far-field sound pressure levels and surface pressure fluctuation levels, cited as SPL and surface SPL respectively, were measured in decibels referenced to 2×10^{-5} newtons per square meter (2×10^{-4} microbar). All microphones were calibrated daily with a 250 Hz pistonphone.

Airfoil Modifications

Experimental studies have been conducted (e.g., references 35-41) of shape and surface modifications to reduce noise of airfoils with incident turbulence and of externally blown flaps. As described by Hayden in reference 35, these modifications usually can be classed as (1) changes of edge impedance, (2) changes of surface impedance, and (3) changes of flow mean and fluctuating

properties. The first category includes serrated and slotted leading and trailing edges (references 35 and 40) to provide spanwise variation of edge location, perforated or porous surfaces near the edges (references 35, 36, 37, and 40) to provide a gradual change of impedance with distance, and compliant flexible surfaces near the edges (reference 40) for the same purpose. Serrated leading edges tested at low Reynolds numbers and low turbulence (reference 41) have caused transition of an airfoil laminar boundary layer and therefore eliminated airfoil tone noise (reference 42). Except for that one case, serrations and slots at leading and trailing edges have not reduced noise and sometimes (reference 35) increased noise. Porous material with a relatively large (40%) open volume, and perforated thin sheet surfaces with or without acoustic bulk-absorbing backing, sometimes (references 36 and 37) were reported to give 6 to 10 dB noise reduction. In contrast, other studies (references 35 and 40) achieved a maximum of 2 to 3 dB reduction with similar materials and geometry. Flexible surfaces (reference 40) had no effect on noise radiation, as might be expected from the relatively high frequencies at which acoustic radiation is important and the relatively large inertia of practical surface materials. Distributed surface impedance by use of complaint surfaces (reference 40) had no effect on noise. Distributed impedance in the sense of acoustically lined splitter plates (reference 43) caused noise reduction at design frequencies of the acoustic absorbing material but had less effect on added low-frequency noise. This added noise was produced by both a lined and a hard-wall splitter within a fan exit duct flow. For a range of frequency, noise radiated from the exit duct with an acoustically lined splitter was found to exceed that for a hardwall duct without splitters (figure III-37 of reference 43). Changes of flow properties have been accomplished with fine-mesh screens (reference 36) to reduce mean velocity, turbulence scale length, and possibly turbulence intensity of airflow near a surface. These noise-reducing effects were achieved at the expense of increased aerodynamic drag and, for lifting surfaces, reduced time-average aerodynamic lift.

Changes of both edge impedance and flow properties are achieved by use of slot blowing. Interposing a layer of air with high momentum, low turbulence, and small turbulence length scale may shield a noise-radiating surface from the outer flow and locally change that flow. Trailing edge blowing may also affect the unsteady shedding of circulation at the edge, decreasing the lift force fluctuations and noise radiation. For externally blown flaps, trailing edge blowing was reported in references 37 and 39 to produce 3 to 6 dB noise reduction. Smaller reductions were reported in reference 38 for tests at larger scale.

After reviewing these and other experimental studies, four concepts were selected for tests to reduce incidence fluctuation noise. One was the use of removable perforated leading and trailing edge regions to provide a gradual change of surface impedance. These were tested as replacements for corresponding portions of a hard-wall splitter plate airfoil with 45.7 cm (18 in.) chord,

53.3 cm (21 in.) span, and 2.54 cm (1.0 in.) thickness. This model, shown in figure 40, had been utilized in tests reported in reference 1. From the data of reference 35, use of either a bulk absorber or perforated plate backed by an air cavity could cause about 2 dB noise reduction. From the data of reference 40, perforated plate with a bulk absorber backing material sometimes caused about 1 dB additional noise reduction over the 1 to 2 dB reduction achieved from perforated plate with an air cavity. Because different tests reported in references 35, 36, and 40 did not give a clear indication of optimum porosity, two different sets of perforated-plate edge regions were used. Both had 26 gage (approximately 0.051 cm, 0.020 in. thickness) perforated sheet steel surfaces. One set had 18% open area with 0.061 cm (0.020 in.) dia holes, and the other had 30% open area with 0.051 cm (0.020 in.) dia holes. These leading and trailing edge regions, sketched in figure 41, had 6.4 cm (2.5 in.) and 10.2 cm (4.0 in.) chordwise extent, respectively. The 1.27 cm (0.5 in.) portion adjacent to each unperforated central part of the chord was backed by a solid structural member. The remainder of each removable leading and trailing edge region was filled with steel wool as a broadband bulk absorber of acoustic energy. Special attention was given to construction of the nominal 0.1 cm (0.04 in.) thick trailing edge so that only the two rows of perforations closest to the edge were obstructed. Each percentage open area was tested on the leading edge region alone (forward 14% chord), trailing edge region alone (aft 22% chord), and both leading and trailing edge regions.

Because noise radiation caused by incident turbulence is generated by lift force fluctuations, any airfoil shape modification that reduces lift response might reduce noise. Airfoils which have thick blunt trailing edges are known to have small steady-state lift coefficient slopes at subsonic speeds. A hard-wall blunt trailing edge configuration is sketched in figure 41. This was obtained from the basic airfoil model by removing the curved aft trailing edge region and fairing the surface to constant 2.54 cm (1.0 in.) thickness at the rear spar. This change decreased the chord to 36.8 cm (14.5 in.) and would be expected to produce vortex shedding noise at a Strouhal number near 1/3 referenced to maximum thickness. The resulting discrete-frequency noise might be more easily absorbed by acoustic lining than the broadband noise caused by incident turbulence.

Trailing edge blowing was tested as a spanwise slot located at the airfoil trailing edge. To obtain this configuration, shown in figure 41, the solid trailing edge which occupied the aft 2.54 cm (1.0 in.) of the original model was removed and all joints between the curved sheet-metal skin and the aft spar were sealed. A perforated tube extended across the model span within this plenum chamber and was supplied with compressed air at both ends. Pitot probes were located in this chamber to allow measurement of flow rate and spanwise uniformity. The downstream edges of the model surfaces were thinned and rounded to serve as a slot nozzle. Set screws at 5.1 cm (2.0 in.) spanwise spacing were adjusted to provide 0.25 cm (0.10 in.) slot height. This

46

height is approximately equal to the sum of the upper-surface and lower-surface turbulent boundary layer displacement thickness at the airfoil trailing edge.

The fourth configuration consisted of wire mesh screens tangent to the rounded solid leading edge. As sketched in figure 42, each screen was about 30 cm (12 in.) long. It trailed above and below the airfoil at 45° from the downstream direction, and was attached to the tunnel sidewalls. Endpoints of the screen were about 10.3 cm (4.1 in.) downstream, and 11.0 cm (4.4 in.) above and below the leading edge position. A fine mesh (3.5 mesh/cm, 0.20 cm (0.078 in.) diameter holes, 39% open area) and a coarse mesh (1.6 mesh/cm, 0.51 cm (0.20 in.) square holes, 64% open area) were utilized to provide arbitrary changes in local velocity, turbulence scale length, and turbulence intensity.

Analysis of Data

The acoustic wind tunnel configuration used in these tests differed from that described in reference 34 in having more than twice as large an open jet length, followed by a new larger flow collector. This change had been adopted to decrease the flow velocities in the shear layer where it impinges against the collector. Broadband noise was expected to be decreased relative to levels shown in reference 34. Background noise measured 2.13 m (7 ft) directly above the airfoil position, in the empty tunnel, is compared in figure 43 for the new and old collector configurations and both grid-generated turbulence levels. Background noise with the medium grid, shown in figure 43 (a), was reduced several dB for low velocities up to 80 m/sec. About 3 dB reduction was obtained at 125 m/sec over the entire frequency range, but up to 5 dB noise increase occurred at the lowest frequencies and 172 m/sec velocity. In contrast, spectra for the new collector and large grid, shown in figure 43 (b), were lowered about 5 dB at frequencies below 500 Hz and essentially unaffected at higher frequencies.

The hard-wall splitter plate airfoil for which noise data had been reported in references 1 and 2 was used as a basic reference configuration. Spectra measured directly above the model in that and the present test program, uncorrected for tunnel background noise, are given in figure 44. These spectra were in good agreement for tests with the large turbulence grid. Spectra measured with the medium grid, shown in figure 44 (a), were louder by more than 5 dB for low frequencies corresponding to Strouhal numbers fc/U less than about 1.5. It was found that the tested configuration had not used a solid leading edge but used the 18% porosity perforated sheet covered with tape . This taped leading edge also had been used as part of the configurations having porous trailing edges and nominal hard leading edge with the medium grid. It is possible that either the tape was loose and fluttered, or the perforated material was not sufficiently rigid, causing surface vibrations that produced excess low-frequency noise. Data

are presented here for both of these configurations because the taped porous leading edge serves as the reference case for some test models.

The above data have not been corrected for wind tunnel background noise. A comparison of uncorrected and corrected spectra for this model as tested with the old jet collector, reproduced from figures 22 and 23 of reference 1, is given in figure 45. The uncorrected spectra for frequencies above several thousand Hz were dominated by background noise. Spectrum decay rate became smaller as the airfoil spectrum decayed into background noise which decreased slowly as frequency was increased. If an airfoil modification would reduce the noise radiation, its corrected spectrum would have to be omitted at frequencies where it had decayed into the noise floor. Comparison of uncorrected spectra would at least illustrate whether some minimum amount of noise reduction was achieved at each center frequency. The following comparisons therefore are for spectra that have not been corrected for tunnel background noise. Corrected spectra are shown only for a modification that reduced the incidence fluctuation noise.

The tested modifications are listed in Table II along with the maximum noise reduction achieved. These listed reductions are for the three adjacent 1/3-octave frequency bands in which each device was most effective. Generally, noise reduction within one region of frequency was accompanied by increased noise at other frequencies.

The effect of 18% porosity leading and trailing edges on sound caused by incidence fluctuation is shown in figure 46. Data for the medium grid, given in figure 46 (a), use the taped porous leading edge as the basic hard-wall configuration. The porous leading edge and solid trailing edge was several dB quieter than the basic configuration at frequencies up to about 500 or 630 Hz but was louder at those frequencies than the basic solid-leading-edge model (figure 45). However, at center frequencies above 500 Hz at 80 m/sec velocity and 630 Hz at the higher velocities it became quieter than either hard-wall model. More than 6 dB noise decrease generally was achieved before the airfoil noise decayed into the tunnel background. Thus the flat portions of these spectra above 1000, 1600, and 2000 Hz for these test velocities (a Strouhal number of about 6) are the background noise floor. Use of a porous trailing edge and taped leading edge caused either no noise reduction or several dB noise increase. With both leading and trailing edge porous, about 3 dB noise reduction was obtained over about an octave of frequency centered near a Strouhal number of 6. About 2 dB noise increase occurred at the lowest frequency.

Spectra for this porosity and the large grid are given in figure 46 (b). Here the basic configuration had the solid leading edge. Porous edges again caused several dB noise increase at low frequencies. The porous leading edge

and solid trailing edge became about 4 dB quieter than the basic configuration at somewhat larger frequencies and its sound level decreased into the background noise floor.

The effect of 30% porosity leading and trailing edges on sound caused by incidence fluctuation is shown in figure 47. For both the medium and the large grid, the porous leading edge produced small increases of noise at the lowest test frequencies but about 5 dB uncorrected noise reduction at higher frequencies. Spectra for these higher frequencies decayed into the tunnel background noise level. Use of a porous trailing edge alone caused small increases of noise. The combination of a porous leading edge and porous trailing edge caused slightly less noise reduction than the porous leading edge alone.

Directivity of incidence fluctuation noise measured with the basic hardwall model and with porous edges resembled what would be expected for lift dipole noise. The measurement location directly over the model was 1 to 2 dB louder than locations 60° from either upstream or downstream, and spectrum shape was about the same for all positions. Spectra measured 60° and 90° from the upstream direction, and corrected for background noise at the measurement position, are given in figure 48 for both porosities and the large grid. Corrected amplitudes measured 60° from upstream have been increased 1.25 dB to compensate for the expected variation with cosine squared of this angle. Circle symbols for the basic airfoil and triangles for the airfoil with porous leading edge are shown for those 1/3 octave bands for which measurements were more than 2 dB above background. Straight lines with decay rates that correspond to inverse decay with frequency cubed for the basic airfoil and frequency to the fourth power for the porous leading edge are drawn through the high-frequency parts of these spectra. It is not obvious whether the apparent steeper decay of spectra for the porous leading edge corresponds to a change in the noise radiation process or is within the data scatter. About 7 dB noise decrease was obtained by the porous leading edge at the highest frequencies for which symbols are shown, before the spectra disappeared into tunnel background noise. This noise decrease occurred at Strouhal numbers of about 6 based on airfoil chord. If the porous leading edges were acting as absorbers of acoustic energy, each porosity would be expected to provide greatest attenuation at some frequency that was independent of flow velocity.

Effects of porous leading and trailing edges on surface pressure spectra at midchord are shown in figures 49 and 50 for 18% and 30% porosity. Surface pressure fluctuations on the airfoil with a porous leading edge were of the order of 10 dB stronger than those for the basic hard-wall airfoil. Adding a porous trailing edge to the airfoil with either a hard or porous leading edge generally caused little change in surface pressure spectra. These surface pressure data provide no indication of how the porous leading edges caused reductions of incidence fluctuation noise.

The effect of a blunt trailing edge on noise radiation from a hard-wall model is shown in figure 51. The basic configuration with the medium grid for this and the remaining configurations is that from reference 1 rather than the model with taped porous leading edge. The blunt trailing edge caused tone radiation at a Strouhal number of about 1/3 and an amplitude about 8 dB above the broadband level. For this turbulence level, the blunt trailing edge sometimes caused about 2 dB noise reductions over about an octave of lower frequency. For some applications, this tradeoff may be useful for struts or splitter plates in an exhaust duct that already contains acoustic absorbing material sharply tuned to the tone frequency. In contrast, at the larger turbulence level produced by the larger grid, the blunt trailing edge slightly increased the noise at most frequencies but produced weaker tone noise. Surface pressure spectra, shown in figure 52, contain strong peaks at the tone frequency. For the medium grid, these peaks were about 15 dB above the broadband surface pressure level except at the highest velocity. At other frequencies the surface pressure spectra were not clearly affected by the blunt trailing edge. With the large grid, the blunt trailing edge generally decreased the low-frequency surface pressure levels although it did not reduce far-field sound radiation at those frequencies.

Effects of trailing edge blowing on sound radiation is shown in figure 53. There was no significant noise reduction. However, the high subsonic slot jet produced jet noise that increased roughly 8 dB per octave at high frequencies (not shown except for 80 m/sec flow velocity). Peak amplitude of this jet noise occurred in the 20 kHz third-octave band for the velocity and was stronger than incidence-fluctuation noise from the basic airfoil, dominating the measured OASPL. At larger flow velocities the slot jet noise was unchanged but the airfoil noise caused by incidence fluctuation had increased, drowning out the jet noise in the limited frequency range shown. Surface pressure spectra, given in figure 54, generally were slightly increased by trailing edge blowing.

Swept screens were installed at the airfoil leading edge in an attempt to provide gross changes in turbulence structure. These screens were tested only at the two lowest airspeeds of 31.5 and 50 m/sec for structural reasons. It was expected that the grids would decrease turbulence intensity and therefore decrease noise at low frequencies while generating turbulence and noise at high frequencies. Effects of these screens on far-field sound are shown in figure 55. With the medium screen (figure 55 (a)), sound was reduced by about 8 dB at the lower velocity and 4 dB at the higher velocity for frequency bands to about 800 Hz. At somewhat larger frequencies, noise levels measured with both grids were approximately equal to tunnel background noise. At still higher frequencies the screens generated broadband peaks that exceeded tunnel background noise. When these high-frequency parts of the spectra at the two velocities were compared at constant Strouhal number, differences between

corresponding 1/3 octave levels were found to be about 12 dB. For this velocity ratio, this difference corresponds to a variation with velocity to the sixth power, showing that the added high-frequency noise is a dipole noise caused by fluctuating airloads on the screens. Surface pressure spectra, given in figure 56, contain near-field pressure fluctuations caused by the screens. At frequencies for which the far-field sound spectra were dominated by tunnel background noise, surface pressures of the basic airfoil without a screen were dominated by the airfoil turbulent boundary layer. These levels were greatly reduced by the screens, which reduced the flow velocities and turbulence levels in this layer.

Fan Exit Duct Turbulence Measurements

Apparatus and Procedure

Streamwise and radial components of turbulence were measured in the exit duct of a simulated high bypass ratio single-stage turbofan without inlet guide vanes. The fan stage was simulated by use of an available large-scale single-stage rotor and stator test rig sketched in figure 57. This rig operates at a low enough rotational speed and axial velocity to permit use of conventional hot-wire instrumentation. Data were obtained at midspan, where relatively two-dimensional blade wakes would be expected. Data also were obtained near the inner and outer casings, where the flow field might contain secondary-flow vortices generated near the rotor tip and stator hub.

The test rig is in the form of an open-circuit wind tunnel. Flow enters the tunnel through a 3.66 m (12 ft) diameter inlet. A 15 cm (6 in.) thick section of honeycomb is mounted at the inlet face to remove any crossflow effects. The inlet smoothly contracts the cross-section diameter down to about 1.5 m (5 ft). Flow is then passed through a series of three fine mesh screens to reduce turbulence level. Immediately downstream of the screens is a telescoping section which slides axially and permits access to the test section. The test section consists of an axial series of constant diameter casings enclosing the rotor assembly. These casings can be wholly or partially transparent, which facilitates flow visualization, holography, and laser-doppler-velocimeter studies. The rotor shaft is cantilevered from two downstream bearings. Axial length of the test section (excluding the hub spinner length) is 0.915 m (3 ft). The rotor is driven by a hydraulic motor which is capable of turning the shaft at up to 660 rpm.

The hydraulic motor is also capable of being used as brake for absorbing turbine stage work. Downstream of the test section, flow passes through an annular diffuser into a centrifugal fan and is subsequently exhausted from the rig. A vortex valve is mounted at the fan inlet face for control of axial flow rate. The fan is capable of providing an axial velocity in the test section of approximately 21 m/sec (70 ft/sec) with a 0.5 hub-tip ratio rotor assembly.

For these tests the rotor contained 36 blades and was turned at 550 rpm producing a 330 Hz blade passing frequency. The stator consisted of 47 blades cantilevered from the outer casing. Both the rotor and stator had 38 cm (15 in.) inner and 76 cm (30 in.) outer diameter. The small rotational speed and consequent small pressure ratio allowed use of a constant-diameter hub and outer casing. Rotor and stator blades had multiple circular arc airfoil sections. Camber, twist, and chord were typical of the inboard portion of the fan rotor and stator of high bypass ratio turbofan engines. All measurements were taken at one arbitrary flow condition which was well below the stall point.

Axial location of the measurements was 14.7 cm (5.8 in.) downstream of the stator trailing edge plane. This distance was about 1.75 stator axial chords, sufficiently far downstream so that strong local irregularities of turbulence intensity should have decayed. Stator wake locations at this axial distance were estimated by measuring the wake swirl angle just downstream of the stator trailing edge and assuming constant swirl from there to the measurement plane. Swirl angles were measured near the hub, midspan, and tip by use of a calibrated multitube static pressure probe. Two radial traverse lines at different angular positions were selected for hot-wire measurements. Positions of these traverses relative to the stator trailing edges and the estimated stator wakes are sketched in figure 58. Portions of the stator wakes shed near the hub were estimated to have traveled through a larger circumferential angle than the portions from midspan or the tip. One traverse line passed about midway between two wakes near the inner casing, crossed a stator wake near midspan, and was close to that wake near the outer casing. The other traverse line was close to a wake near the inner casing and between stator wakes near midspan and the outer casing. Detailed measurements were made at three radial positions on each traverse line. The nominal outer, midspan, and inner positions were at radial distances 68.6 cm (26.0 in.), 57.2 cm (22.5 in.), and 40.6 cm (16.0 in.) from the rotational axis. These locations were 86.7 percent, 75.0 percent, and 53.3 percent of the outer casing radius for this 50 percent radius ratio fan exit duct.

At each of these positions, a cross-wire hot probe was utilized to measure mean velocity, rms streamwise and radial components of turbulence, and streamwise and radial turbulence spectra. The wires were aligned 45° to the flow and approximately in the plane which contains the mean streamwise velocity vector and is perpendicular to the tangential plane. Streamwise autocorrelations were obtained from a single hot wire probe by using the known time scale and mean velocity to determine spatial distances assuming frozen turbulence. For radial cross correlations, two cross-wire probes were used with the wires aligned 45° to the flow in the radial plane. One probe was held at a fixed position and the other was traversed radially; cross correlations of the radial component of turbulence were evaluated at zero delay time. Radial cross correlations were obtained only for the traverse line between stator wakes at midspan, due to an instrumentation error.

Discussion of Turbulence Data

Measured variations of rms turbulence level with normalized radial distance are shown in figure 59 for two angular locations. Streamwise turbulence levels were about 18 percent in the hub secondary flow region at both angular positions. They decreased to about 5 percent between the stator wakes but were about 12 percent where one traverse line crossed the center of a stator wake. Radial turbulence levels were about 10 percent near the inner casing, 4 percent between the stator wakes, and 8 percent within the stator wakes. Of course, these turbulence measurements in the nonrotating frame of reference are a combination of stator wake turbulence, rotor wake turbulence, and fluctuations of rotor wake mean velocity in a frame of reference that turns with the rotor. Mean and fluctuating velocities within a rotor wake, measured in a rotating coordinate system, were reported in reference 44. It was shown that in accordance with analytical predictions, turbulence intensity in a rotor wake decays more rapidly than in a cascade wake. This, in turn, decays more rapidly than in the wake of an isolated airfoil. Turbulence intensities shown in figure 59 for positions between the stator wakes are considerably larger than the 2 percent turbulence levels shown in reference 44 at the most rearward measurement position midspan within rotor wakes. However, they genrally agree with the streamwise component of mean velocity defect and the radial component of mean velocity measured in the rotating coordinate system as given in reference 44. Minimum turbulence levels in the fan exit duct as measured in nonrotating coordinates therefore are produced by angular rotation of the rotor wake mean velocity field, a result that also was found in reference 45. This velocity field is distorted as it passes through the stators but apparently its absolute levels are not greatly changed.

Radial cross correlations of radial turbulence velocity are shown in figure 60 for three different radial positions of the fixed hot-wire probe. Cross correlation signals at each radial station were largest at approximately zero time delay as would be expected for turbulent eddies convected along the duct. Maximum values of normalized cross correlations can be seen in figure 60 to decay exponentially with the inverse of radial distance. Integral scale length in the radial direction then is equal to the distance at which the normalized amplitude is equal to $1/e$. Resulting scale lengths increased with increasing radial location across the duct. At the outer and midspan positions, integral scale lengths were roughly equal to the azimuthal spacing between adjacent stator blades and were about 10 percent of the duct height. Integral scale length near the inner casing was only 30 percent of that near the outer part of the duct.

Autocorrelations of the streamwise component of fluctuating velocity (not shown) decayed exponentially with the inverse of delay time. Streamwise integral scale lengths were determined as the product of local mean velocity and

the time at which the autocorrelations had decayed to 1/e of its maximum. Mean velocities and streamwise integral scale lengths obtained from these tests are listed below.

Measured Turbulence Integral Scale Lengths

Quantity	Inner Position	Midspan	Outer Position
Radial Location	53.3%	75%	90%
Swirl Angle	30°	21°	21°
	Within wakes at midspan		
Streamwise velocity, m/sec	18.5	20.9	19.1
Streamwise scale length, cm	2.9	2.2	1.4
	Between wakes at midspan		
Streamwise velocity, m/sec	21.8	28.7	24.8
Streamwise scale length, cm	4.5	2.4	2.7
Radial scale length, cm	1.5	3.5	5.0

In contrast to the radial scale lengths, streamwise scale lengths decreased as radial location was increased. The largest steamwise integral scale length was measured at the inner radial position and azimuthal location of a convected stator wake. It was about 50 percent larger than for the same radial location but between stator wakes. This increased length and large turbulence intensity may correspond to the stator hub vortex. Effects of a distinct rotor tip vortex were not observed, possibly because the test rotor was not highly loaded near the tip.

Measured streamwise and radial turbulence spectra are shown in figure 61 for the two azimuthal and three radial positions. Vertical ordinates are proportional to the rms turbulence amplitude within a constant bandwidth of frequency and thus are proportional to the square root of power spectral density. When measured spectra seemed highly oscillatory, three spectra were recorded at successive times and their traces were superimposed. Also shown as smooth curves are normalized spectra calculated from the square root of equation (14), taken from equation 1-95 of reference 31. Streamwise turbulence spectra calculated from the above measured integral scale lengths and mean velocities generally were in good agreement with measured spectra. Scale lengths measured on the azimuthal traverse between stator wakes (lower parts of the figure) were up to twice as large as those for the other traverses. These spectra decayed more rapidly so they are plotted for half the range of frequency. Changes in spectrum shape caused by more than a factor of 3 in streamwise integral scale length, from the upper left spectrum of figure 61(a) to the lower left spectrum of figure 61(c), were correctly given by this equation.

Integral scale lengths in the radial direction had been obtained for only one azimuth position (between the wakes at midspan). Spectra measured at this angular position differed from the other spectra by having local peaks at frequencies up to the rotor blade passing frequency (330 Hz) followed by considerably lower amplitude over a small range of higher frequencies. Spectra measured near the inner casing at this azimuth and at midspan between the wakes were well predicted by use of the equation and the measured radial scale length. However, spectra measured at the other positions decayed less rapidly than had been calculated in that manner. The curves shown in figures 61(a) and (b) for these cases were calculated by arbitrarily taking the correlation length equal to the ratio of local streamwise velocity to rotor blade passing frequency, rad/sec. Just as the amplitude of radial rms turbulence intensity was found to correspond to mean velocity defects in the rotor wake, radial length scale in the stator wake and near the outer casing seems to be associated with chopped segments of rotor wake.

One unexpected result of this comparison is the relatively good agreement between turbulence spectrum shapes measured within wakes, and possibly within the hub vortex, and the shape given in equation (15). That equation had been presented in reference 31 as valid for isotropic turbulence. Turbulence measured in this fan exit duct was far from isotropic. Streamwise turbulence levels were up to twice those in the radial direction rather than being equal in all directions. Streamwise integral scale lengths ranged from half to three times the radial integral scale length rather than being twice that length. Use of this simple equation for turbulence spectrum in a fan exit duct facilitates calculation of noise generated by struts and splitter plates within the duct.

Fan Exit Duct Splitter Ring Noise

Acoustically lined splitter rings within turbofan exit ducts can absorb aft-radiated fan noise, but as airfoils within turbulent flow they act as noise generators. Spectra of sound power level in the aft hemisphere of the nominal 1.83 m (6 ft) diameter fan D, taken from figure III-37 of reference 43, are shown in figure 67(a). Placing a large hard-wall splitter ring in the fan exit duct markedly increased aft-radiated sound power above that for the hard-wall nacelle at frequencies between 400 and 10,000 Hz. Use of soft acoustic linings on the exit duct walls, exit duct splitter ring, and the inlet duct walls and splitter rings caused 15 to 20 dB noise reduction over much of this range. However, aft-radiated sound power from the lined duct and splitter ring was 1 to 2 dB noisier than that of the bare hard-wall duct between 400 and 1000 Hz frequency. It was concluded on p. 77 of reference 43 that noise generation processes therefore occur in lined passages containing splitters. The acoustic suppression liners had been designed for broadband noise attenuation near the 2500 Hz blade passing

frequency and its harmonics. They would not be expected to be highly effective at the low frequencies where additional noise was generated by the hard-wall splitter ring.

The increase of aft sound power level caused by placing the hard splitter ring in the hard exit duct was calculated from those two measured spectra and is given in figure 62(b). This added noise increased at about 6 dB per octave of frequency at low frequencies, peaked at about the 2500 Hz blade passing frequency, and decayed into the noise floor set by rotor harmonics at higher frequencies. The relatively gradual rise and decay of this spectrum resembles the behavior of incidence fluctuation noise.

Dipole noise directivity for a flat plate airfoil varies with cosine squared of the azimuth angle measured from a normal to the plate. However, dipole noise directivity for an annular ring airfoil is independent of azimuth angle. Acoustic intensity radiated by a ring airfoil can be shown to be $\pi/2$ times that for the plane of symmetry of a rectangular strut with span equal to the ring diameter. Sound power for a ring airfoil is the integral of acoustic intensity over a sphere of radius r and can be shown to be $(\pi r)^2$ times the maximum acoustic intensity. Therefore, sound power levels generated by a splitter ring in turbulent flow can be calculated by adding one term to sound pressure levels calculated from equations (14) or (20) for a position directly above a flat plate with span equal to the ring diameter.

$$PWL_{1/3} = SPL_{1/3} + 10 \log (\pi^3/2) r^2 I_{ref} / W_{ref} \qquad (21)$$

The reference acoustic intensity that corresponds to 2×10^{-4} microbar reference pressure is 10^{-12} w/m^2 and the reference acoustic power is 10^{-13} w so the argument of the logarithm is approximately $155 r^2$ with far-field distance r measured in meters.

The above discussion applies to sound radiation from a splitter ring in turbulent flow within free space. Instead, the ring was located near the end of an enclosed duct. An approximate solution given in reference 46 had concluded that a lift dipole would not radiate sound in an infinite duct. For low frequencies, reflected sound waves from corresponding points on upper and lower surfaces would degenerate into plane waves of equal and opposite strength, moving axially down the duct. End effects would alter this prediction, causing the sound radiation to approach that for the free field. Also, forward-radiated sound could be reflected by the fan stators. It was arbitrarily assumed herein that aft-radiated sould power due to the splitter ring within the duct was equal to the total sound power (both forward and aft) calculated for the ring in the free field.

Splitter rings for fan exit ducts of these nominal 1.83 m (6 ft) diameter fan exit ducts were indicated in reference 47 to have about 3.66 m (12 ft) chord and 1.37 m (4.5 ft) diameter. The duct flow Mach number was near 0.50 corresponding to 170 m/sec (558 ft/sec) flow velocity. From figure 59, radial turbulence intensity was taken as 5 percent. The most arbitrary assumption was in the choice of a turbulence integral scale length. If this was taken as the largest value from figure 60 of about 13 percent of the duct passage height, the resulting 6 cm scale length would cause maximum calculated sound power level to occur at too low a frequency. The resulting calculated spectrum would be in poor agreement with the data shown in figure 62(b). Radial turbulence spectra given in figure 61 were found to be better predicted if the radial scale length was taken as a much smaller distance. One possible distance was the ratio of flow velocity to blade passing frequency, rad/sec. It is associated with slicing of the rotor blade wakes by the stator, and for this large-scale fan was about 1.1 cm. Another such distance was the 2.2 cm streamwise scale length measured in the stator blade wake of the low-speed rotating rig at midspan.

Sound power spectra calculated from Eq. (21) combined with the methods of reference 1 and reference 32 for sound pressure level are compared with the data in figure 62(b). Spectra calculated by the method of reference 32 for both scale lengths predict the approximate peak values of 1/3 octave sound power level. The shape of the measured spectrum is generally predicted, and the calculated curve is in close agreement with data for the larger scale length. In contrast, the spectrum calculated by the method of reference 1 for the smaller scale length has the measured shape but its amplitude is about 20 dB below the data. Doubling the scale length increased the amplitude about 8 dB at low frequencies but halved the peak frequency, displacing the calculated spectrum away from the data. This large difference between sound power levels calculated by the two methods was caused by the differing variations of unsteady lift response with aspect ratio and with ratio of turbulence scale length to chord. Lift response as calculated by the method of reference 29 for configurations having small ratios of correlation length to span tends to approach that for a large number of uncorrelated very low aspect ratio wings, each with a span equal to the correlation length. Lift force response of a low aspect ratio wing is proportional to span squared, so the functional dependence on airfoil span (splitter ring diameter) partly changes to a variation with correlation length. In contrast, the method of reference 32 uses the unsteady lift response given in reference 33 which gives a much weaker variation with turbulence scale length. Also, the portion of that solution used in reference 32 corresponds to a spanwise segment of an infinite span airfoil rather than a wing of finite span. This representation is probably more valid for a splitter ring than is the finite aspect ratio solution used in reference 1.

CONCLUSIONS

1.   The method presented in this report for calculating externally blown flap (EBF) noise is in good agreement with data from small-scale models for both under-the-wing and upper-surface-blowing configurations.

2.   Deflecting a wing flap into an exhaust jet causes lift dipole noise normal to the flap and increased quadrupole jet noise at moderate angles from downstream of the deflected jet. Therefore, an under-the-wing EBF will be noisier than an upper-surface-blowing EBF at constant exhaust velocity and exhaust area.

3.   Noise radiation from an airfoil in turbulent flow can be decreased at high frequencies by use of a porous leading-edge region.

REFERENCES

1.   Fink, M. R.: Investigation of Scrubbing and Impingement Noise, NASA CR-134762, Feb. 1975.

2.   Fink, M. R.: Experimental Evaluation of Trailing Edge and Incidence Fluctuation Noise Theories. Paper 75-206, AIAA, Jan. 1975.

3.   Fink, M. R.: Scrubbing Noise of Externally Blown Flaps. Paper 75-469, AIAA, Mar. 1975.

4.   Siddon, T. E.: Surface Dipole Strength by Cross-Correlation Method. J. Acoust. Soc. Am., Vol. 53, No. 2, Feb. 1973, pp. 619-633.

5.   McKinzie, D. J., Jr. and Burns, R. J.: Analysis of Noise Produced by Jet Impingement Near the Trailing Edge of a Flat and a Curved Plate. NASA TM X-3171, Jan. 1975.

6.   Olsen, W. A., Dorsch, R. G., and Miles, J. H.: Noise Produced by a Small-Scale, Externally Blown Flap. NASA TN D-6636, Mar. 1972.

7.   Dorsch, R. G., Kreim, W. J., and Olsen, W. A.: Externally-Blown-Flap Noise. Paper 72-129, AIAA, Jan. 1972.

8.   Fink, M. R.: Mechanisms of Externally Blown Flap Noise. Paper 73-1029, AIAA, Oct. 1973.

9.   Olsen, W. A., Miles, J. H., and Dorsch, R. G.: Noise Generated by Impingement of a Jet Upon a Large Flat Board. NASA TN D-7075, Dec. 1972.
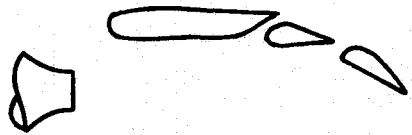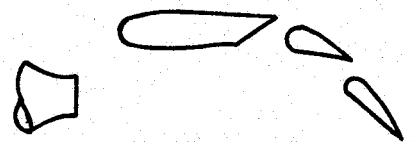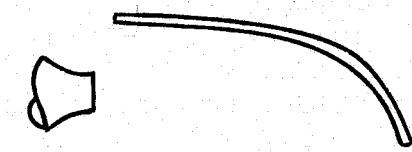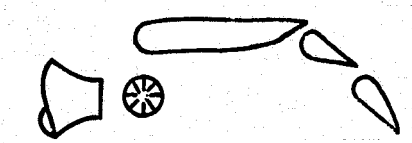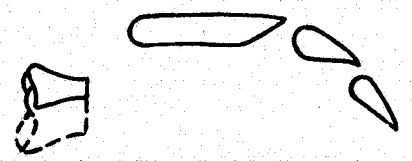
10. Stone, J. R.: Interim Prediction Method for Jet Noise. NASA TM X-71618, 1975.

11. Neuwerth, G.: Acoustic Feedback of a Subsonic and Supersonic Free Jet Impinging on a Foreign Body. NASA TT F-15719, 1974.

12. Dorsch, R. G., Goodykoontz, J. H., and Sargent, N. B.: Effect of Configuration Variation on Externally Blown Flap Noise. Paper 74-190, AIAA, Jan. 1974.

13. Foss, J. F.: Research on Free and Impinging Jets for the Development of STOL Aircraft. NASA CR-138031, Jan. 1974.

14. Ffowcs Williams, J. and Hall, L. H.: Aerodynamic Sound Generation by Turbulent Flow in the Vicinity of a Scattering Half Plane. J. Fluid Mech., Vol. 40, Part 4, Mar. 1970, pp. 657-670.

15. von Glahn, U., Groesbeck, D., and Reshotko, M.: Geometry Considerations for Jet Noise Shielding With CTOL Engine-Over-the-Wing-Concept. Paper 74-568, AIAA, June 1974.

16. von Glahn, U., Reshotko, M., and Dorsch, R.: Acoustic Results Obtained With Upper-Surface-Blowing-Lift-Augmentation Systems. NASA TM X-68159, Nov. 1972.

17. Guinn, W. A., Blakney, D. F., and Gibson, J. S.: V/STOL Noise Prediction and Reduction. FAA-RD-73-145, Aug. 1973.

18. Dunn, D. G., and Peart, N. A.: Aircraft Noise Source and Contour Estimation. NASA CR-114649, July 1973.

19. Dorsch, R. G., Clark, B. J., and Reshotko, M.: Interim Prediction Method for Externally Blown Flap Noise. NASA TM X-71768, Aug. 1975.

20. Goodykoontz, J. H., Olsen, W. A., and Dorsch, R. G.: Small-Scale Tests of the Mixer Nozzle Concept for Reducing Blown-Flap Noise. NASA TM X-2638, Nov. 1972.

21. Dorsch, R. G., Lasagna, P. L., Maglieri, D. J., and Olsen, W. A.: Flap Noise. Paper XII, Aircraft Engine Noise Reduction, NASA SP-311, May 1972, pp. 259-290.

22. Reshotko, M., Olsen, W. A., and Dorsch, R. G.: Preliminary Noise Tests of the Engine-Over-The-Wing Concept, II. 10°-20° Flap Positions. NASA TM X-68104, June 1972.

23. Reshotko, M. and Friedman, R.: Acoustic Investigation of the Engine-Over-The-Wing Concept Using a D-Shaped Nozzle. NASA TM X-71419, Paper 73-1030, AIAA, Oct. 1973.

24. Dorsch, R. G., Reshotko, M., and Olsen, W. A.: Flap Noise Measurements for STOL Configurations Using External Upper Surface Blowing. Paper 72-1203, AIAA, Dec. 1972.

25. Heidelberg, L. J., Homyak, L., and Jones, W. L.: Full-Scale Upper-Surface-Blown Flap Noise. Paper 750609, SAE, May 1975.

26. Reddy, N. N., and Brown, W. H.: Acoustic Characteristics of Upper Surface Blowing Concept of Power Lift System. Paper 75-204, AIAA, Jan. 1975.

27. Reshotko, M., Olsen, W. A., and Dorsch, R. G.: Preliminary Noise Tests of the Engine-Over-The-Wing Concept, I. 30°-60° Flap Positions. NASA TM X-68032, Mar. 1972.

28. Karchmer, A. M., and Friedman, R.: Noise Tests on an Externally Blown Flap With the Engine In Front of the Wing. NASA TM X-2942, Dec. 1973.

29. Filotas, L. T.: Theory of Airfoil Response in a Gusty Atmosphere, Part II - Response to Discrete Gusts or Continuous Turbulence. University of Toronto, Institute for Aerospace Studies, UTIAS Report No. 141, AFOSR 69-3089TR, Nov. 1969.

30. Hayden, R. E.: Noise from Interaction of Flow with Rigid Surfaces: A Review of Current Status of Prediction Techniques. NASA CR 2126, Oct. 1972.

31. Hinze, J. O.: Turbulence, McGraw-Hill Book Co., New York, 1959.

32. Goldstein, M.: Aeroacoustics, NASA SP-346, 1974, pp. 209-219.

33. Mugridge, B. D.: Sound Radiation from Aerofoils in Turbulent Flow. Journal of Sound and Vibration, Vol. 13, No. 3, Nov. 1970, pp. 362-363.

34. Paterson, R. W., Vogt, P. G., and Foley, W. M.: Design and Development of the United Aircraft Research Laboratories Acoustic Research Tunnel. J. Aircraft, Vol. 10, No. 7, July 1973, pp. 427-433.

35. Potter, R. C.: An Experiment to Examine the Effect of Porous Trailing Edges on the Sound Generated by Blades in an Airflow. NASA CR-66565, March 1968.

36. Hayden, R. E., Kadman, Y., and Chanaud, R. C.: A Study of the Variable Impedance Surface Concept as a Means for Reducing Noise from Jet Interation with Deployed Lift-Augmenting Flaps. NASA CR-112166, July 1972.

37. Hayden, R. E., et al: A Preliminary Evaluation of Noise Reduction Potential for the Upper Surface Blown Flap. NASA CR-112246, 1972.

38. McKinzie, D. J. and Burns, R. J.: Externally Blown Flap Trailing Edge Noise Reduction by Slot Blowing - Preliminary Study. Paper No. 73-245, AIAA, Jan. 1973.

39. Scharton, T. D., et al: A Study of Trailing Edge Blowing as a Means of Reducing Noise Generated by the Interaction of Flow With a Surface. NASA CR-132270, Sept. 1973.

40. Pennock, A. P., Swift, G., and Marbert, J. A.: Static and Wind Tunnel Tests for the Development of Externally Blown Flap Noise Reduction Techniques. NASA CR-134675, Feb. 1975.

41. Hersh, A. S., Hayden, R. E., and Soderman, P.: Investigation of Acoustic Effects of Leading-Edge Serrations on Airfoils. J. Aircraft, Vol. 11, No. 4, April 1974, pp. 197-202.

42. Fink, M. R.: Prediction of Airfoil Tone Frequencies. J. Aircraft, Vol. 12, No. 2, Feb. 1975, pp. 118-120.

43. Feiler, C. E., et al: Fan Noise Suppression. Aircraft Engine Noise Reduction. NASA SP-311, May 1972, pp. 63-102.

44. Raj, R., and Lakshminarayana, B.: Three Dimensional Characteristics of Turbulent Wakes Behind Rotors of Axial Flow Turbomachinery. ASME Paper No. 75-GT-1, March 1975.

45. Kiock, R.: Turbulence Downstream of Stationary and Rotating Cascades. ASME Paper 73-GT-80, April 1973.

46. Heller, H. H., Widnall, S. E., and Gordon, C. G.: Correlation of Fluctuating Forces With the Sound Radiation from Rigid Flow Spoilers. NASA CR-1340, May 1969.

47. Cornell, W. G.: Experimental Quiet Engine Program - Summary Report, NASA CR-2519, March 1975.

TABLE I

EXTERNALLY BLOWN FLAP MODELS FOR COMPARISON
OF MEASURED AND PREDICTED NOISE

Sketch	Description	Data, Reference No.	Agreement*
	UTW, 20° flap	6	good to excellent
	UTW, 60° flap	6	good
	UTW, 60° flap slotless wing	6	excellent, low pressure, fair, high pressure
	UTW, 60° flap mixer nozzle	20	good
	UTW, 60° flap vary diameter	21	good to excellent (low-frequency spectra fair)

* Agreement	Accuracy of OASPL, dB	Accuray of $SPL_{1/3}$, dB
Excellent	2	4
Good	4	7
Fair	6	10
Poor	worse than 6	worse than 10

TABLE I (Cont'd)
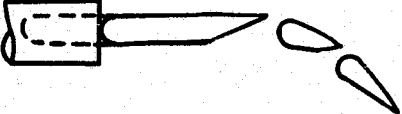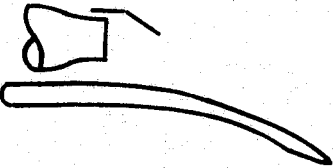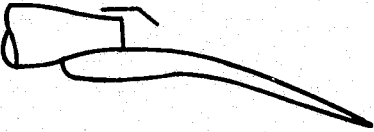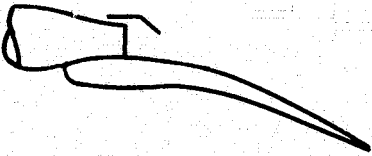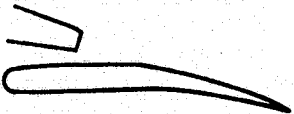
Sketch	Description	Data, Reference No.	Agreement*
	UTW, 60° flap vary position	6	good
	Front of wing 20° and 60° flap	28	good
	USB, 20° flap circular nozzle	22	good to excellent
	USB, 60° flap circular nozzle	22	good to excellent
	USB, 20° flap D nozzle	23	fair, low pressure good, high pressure
	USB, 60° flap D nozzle	23	fair to poor
	USB, 20° flap canted 5:1 slot	24	good

TABLE I (Cont'd)
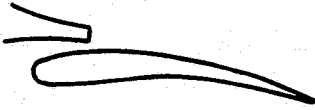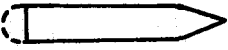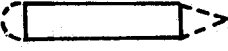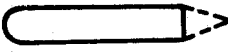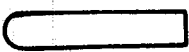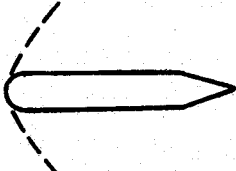
Sketch	Description	Data, Reference No.	Agreement*
	USB, 20° flap canted 10:1 slot	24	excellent
	USB, long 20° flap, 10:1 slot	24	good

TABLE II

REDUCTIONS OF INCIDENCE FLUCTUATION NOISE
BY AIRFOIL MODIFICATIONS

Note: Reductions listed are for the octave of frequency in which maximum reductions were achieved. SPL may have been increased within other octave bands.

Sketch	Modification	Reduction, dB	Comment
	Porous leading edge	6	Most effective
	Porous leading and trailing edges	3	Noise added by trailing edge
	Porous trailing edge	0	Noise generally increased
	Blunt trailing edge	2	Noise increase at shedding frequency
	Trailing edge blowing	0	High-frequency jet noise
	Leading edge screen	8	High-frequency dipole noise
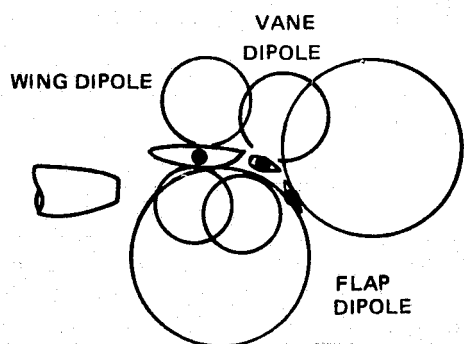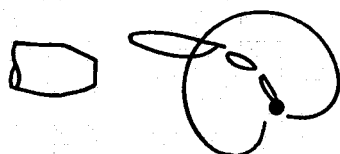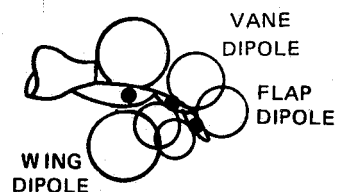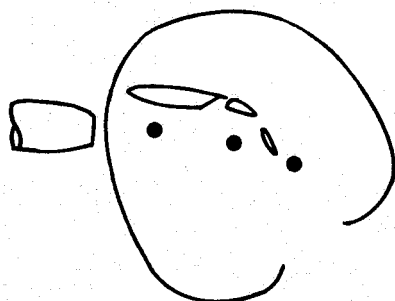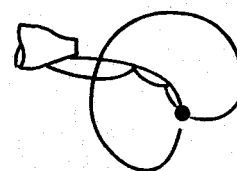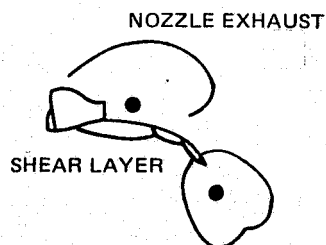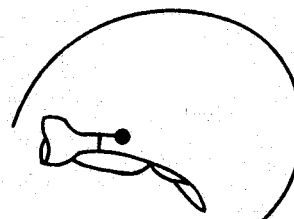
FIGURE 1. — SKETCH OF DIRECTIVITIES FOR DIFFERENT MECHANISMS OF EXTERNALLY BLOWN FLAP NOISE

RO2–143–6

CIRCLE SYMBOLS ARE SUM OF UNSCRUBBED SIDE, NOZZLE DIRECT RADIATED SOUND,
AND NOZZLE REFLECTED SOUND
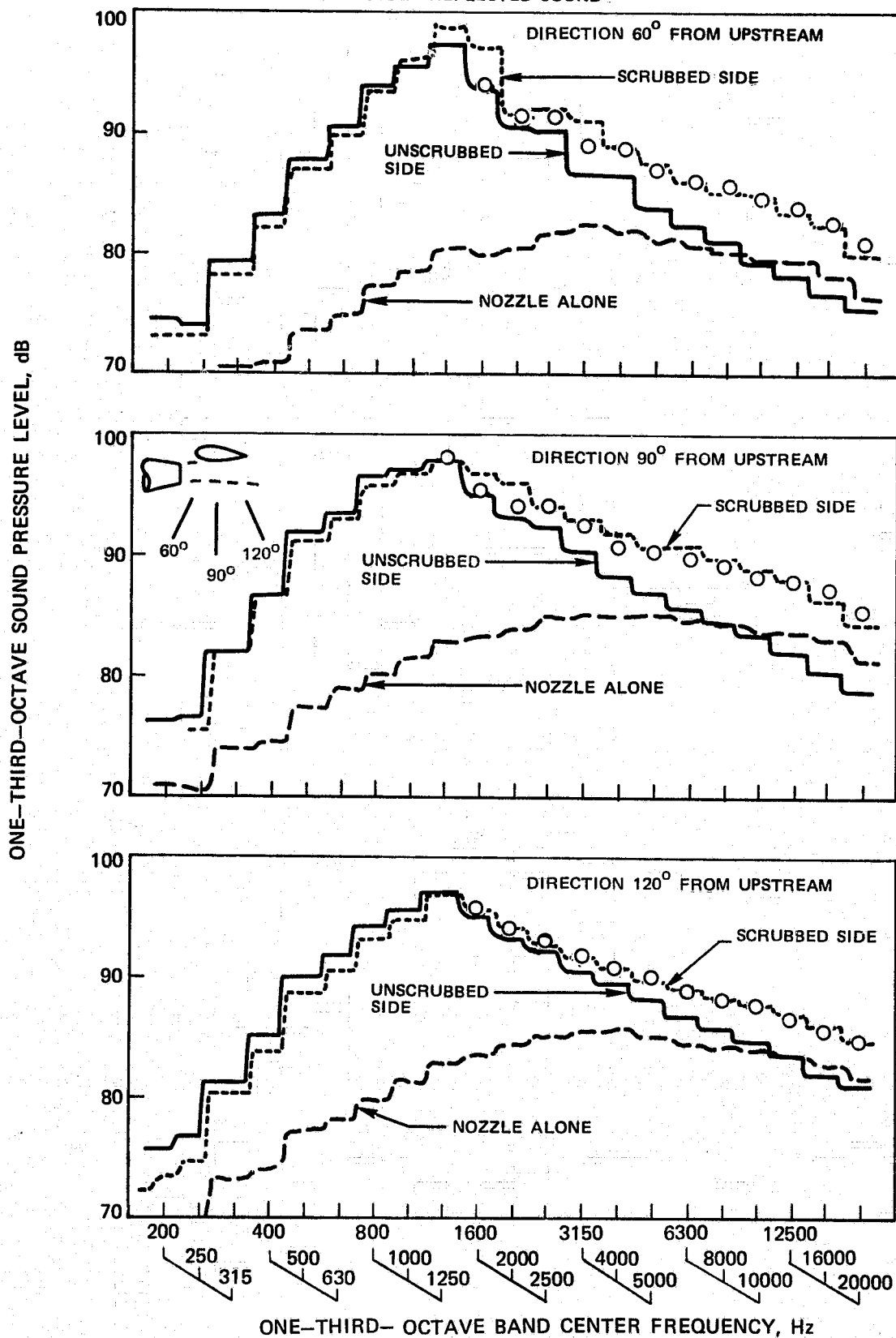
FIGURE 2. – COMPARISON OF FAR–FIELD SPECTRA IN THE SCRUBBED AND UNSCRUBBED
DIRECTIONS FROM AN UNDEFLECTED EXTERNALLY BLOWN WING AT 250 M/SEC VELOCITY

67

CIRCLE SYMBOL ARE SUM OF UNSCRUBBED SIDE, NOZZLE DIRECT RADIATED SOUND,
AND NOZZLE SOUND REFLECTED BY WING

(a) PRESSURE RATIO 1.25

(b) PRESSURE RATIO 1.7
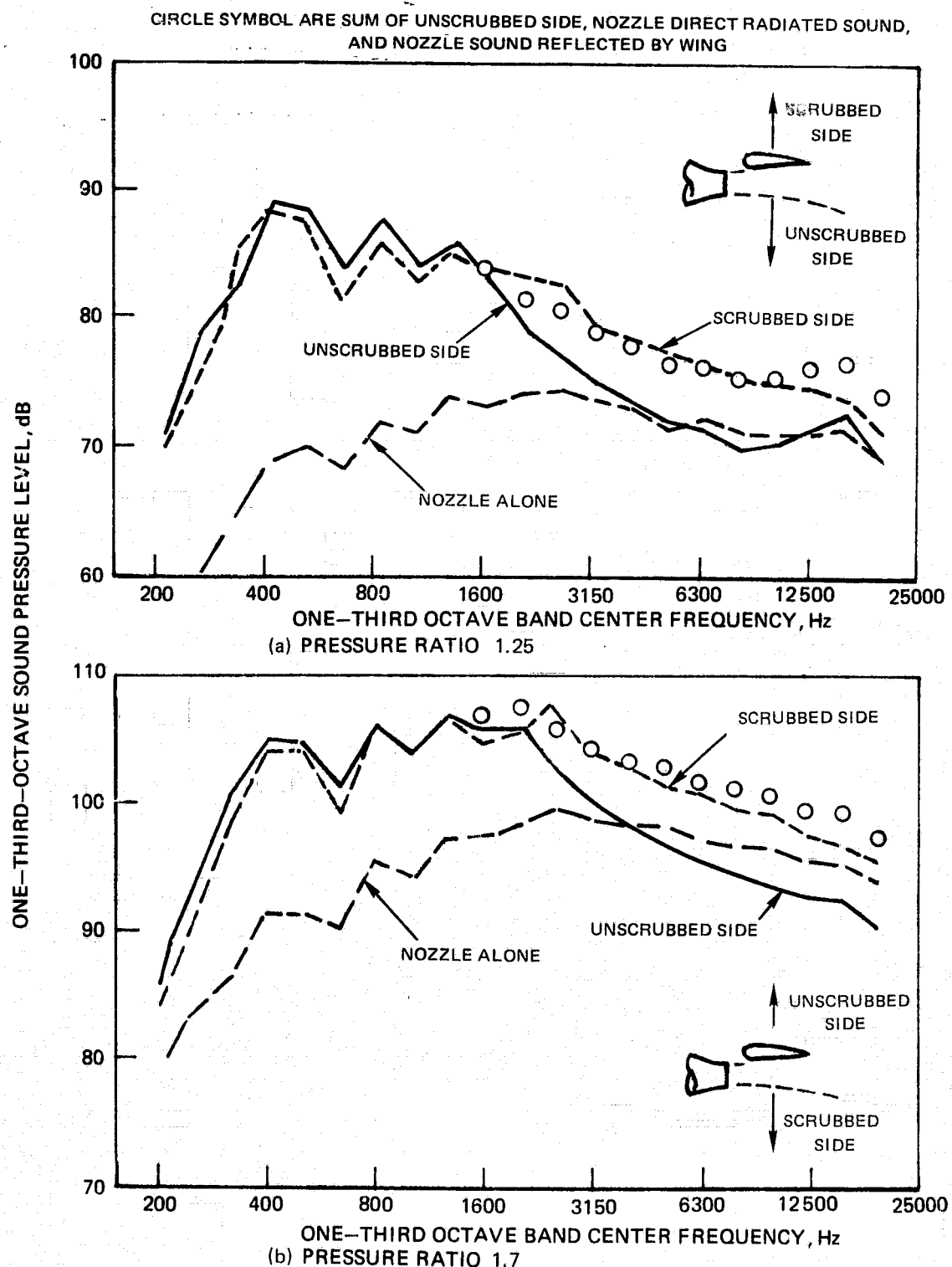
FIGURE 3. — COMPARISON OF FAR—FIELD SPECTRA IN THE SCRUBBED AND
UNSCRUBBED DIRECTIONS FROM A RETRACTED EXTERNALLY
BLOWN FLAP

68

R07—74—1
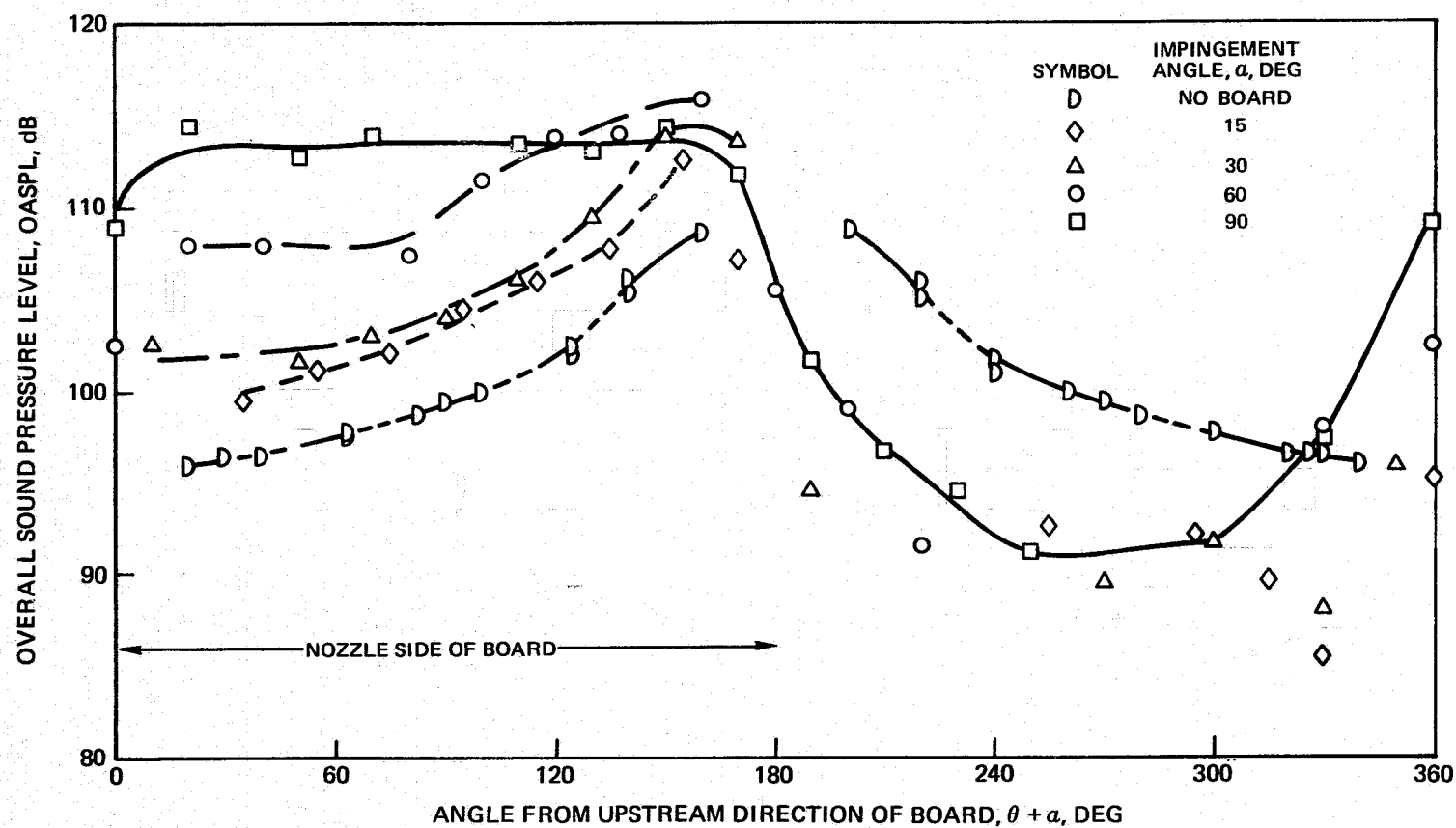
FIGURE 4 — EFFECT OF IMPINGEMENT ANGLE ON DIRECTIVITY FOR
ZERO AZIMUTHAL ANGLE AND 286 M/SEC NOZZLE VELOCITY
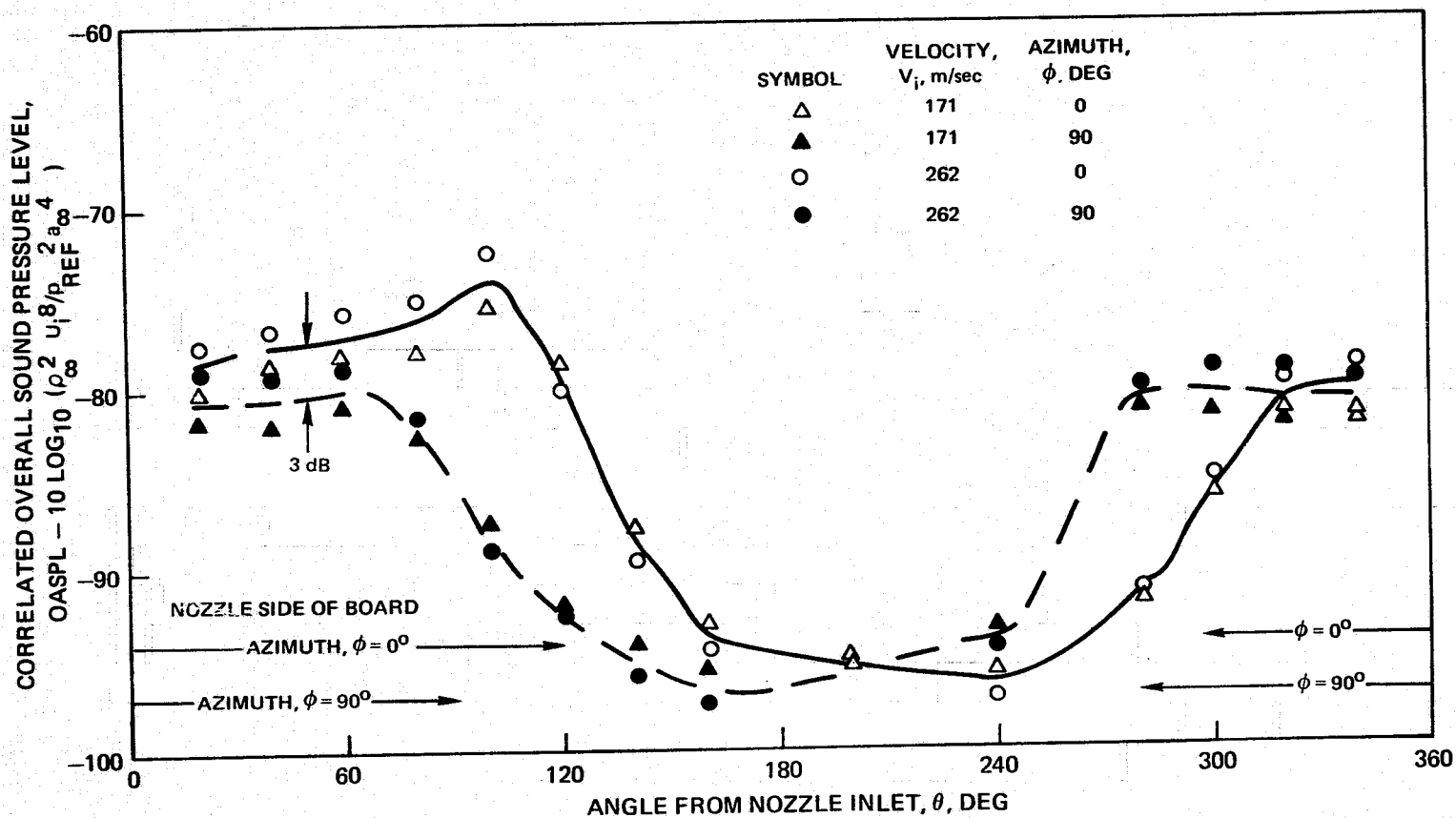
FIGURE 5 — EFFECT OF AZIMUTH ANGLE AND IMPINGEMENT VELOCITY ON DIRECTIVITY
FOR 60° IMPINGEMENT ANGLE

FIGURE 6. NORMALIZED SPECTRA AT DIRECTIONS NEAR PERPENDICULAR TO LARGE FLAT BOARD
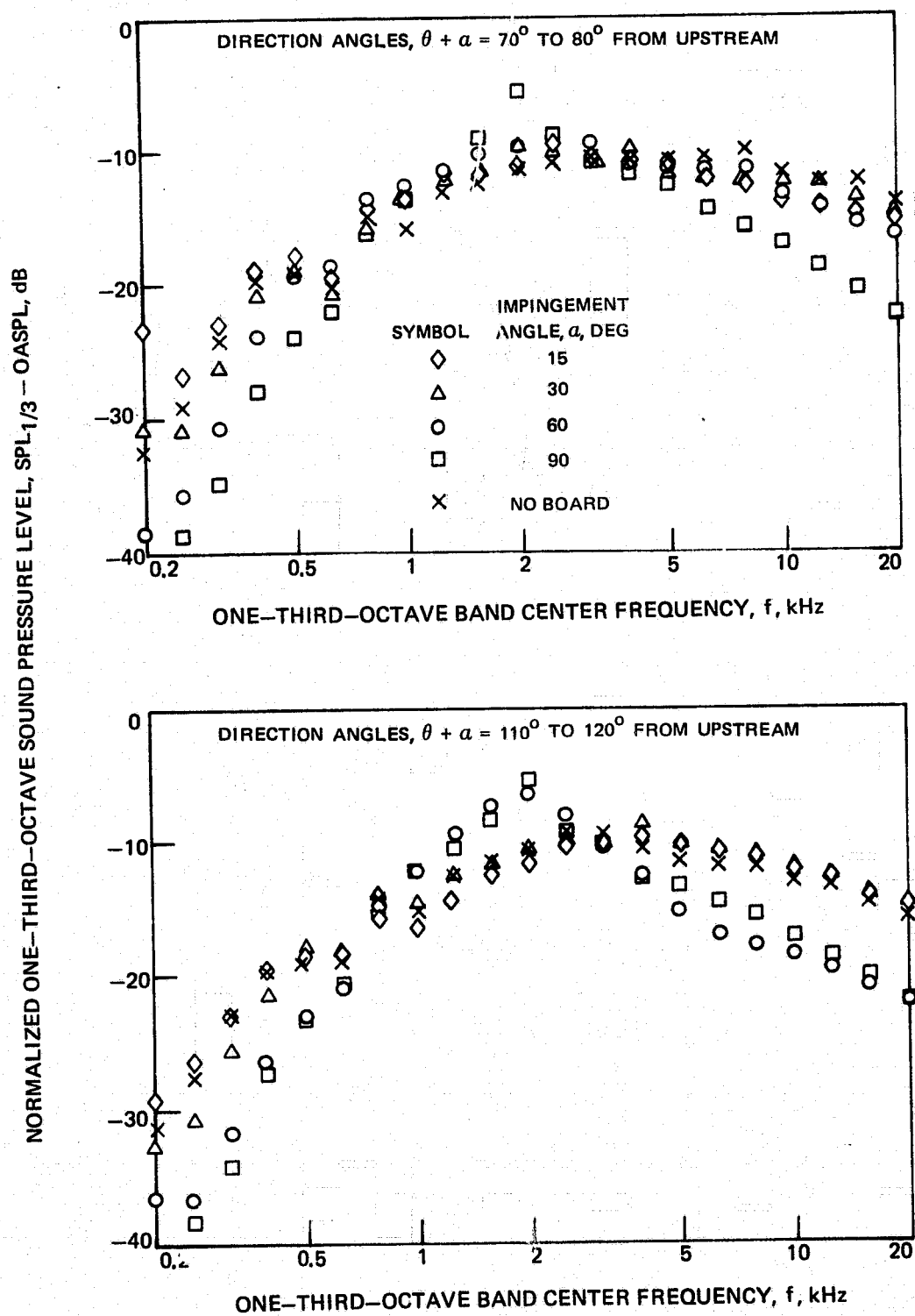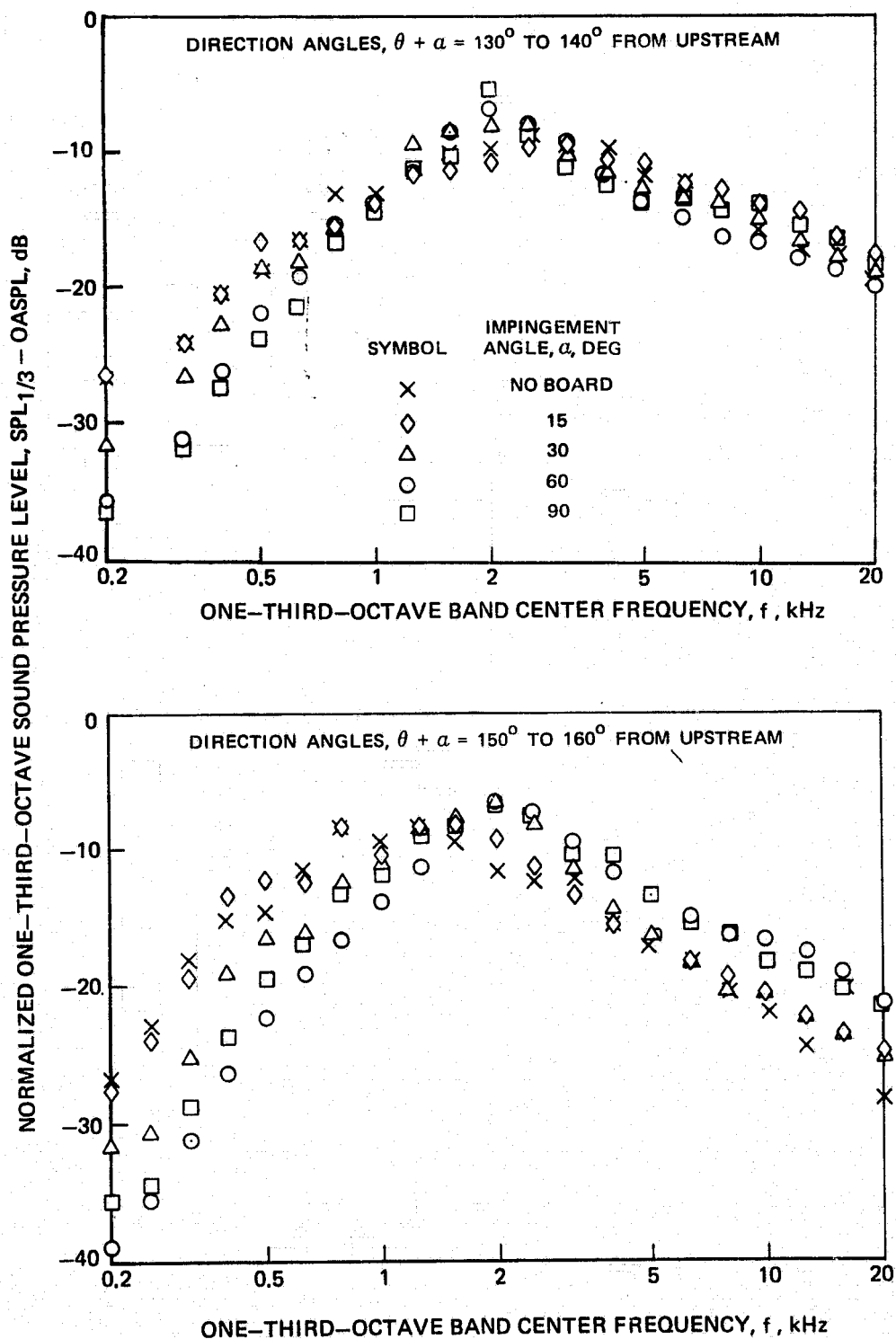
FIGURE 7 — NORMALIZED SPECTRA AT SHALLOW ANGLES FROM DOWNSTREAM
DIRECTION ALONG LARGE FLAT BOARD

N08—172—2

RETRACTED FLAP

TAKEOFF (10°–20°) FLAP DEFLECTION
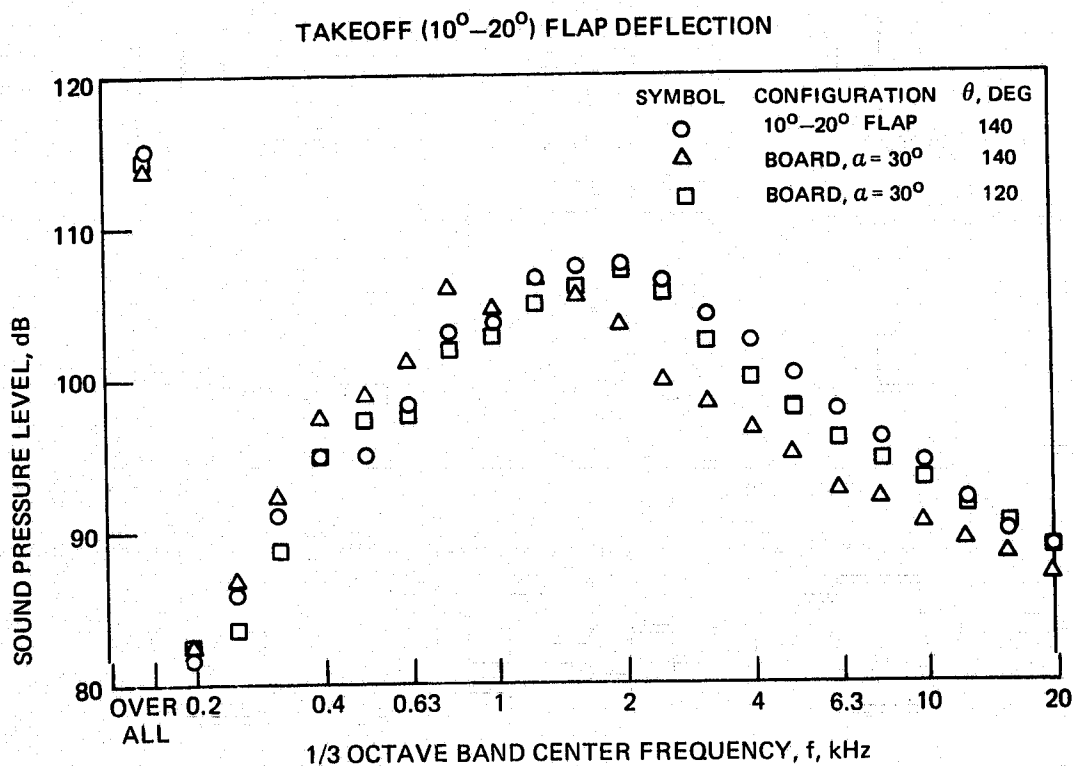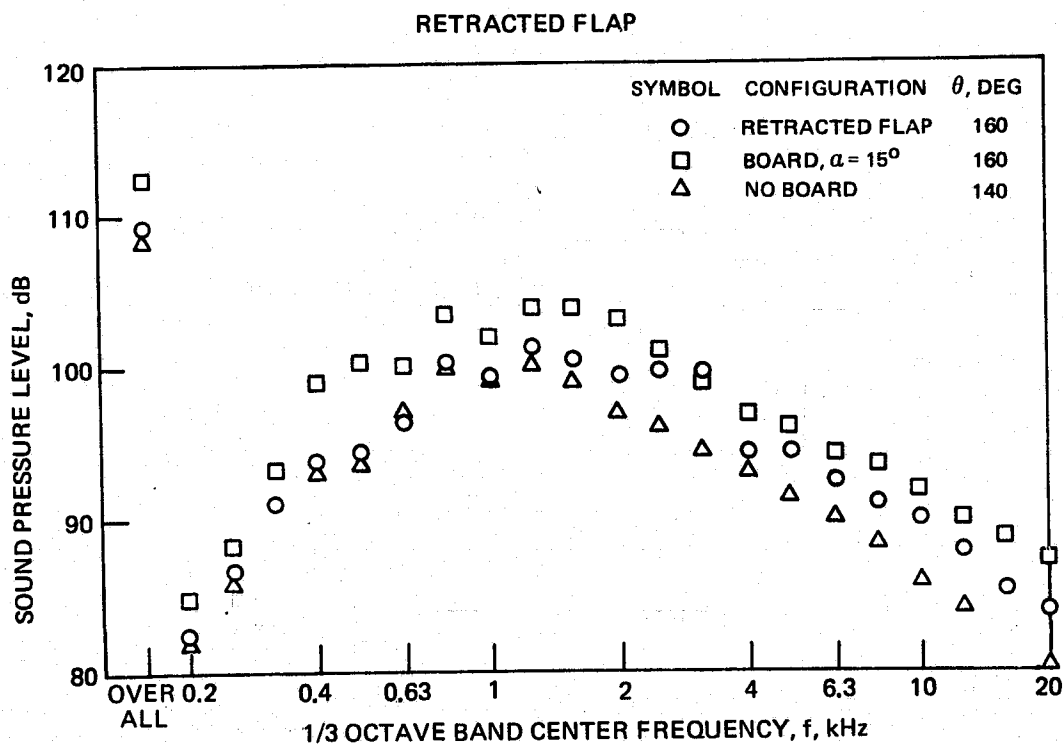
FIGURE 8 — COMPARISONS OF SPECTRA FOR LARGE FLAT BOARD AND
DOUBLE SLOTTED FLAP

73

COMPARISON WITH SPECTRA FOR BOARD

SYMBOL	CONFIGURATION	θ, DEG
○	30°–60° FLAP	100
△	BOARD, $a = 60°$	100
□	BOARD, $a = 60°$	80

SOUND PRESSURE LEVEL, dB

OVER ALL

1/3 OCTAVE BAND CENTER FREQUENCY, f, kHz
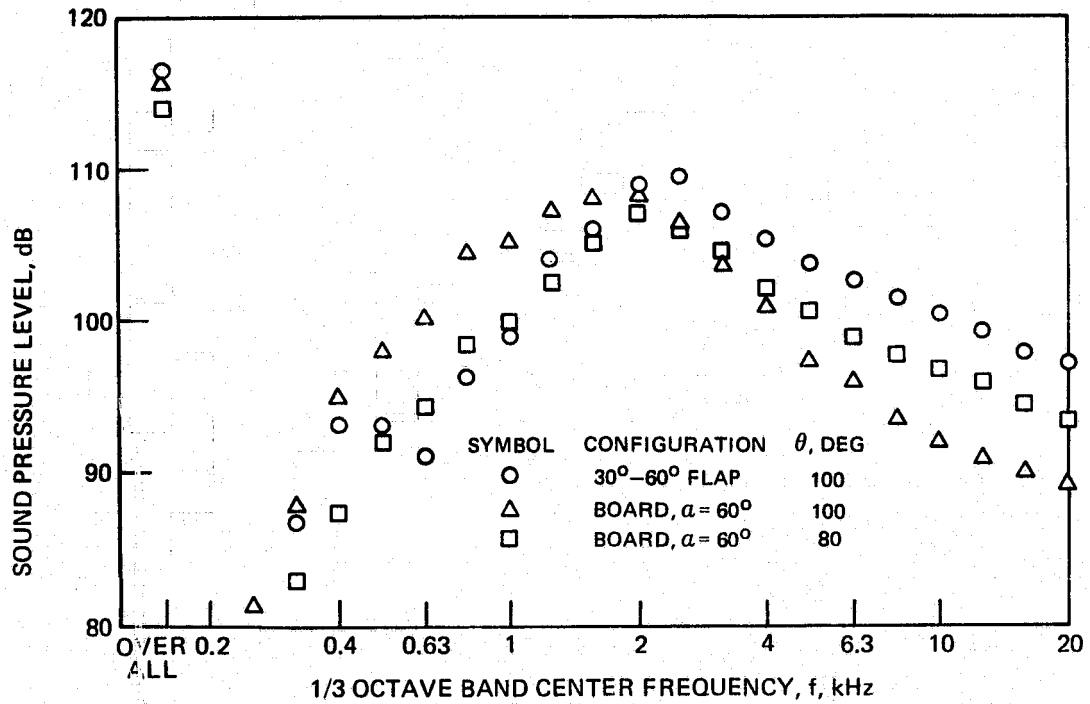
COMPARISON WITH SPECTRA FOR NOZZLE

SYMBOL	CONFIGURATION	θ, DEG
○	30°–60° FLAP	100
△	NO BOARD	160
□	NO BOARD	140

SOUND PRESSURE LEVEL, dB

OVER ALL

1/3 OCTAVE BAND CENTER FREQUENCY, f, kHz
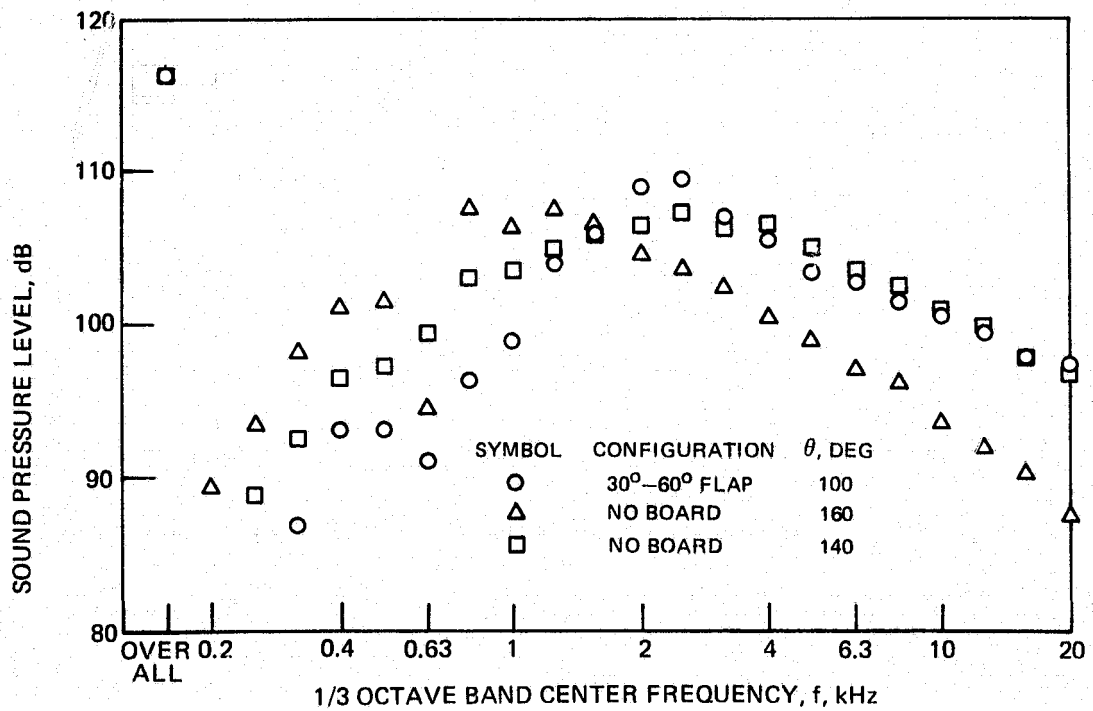
FIGURE 9 – COMPARISONS OF SPECTRA FOR DOUBLE SLOTTED FLAP AT APPROACH (30°–60°) DEFLECTION WITH THOSE FOR LARGE FLAT BOARD AND ISOLATED NOZZLE

N09–42–4

FIGURE 10 — COMPARISON OF PREDICTED AND MEASURED EFFECT OF
IMPINGEMENT ANGLE ON DIRECTIVITY

N11-174-3
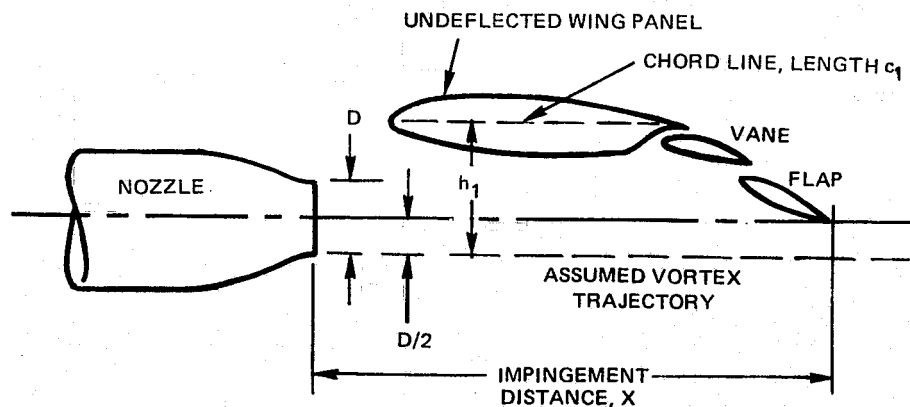
(a) UTW, SMALL FLAP DEFLECTION
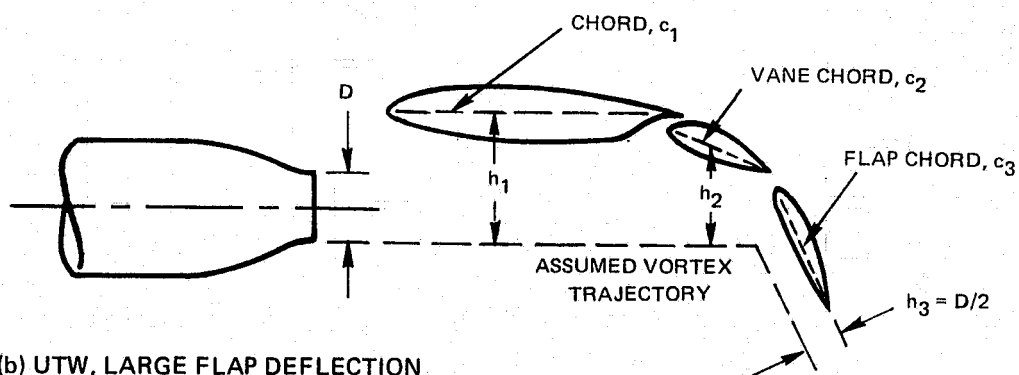
(b) UTW, LARGE FLAP DEFLECTION
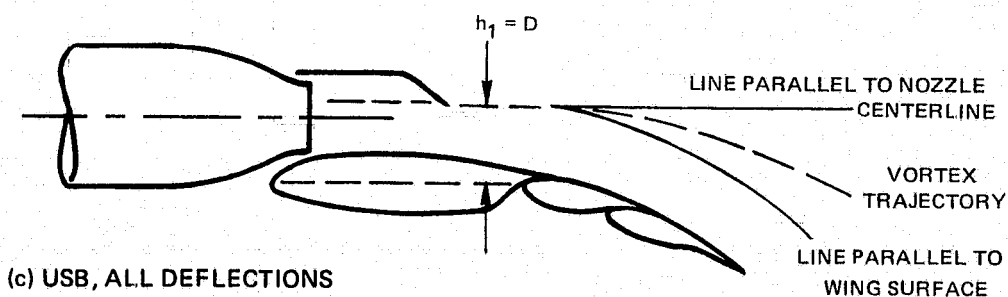
(c) USB, ALL DEFLECTIONS

FIGURE 11.— SKETCH OF ASSUMED VORTEX TRAJECTORIES FOR
CACULATION OF EBF SCRUBBING NOISE

R07—97—1

76

FIGURE 12. – COMPARISON OF NORMALIZED SUBSONIC JET EXHAUST NOISE
SPECTRA WITH EMPIRICAL EQUATION

R07–74–6

77
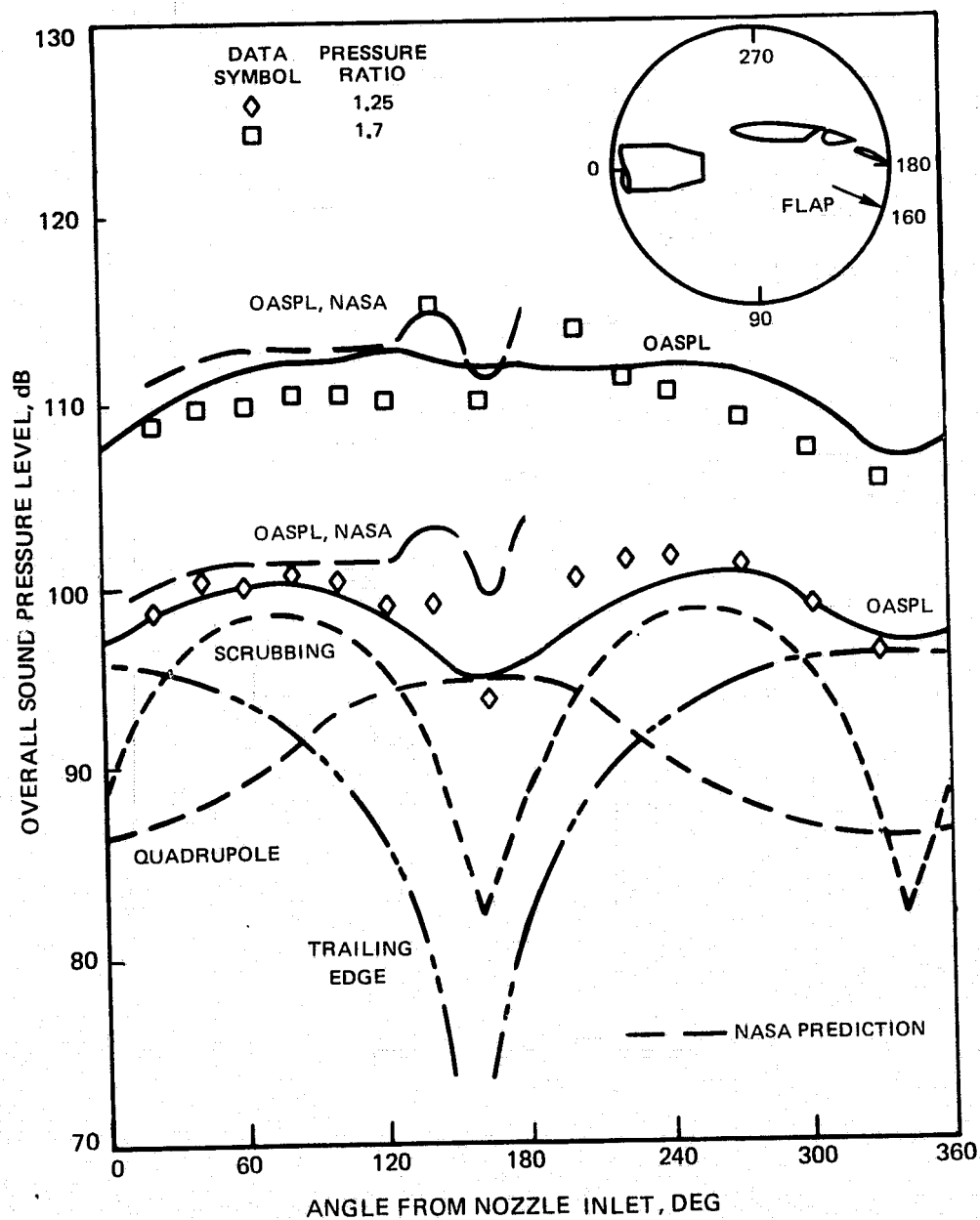
FIGURE 13.— COMPARISON OF CALCULATED AND MEASURED NOISE RADIATION PATTERNS FOR AN UTW DOUBLE SLOTTED FLAP AT 10°−20° DEFLECTION

(a) 120° FROM NOZZLE INLET DIRECTION

(b) 100° FROM NOZZLE INLET DIRECTION
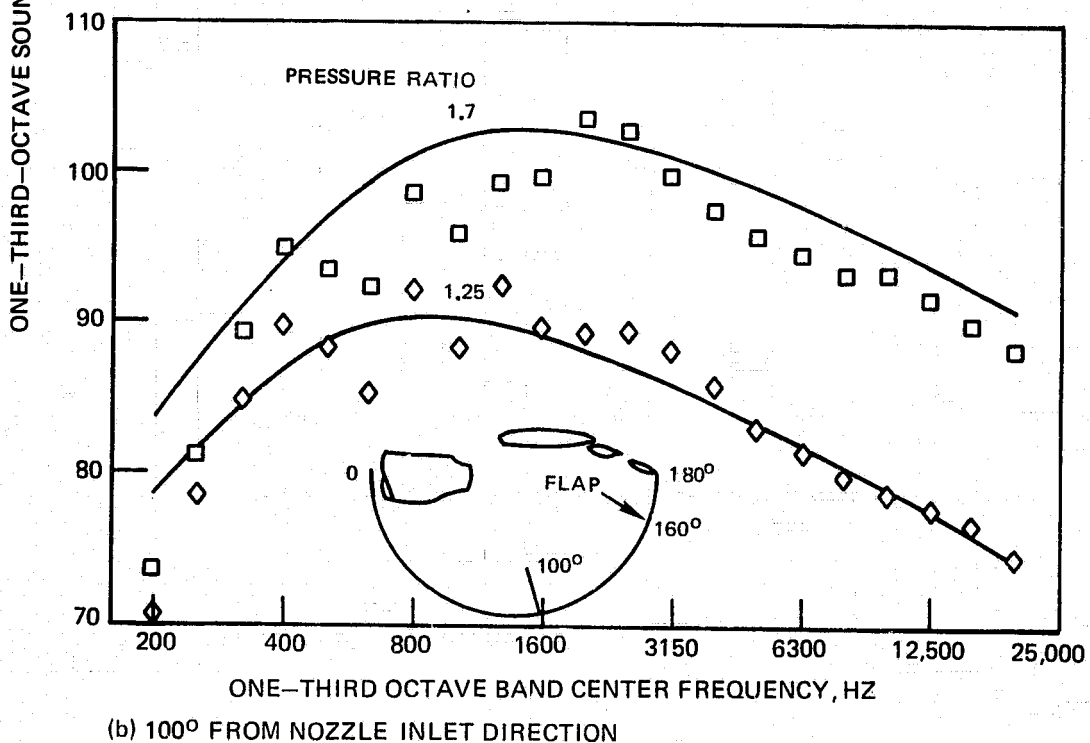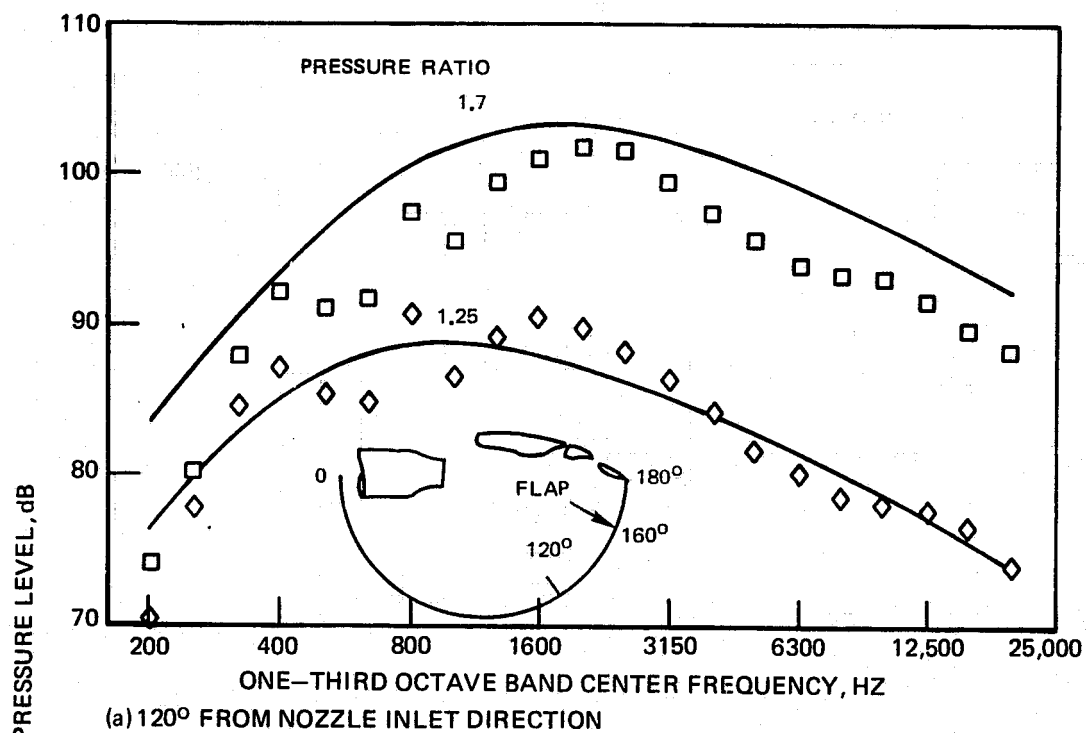
FIGURE 14. — MEASURED AND CALCULATED SPECTRA FOR UTW DOUBLE
SLOTTED FLAP AT 10°–20° DEFLECTION

79
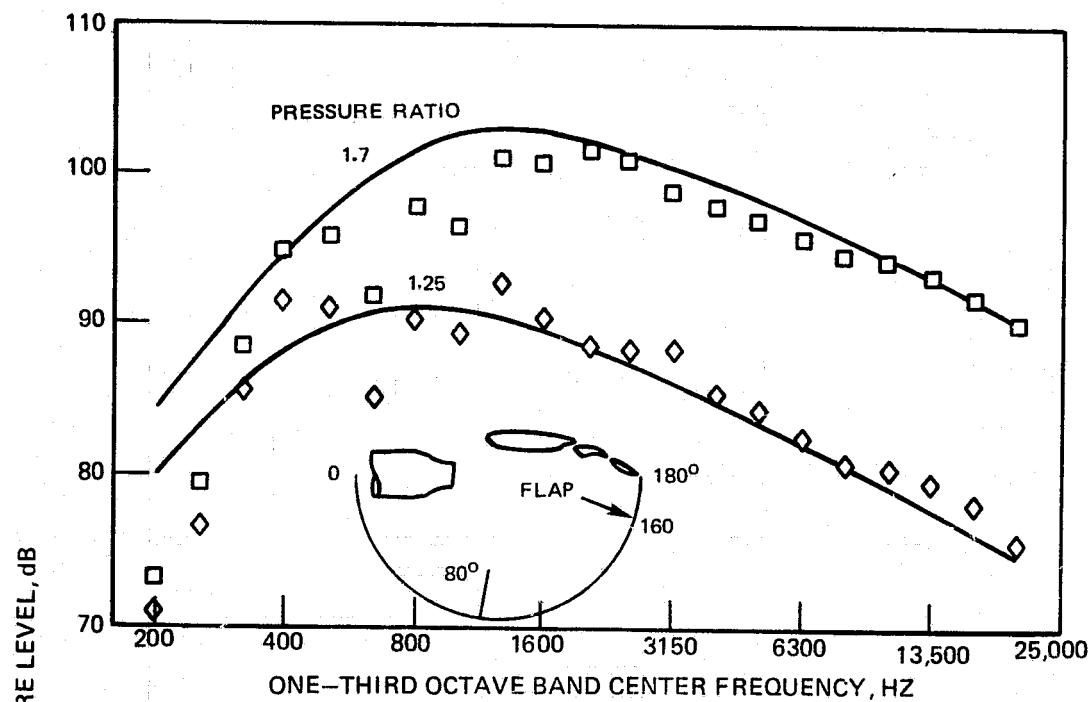
(c) 80° FROM NOZZLE INLET DIRECTION
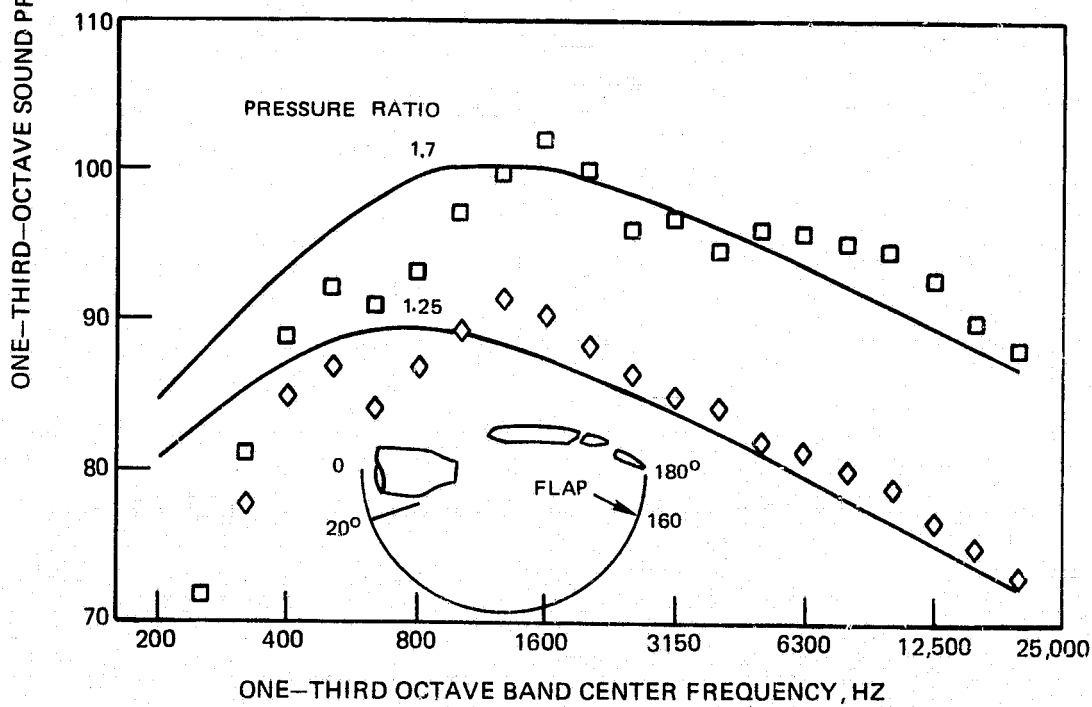
(d) 20° FROM NOZZLE INLET DIRECTION

FIGURE 14. CONCLUDED
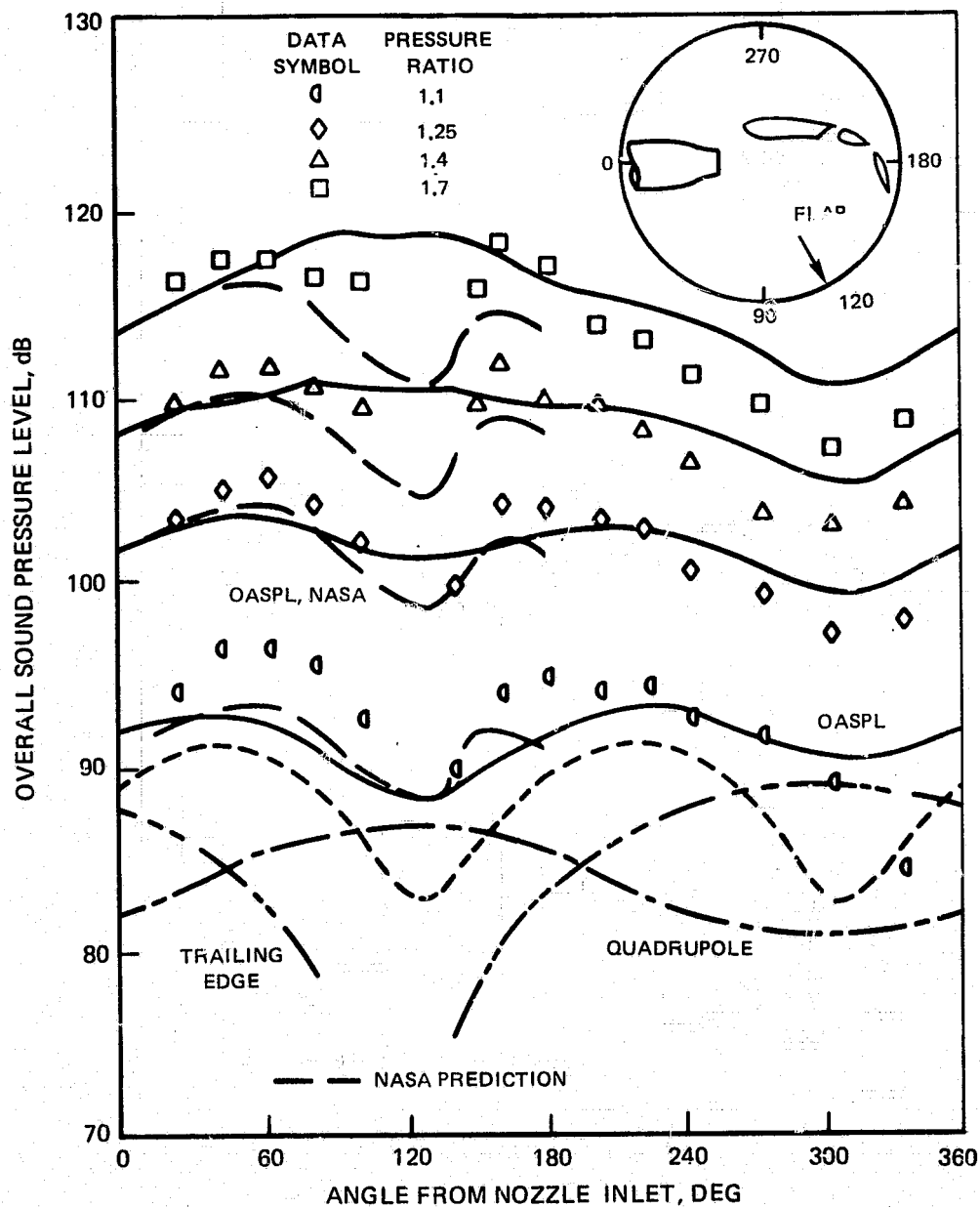
FIGURE 15. — COMPARISON OF CALCULATED AND MEASURED NOISE RADIATION PATTERNS FOR AN UTW DOUBLE SLOTTED FLAP AT 30°–60° DEFLECTION
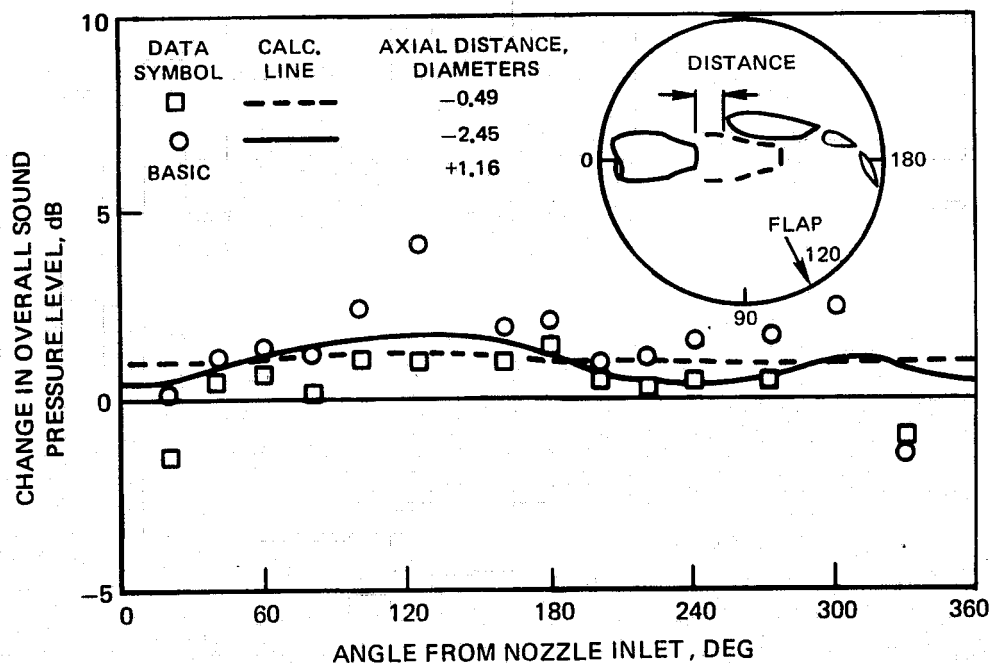
(a) EFFECT OF AXIAL DISTANCE
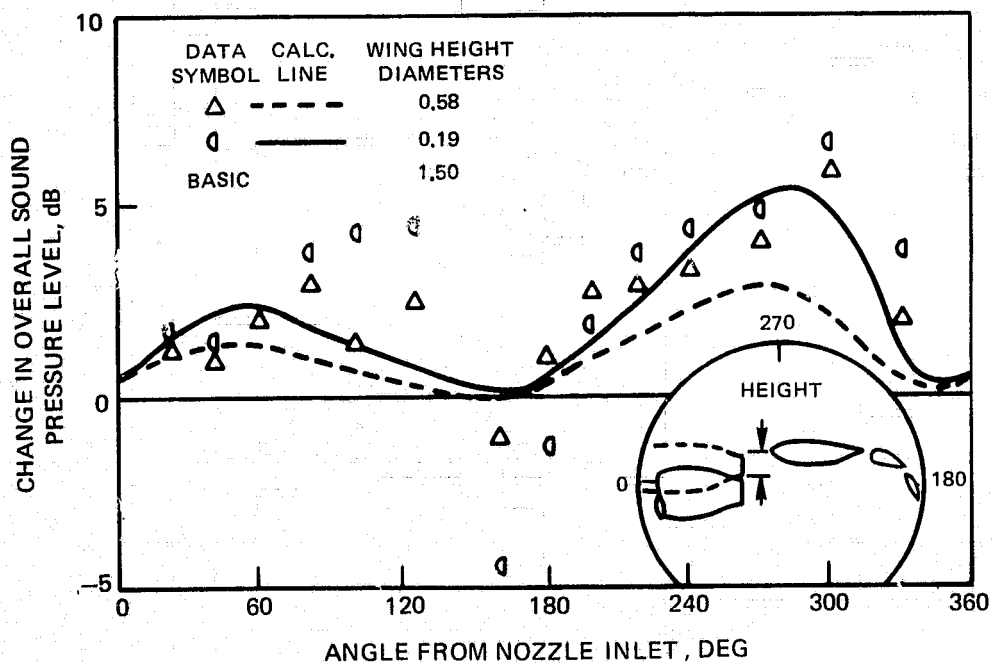
(b) EFFECT OF WING HEIGHT

FIGURE 16.—CHANGES IN SOUND RADIATION, RELATIVE TO THAT OF THE BASIC
CONFIGURATION, AS THE NOZZLE POSITION IS VARIED, UTW DOUBLE
SLOTTED FLAP AT 30°–60° DEFLECTION AND PRESSURE RATIO 1.7.

R02–72–3
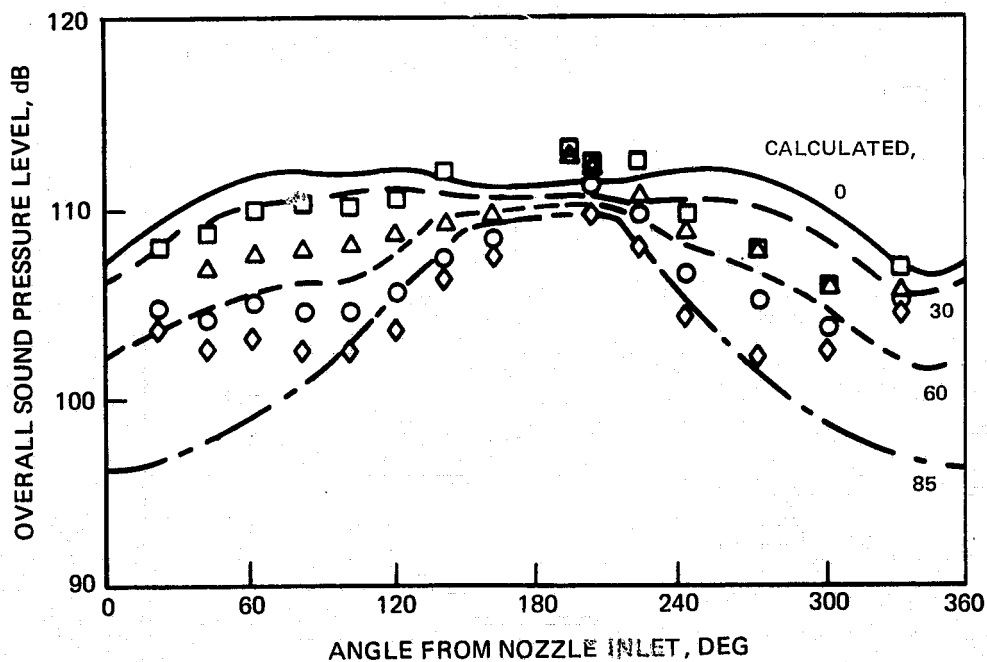
(a) 10°–20° DOUBLE SLOTTED FLAP DEFLECTION
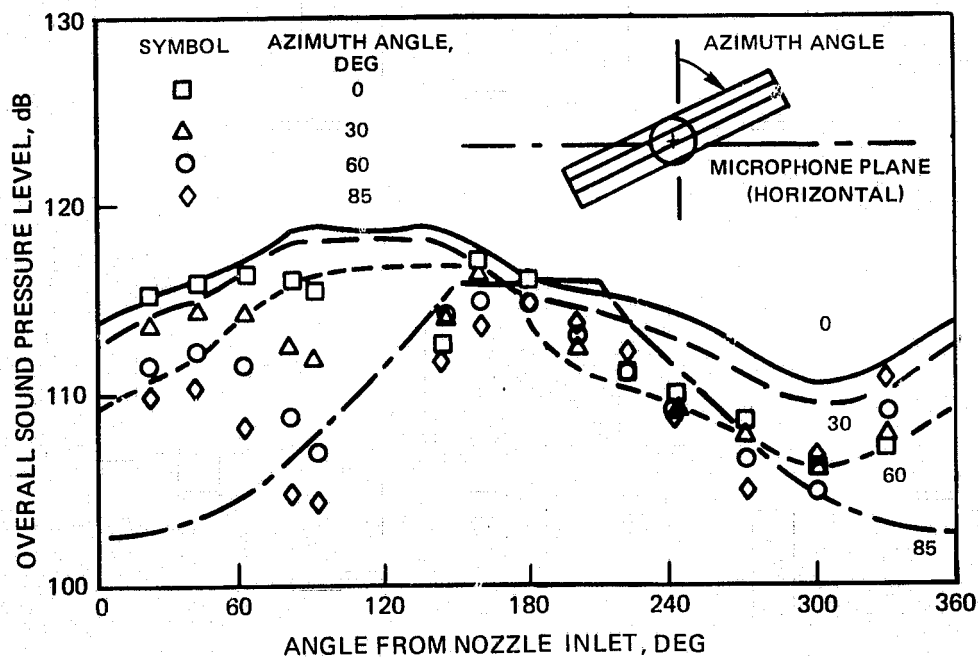
(b) 30°–60° DOUBLE SLOTTED FLAP DEFLECTION

FIGURE 17.– VARIATION OF CALCULATED AND MEASURED NOISE RADIATION PATTERNS WITH AZIMUTH ANGLE FOR UTW AT PRESSURE RATIO 1.7.

R02–72–8

83
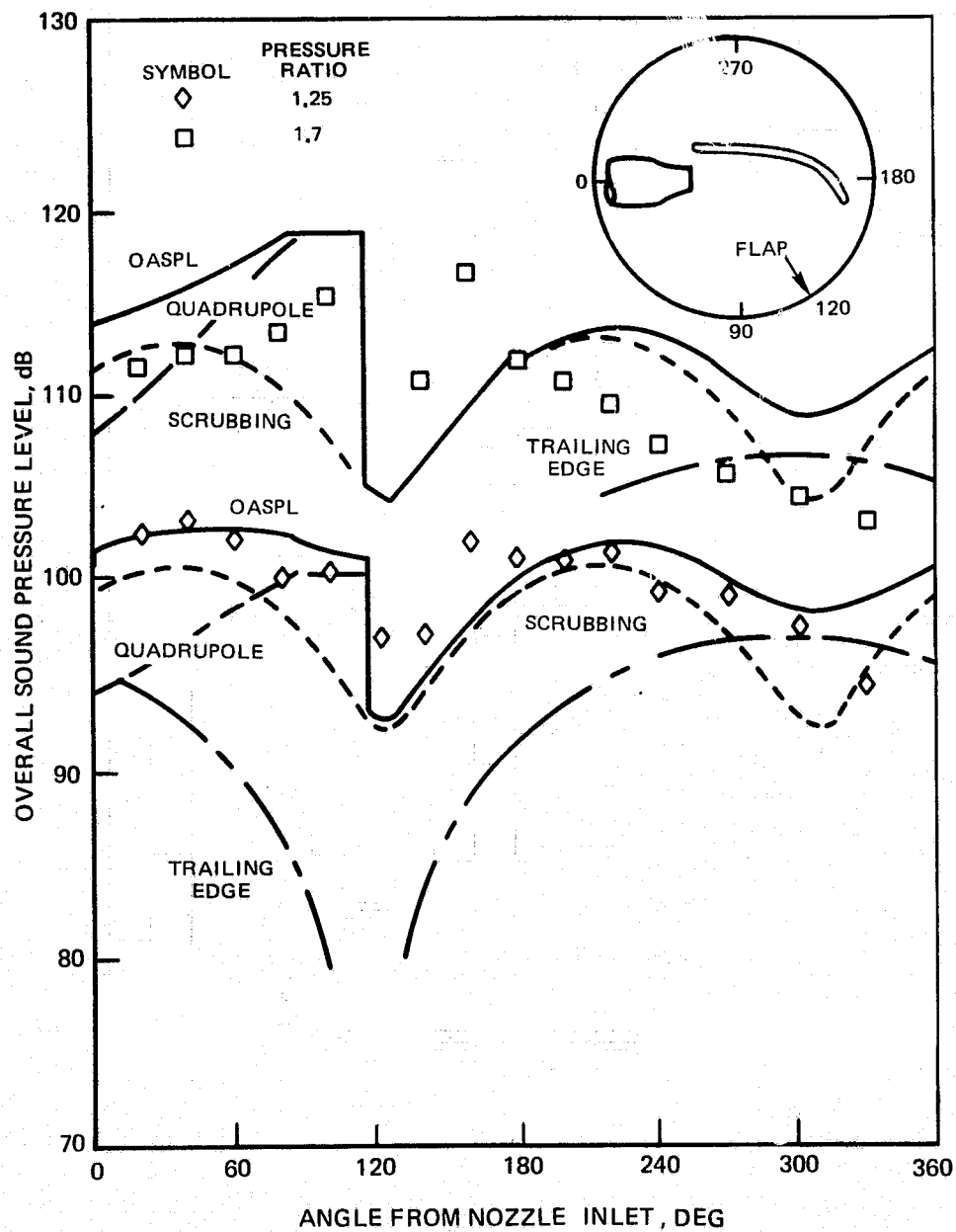
FIGURE 18. — COMPARISON OF CALCULATED AND MEASURED NOISE RADIATION
PATTERNS FOR AN UTW SLOTLESS WING WITH 60° AFT DEFLECTION
DATA OF NASA TN D—6636.

R02—72—1

84

OPEN SYMBOLS ARE DATA FOR DOUBLE SLOTTED FLAP

SOLID SYMBOLS ARE DATA FOR SLOTLESS WING
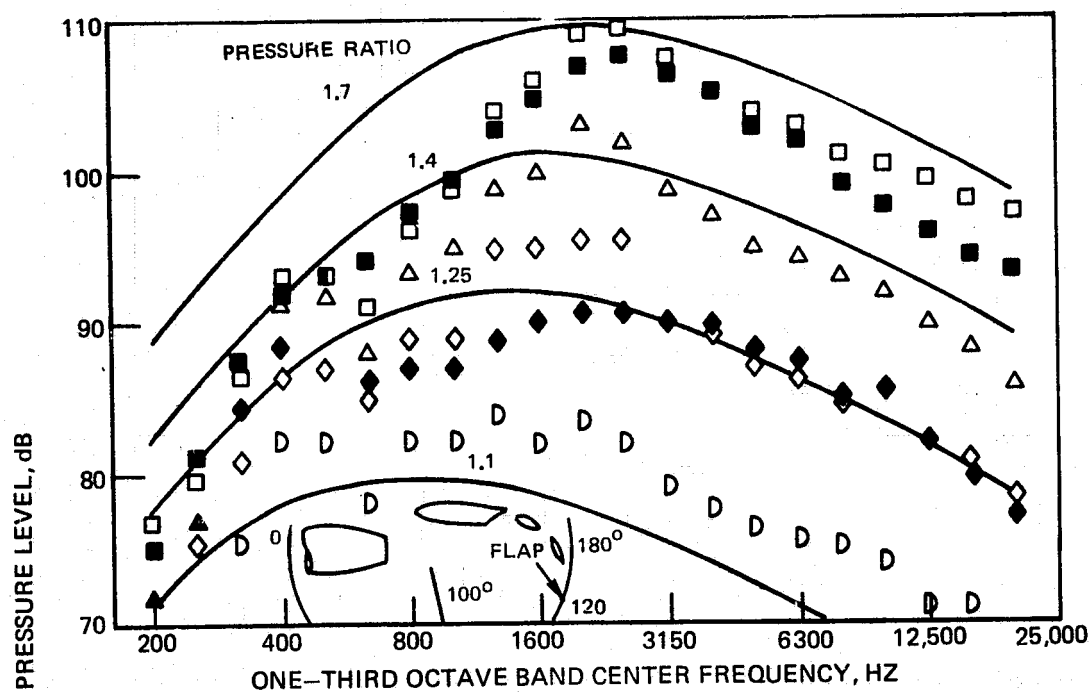
(a) 100° FROM NOZZLE INLET DIRECTION
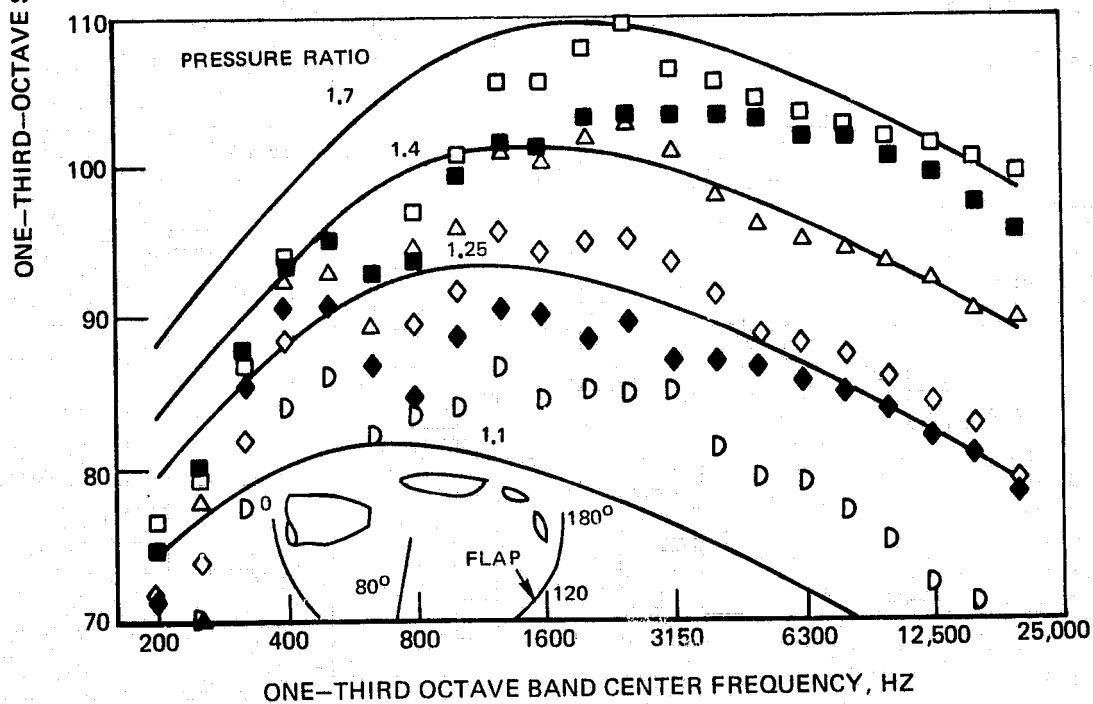
(b) 80° FROM NOZZLE INLET DIRECTION

FIGURE 19. — MEASURED AND CALCULATED SPECTRA FOR UTW DOUBLE SLOTTED FLAP AND SLOTLESS WING AT 30°–60° DEFLECTION

RO2–143–2

85

(c) 60° FROM NOZZLE INLET DIRECTION

(d) 20° FROM NOZZLE INLET DIRECTION
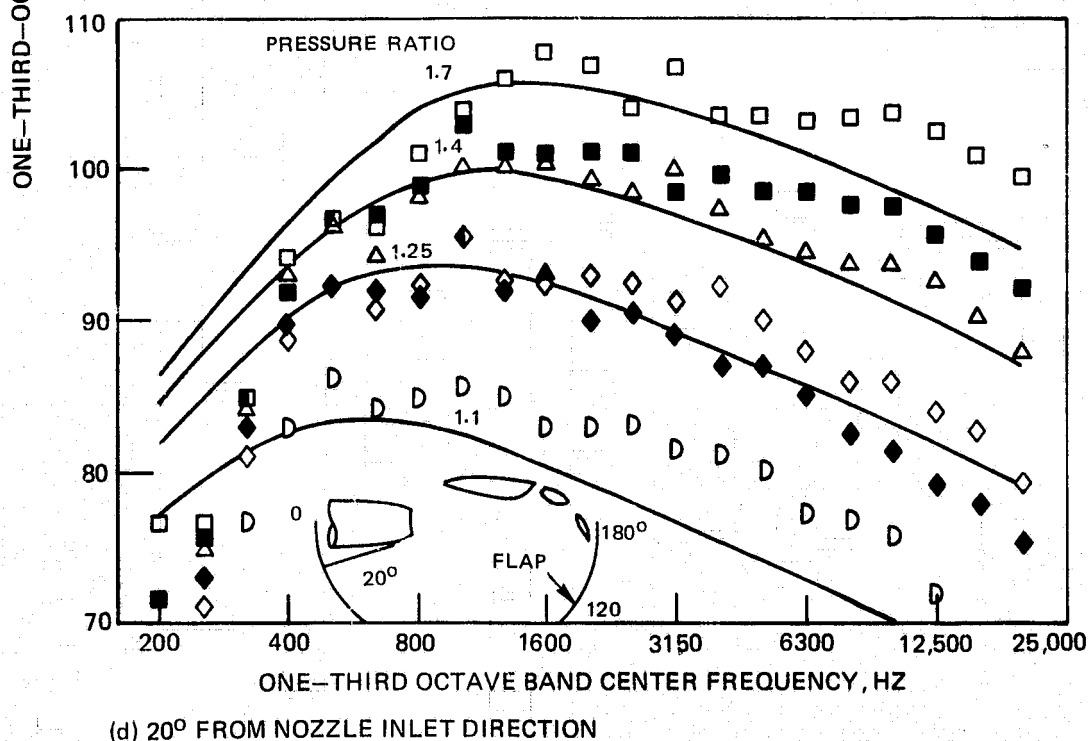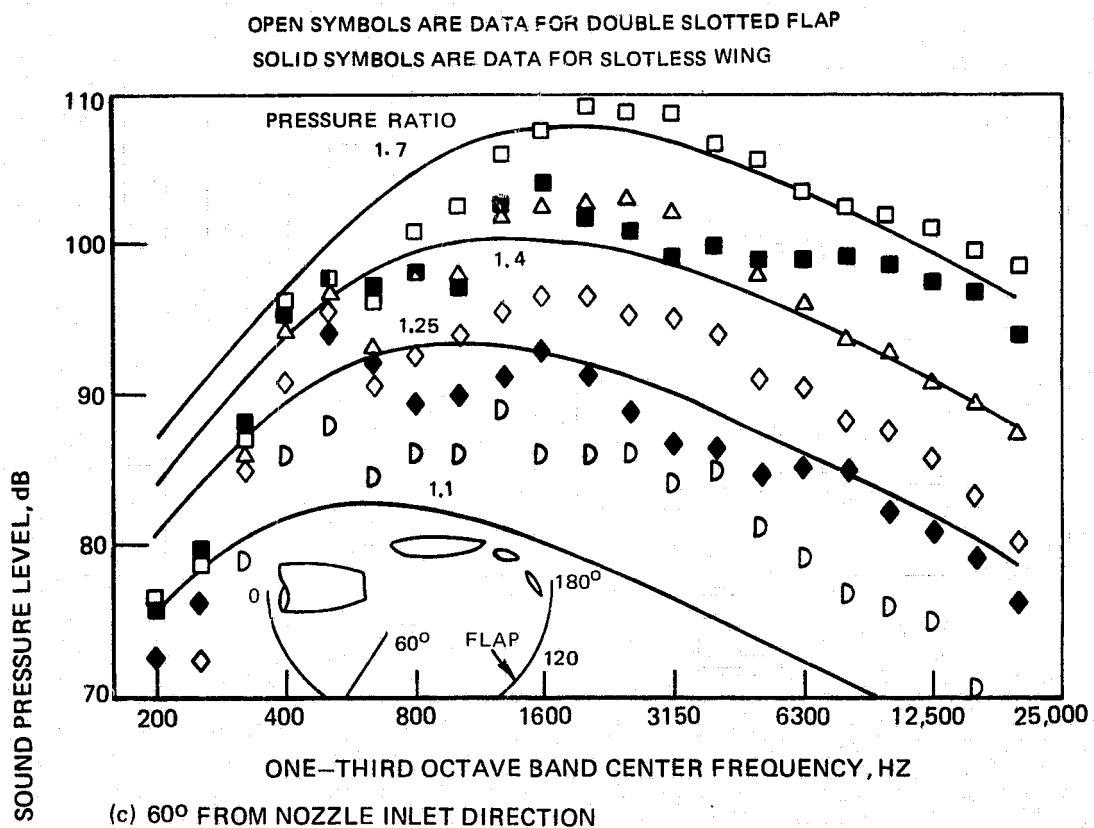
FIGURE 19. — CONCLUDED.

RO2—143—3

86
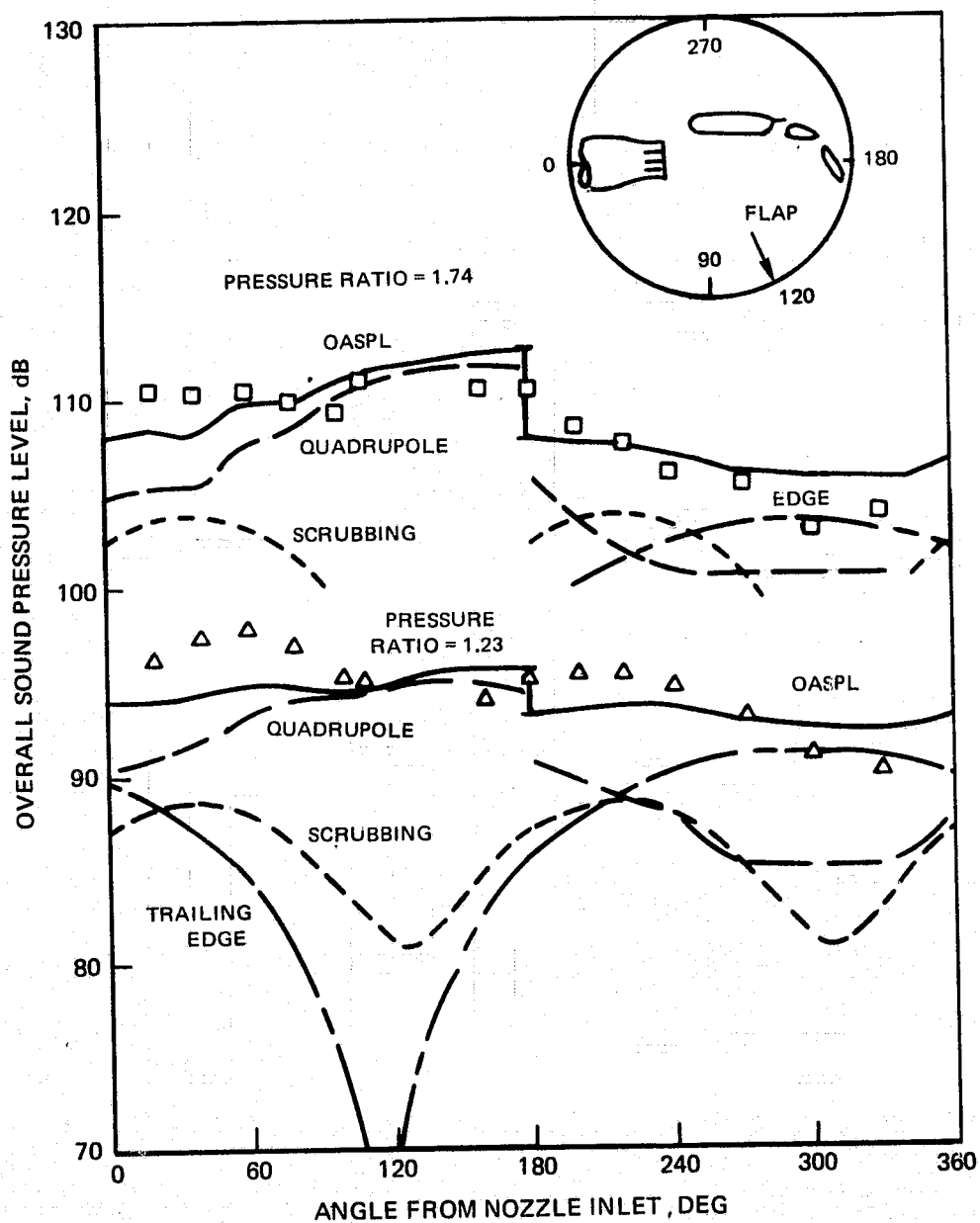
FIGURE 20. — COMPARISON OF CALCULATED AND MEASURED NOISE RADIATION PATTERNS FOR AN UTW DOUBLE SLOTTED FLAP AT 30°–60° DEFLECTION AND A MIXER NOZZLE.
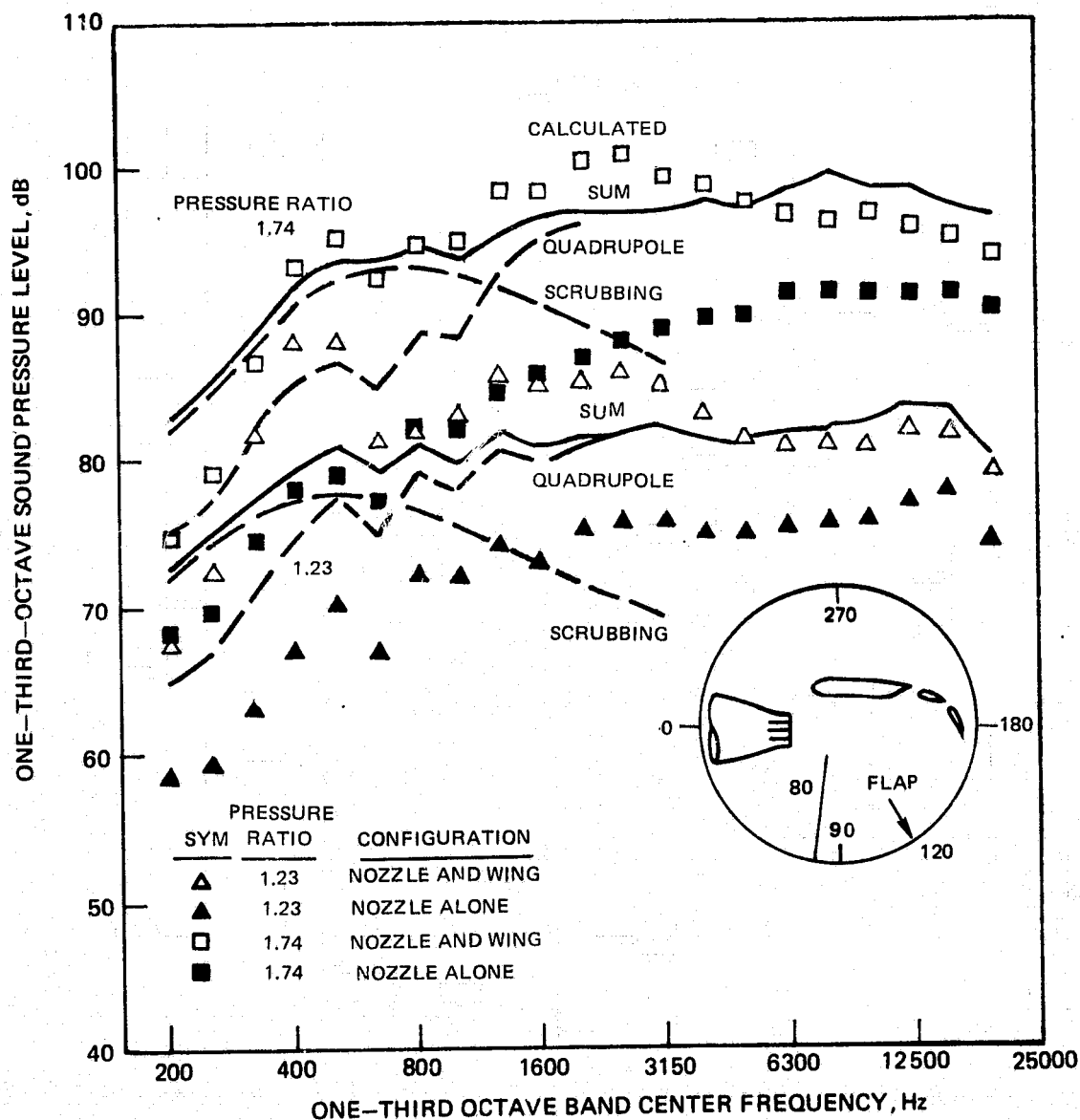
FIGURE 21. — MEASURED AND CALCULATED SPECTRA AT 80° FROM
NOZZLE INLET OF UTW DOUBLE SLOTTED FLAP AT
30°–60° DEFLECTION AND MIXER NOZZLE
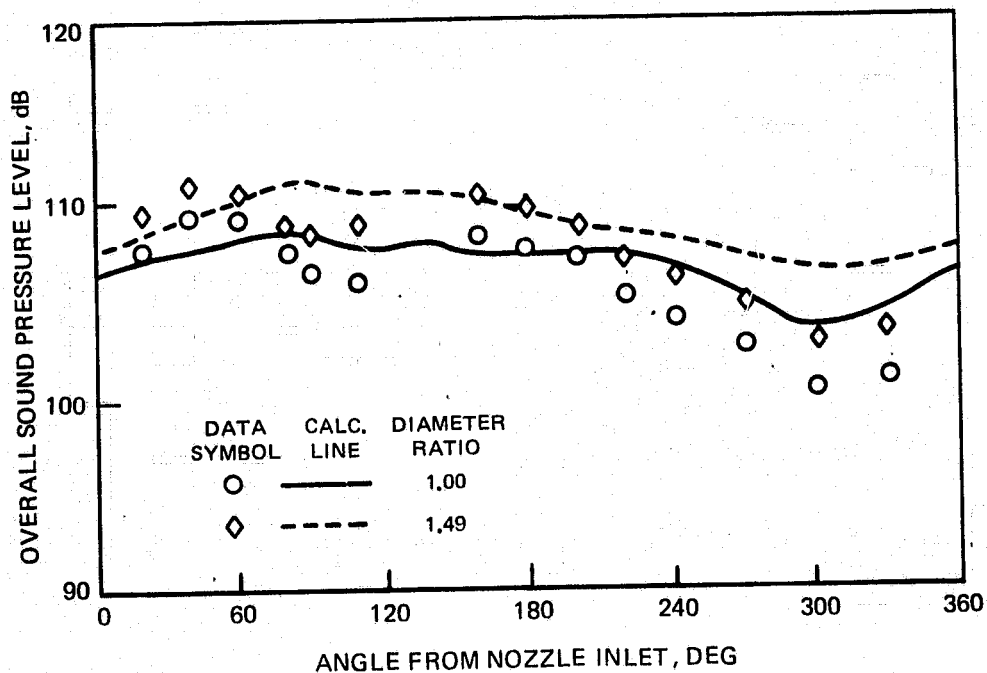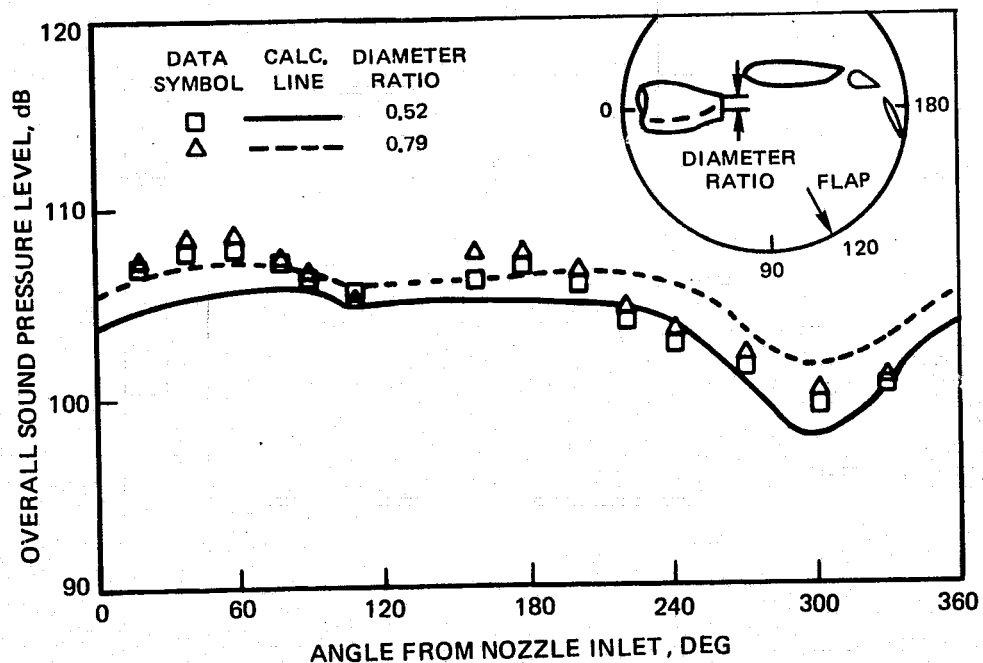
FIGURE 22. — EFFECT OF NOZZLE DIAMETER ON NOISE RADIATION PATTERN OF AN UTW DOUBLE SLOTTED FLAP AT 30°–60° DEFLECTION AND 212 m/sec IMPINGEMENT VELOCITY
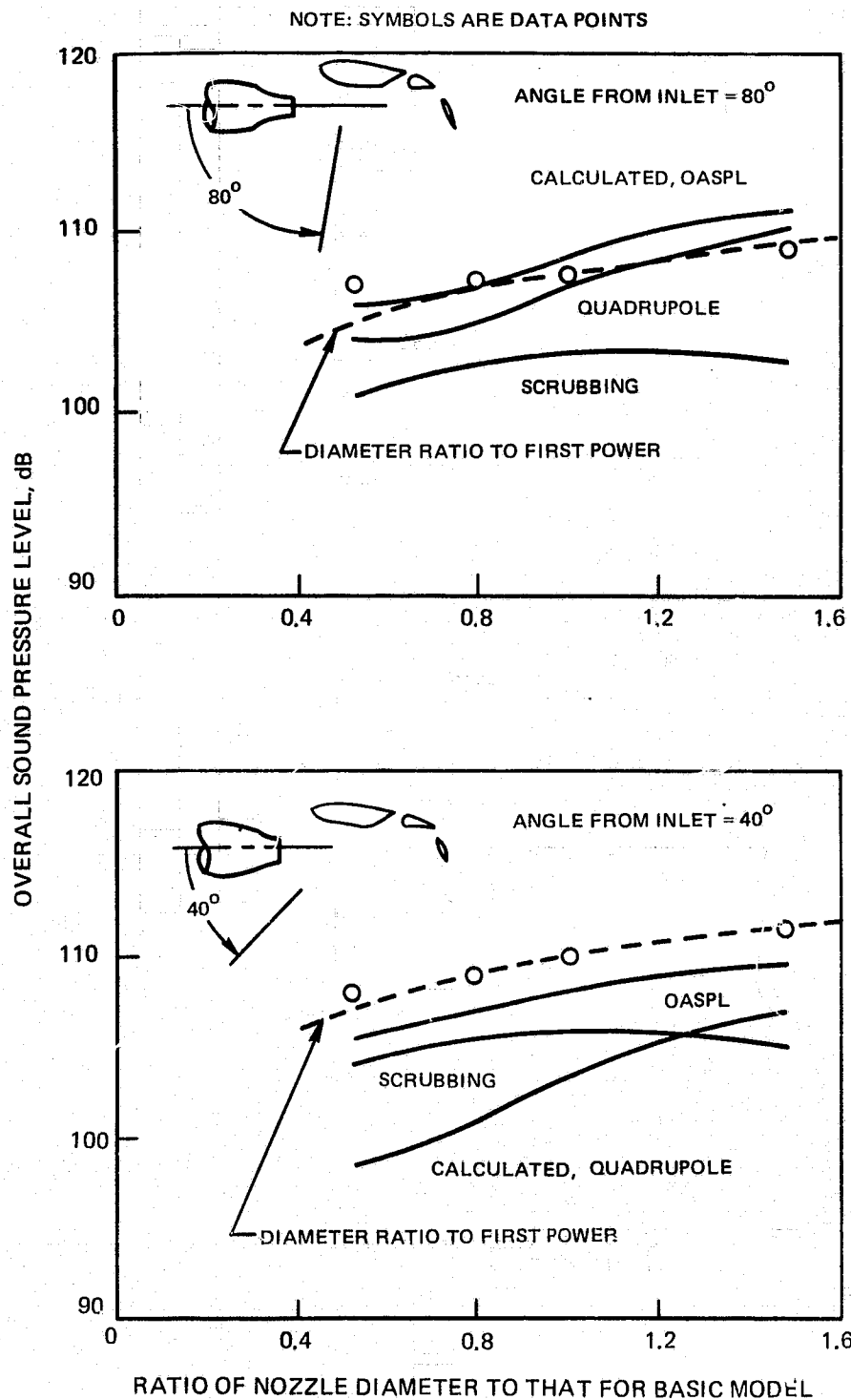
FIGURE 23.– VARIATION OF SOUND RADIATION WITH NOZZLE DIAMETER FOR AN UTW DOUBLE SLOTTED FLAP AT 30°–60° DEFLECTION AND 212 m/sec IMPINGEMENT VELOCITY
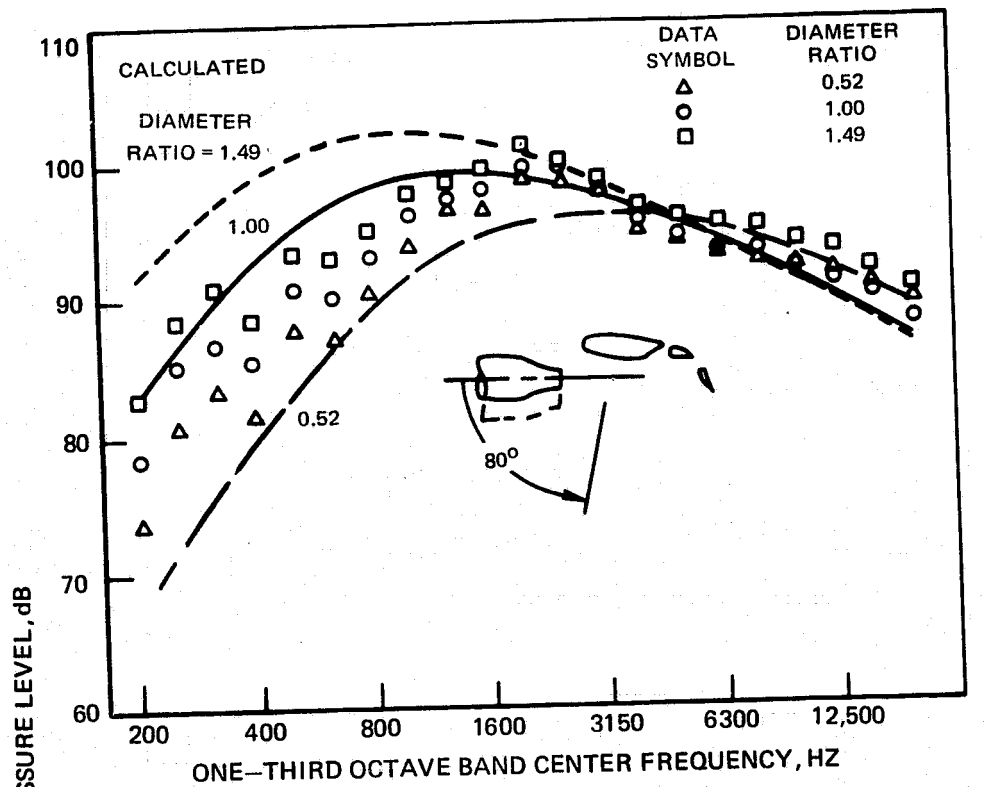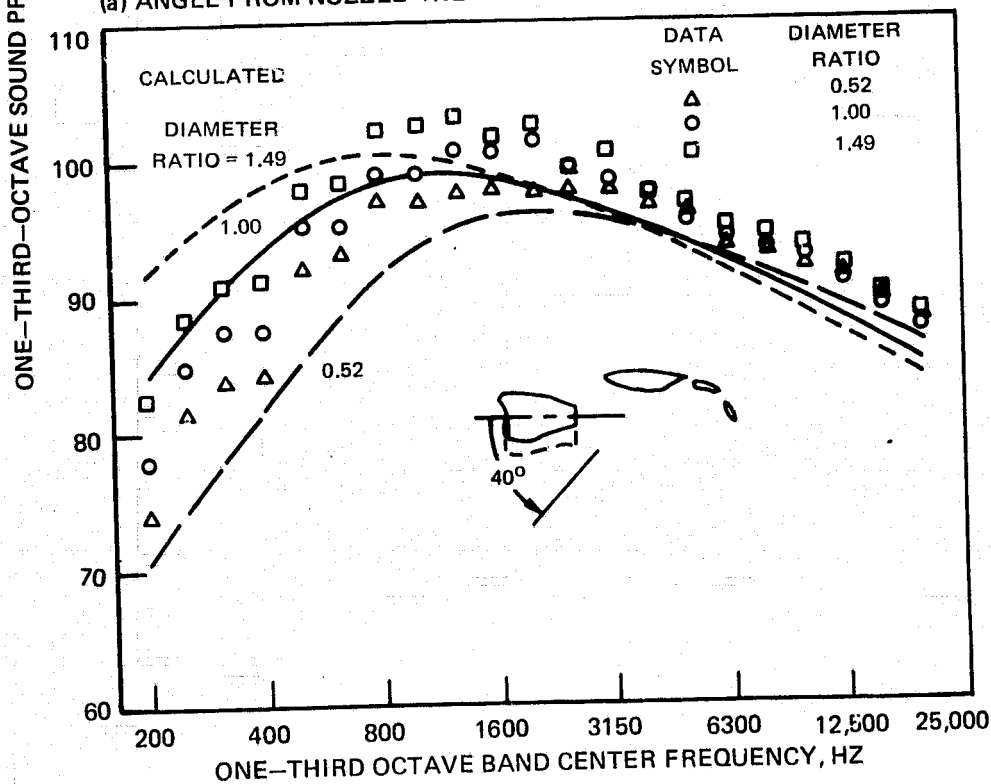
FIGURE 24.— VARIATION OF SPECTRUM SHAPE WITH NOZZLE DIAMETER FOR AN UTW DOUBLE SLOTTED FLAP AT 30°—60° DEFLECTION AND 212 m/sec IMPINGEMENT VELOCITY

RO2—143—1
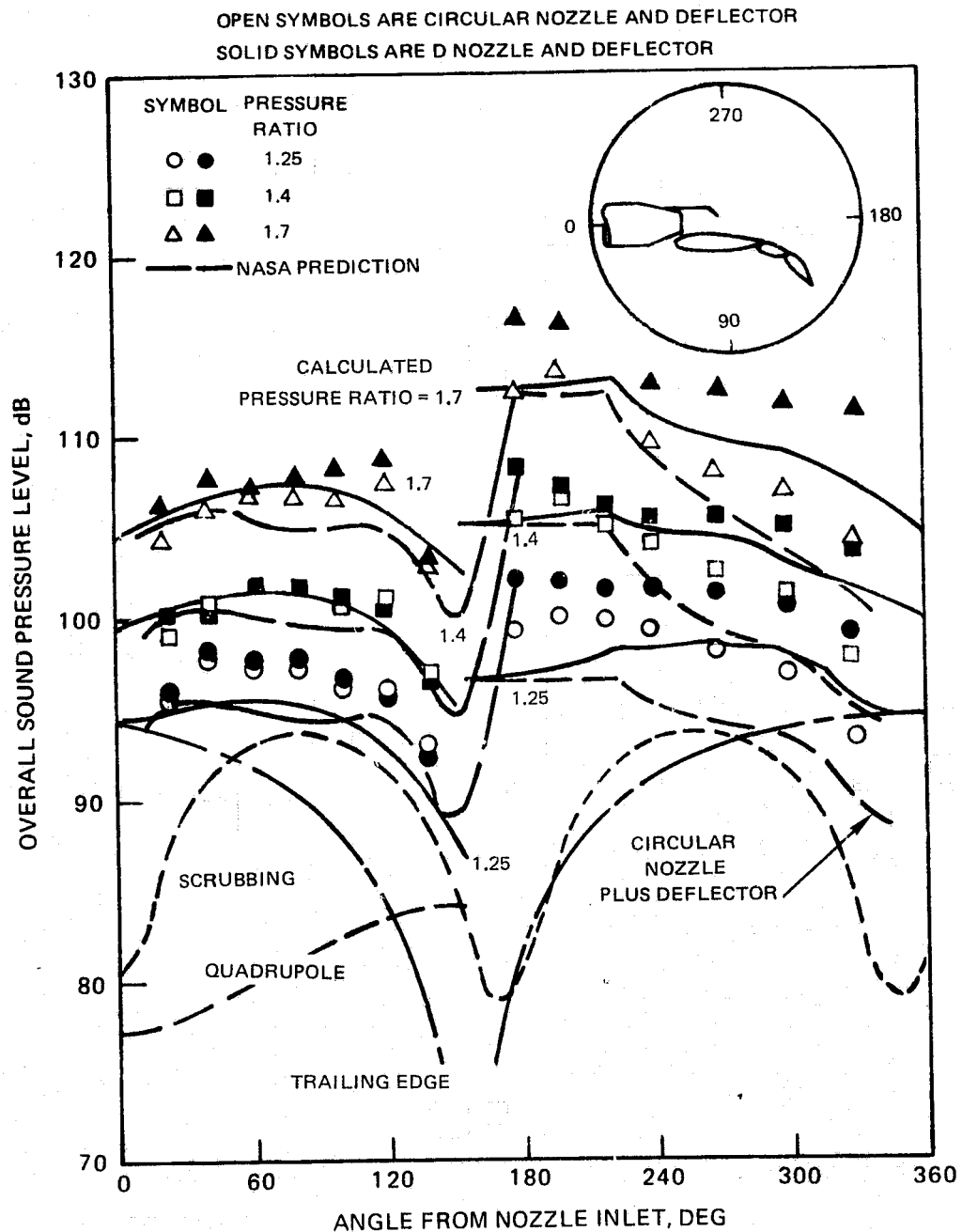
FIGURE 25. — COMPARISON OF CALCULATED AND MEASURED NOISE
RADIATION PATTERNS FOR USB AT 10°–20° DEFLECTION
AND CIRCULAR AND D NOZZLES WITH DEFLECTOR
(a) 0° AZIMUTH

R07--74—9

92

OPEN SYMBOLS ARE CIRCULAR NOZZLE AND DEFLECTOR
SOLID SYMBOLS ARE D NOZZLE AND DEFLECTOR
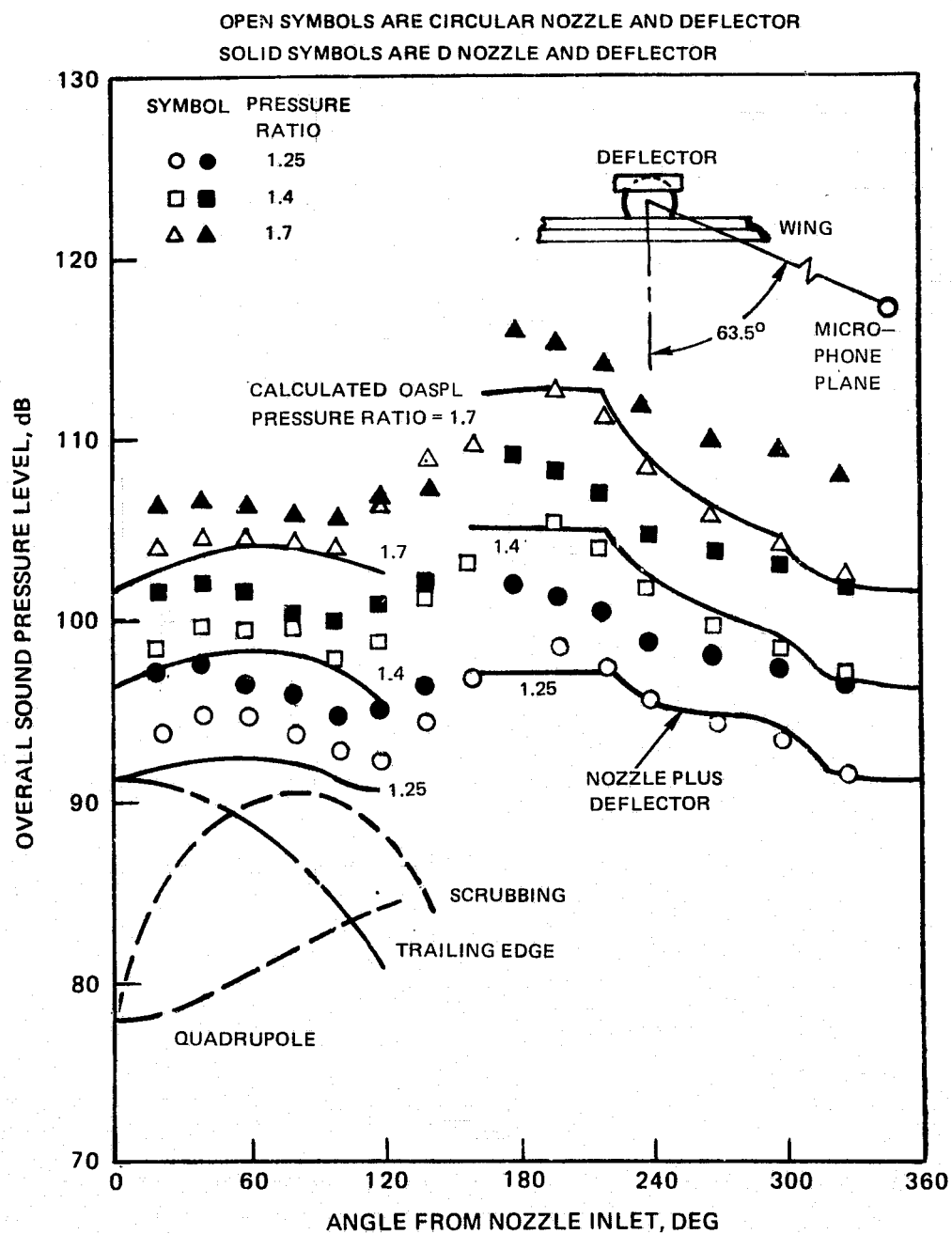
FIGURE 25. — CONCLUDED (b) 63.5° AZIMUTH
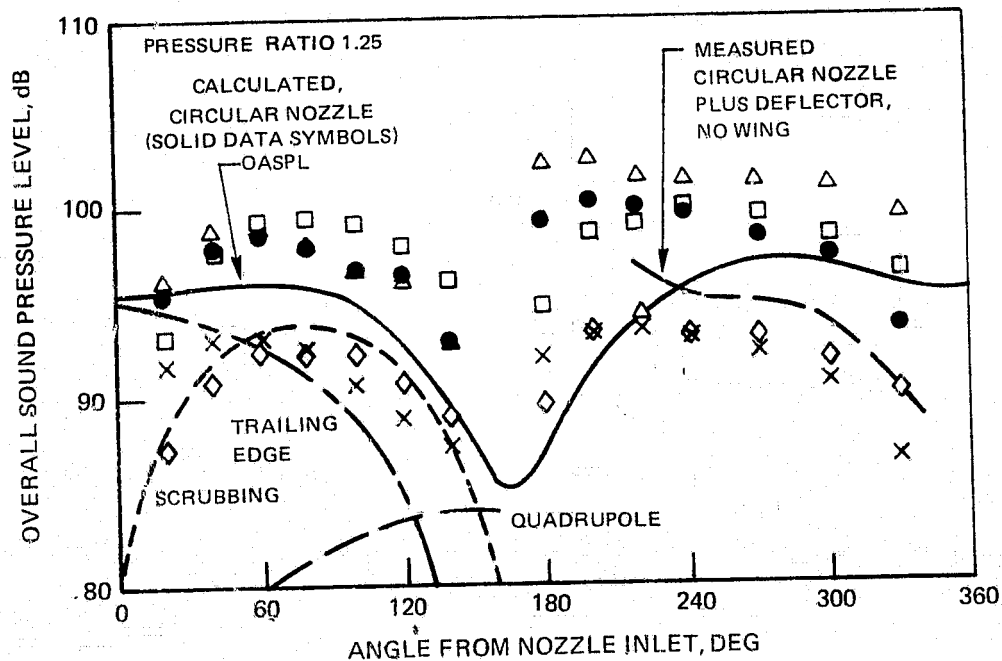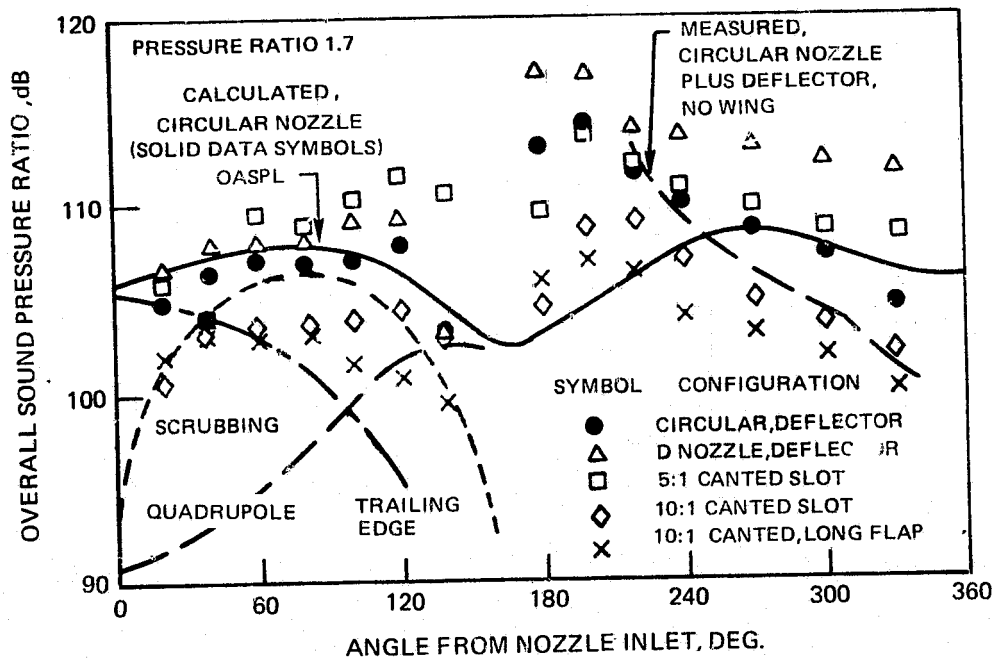
FIGURE 26. — COMPARISON OF CALCULATED NOISE RADIATION PATTERNS FOR USB AT 10°–20° DEFLECTION, WITH CIRCULAR NOZZLE AND DEFLECTOR, WITH DATA FOR FIVE NOZZLE CONFIGURATIONS
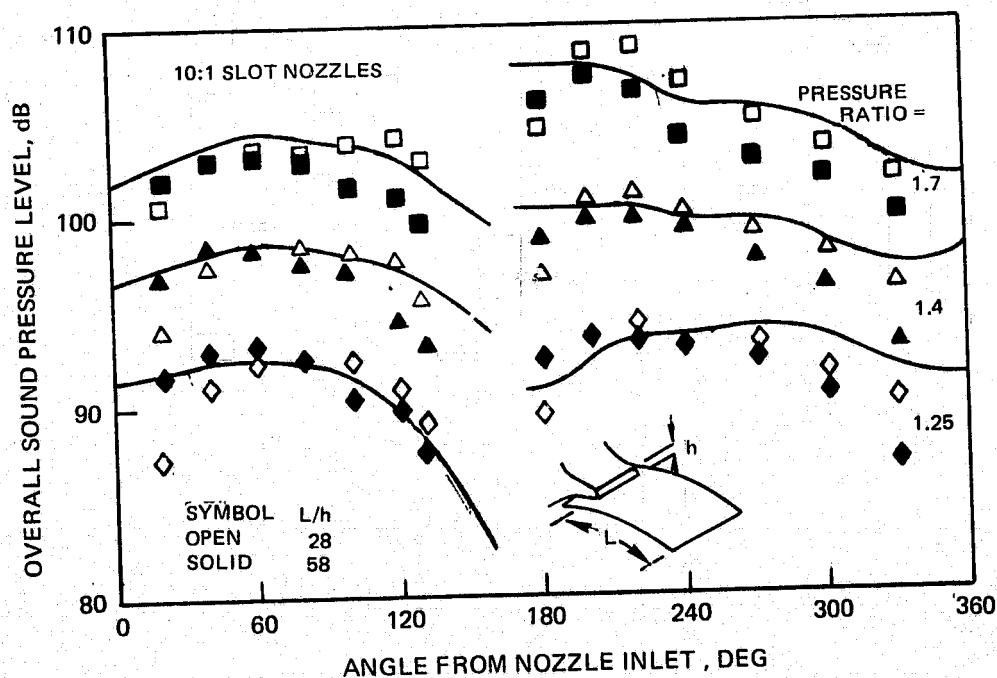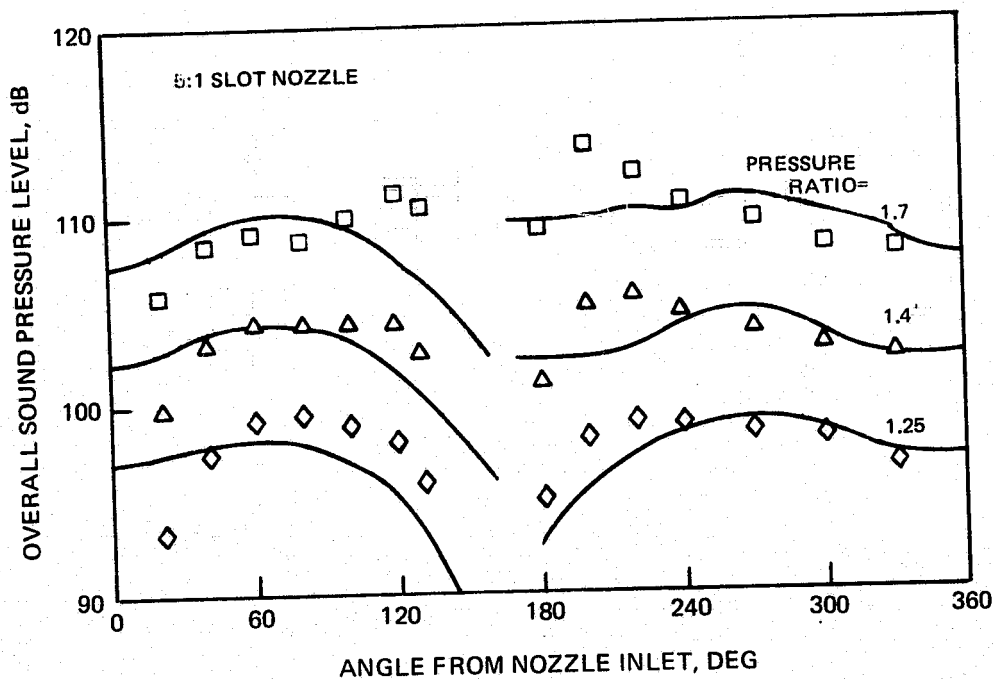
FIGURE 27. — COMPARISON OF CALCULATED AND MEASURED NOISE RADIATION PATTERNS FOR USB WITH SLOT NOZZLES AND 10°–20° FLAP DEFLECTION
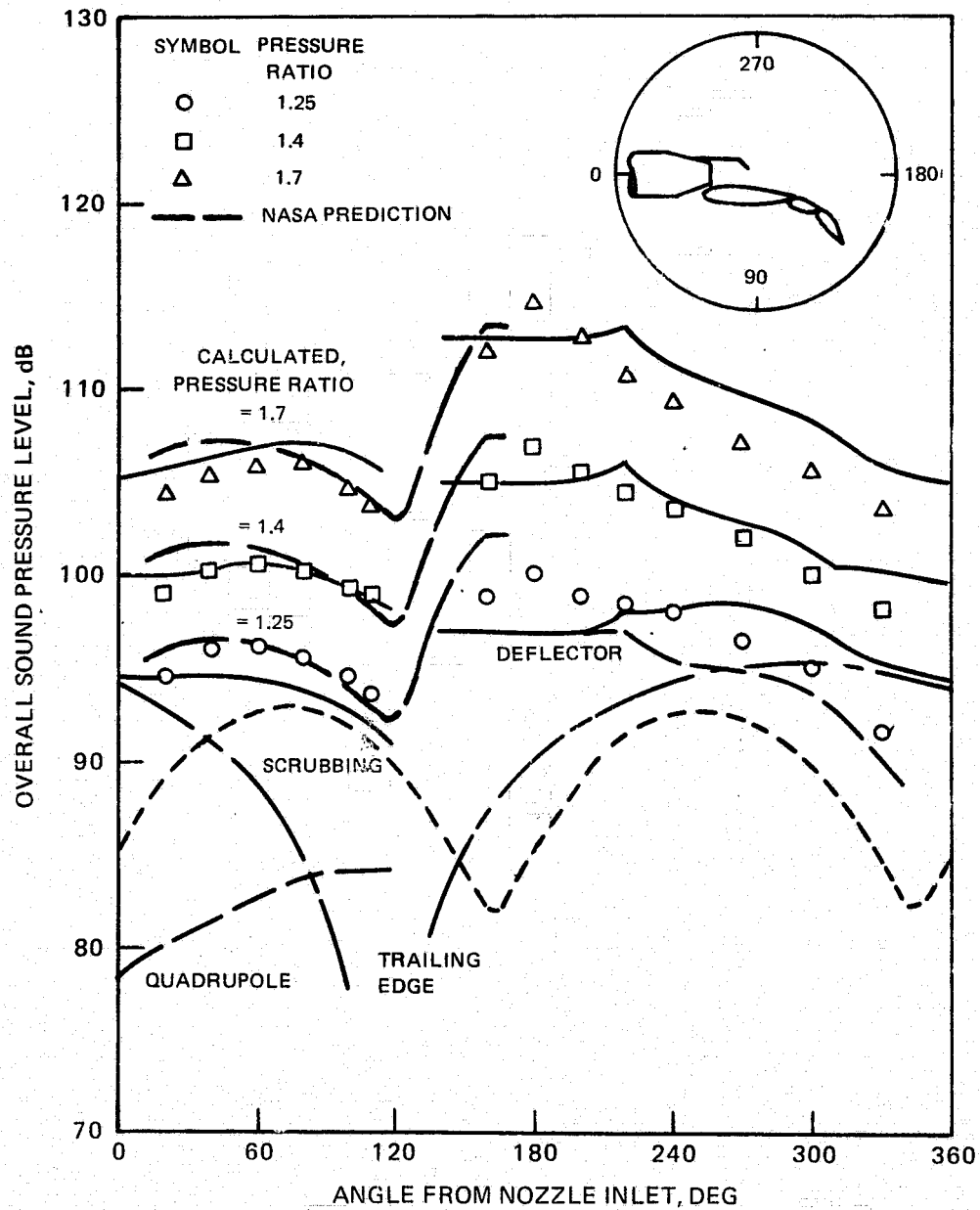
FIGURE 28. – COMPARISON OF CALCULATED AND MEASURED NOISE RADIATION PATTERNS FOR USB AT 30°–60° DEFLECTION WITH CIRCULAR NOZZLE AND DEFLECTOR

96

R06—147—4
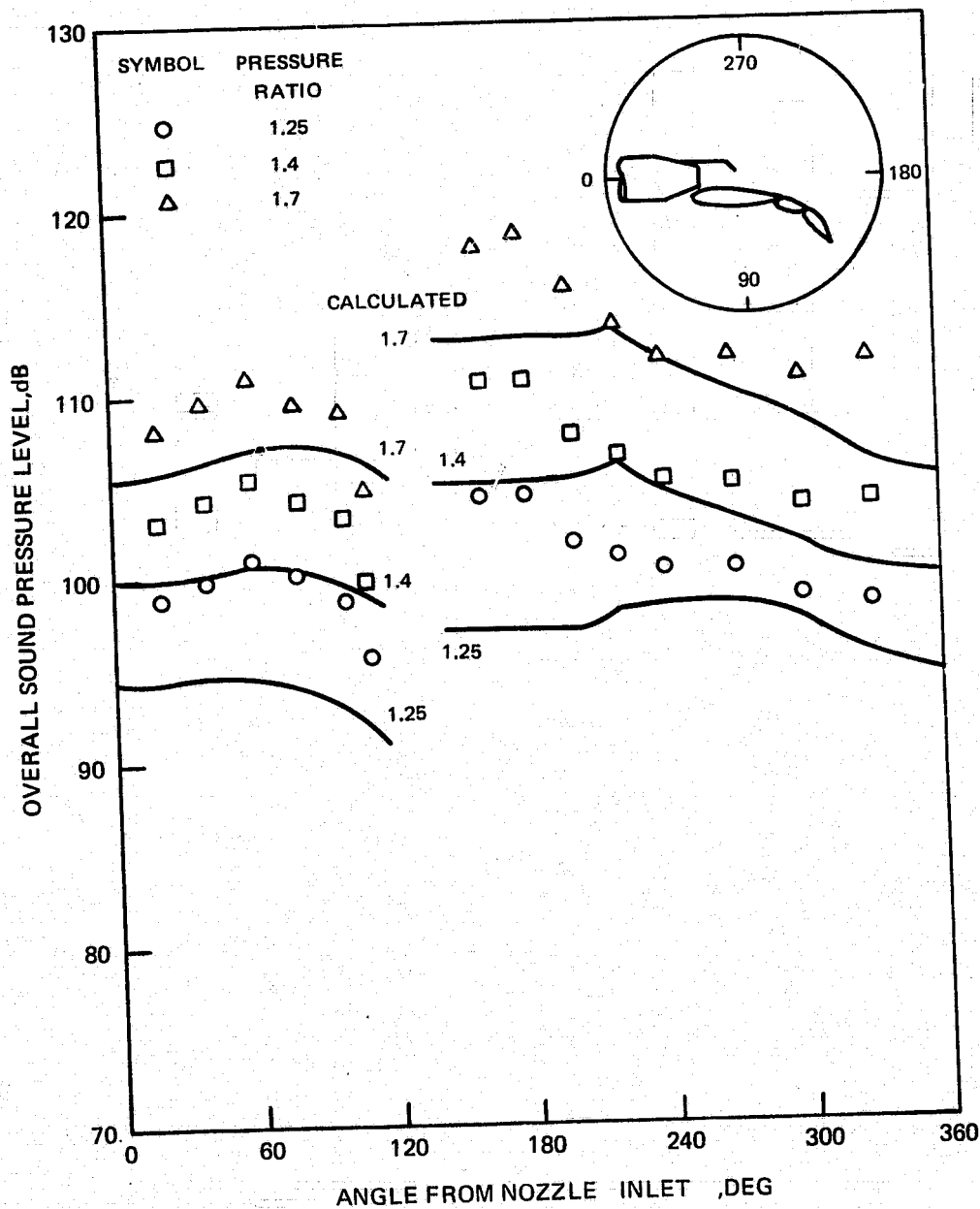
FIGURE 29. — COMPARISON OF CALCULATED AND MEASURED NOISE RADIATION PATTERNS FOR USB AT 30°—60° DEFLECTION WITH D NOZZLE AND DEFLECTOR.

97
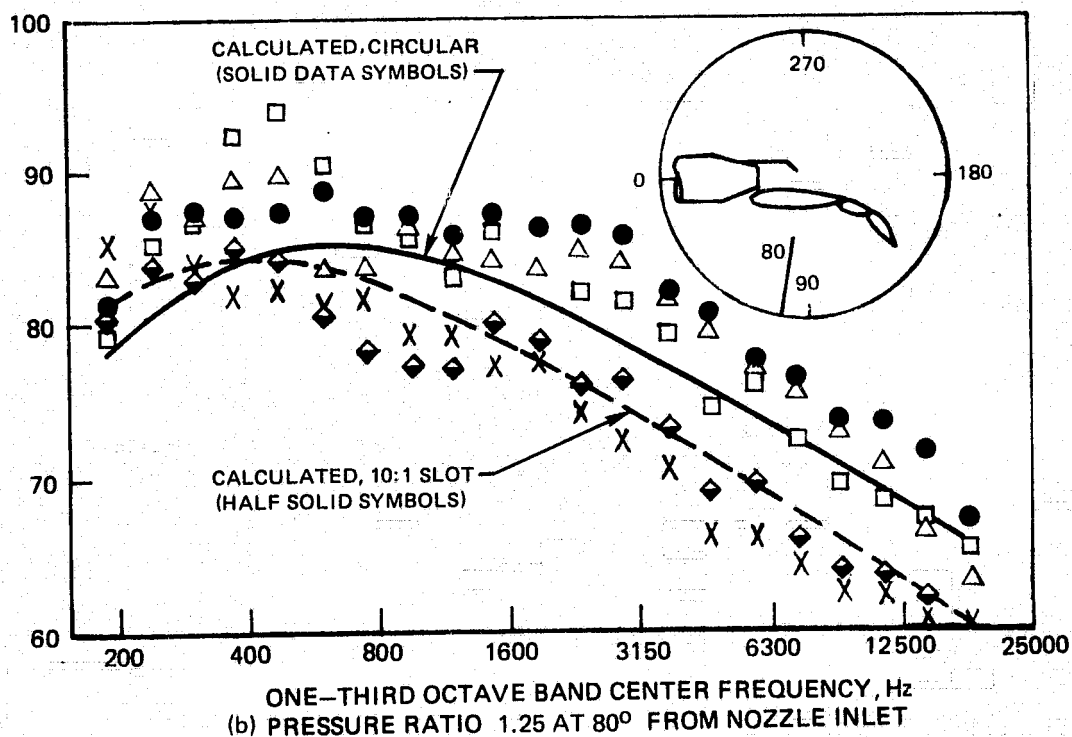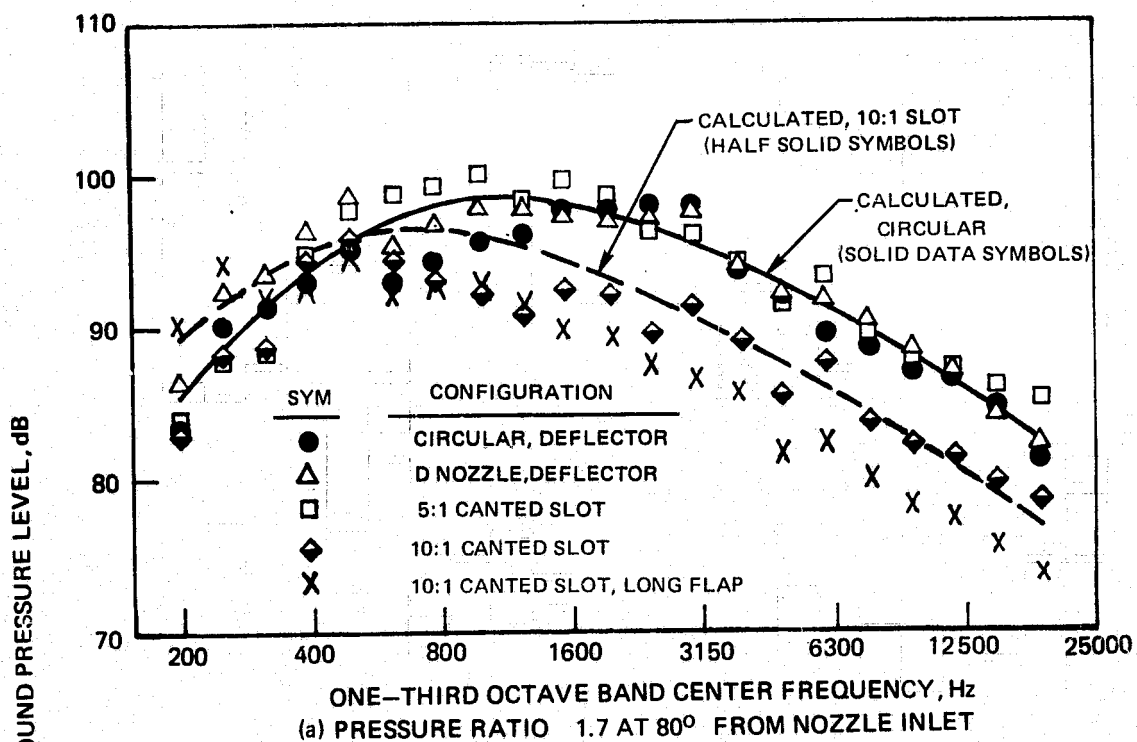
FIGURE 30. — MEASURED AND CALCULATED SPECTRA FOR USB AT 10°–20°
DEFLECTION WITH FIVE NOZZLE SHAPES

98

ONE-THIRD-OCTAVE SOUND PRESSURE LEVEL, dB

CALCULATED, CIRCULAR
(SOLID DATA SYMBOL)

CALCULATED, 10:1 SLOT
(HALF SOLID SYMBOLS)

SYM	CONFIGURATION
●	CIRCULAR, DEFLECTOR
△	D NOZZLE DEFLECTOR
□	5:1 CANTED SLOT
◇	10:1 CANTED SLOT
X	10:1 CANTED SLOT, LONG FLAP

ONE-THIRD OCTAVE BAND CENTER FREQUENCY, Hz

(c) PRESSURE RATIO 1.7 AT 120° FROM NOZZLE INLET

CALCULATED, CIRCULAR
(SOLID DATA SYMBOLS)

CALCULATED, 10:1 SLOT
(HALF-SOLID SYMBOLS)

ONE-THIRD OCTAVE BAND CENTER FREQUENCY, Hz

(d) PRESSURE RATIO 1.25 AT 120° FROM NOZZLE INLET

FIGURE 30. – CONCLUDED

FIGURE 31. — MEASURED AND CALCULATED SPECTRA FOR USB AT 30°–60° DEFLECTION WITH CIRCULAR NOZZLE AND DEFLECTOR

100

(a) 20° FROM NOZZLE INLET

(b) 80° FROM NOZZLE INLET
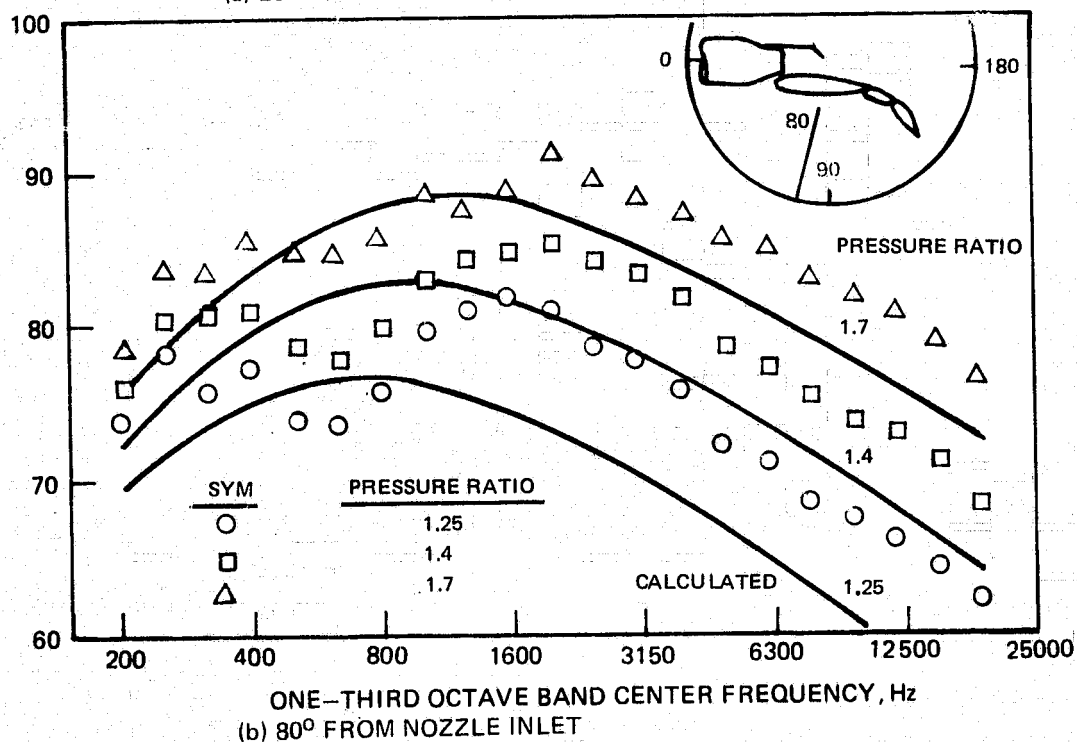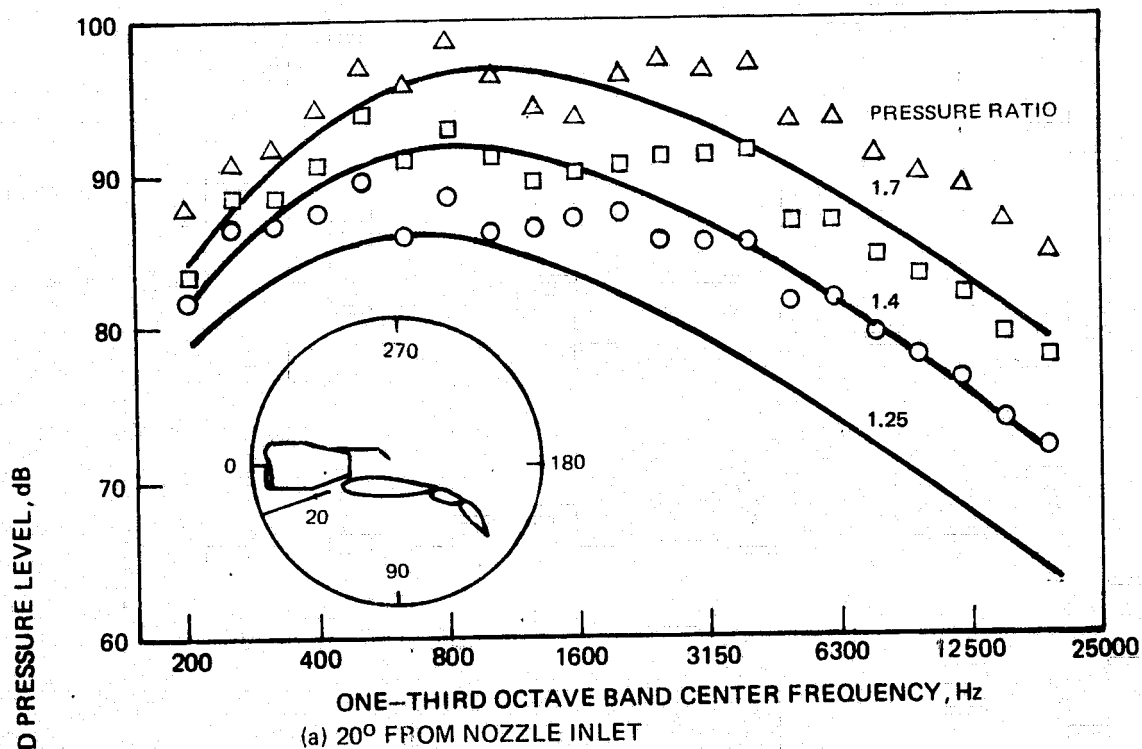
FIGURE 32. — MEASURED AND CALCULATED SPECTRA FOR USB AT 30°–60° DEFLECTION WITH D NOZZLE AND DEFLECTOR
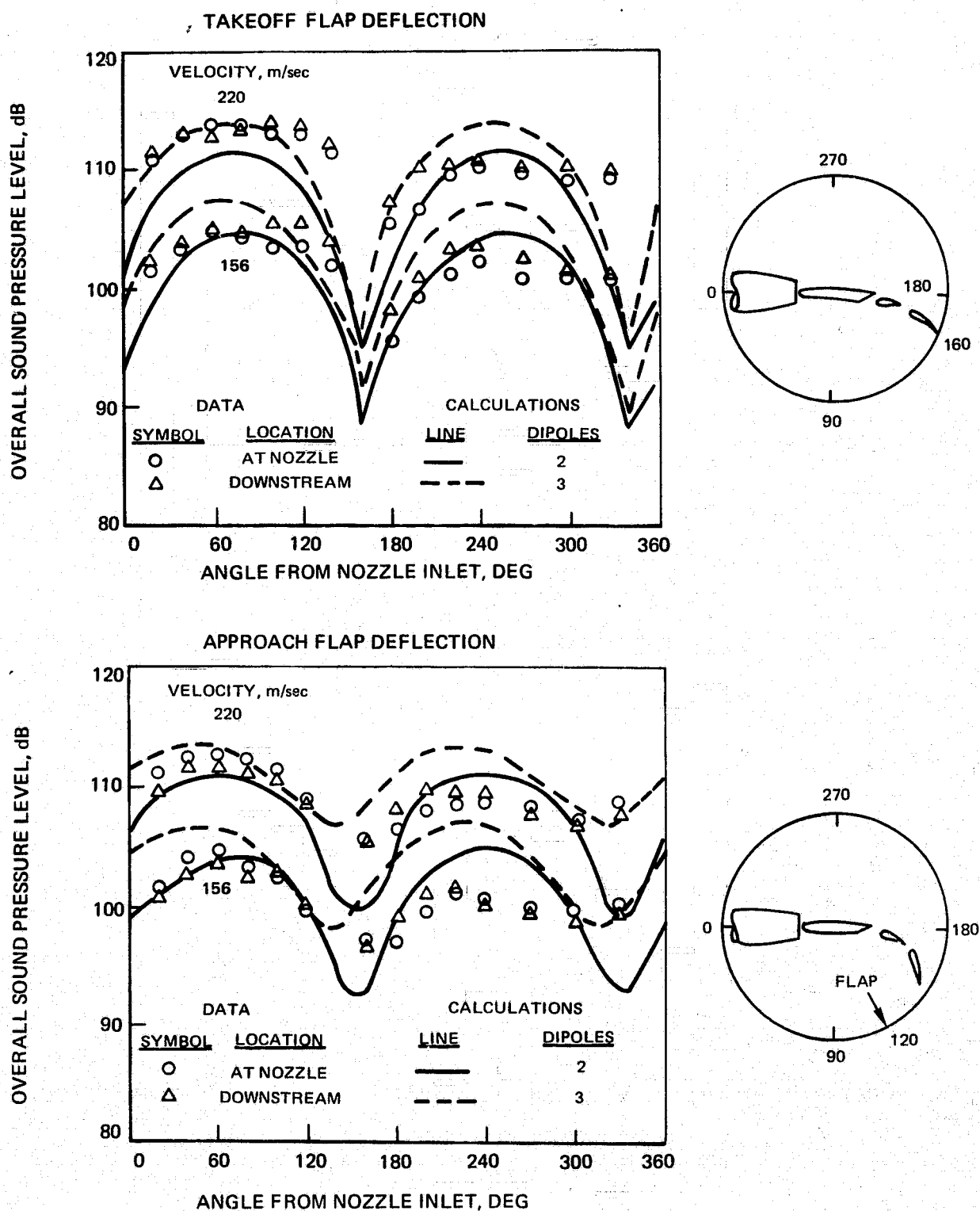
FIGURE 33. – COMPARISON OF CALCULATED AND MEASURED OASPL DIRECTIVITY FOR ENGINE–IN–FRONT–OF–WING MODEL

SYMBOL   CONFIGURATION   LINE   DESCRIPTION

O   WING AT NOZZLE   ———   CALCULATED, 2 DIPOLES

△   WING DOWNSTREAM   — — —   MEASURED, NOZZLE ALONE
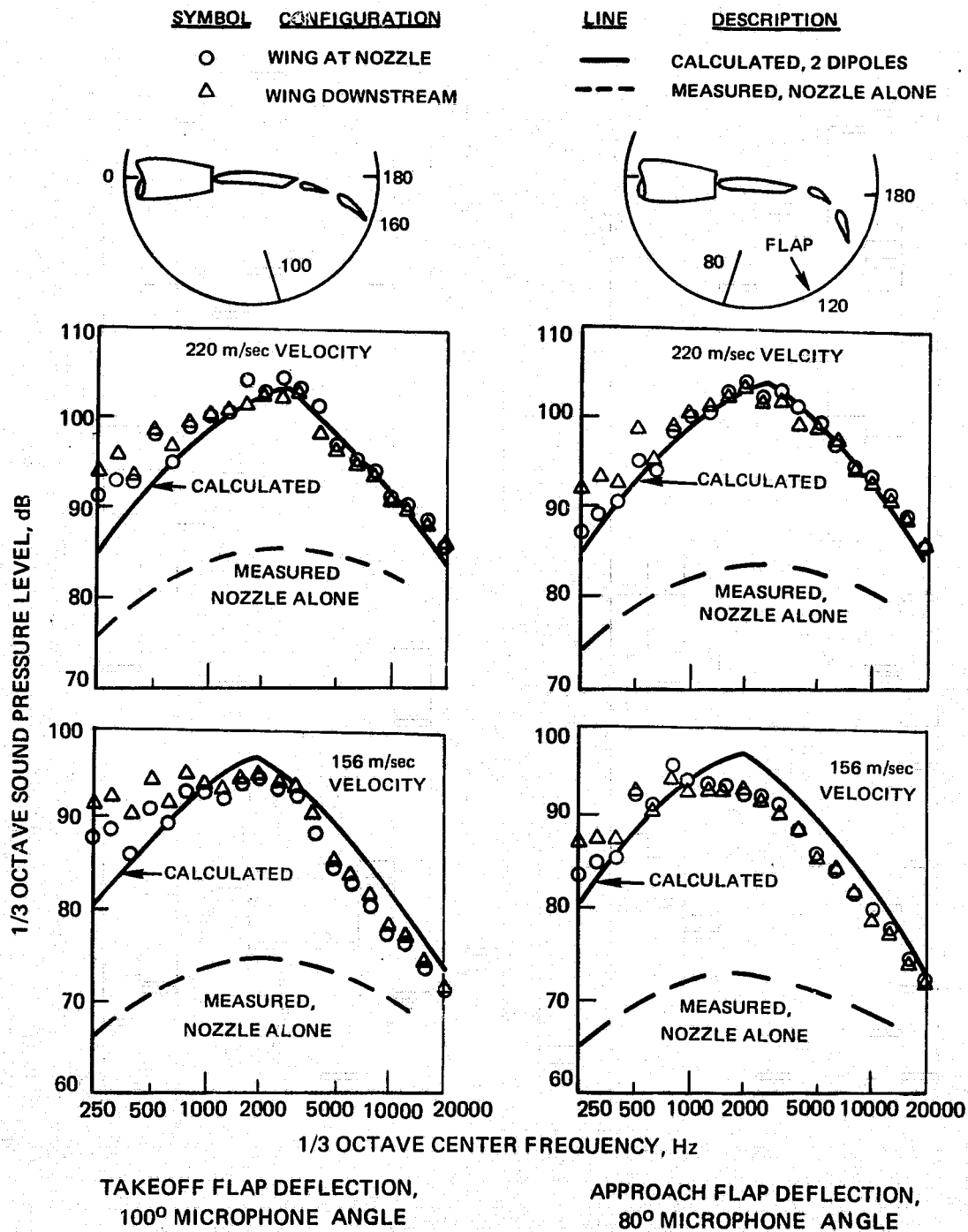
FIGURE 34. — COMPARISON OF CALCULATED AND MEASURED SPECTRA

FOR ENGINE—IN—FRONT—OF— WING MODEL

MEAN SQUARE LIFT FORCE

$$\overline{F^2}(\omega) \sim (\rho U^2 bc)^2 \; \overline{C_L{}^2} \; (\omega) \; \overline{\frac{v^2}{U^2}} \; (\omega)$$

AERODYNAMIC
TRANSFER
FUNCTION, $\overline{C_L{}^2}$

ω^{-2}

STROUHAL NUMBER, fc/U

TURBULENCE
INPUT
SPECTRUM, $\overline{\dfrac{v^2}{U^2}}$

ω^{-2}

STROUHAL NUMBER, fc/U
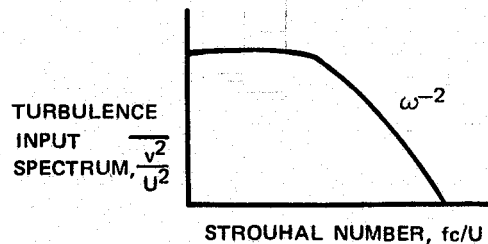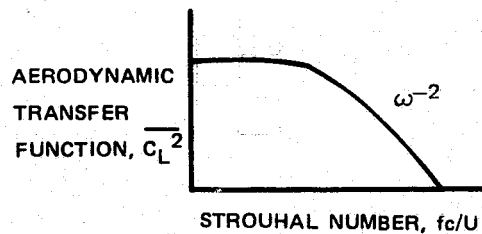
ACOUSTIC INTENSITY

$$I(\omega) \sim \left(\frac{\cos\theta}{r}\right)^2 \left[\frac{\omega^2}{1 + (\omega\,\overline{c}/a)^2}\right] \; \overline{F^2}(\omega)$$

ACOUSTIC
TRANSFER
FUNCTION,

$$\frac{\omega^2}{1 + (\omega\,\overline{c}/a)^2}$$

LOW SUBSONIC U/a

ω^2

ω^0

HIGH SUBSONIC U/a

STROUHAL NUMBER, fc/U
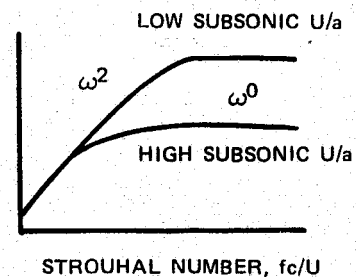
SOUND SPECTRUM IS
PRODUCT OF THREE
FREQUENCY—DEPENDENT
EFFECTS

ACOUSTIC
INTENSITY,

$$I \left(\frac{r}{\cos\theta}\right)^2$$

ω^2

LOW
SUBSONIC

HIGH
SUBSONIC

ω^{-4}

STROUHAL NUMBER, fc/U
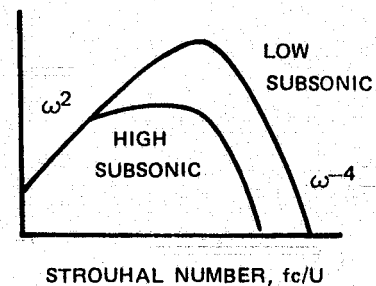
FIGURE 35 – VARIATION OF FREQUENCY–DEPENDENT COMPONENTS OF ACOUSTIC INTENSITY CAUSED BY INCIDENT TURBULENCE

N07—68—4

104

(a.) EXPERIMENTAL CONFIGURATION

VELOCITY, m/sec = 75

CALCULATIONS   SCALE LENGTH
                      0.30 D
                      0.15 D

ONE—THIRD—OCTAVE SOUND PRESSURE LEVEL, dB

ONE—THIRD OCTAVE BAND CENTER FREQUENCY — Hz

(b.) IMPINGEMENT VELOCITIES 75, 114, AND 186 m/sec
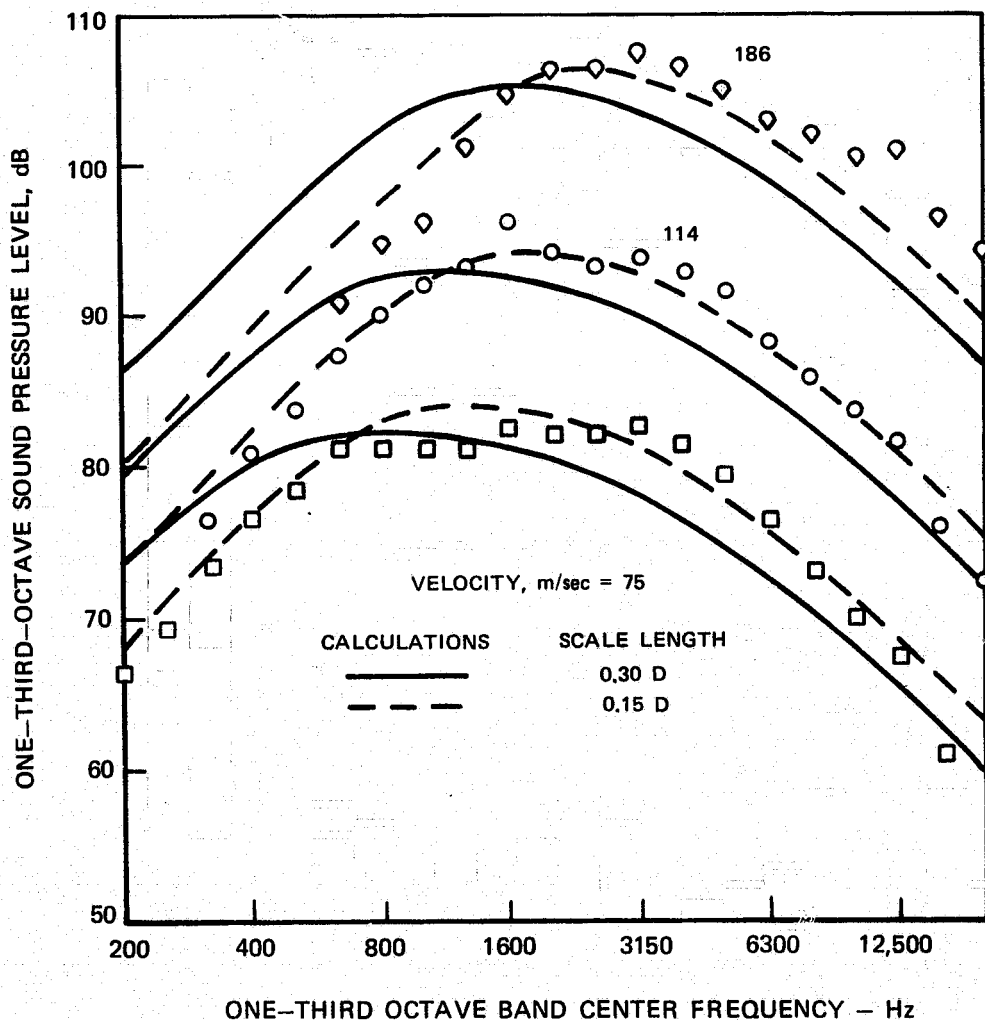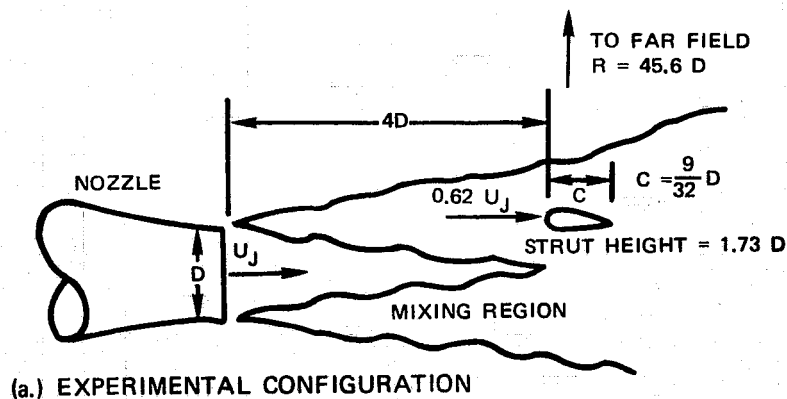
FIGURE 36 — COMPARISON OF MEASURED AND CALCULATED SPECTRA FOR NOISE
RADIATION AT 90° DIRECTION FROM A STRUT IN AN EXHAUST JET
MIXING REGION
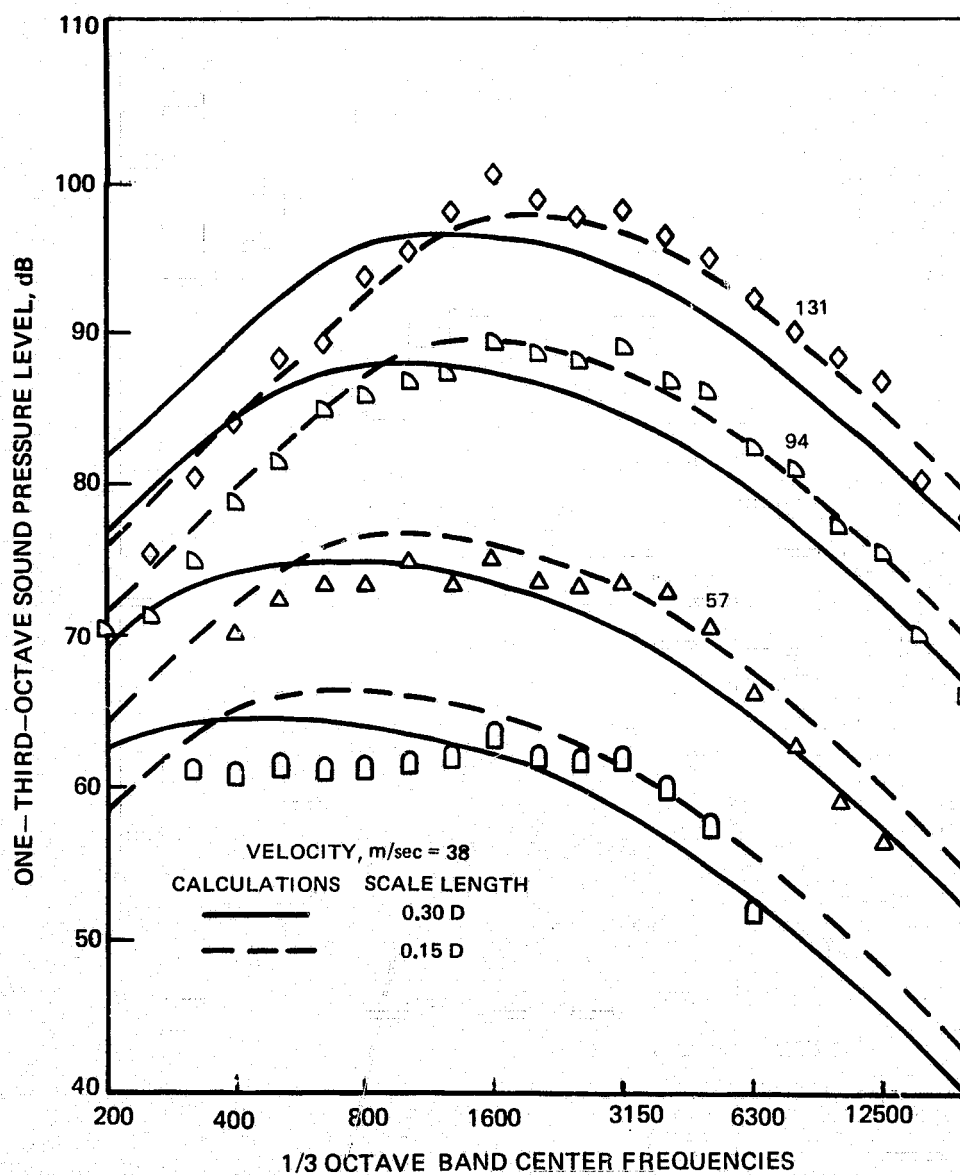
FIGURE 36 . – CONCLUDED (c) VELOCITIES 38, 57, 94, AND 131 m/sec

R02–31–2

106
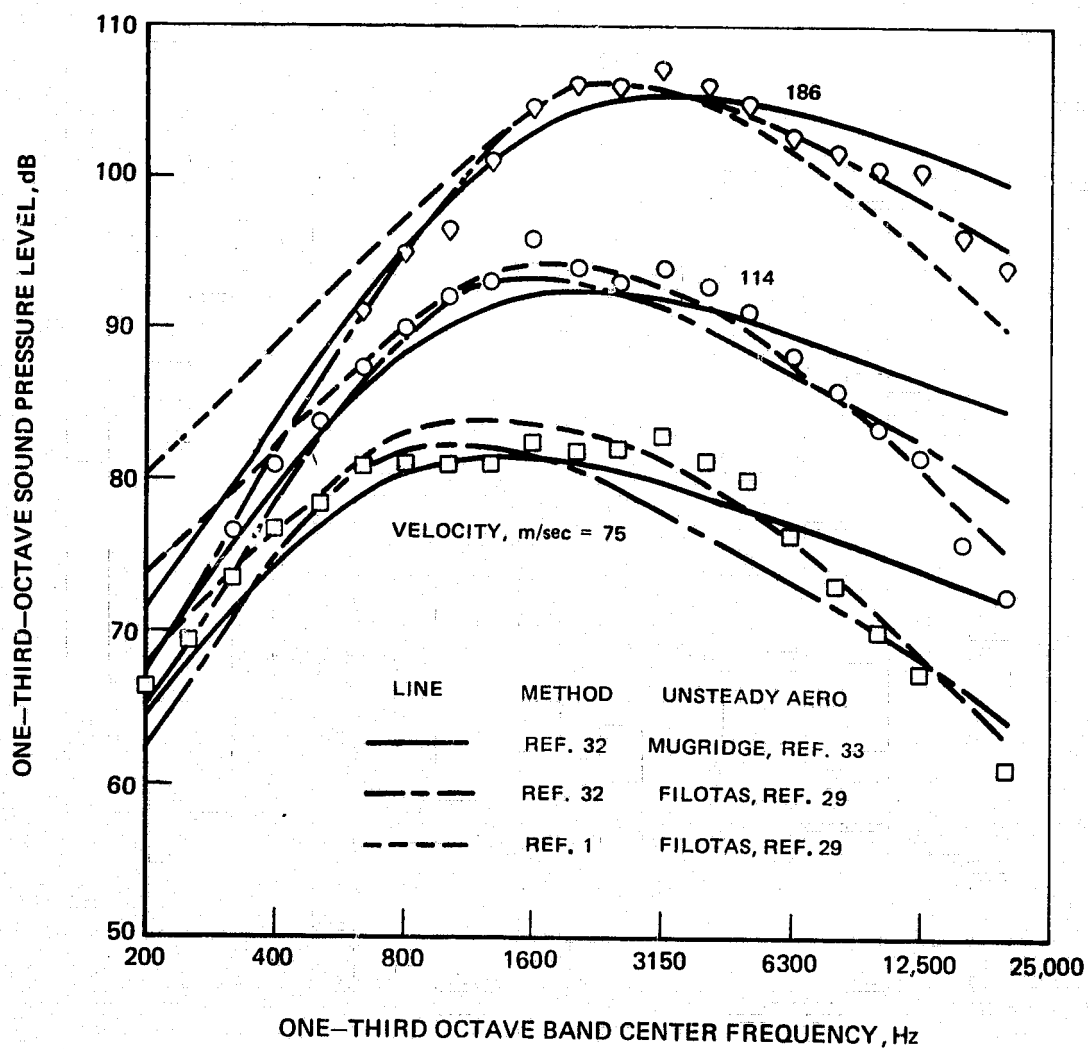
FIGURE 37 — COMPARISON OF MEASURED SPECTRA AT 90° DIRECTION FROM A STRUT IN AN EXHAUST JET MIXING REGION WITH SPECTRA CALCULATED BY DIFFERENT METHODS
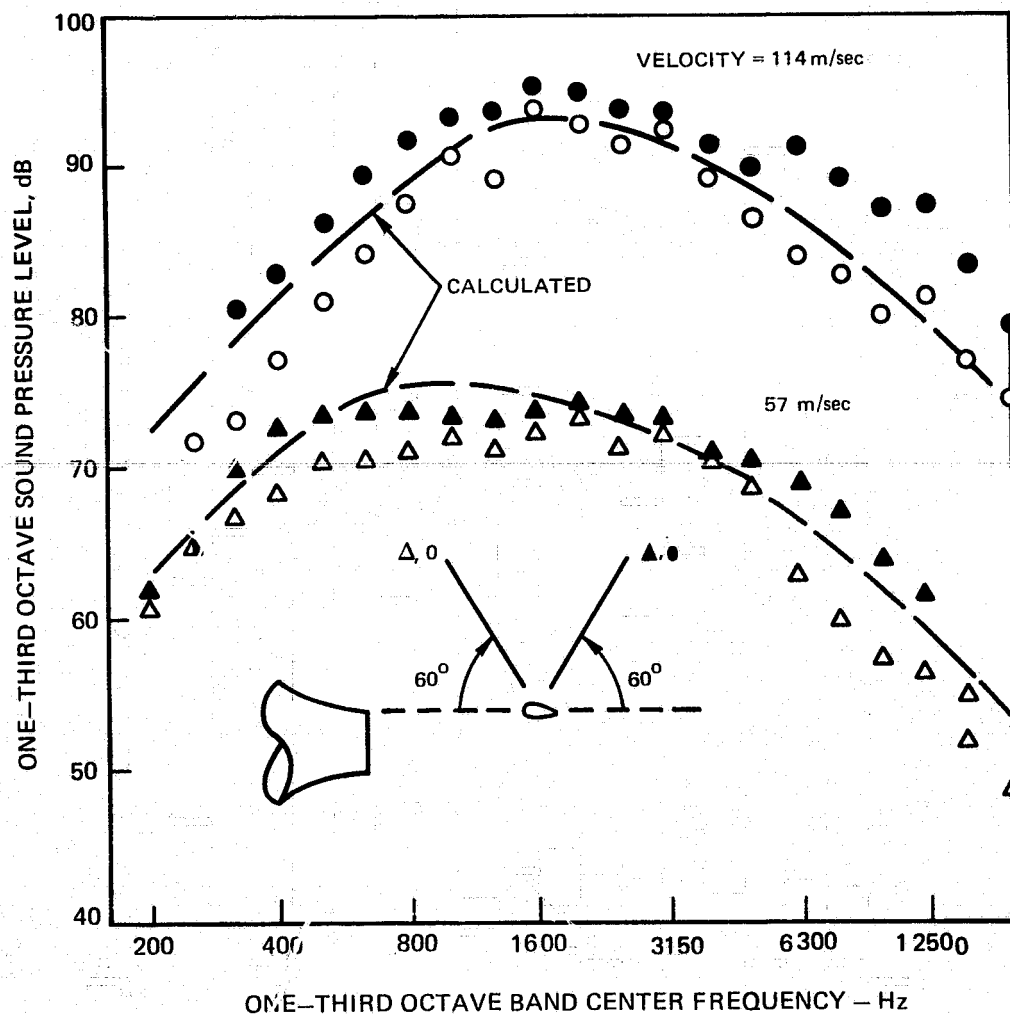
FIGURE 38 – EFFECT OF MEASUREMENT DIRECTION ON SPECTRUM SHAPE FOR
NOISE RADIATION FROM A STRUT IN AN EXHAUST JET MIXING
REGION

R02–72–7
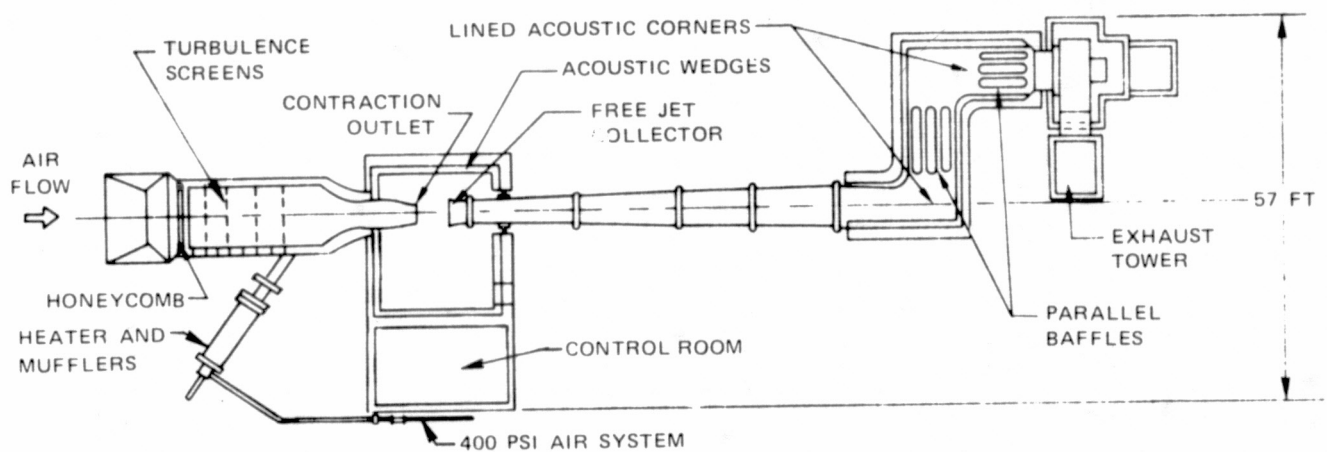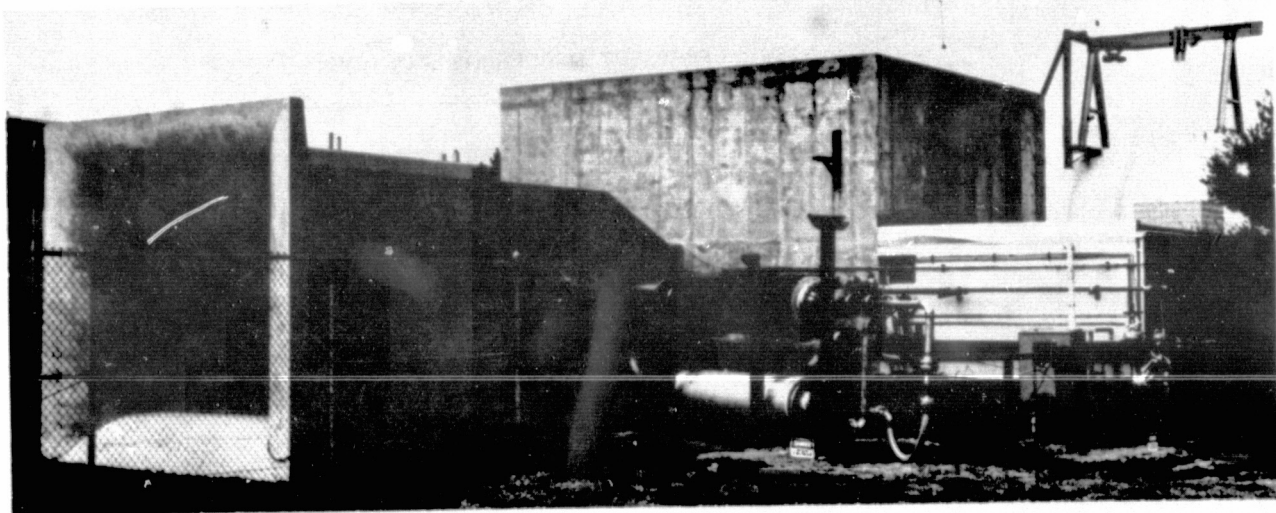
TOP VIEW
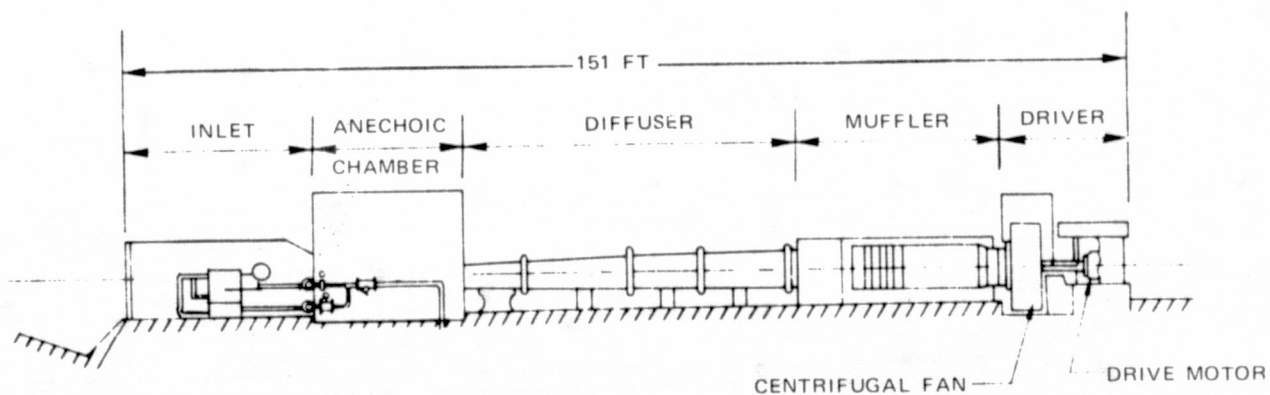
SIDE VIEW

FIGURE 39. — UTRC ACOUSTIC RESEARCH TUNNEL

109

DASHES REPRESENT MICROPHONE LOCATIONS

2.54

5.08

22.86

45.72

15.88

5.08

26.67

0.48

53.34

0.635 CM (1/4 IN.) MICROPHONE INSTALLATION (FULL SCALE)

MICROPHONE

PREAMPLIFIER

RIGHT–ANGLE FLEXIBLE ADAPTER

CLAMP

2.54 CM
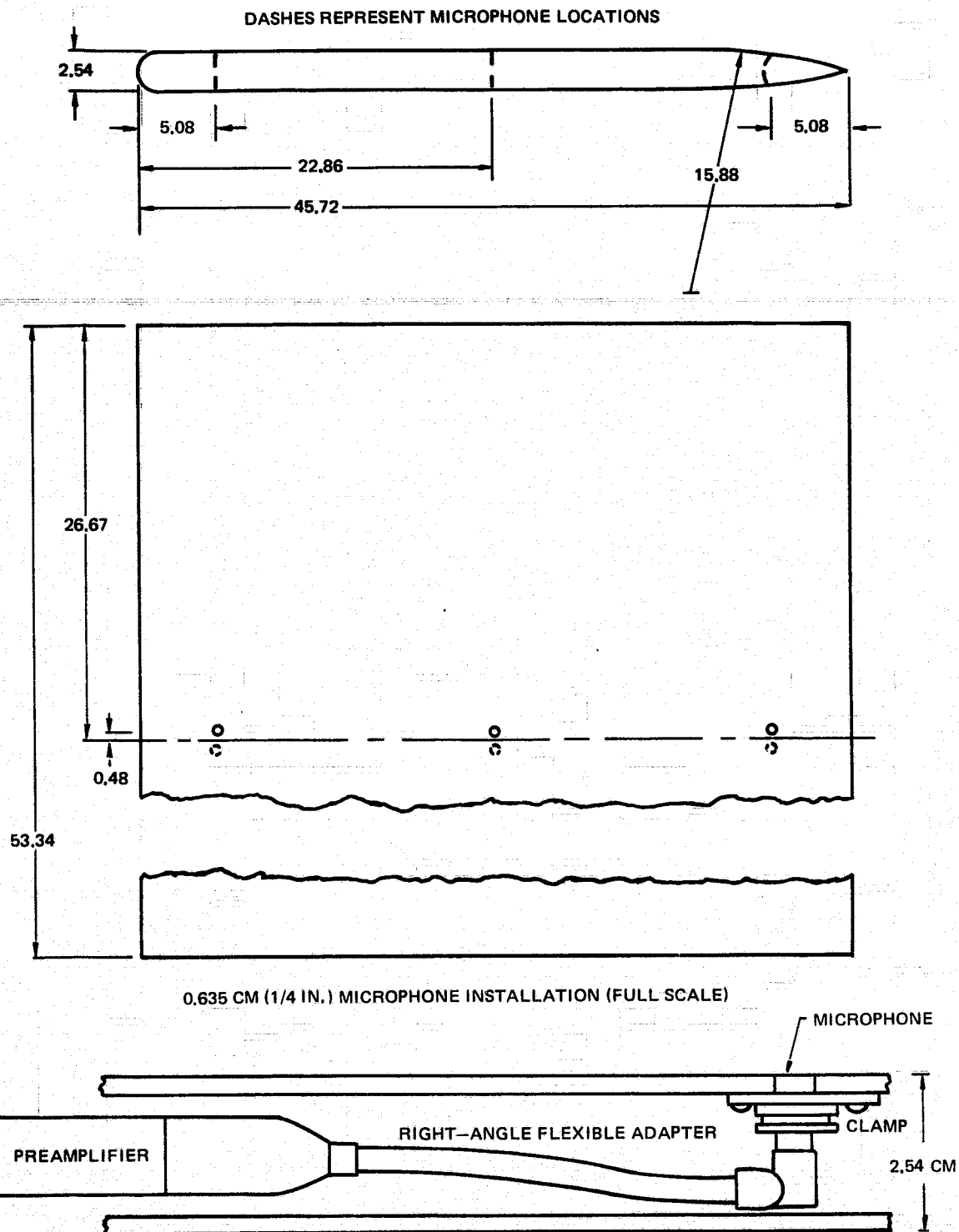
FIGURE 40 — FLAT PLATE AIRFOIL. ONE–QUARTER SCALE EXCEPT WHERE NOTED. ALL DIMENSIONS IN CENTIMETERS
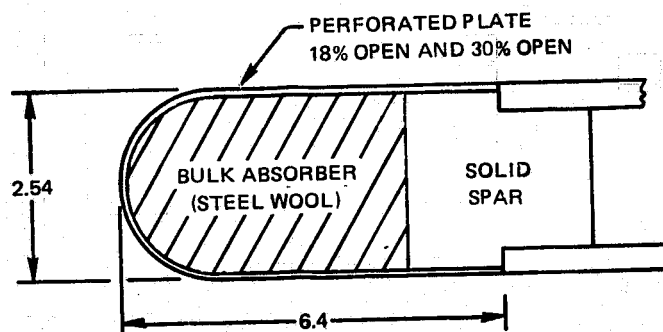
PERFORATED LEADING EDGES
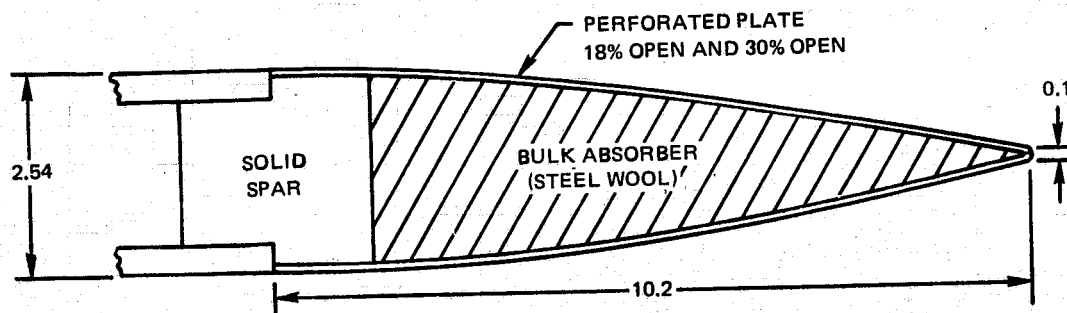
PERFORATED TRAILING EDGES
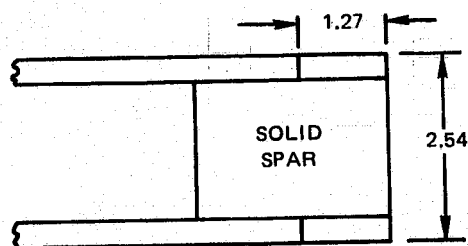
BLUNT TRAILING EDGE
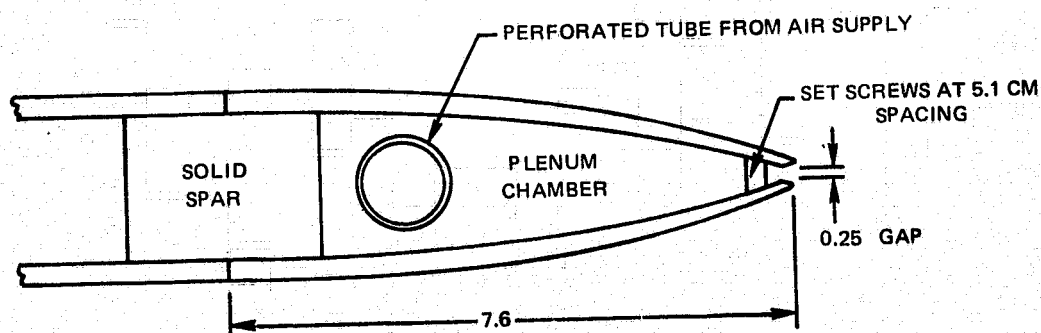
TRAILING EDGE BLOWING

FIGURE 41 — MODIFICATIONS TO LEADING AND TRAILING EDGES OF FLAT PLATE AIRFOIL. FULL SCALE, ALL DIMENSIONS IN CENTIMETERS.

RO3–152–1

111
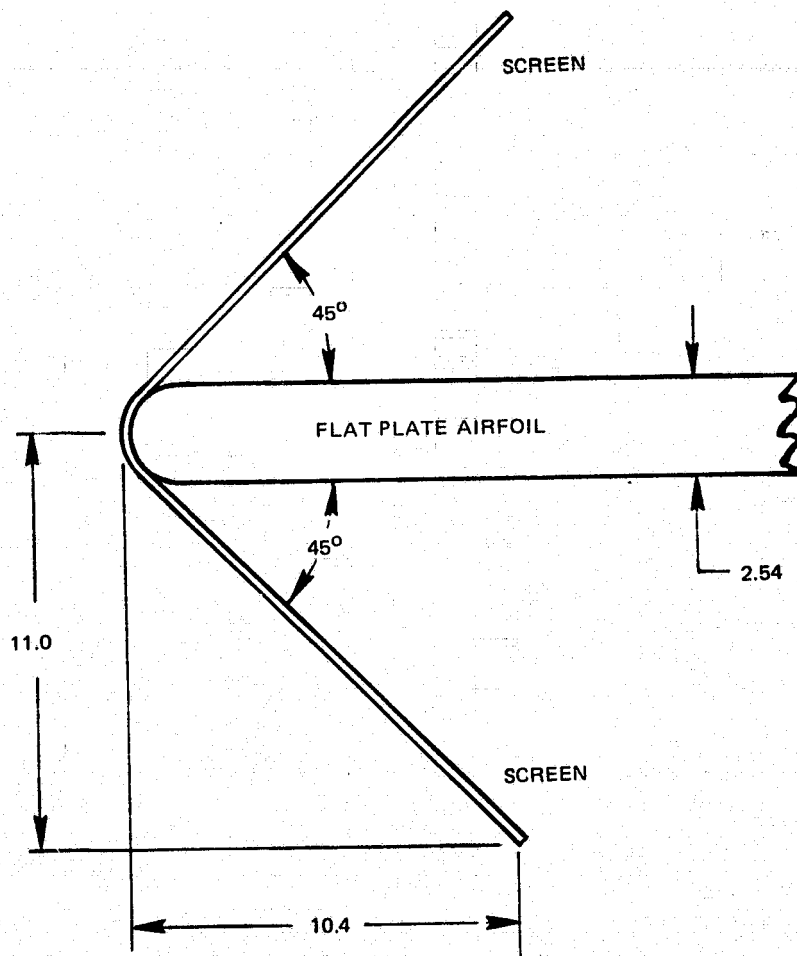
**FIGURE 42 – LEADING EDGE SCREENS WITH FLAT PLATE AIRFOIL.
HALF SCALE, ALL DIMENSIONS IN CENTIMETERS**
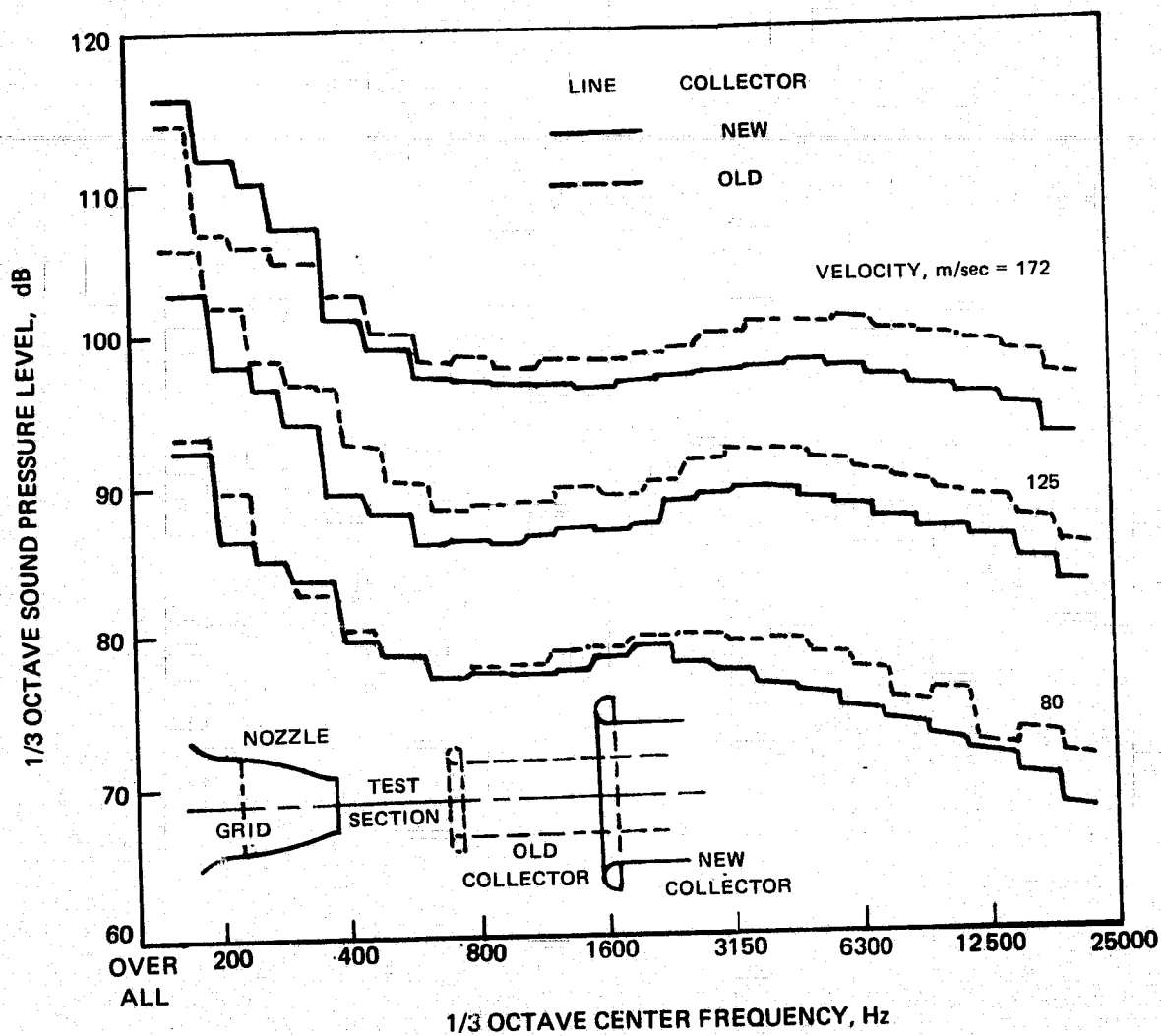
FIGURE 43 – BACKGROUND NOISE 2.13 m DIRECTLY ABOVE AIRFOIL POSITION
WITH NEW AND OLD COLLECTOR (a) MEDIUM GRID

R08–12–4

113
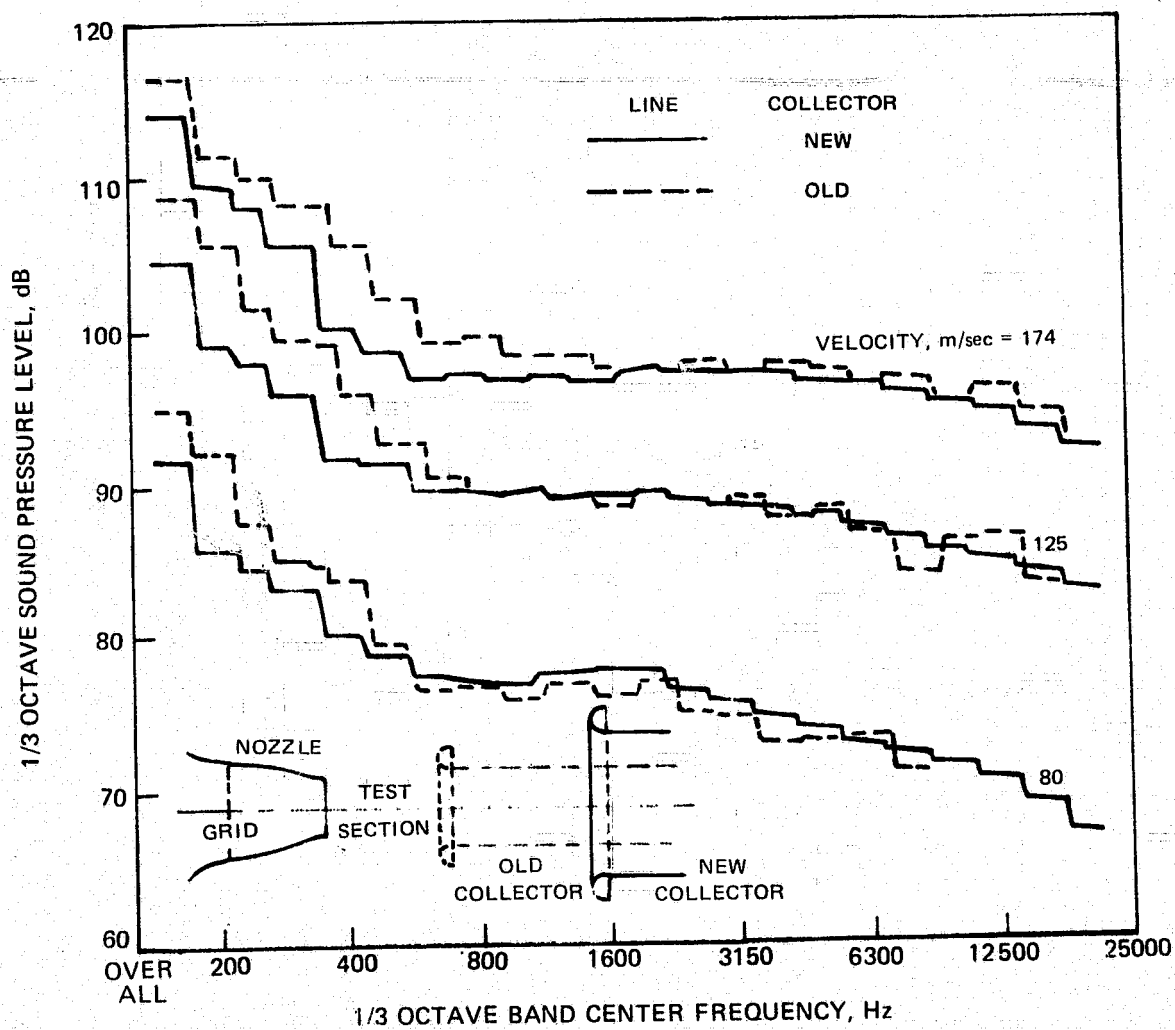
FIGURE 43 — CONCLUDED (b) LARGE GRID
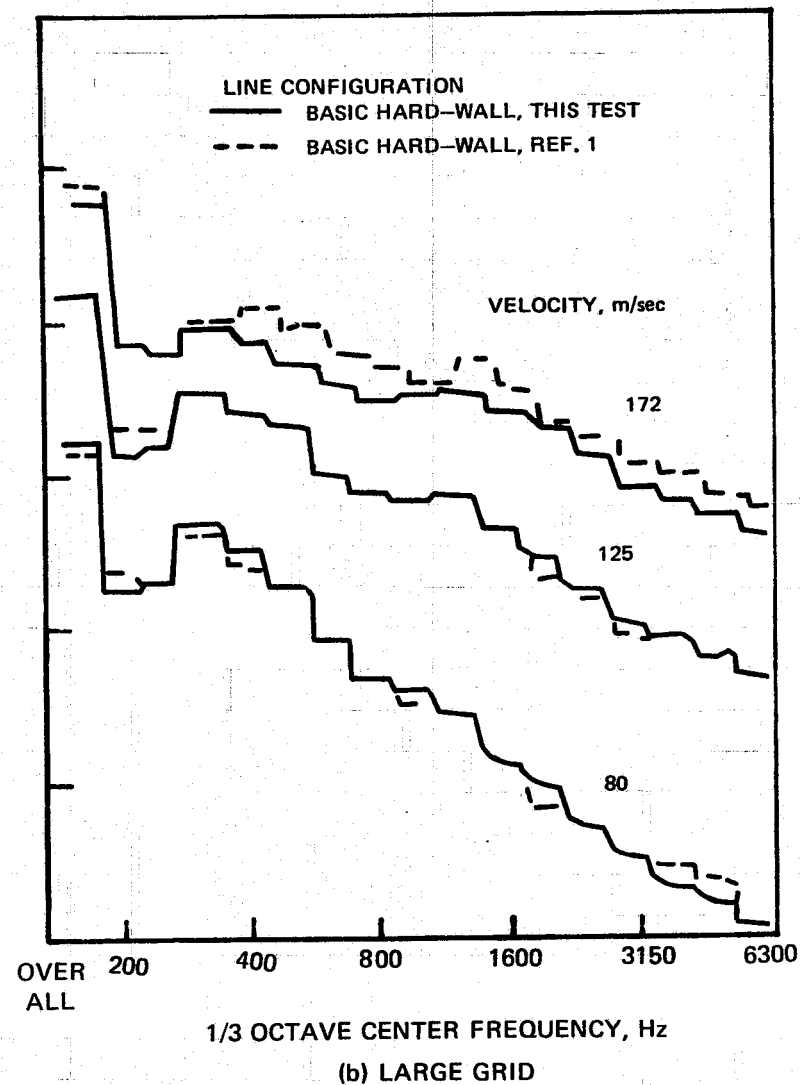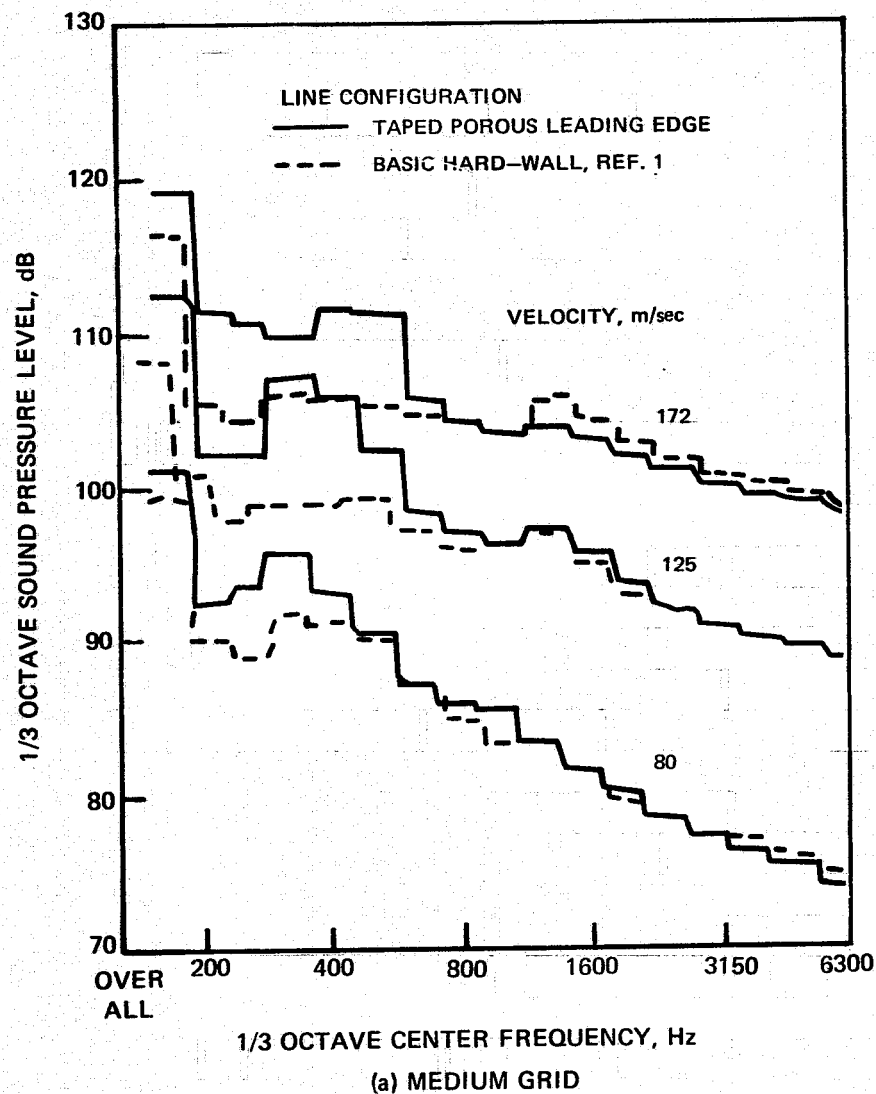
FIGURE 44– EFFECT OF HARD–WALL MODEL CONFIGURATION ON SOUND SPECTRUM
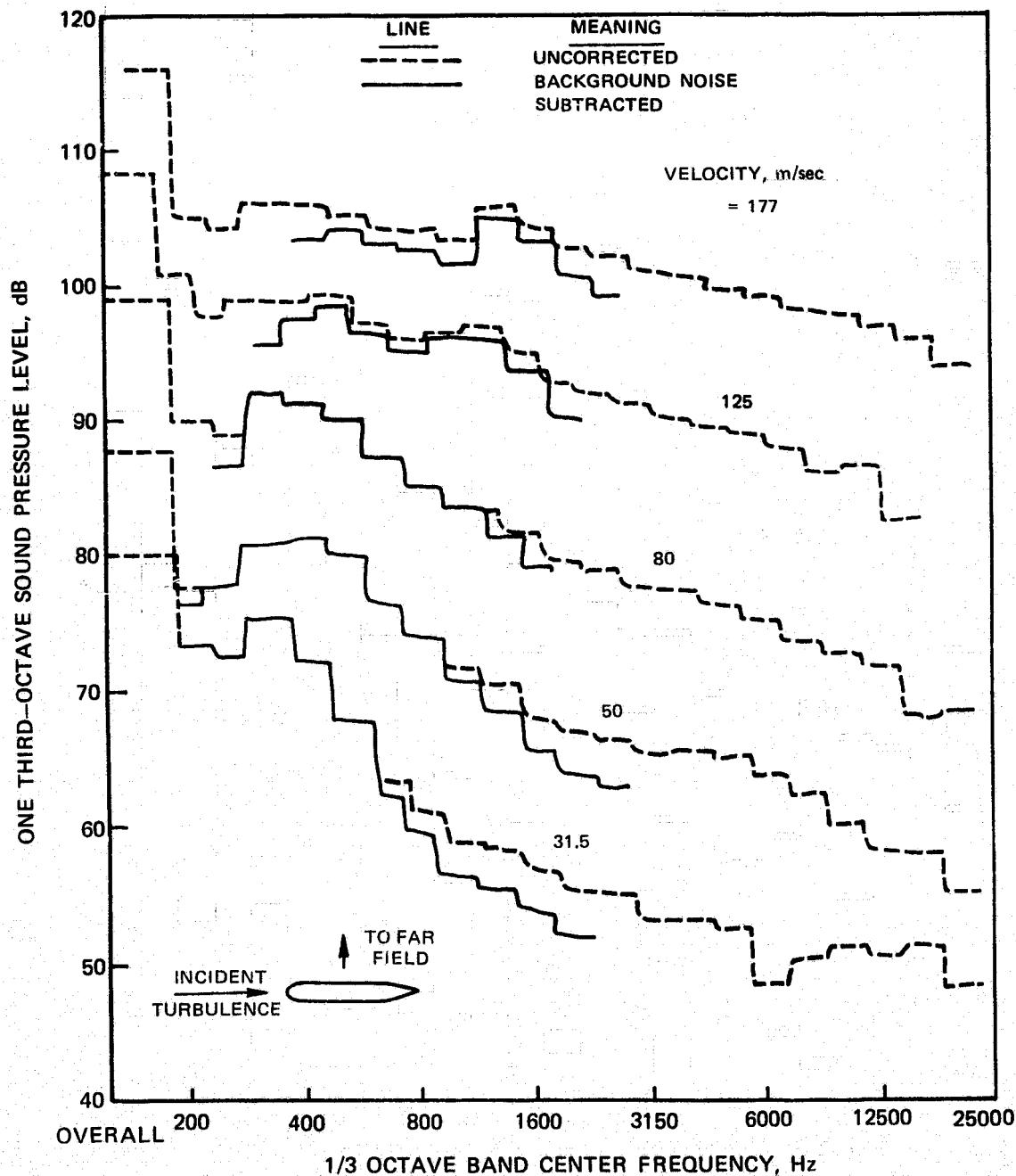
FIGURE 45. – FAR-FIELD SPECTRA FOR AIRFOIL WITH INCIDENT
TURBULENCE, UNCORRECTED AND CORRECTED FOR
TUNNEL BACKGROUND NOISE, 90° FROM DOWNSTREAM.
(a) MEDIUM GRID
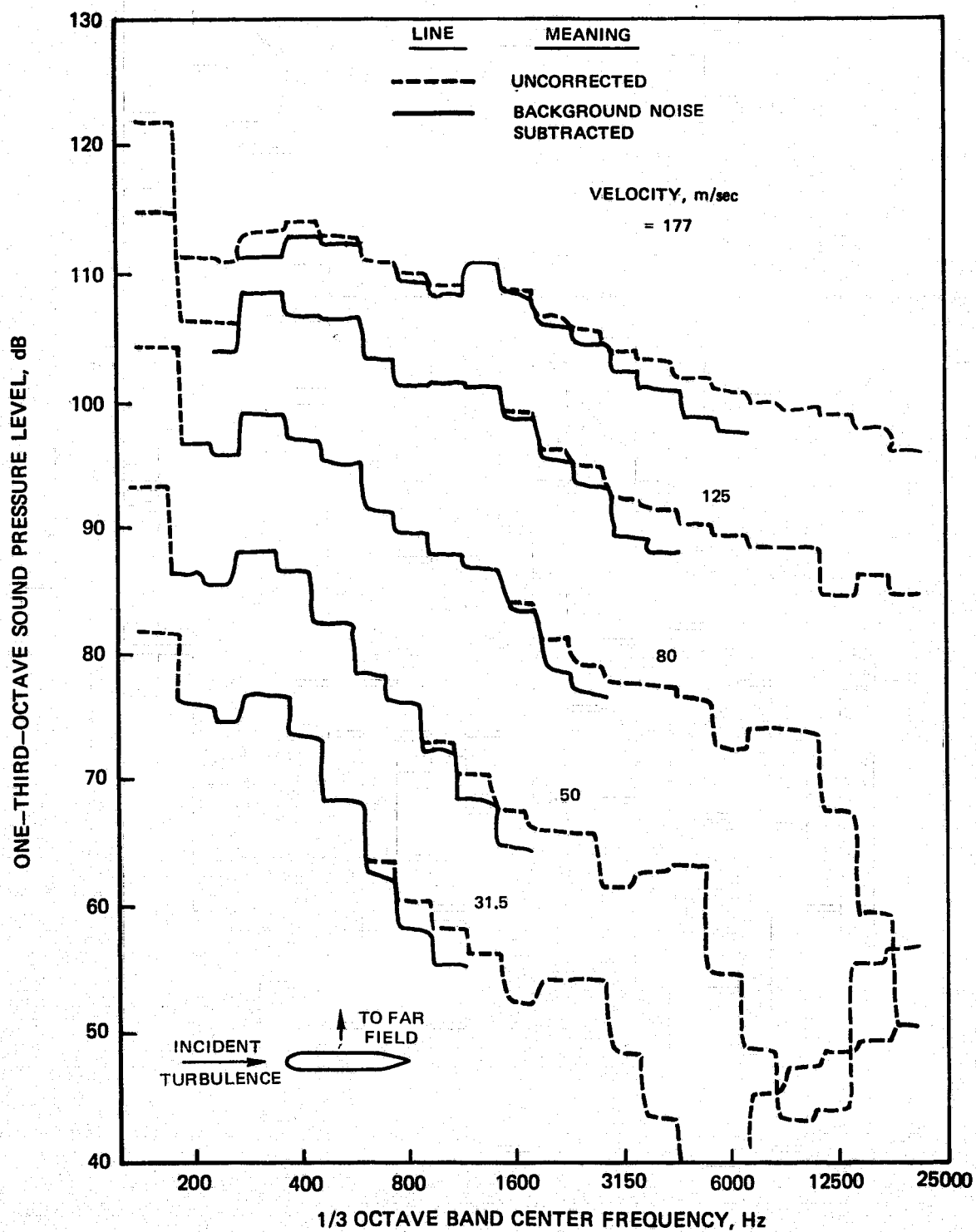
FIGURE 45.— CONCLUDED. (b) LARGE GRID
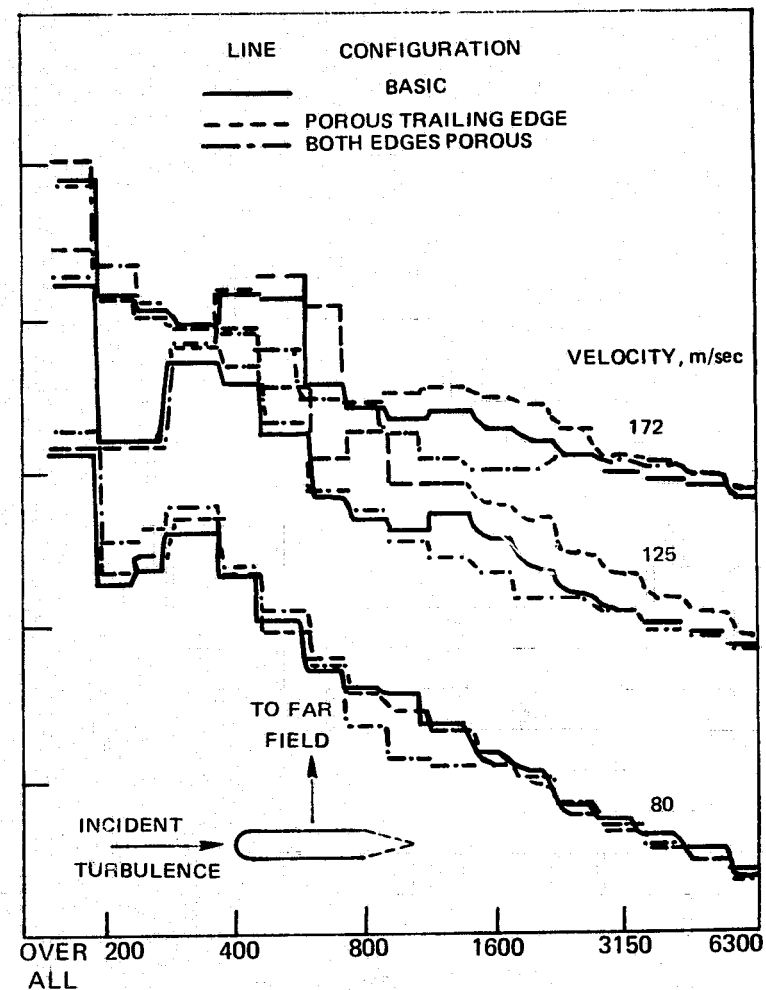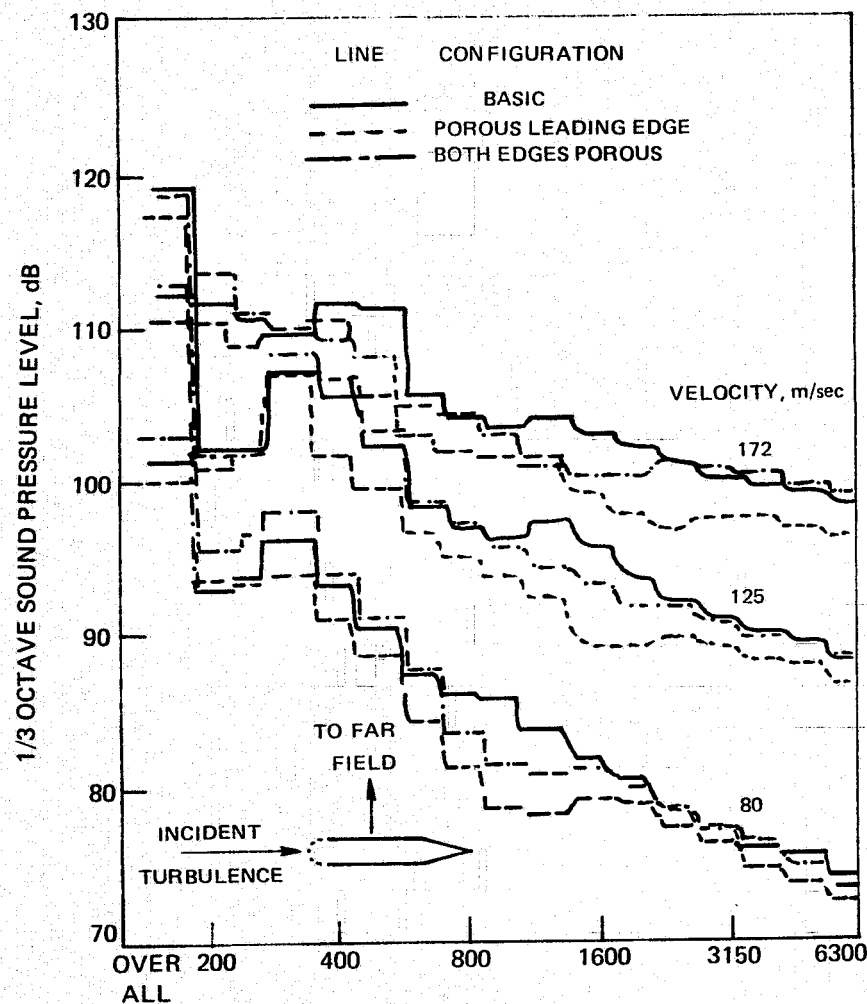
FIGURE 46 — EFFECT OF 18% POROSITY LEADING AND TRAILING EDGES ON SOUND CAUSED BY INCIDENCE FLUCTUATION (a) MEDIUM GRID
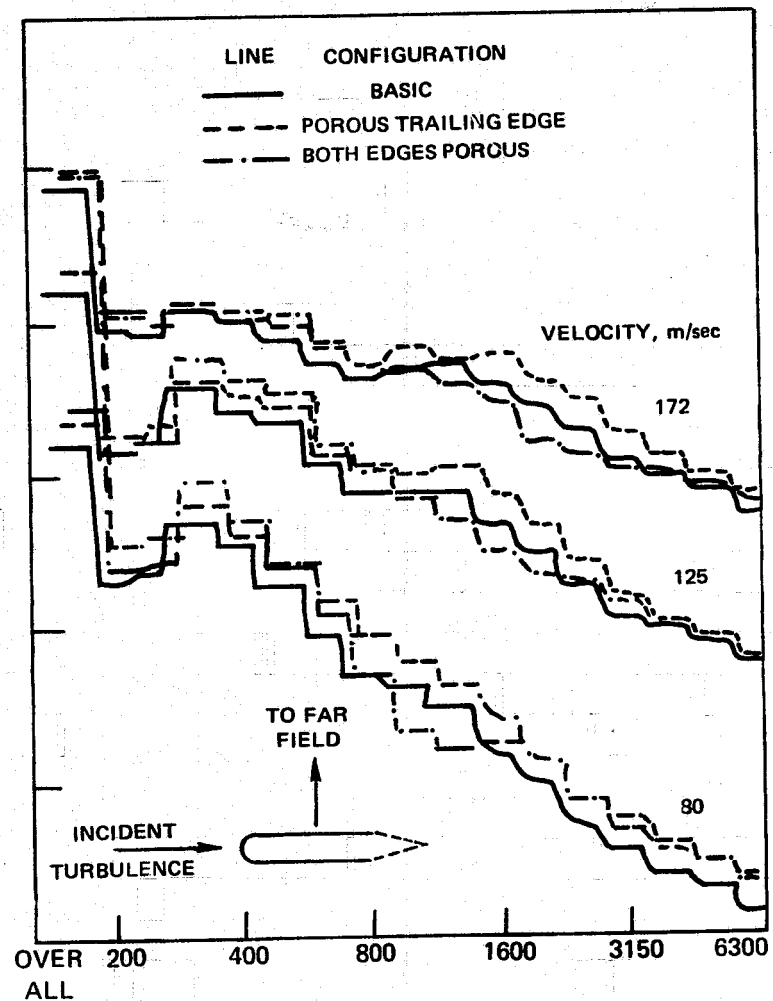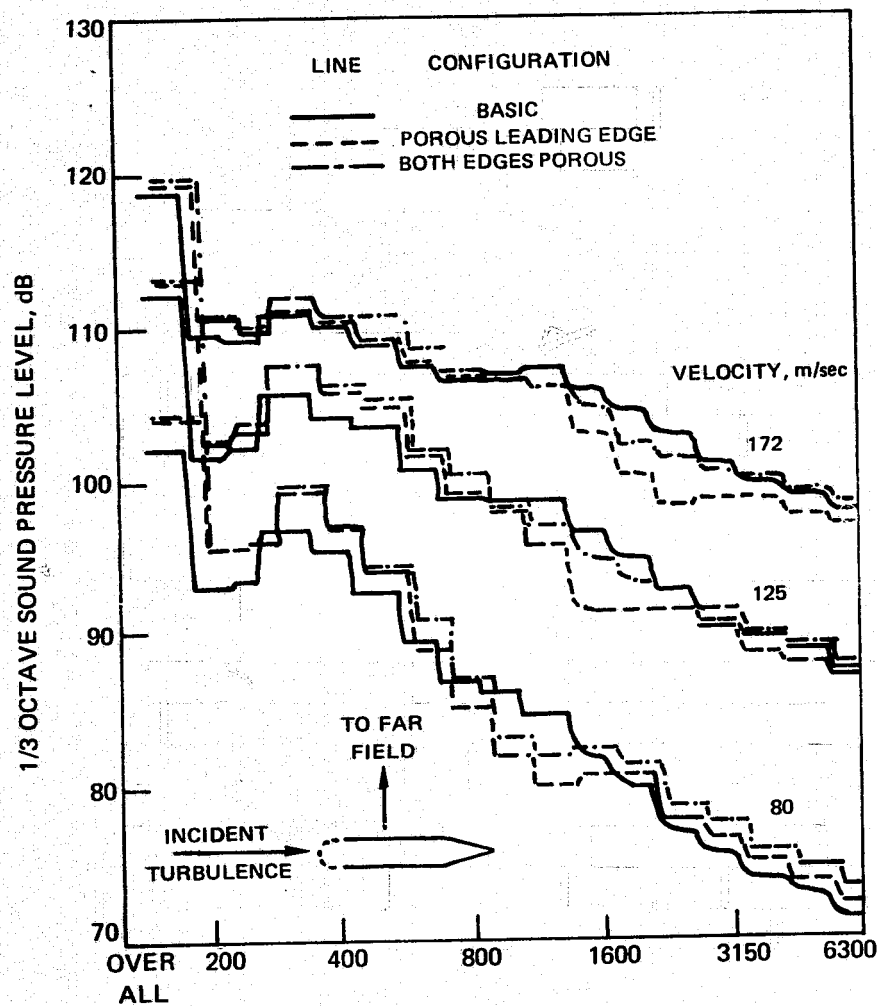
FIGURE 46 – CONCLUDED (b) LARGE GRID
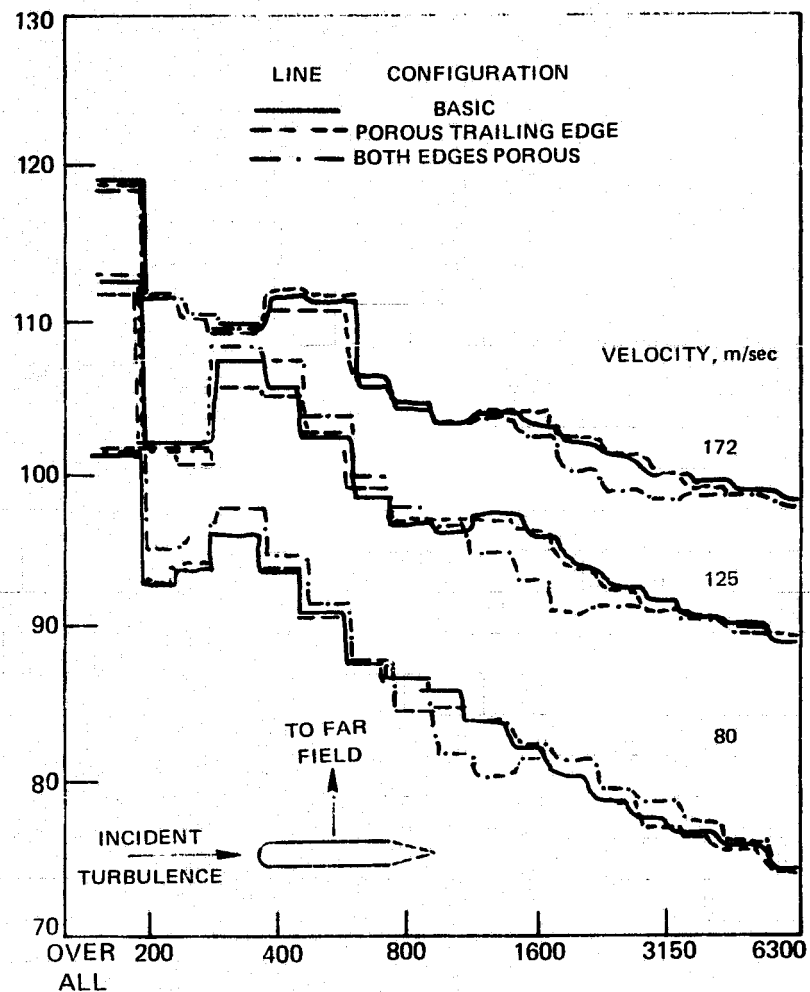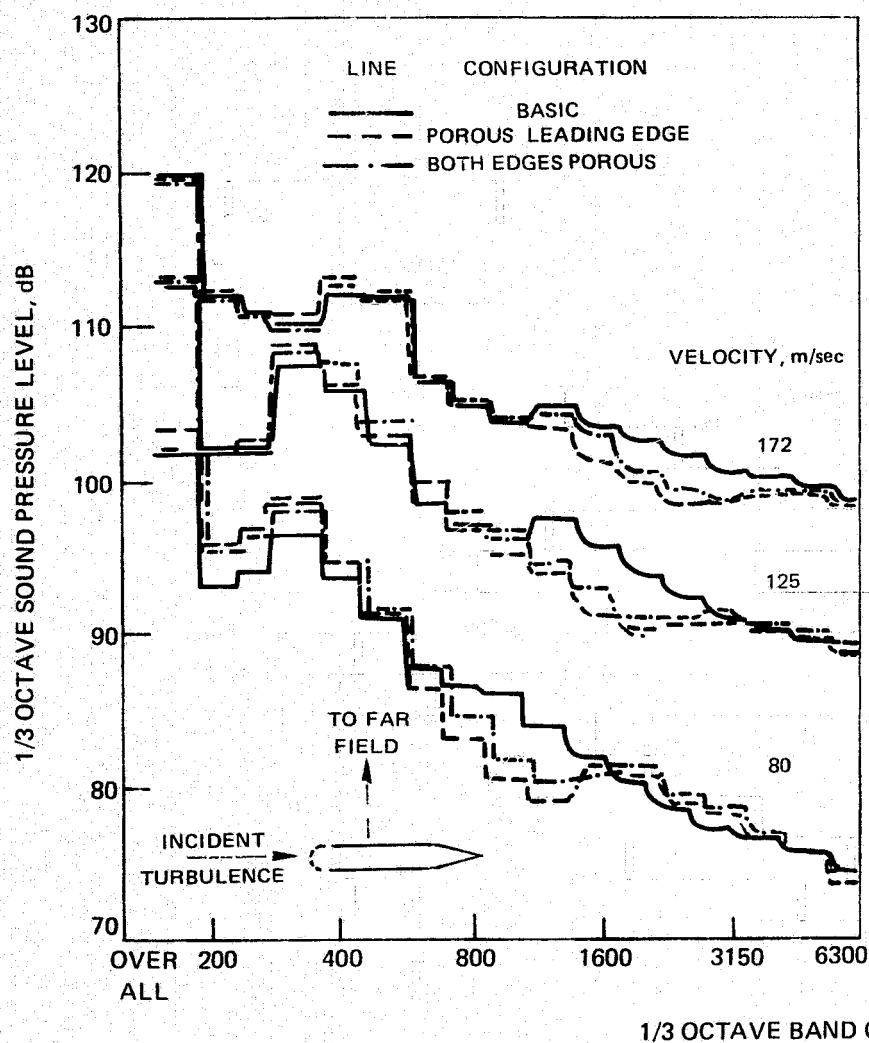
FIGURE 47 — EFFECT OF 30% POROSITY LEADING AND TRAILING EDGES ON SOUND CAUSED BY INCIDENCE FLUCTUATION. (a) MEDIUM GRID
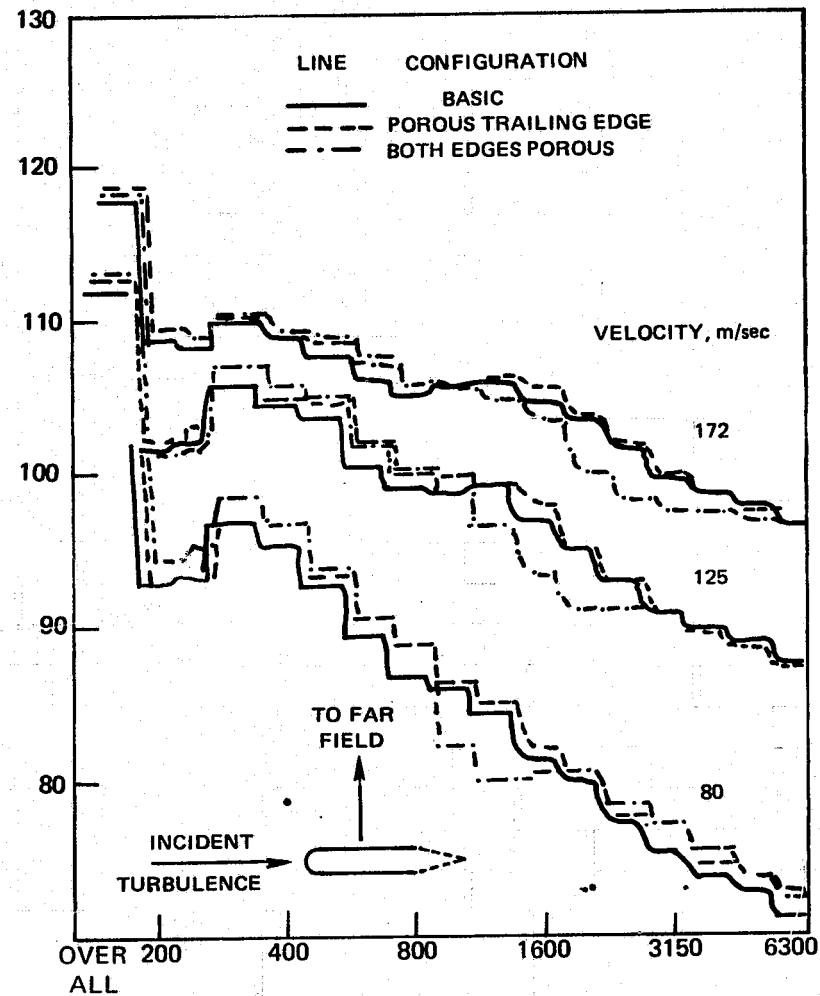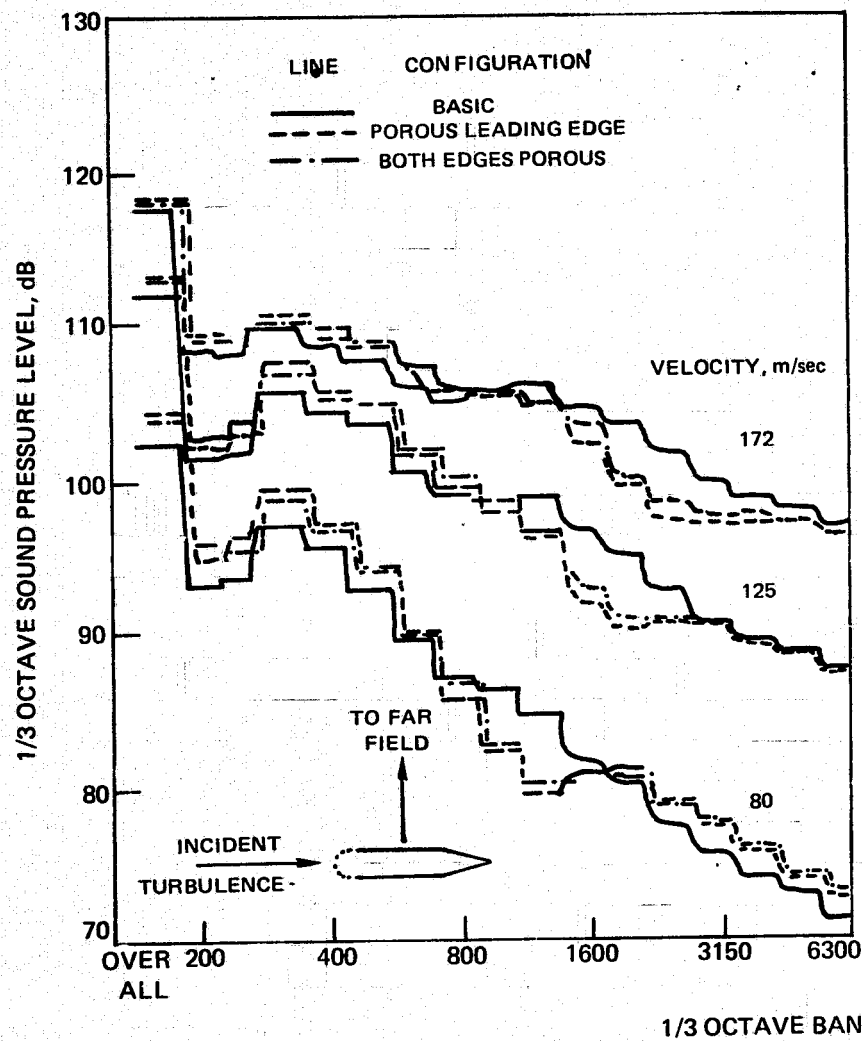
FIGURE 47 — CONCLUDED (b) LARGE GRID
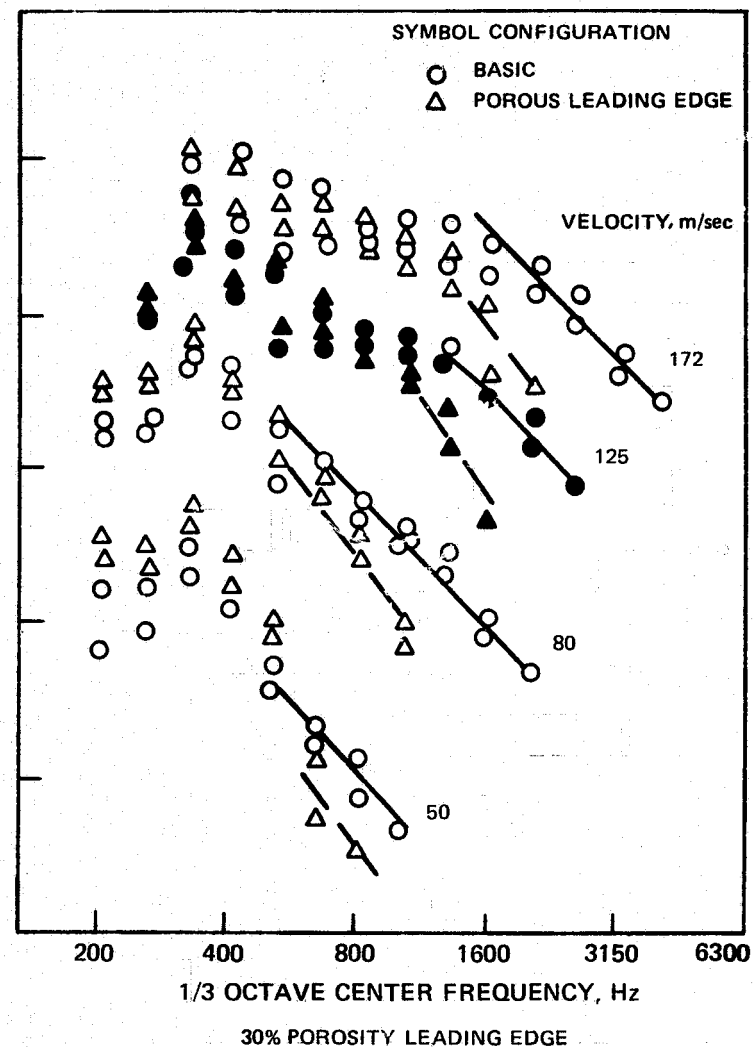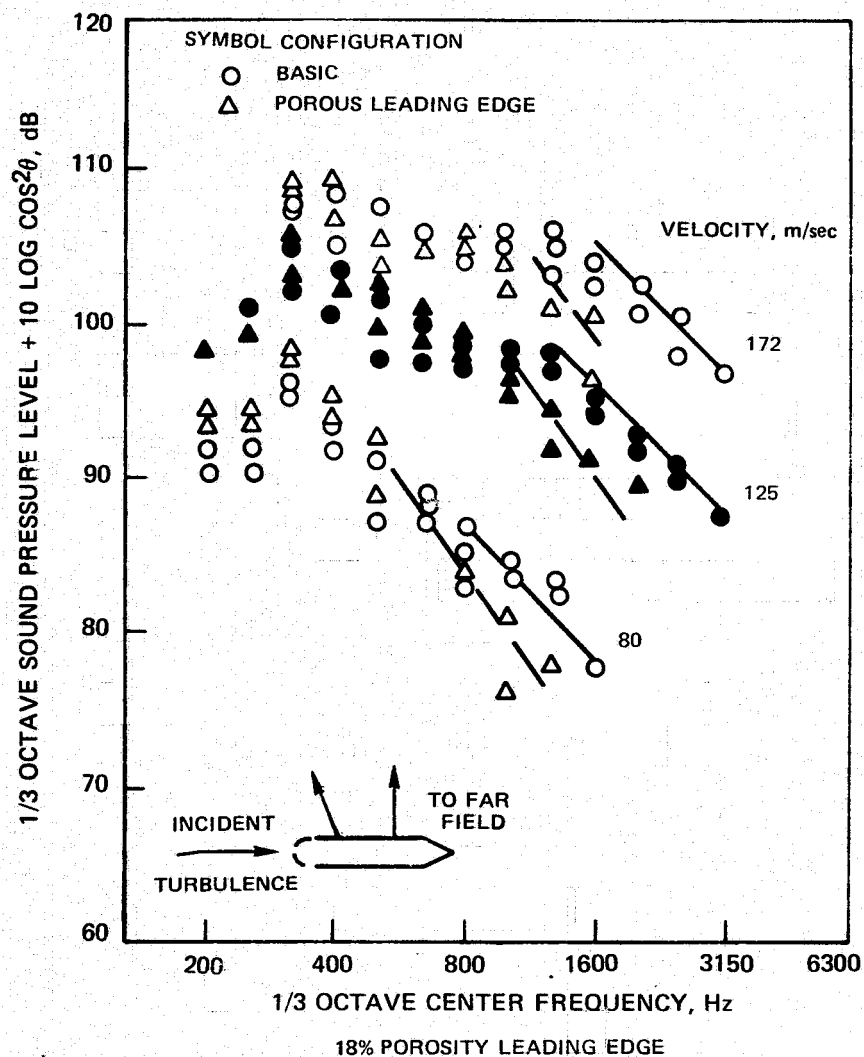
FIGURE 48 – EFFECT OF POROUS LEADING EDGE ON INCIDENCE FLUCTUATION NOISE SPECTRA CORRECTED FOR TUNNEL BACKGROUND NOISE AND DIRECTIVITY

FIGURE 49 – EFFECT OF 18% POROSITY LEADING AND TRAILING EDGES ON SURFACE PRESSURES CAUSED BY INCIDENCE FLUCTUATION, (a) MEDIUM GRID
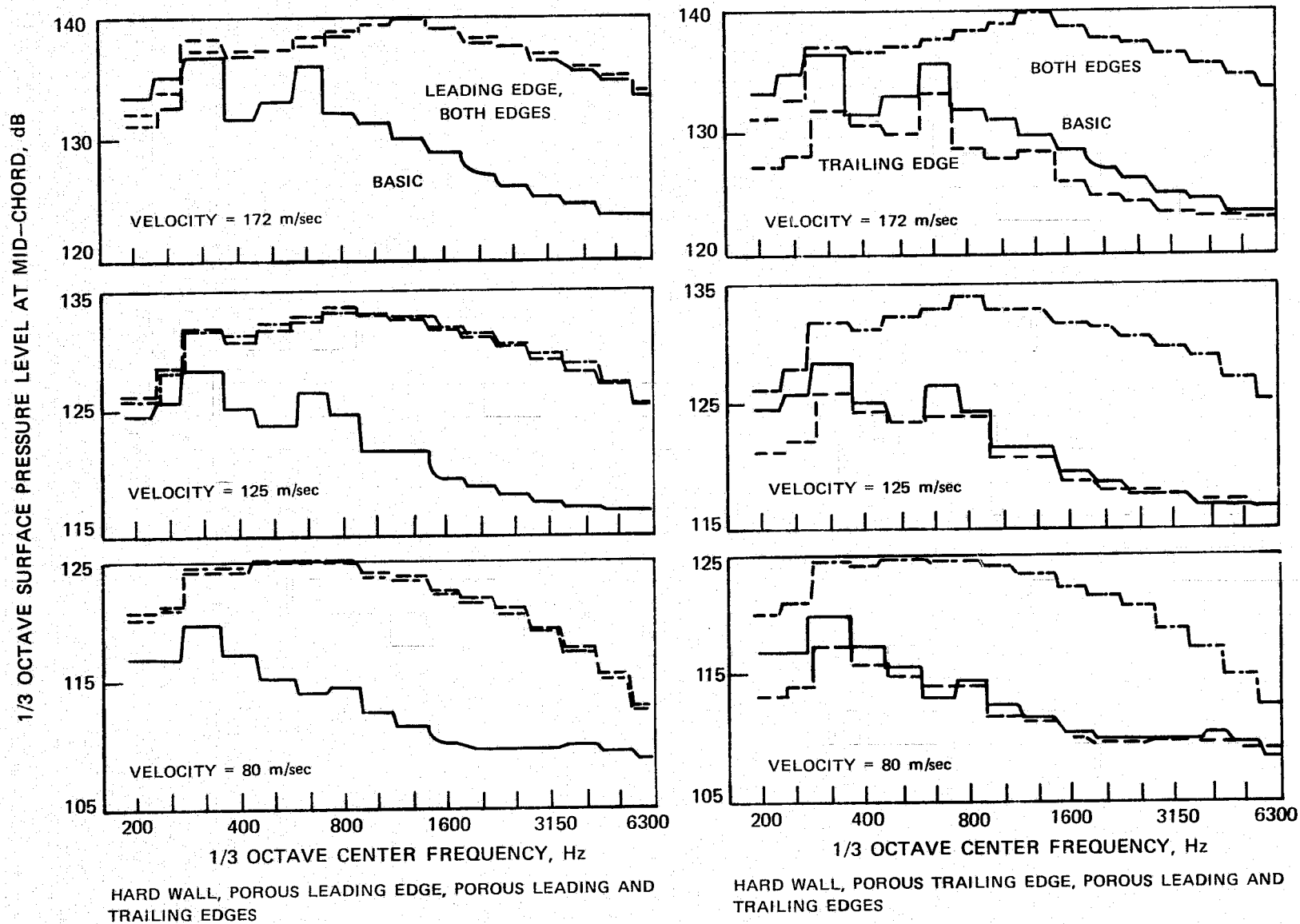
FIGURE 49 – CONCLUDED.
(b) LARGE GRID
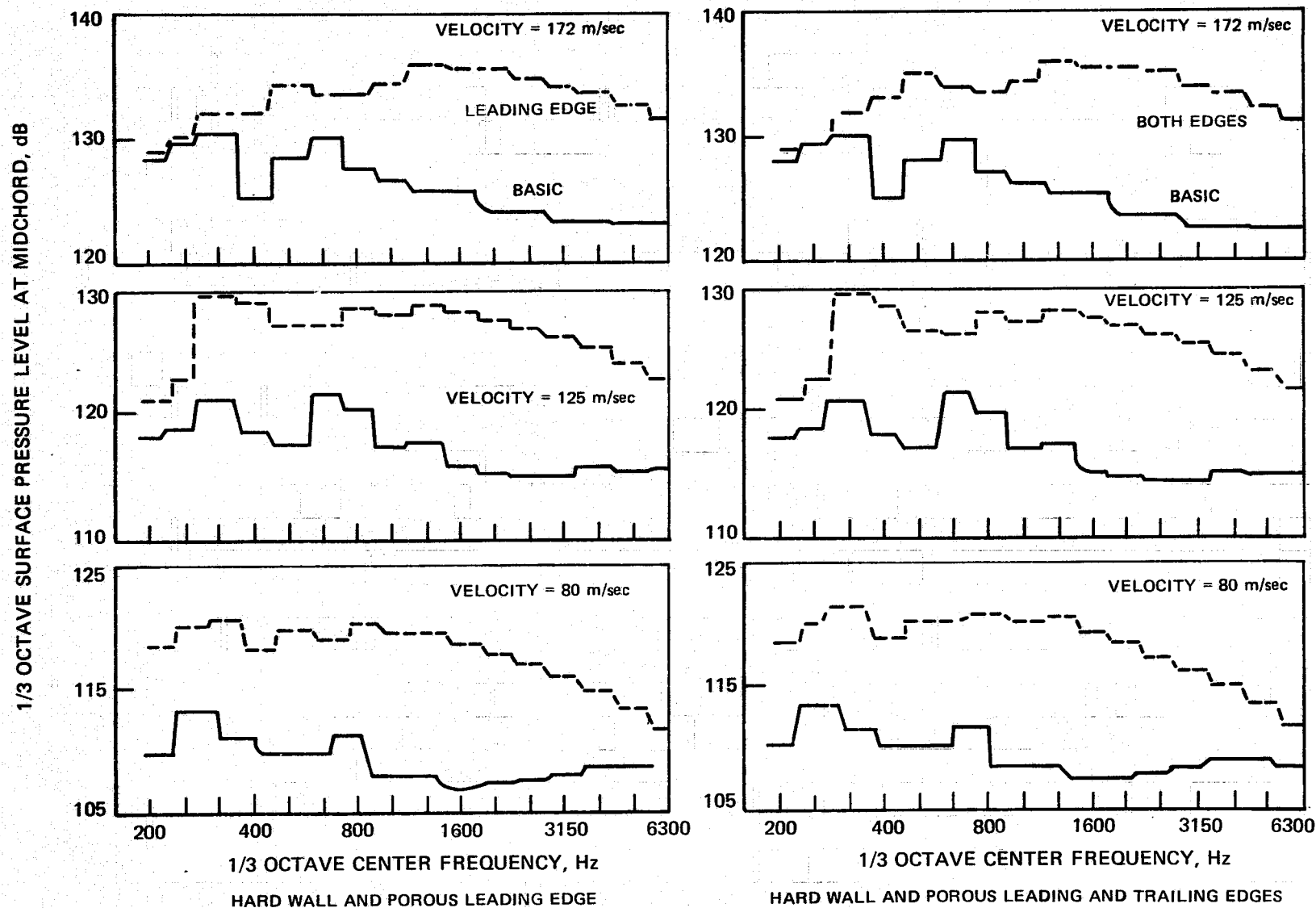
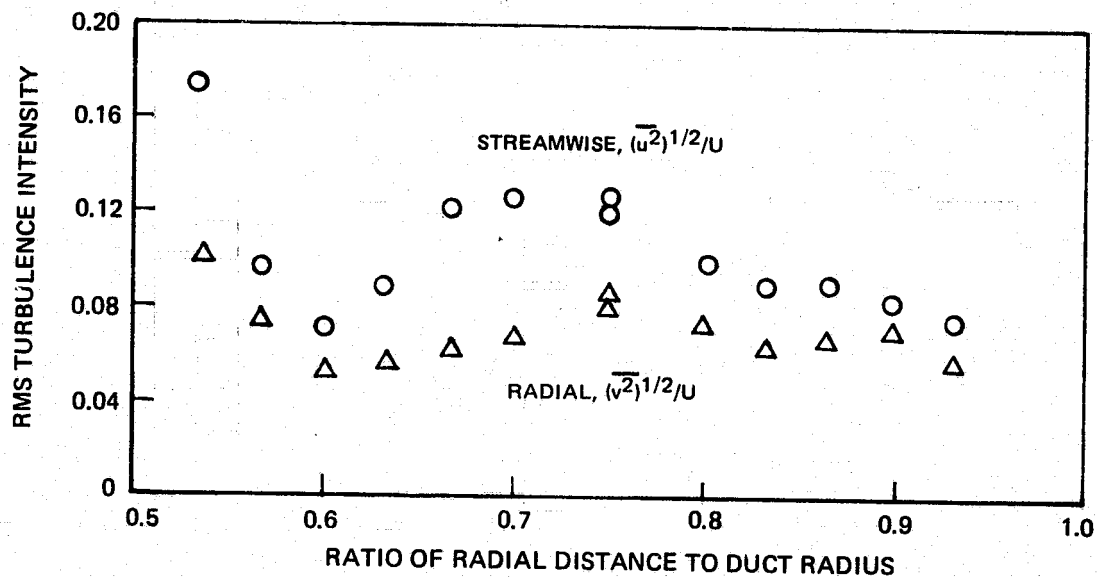FIGURE 50 — EFFECT OF 30% POROSITY LEADING AND TRAILING EDGES ON SURFACE PRESSURE CAUSED BY INCIDENCE FLUCTUATION. (a) MEDIUM GRID

1/3 OCTAVE SURFACE PRESSURE LEVEL AT MIDCHORD, dB

1/3 OCTAVE CENTER FREQUENCY, Hz

HARD WALL, POROUS LEADING EDGE, POROUS
LEADING AND TRAILING EDGE

HARD WALL, POROUS TRAILING EDGE, POROUS
LEADING AND TRAILING EDGE
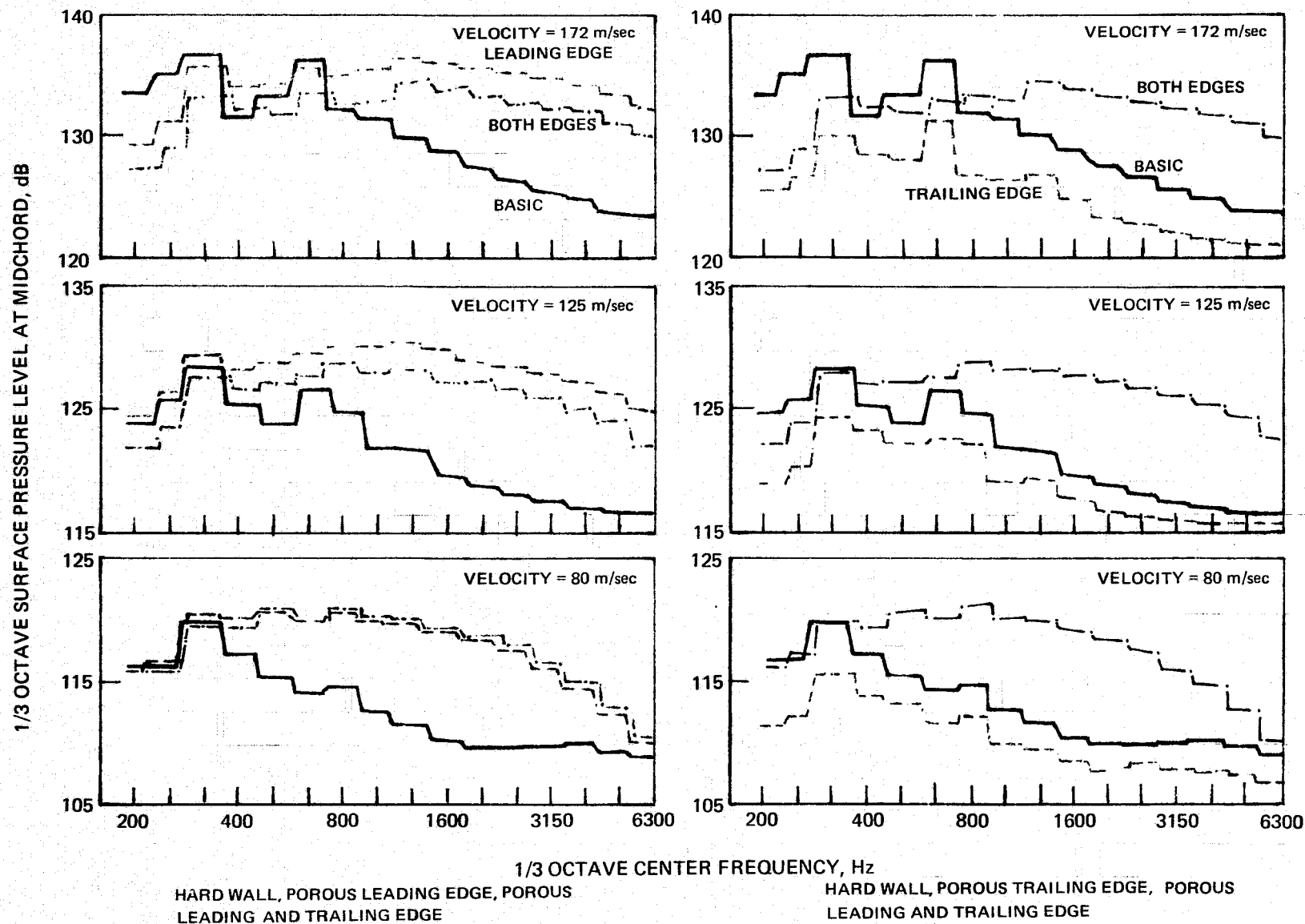
FIGURE 50 – CONCLUDED (b) LARGE GRID
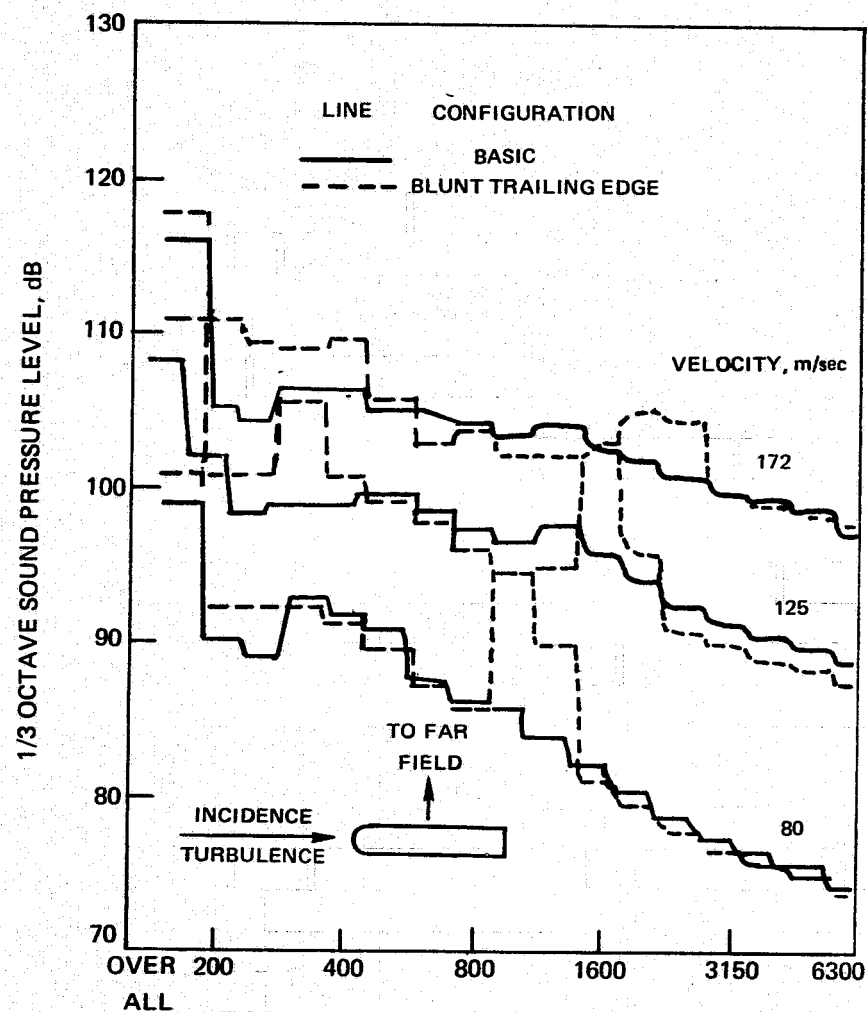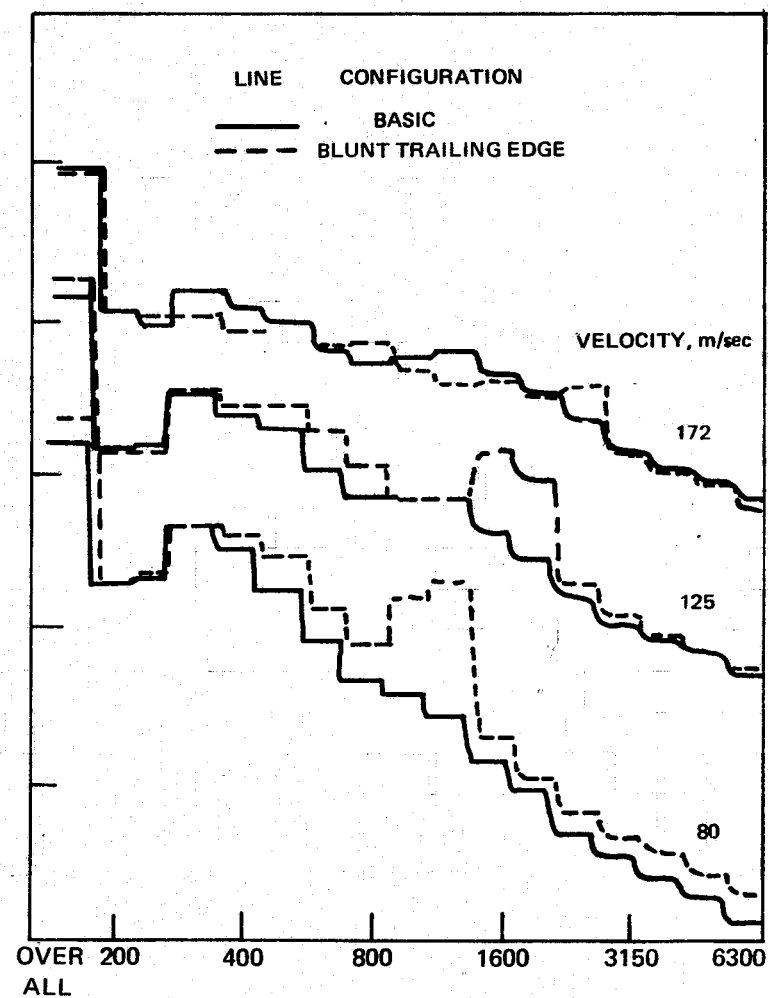
FIGURE 51 – EFFECT OF BLUNT TRAILING EDGE ON SOUND CAUSED BY INCIDENCE FLUCTUATION
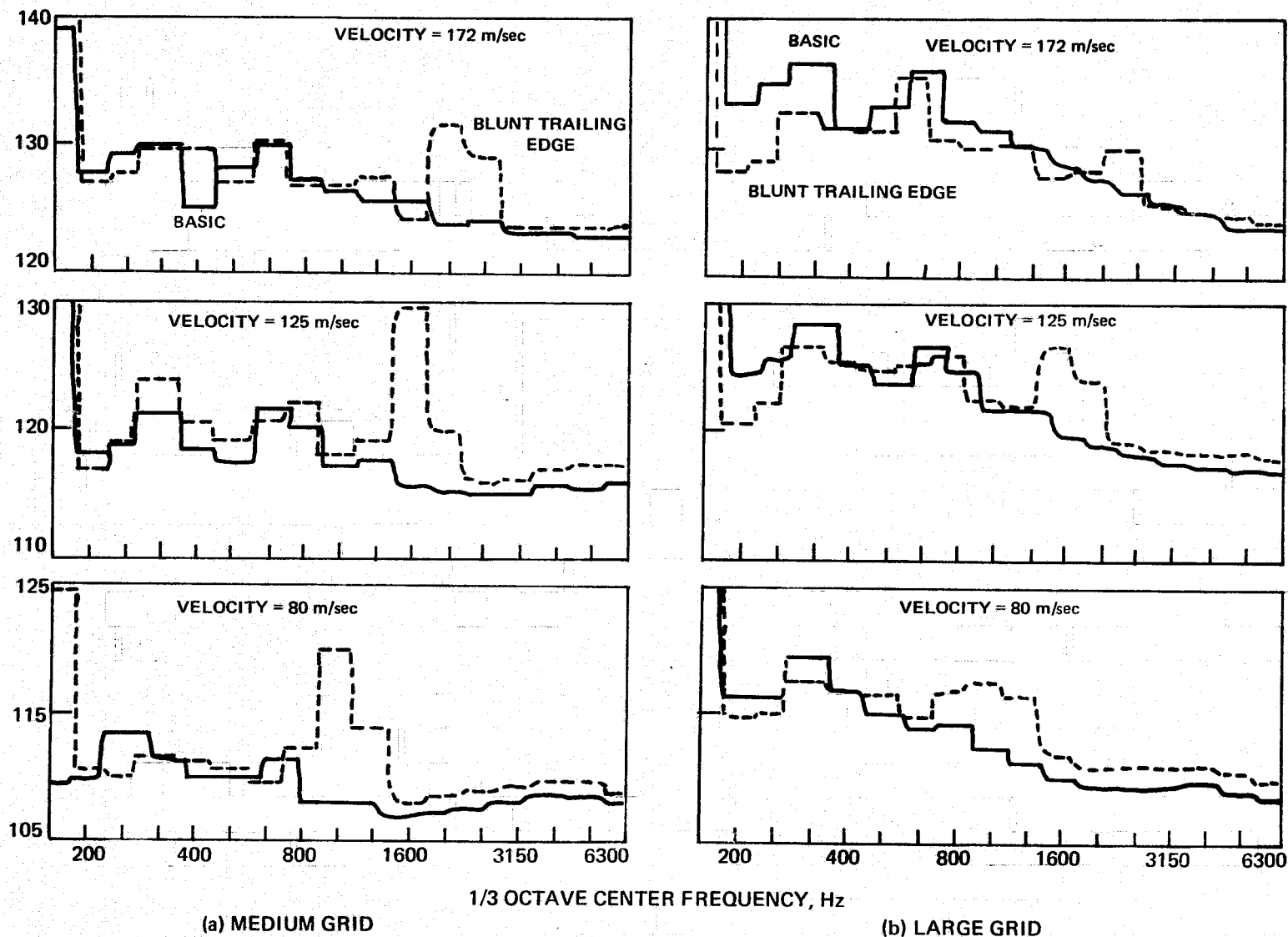
FIGURE 52 – EFFECT OF BLUNT TRAILING EDGE ON SURFACE PRESSURES CAUSED BY
INCIDENCE FLUCTUATION
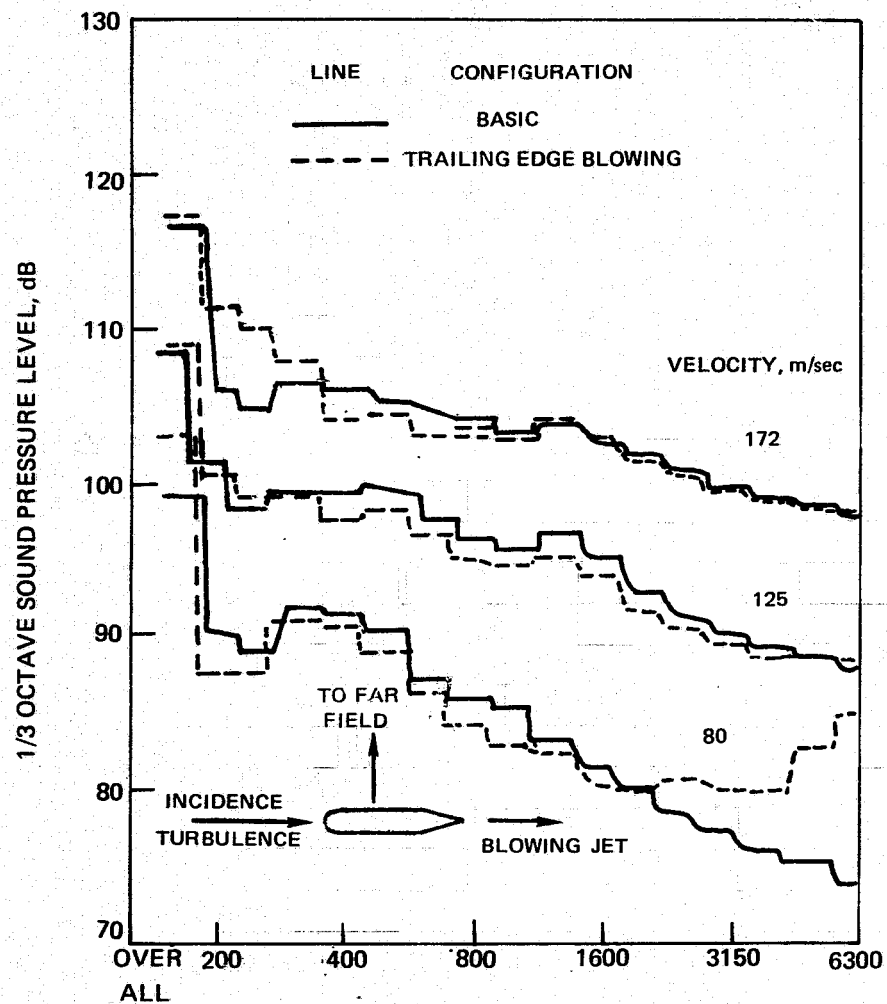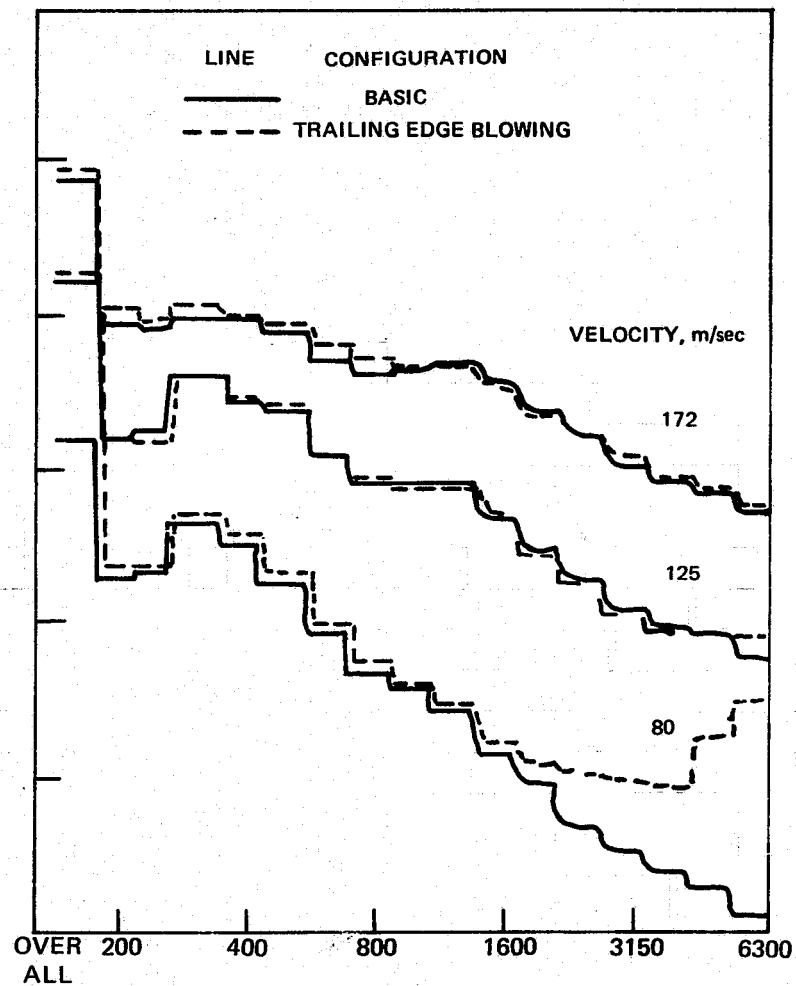
FIGURE 53 – EFFECT OF TRAILING EDGE BLOWING ON SOUND CAUSED BY INCIDENCE FLUCTUATION
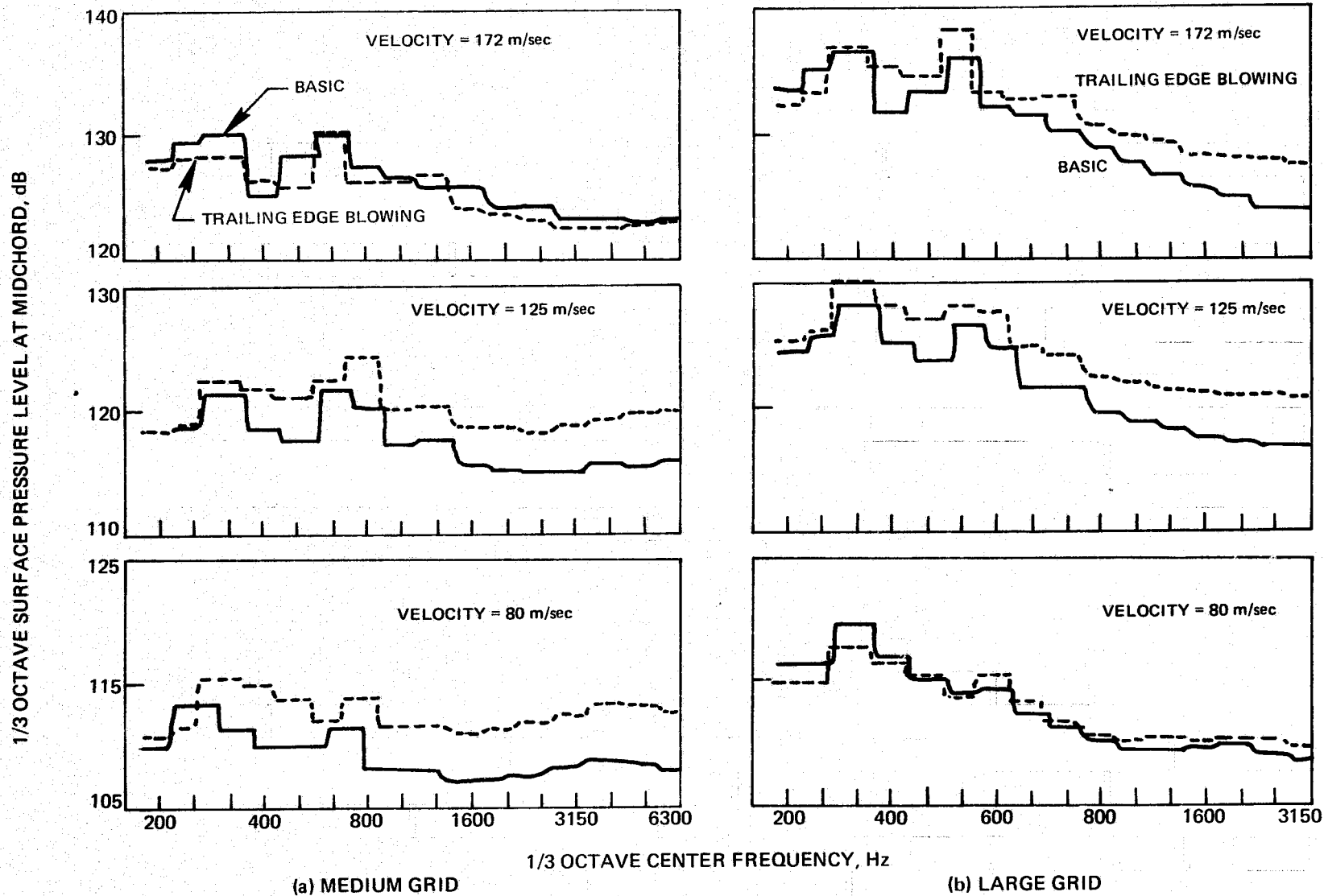
FIGURE 54 – EFFECT OF TRAILING EDGE BLOWING ON SURFACE PRESSURES CAUSED BY INCIDENCE FLUCTUATION
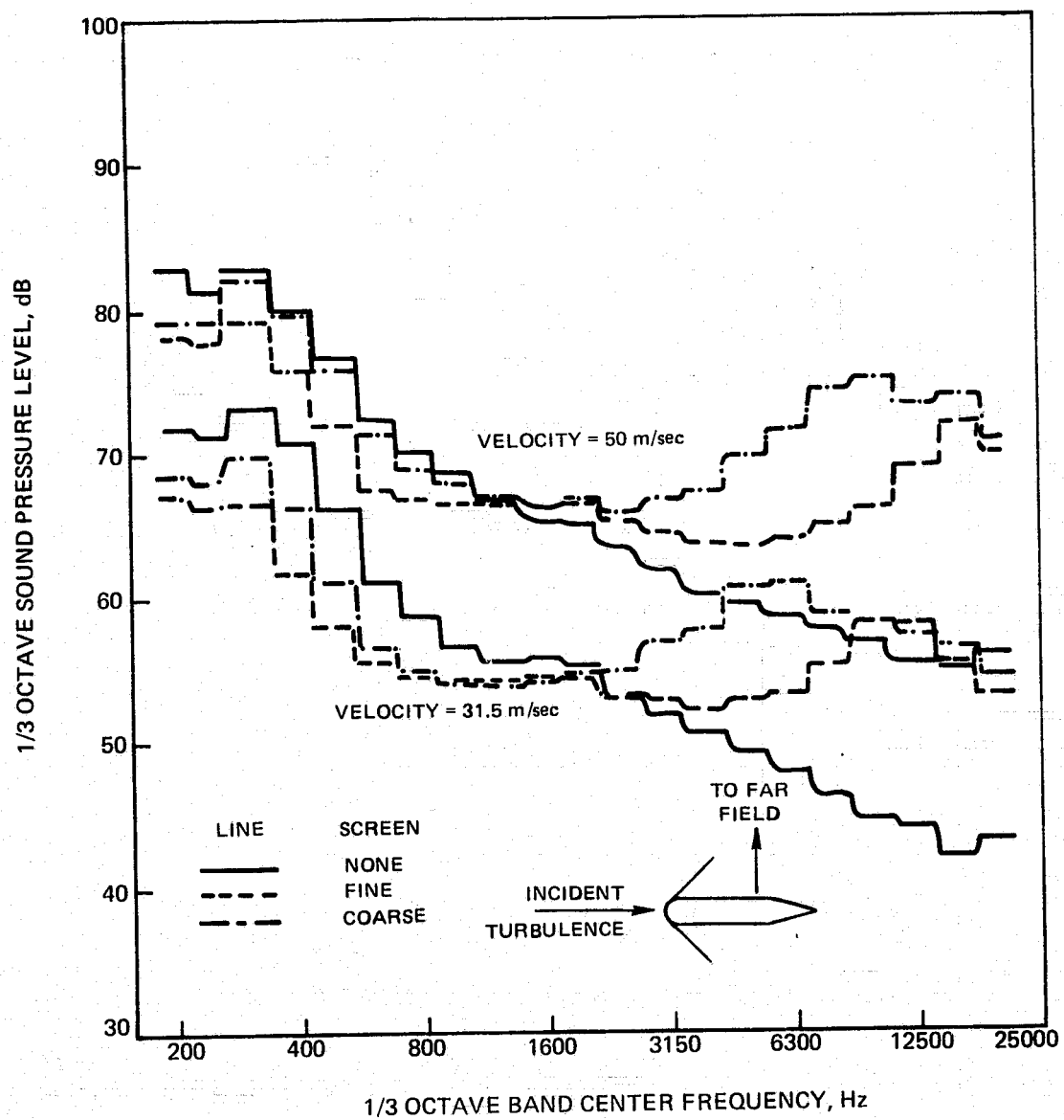
FIGURE 55 — EFFECT OF LEADING EDGE SCREEN ON SOUND CAUSED BY INCIDENCE
FLUCTUATION
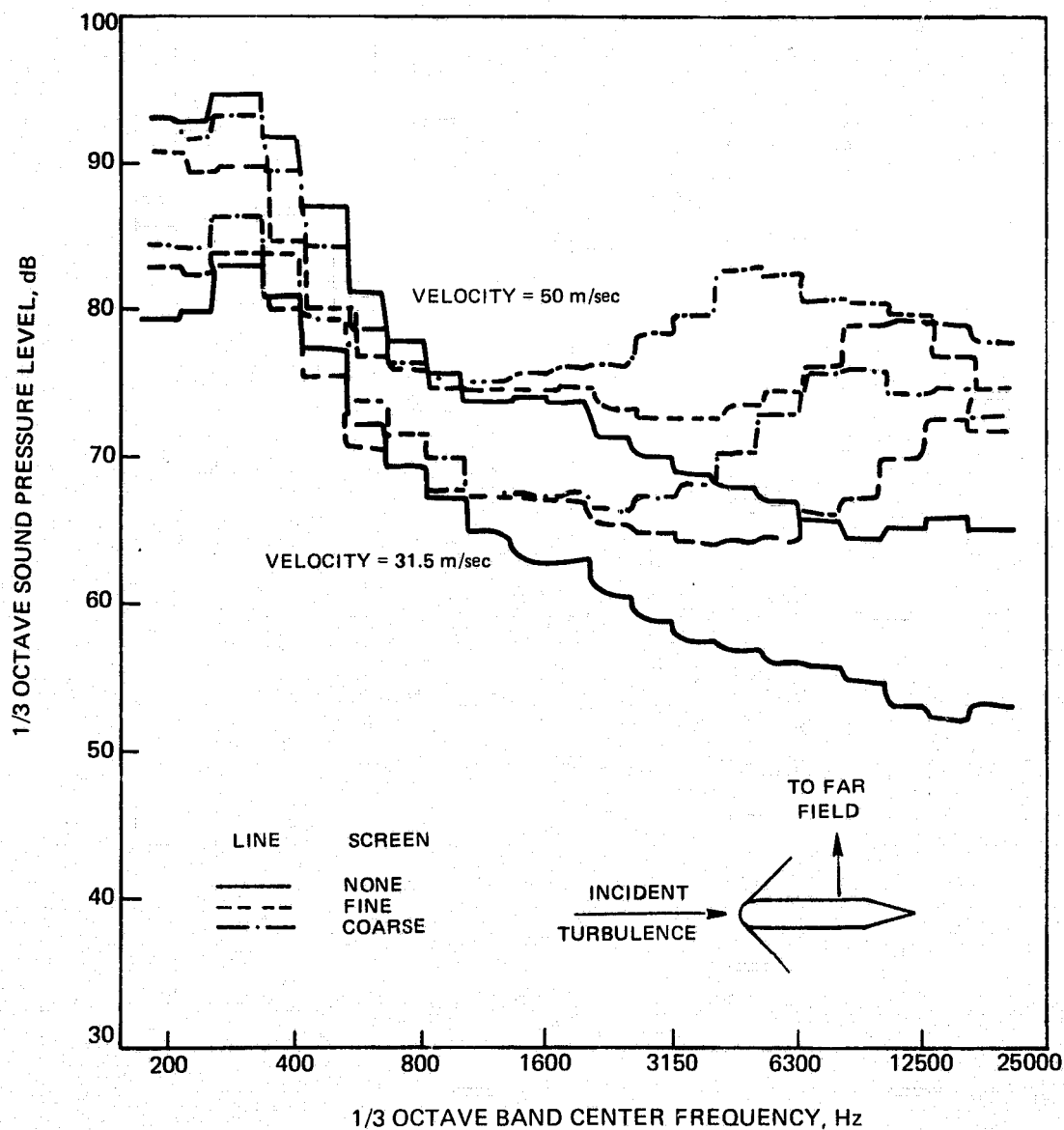
(a) MEDIUM GRID

FIGURE 55 – CONCLUDED (b) LARGE GRID
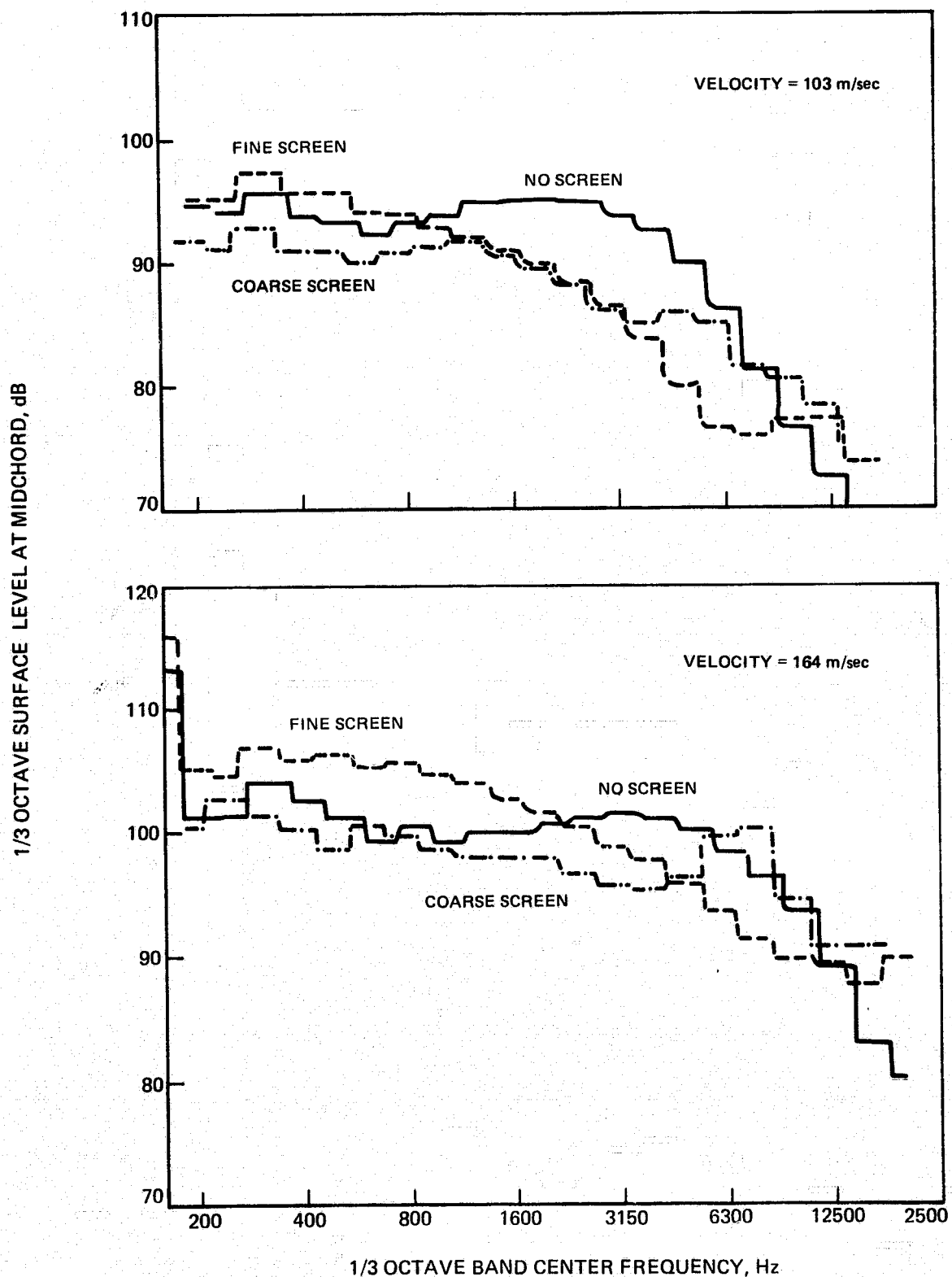
FIGURE 56 – EFFECT OF LEADING EDGE SCREEN ON SURFACE PRESSURES CAUSED BY INCIDENCE FLUCTUATION (a) MEDIUM GRID
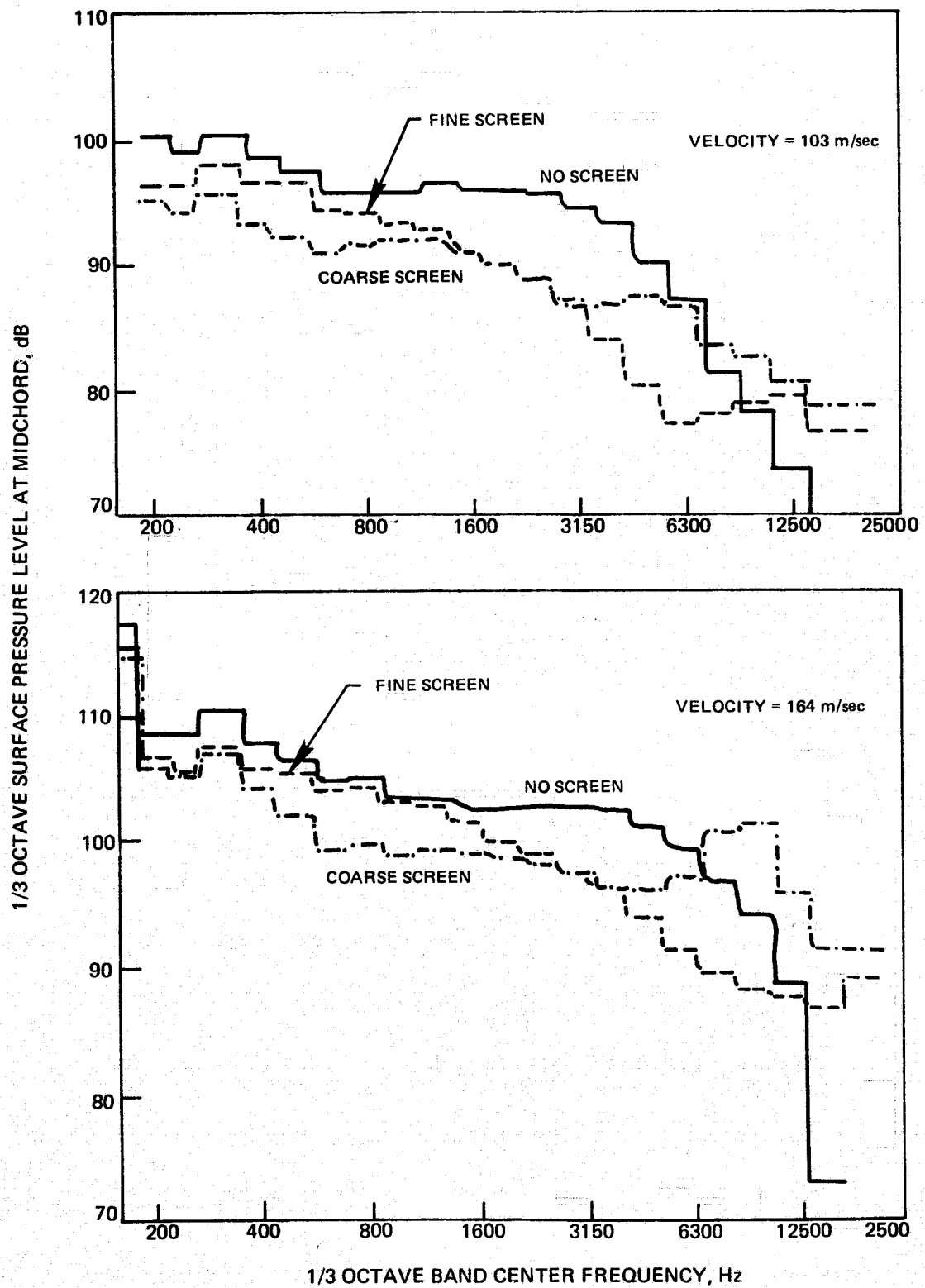
FIGURE 56 – CONCLUDED (b) LARGE GRID
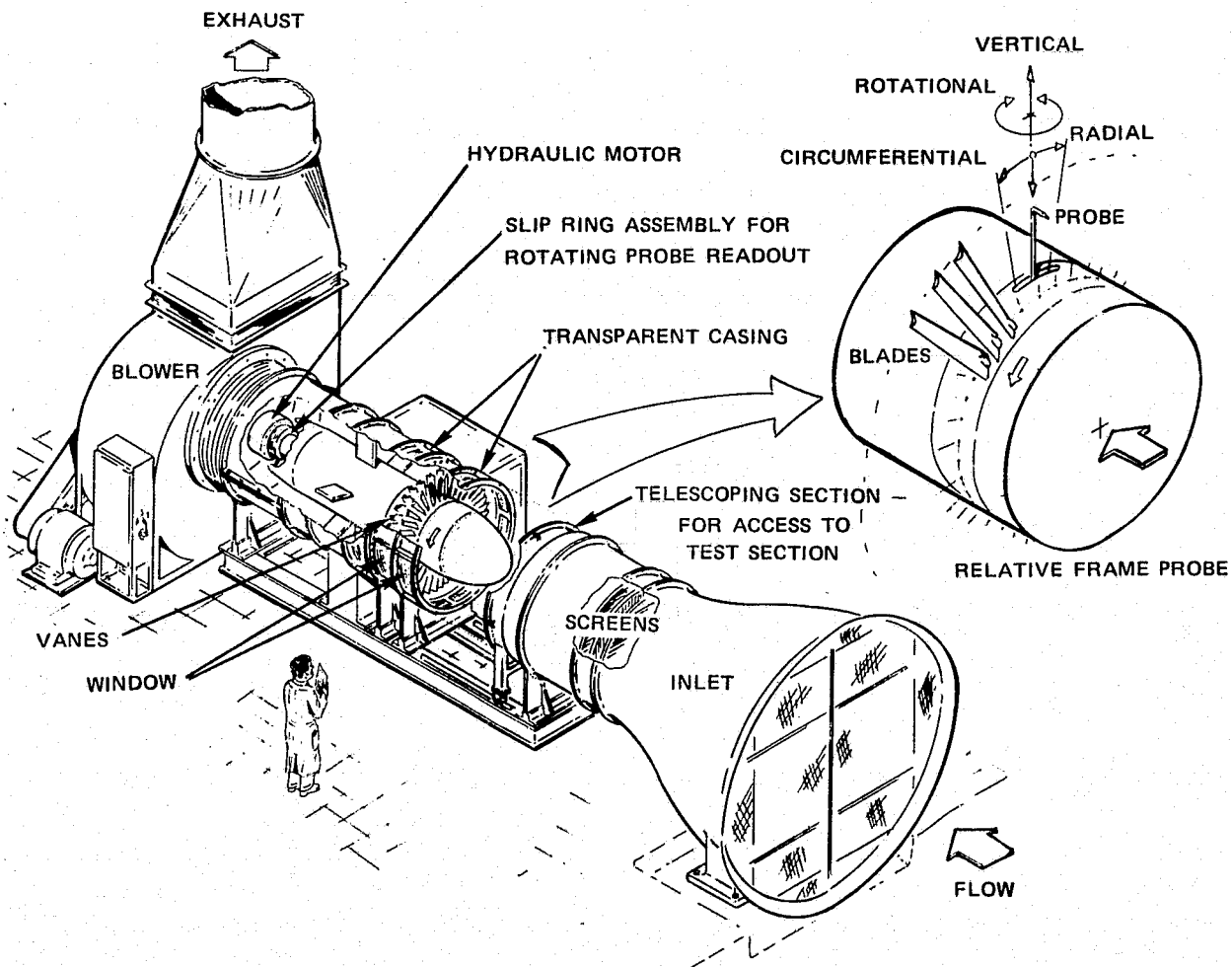
FIGURE 57 — UTRC LARGE SCALE ROTATING RIG
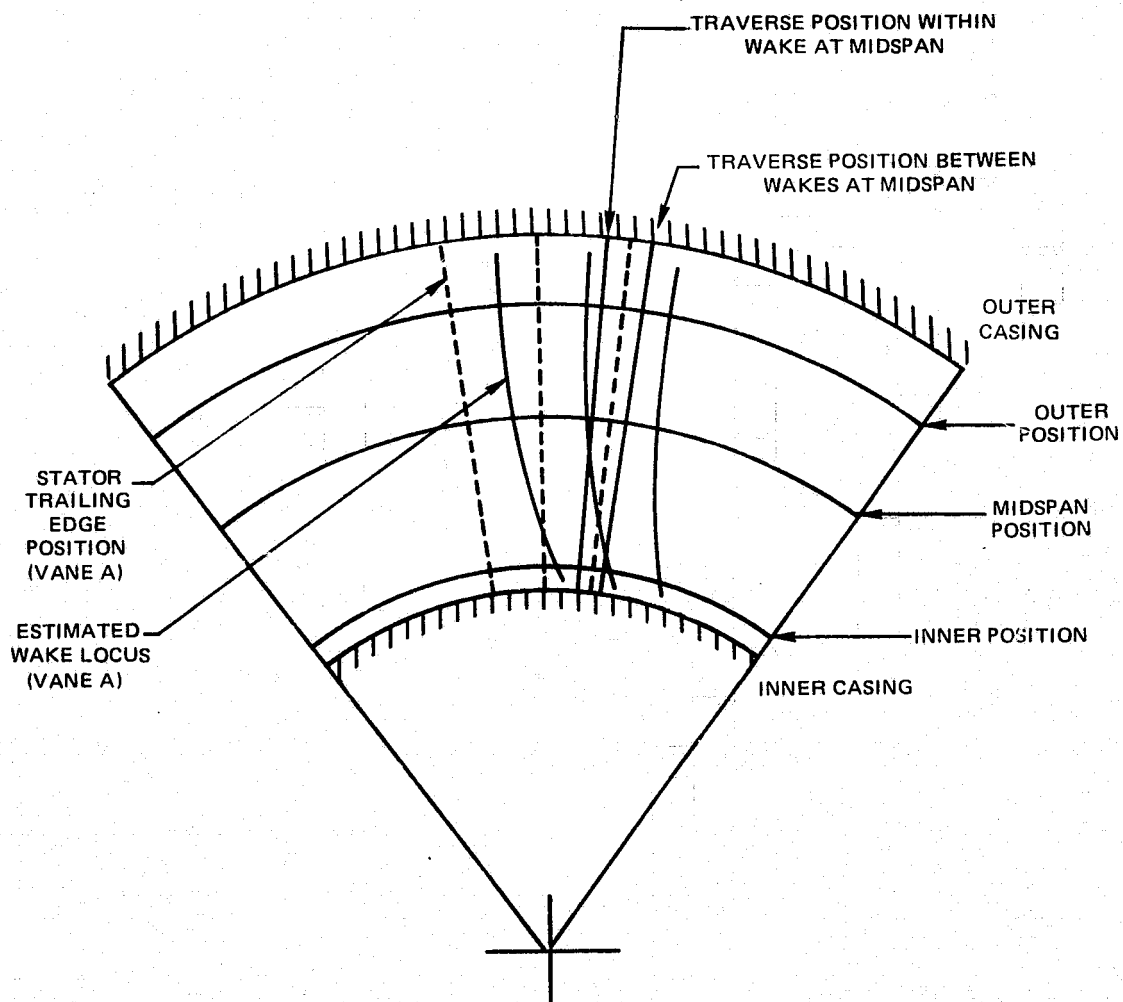
AXIAL VIEW OF LARGE SCALE ROTATING RIG, LOOKING UPSTREAM, DOWNSTREAM OF STATORS

FIGURE 58 – POSITION OF RADIAL TRAVERSE RELATIVE TO STATOR TRAILING EDGES AND STATOR WAKES
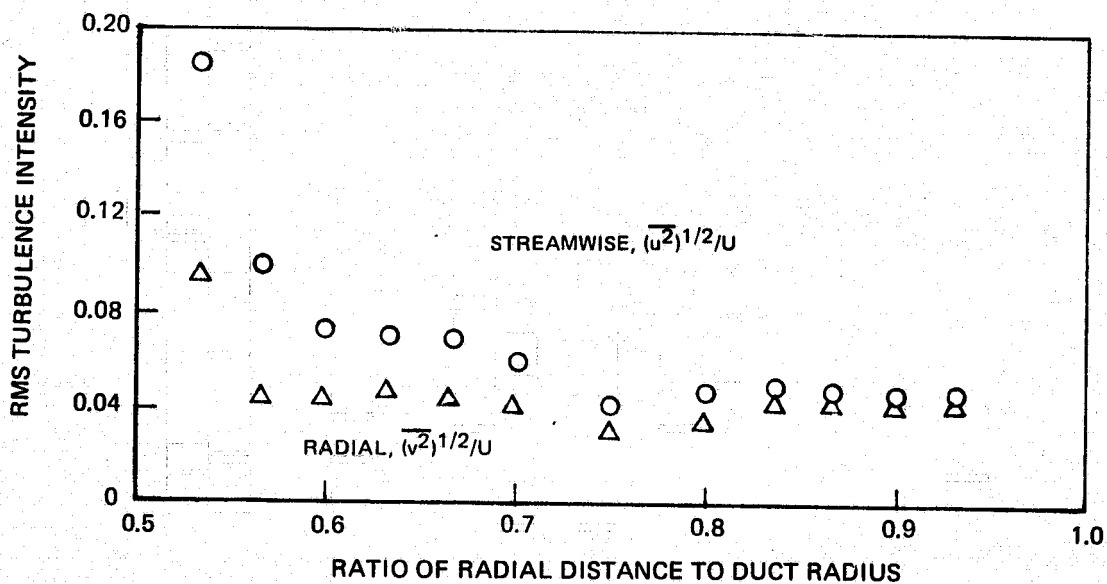
R07–131–4

FIGURE 59 – RADIAL VARIATIONS OF STREAMWISE AND RADIAL TURBULENCE
INTENSITIES ACROSS FAN EXIT DUCT

NORMALIZED CROSSCORRELATION OF RADIAL VELOCITY

OUTER REGION

INTEGRAL SCALE
LENGTH = 5.0 cm

0.5

0

1.0

MIDSPAN REGION

INTEGRAL SCALE
LENGTH = 3.5 cm

0.5

0

1.0

INNER REGION

INTEGRAL SCALE
LENGTH = 1.5 cm

0.5

0

0   4   8   12   16

RADIAL DISTANCE BETWEEN PROBES, cm
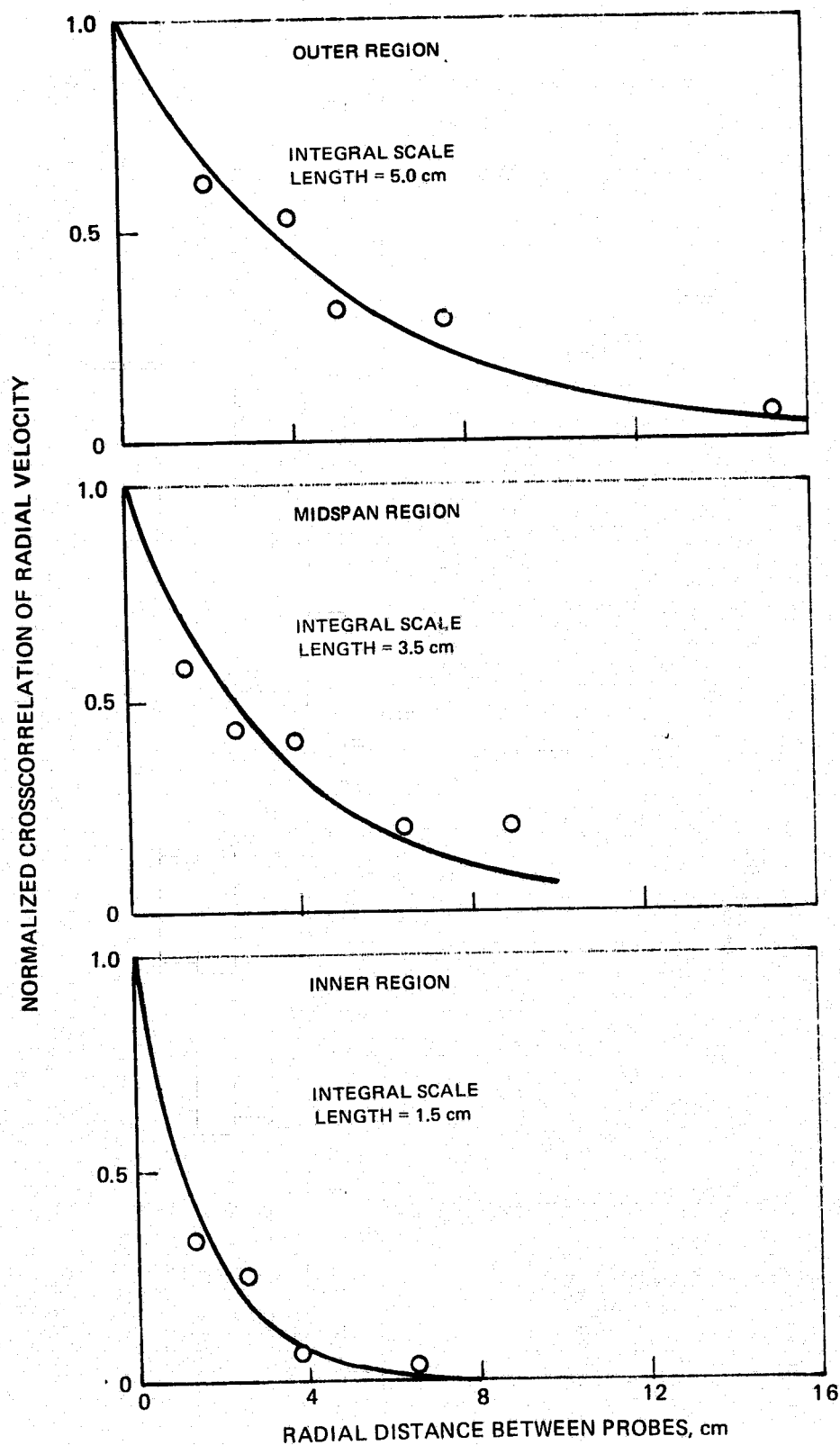
FIGURE 60 — RADIAL CROSSCORRELATION OF RADIAL TURBULENCE IN FAN
EXIT DUCT BETWEEN STATOR WAKES

R07—131—6
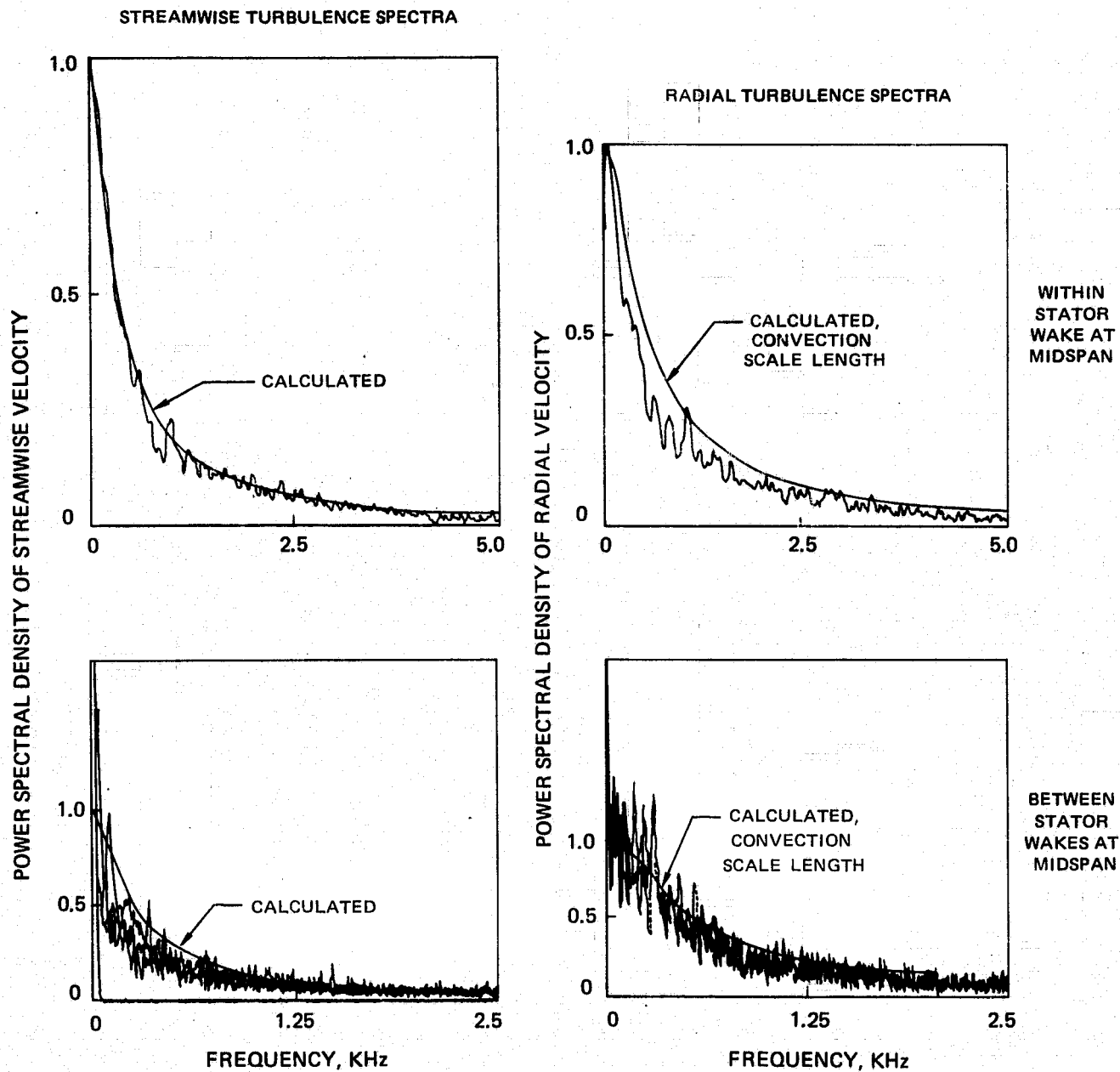
FIGURE 61 — COMPARISON OF MEASURED STREAMWISE AND RADIAL TURBULENCE SPECTRA
WITH THOSE CALCULATED FROM MEASURED INTEGRAL SCALE LENGTH
(a) — OUTER POSITION
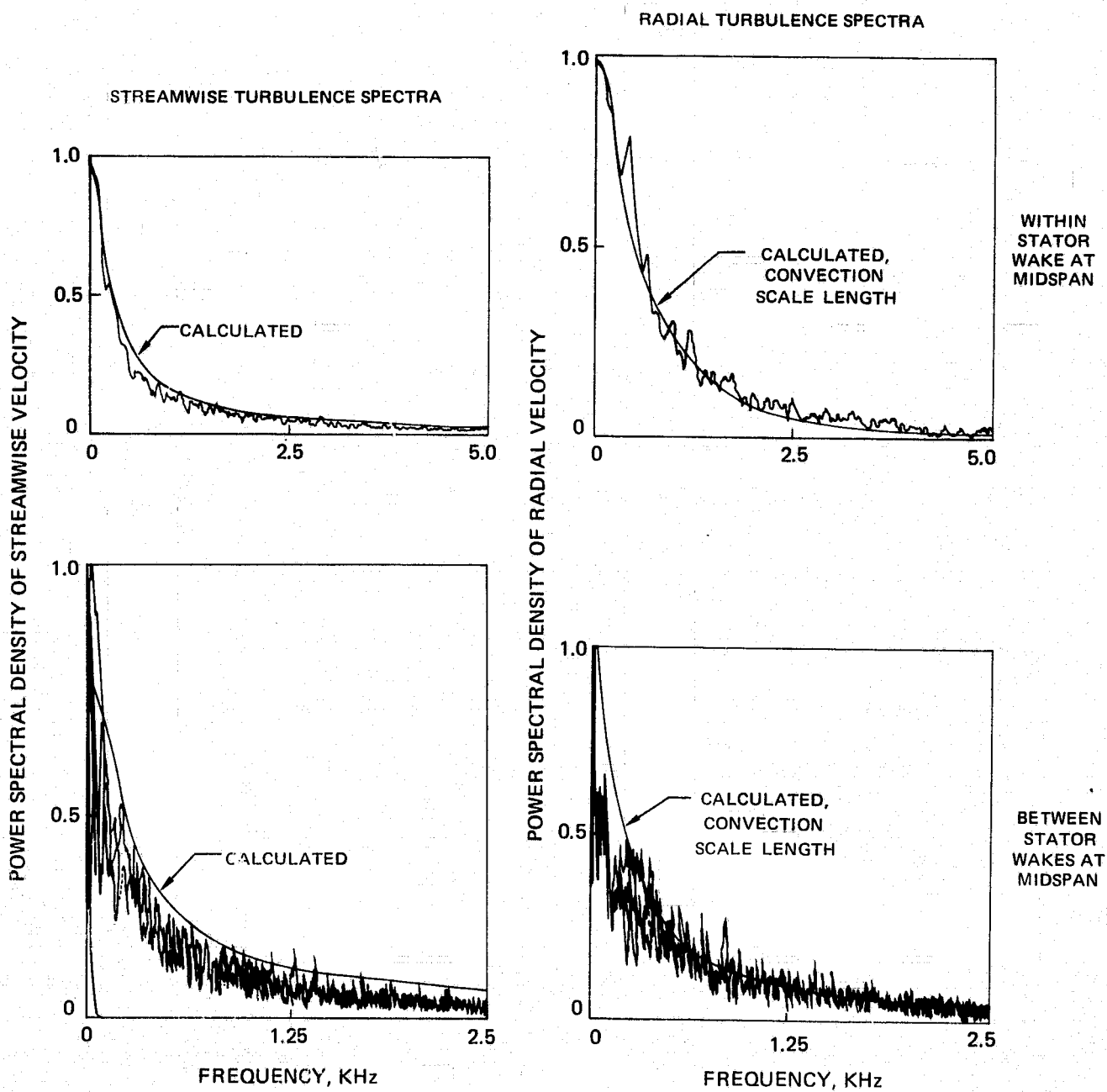
FIGURE 61 — CONTINUED (b) MIDSPAN POSITION

R07—131—1
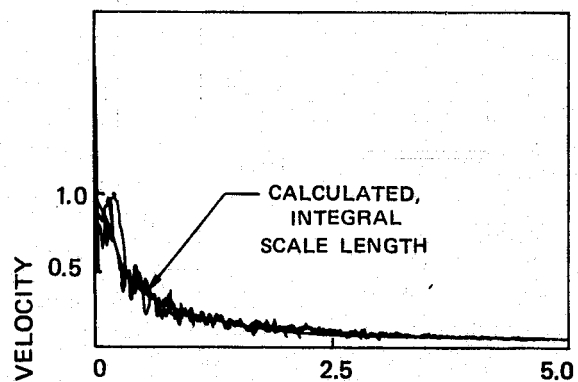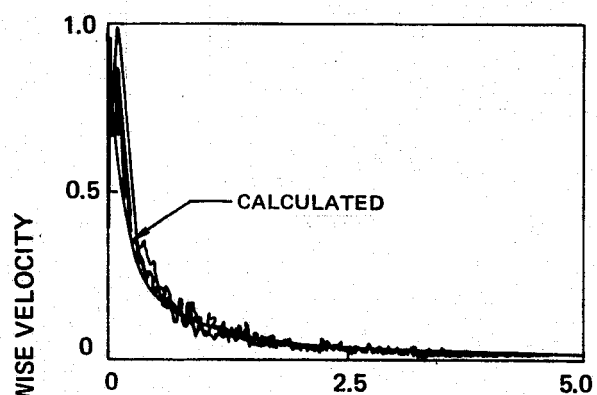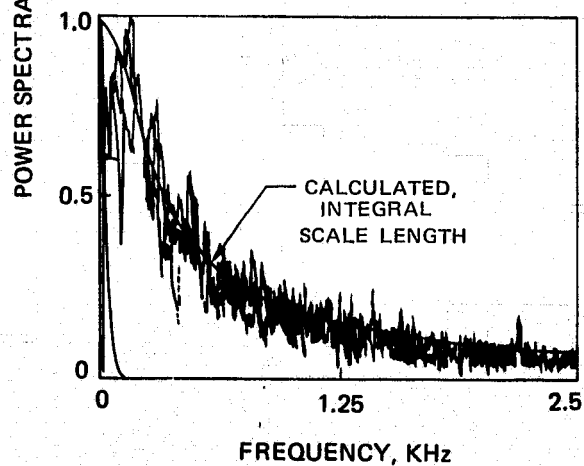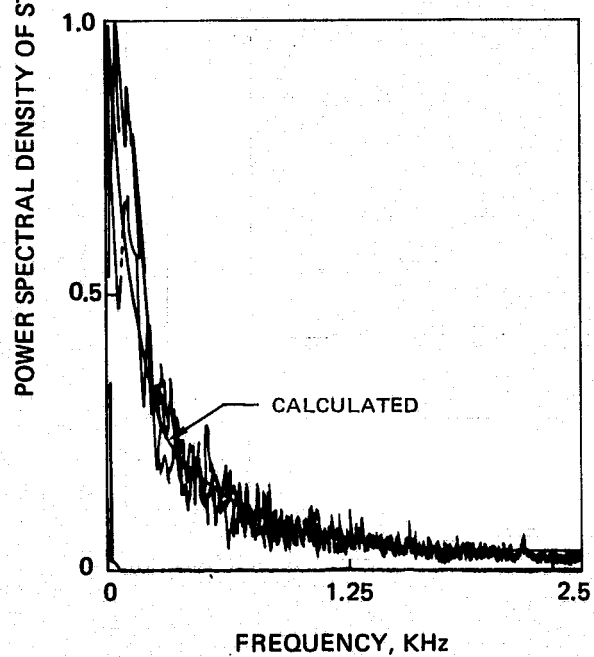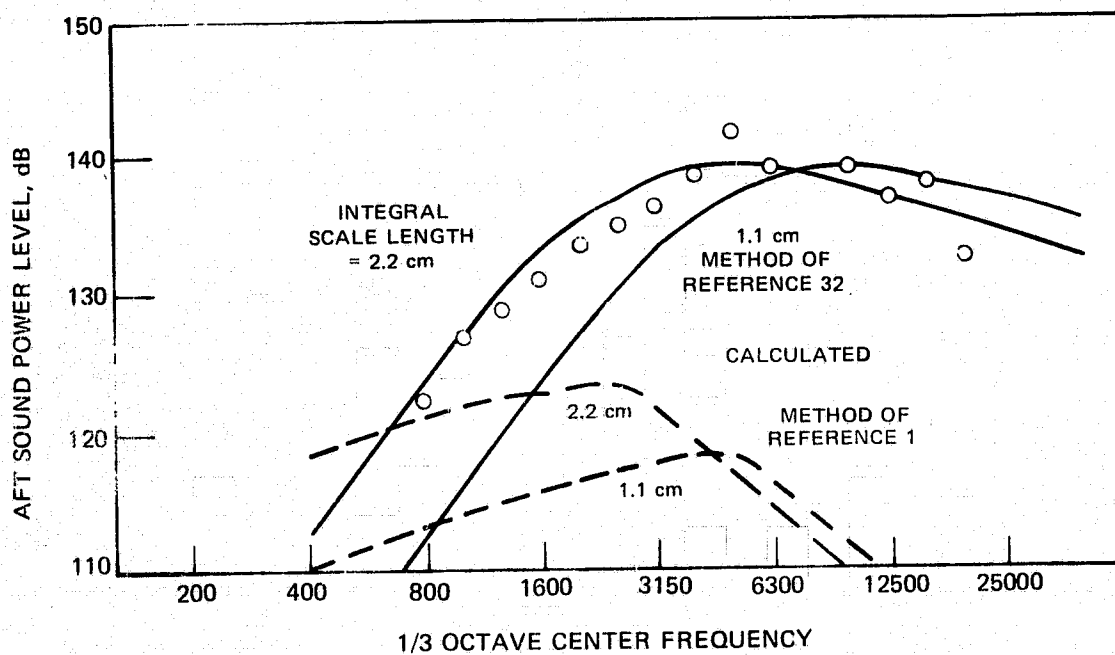
FIGURE 61 — CONCLUDED (c) INNER POSITION
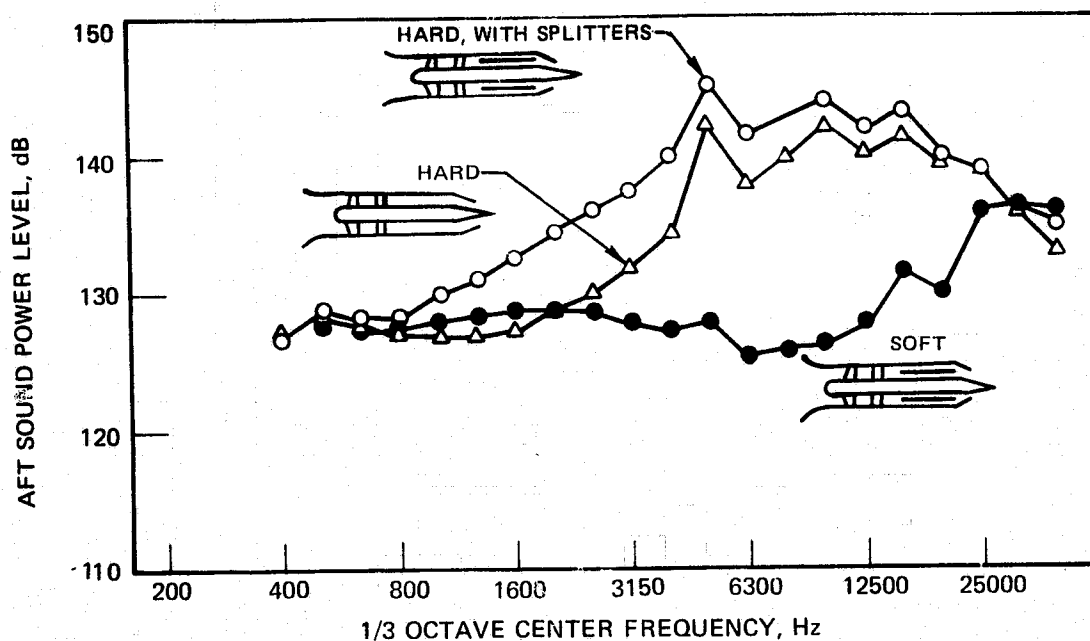
(a) EFFECT OF PASSAGE GEOMETRY ON AFT SOUND POWER LEVEL

(b) COMPARISON OF CALCULATED AND MEASURED INCREASE
OF AFT SOUND POWER LEVEL DUE TO HARD SPLITTER

FIGURE 62 – EFFECT OF FAN EXIT DUCT SPLITTER RING ON AFT SOUND POWER LEVEL

R08–12–2